

# Computer-Support for Intracranial Aneurysms

HABILITATIONSSCHRIFT

zur Erlangung der Venia legendi für  
Computervisualistik

angenommen durch die Fakultät für Informatik  
der Otto-von-Guericke-Universität Magdeburg



von: Dr.-Ing. Sylvia Saalfeld  
geb. am 26.05.1984 in Jena

**Gutachter:**

Prof. Dr.-Ing. habil. Bernhard Preim  
Prof. Dr. rer. nat. habil. Heinz Handels  
Prof. Dr.-Ing. habil. Andreas Maier

Magdeburg, den 03.06.2020





## Computer-Support for Intracranial Aneurysms



---

## ZUSAMMENFASSUNG

---

In den letzten Jahrzehnten hat sich das junge Gebiet der interventionellen Neuro-radiologie und Neurochirurgie zur Behandlung von intrakraniellen Aneurysmen rasant entwickelt. Intrakranielle Aneurysmen sind pathologische Veränderungen der intrakraniellen Gefäßwand, die das Risiko einer Ruptur bergen. Aneurysmarupturen haben oft tödliche Folgen für den Patienten, die Behandlung selbst ist jedoch kompliziert und ebenfalls mit Risiken verbunden. Die Berechnung des Rupturrisikos ist daher ein aktives Forschungsgebiet, das die Segmentierung und anschließende Extraktion von 3D Modellen zur Ableitung von morphologischen und hämodynamischen Eigenschaften sowie die Auswertung der verfügbaren Informationen beinhaltet. Diese Auswertung vereint Klassifizierungsansätze und Visualisierungsalgorithmen, die ein besseres Verständnis der morphologischen und hämodynamischen Besonderheiten des Aneurysmas ermöglichen. Eine arzt- und patientengerechte Aufbereitung der Daten unterstützt dabei die letztlich gemeinsam zu treffende Entscheidung, ob und wie behandelt wird. Die Anwendungsgebiete beinhalten jedoch nicht nur die Beurteilung des Rupturrisikos, sondern auch die Planung von Behandlung und Therapie sowie mögliche Trainingsszenarien.

Für diese Aufgaben ist eine Computer-Unterstützung unabdingbar. In dieser kumulativen Habilitationsschrift werden verschiedene Techniken vorgestellt, die diese Anwendungsbereiche abdecken. Alle Ansätze wurden in meiner Post-Doc-Phase entwickelt und in enger Zusammenarbeit und im interdisziplinären Austausch mit medizinischen Experten realisiert.



---

## ABSTRACT

---

Within the last decades, the young field of interventional neuroradiology and neurosurgery for the treatment of intracranial aneurysms has undergone a rapid and notable improvement. Intracranial aneurysms are pathologic dilations of the intracranial vessel wall that bear the risk of rupture. Aneurysm rupture often yields fatal consequences for the patient, however, treatment itself is complicated and may be accompanied by risks as well. To determine the intracranial aneurysm rupture risk is an active research area, including computer support for the segmentation and subsequent extraction of 3D morphological shape information, paving the way for realistic hemodynamic blood flow simulations as well as the evaluation of the available information. The evaluation comprises classification approaches as well as visualization algorithms that allow a better understanding of the aneurysm's morphological and hemodynamical attributes. A proper analysis of the patient-specific aneurysm supports the physician and the patient regarding the joint decision whether and how it should be treated. Application areas do not only cover the aforementioned aneurysm rupture risk assessment but also the planning of treatment and therapy as well as possible training scenarios.

Computer support for these tasks is mandatory and in this cumulative habilitation thesis, various techniques are presented that cover these application areas. All approaches were developed during my post-doc phase and were realized in close collaboration and interdisciplinary exchange with medical experts.



---

## CONTENTS

---

1	COMPUTER SUPPORT FOR INTRACRANIAL ANEURYSMS	1
1.1	Previous Studies Regarding Intracranial Aneurysms at the Otto-von-Guericke University and the Visualization Group	1
1.2	Embedment in Computational Visualistics	3
1.3	Medical Background	3
1.3.1	Intracranial Arteries	4
1.3.2	Intracranial Aneurysms	5
1.3.3	Treatment of Intracranial Aneurysms	8
1.3.4	Medical Imaging in the Clinical Practice	10
1.4	Computer Support for Treatment and Therapy Planning	10
1.4.1	Medical Imaging in Clinical Research	11
1.4.2	Segmentation of Vessel Surface Models	17
1.4.3	Simulation of the Intracranial Blood Flow	19
1.4.4	Computer-Supported Evaluation	22
1.4.5	Therapy Planning	29
1.5	Outlook	34
<b>I</b>	<b>Cumulative Part - Imaging</b>	<b>37</b>
2	EXPERIMENTAL INVESTIGATION OF INTRAVASCULAR OCT FOR IMAGING OF INTRACRANIAL ANEURYSMS	39
3	VIRTUAL INFLATION OF THE CEREBRAL ARTERY WALL FOR THE INTEGRATED EXPLORATION OF OCT AND HISTOLOGY DATA	51
4	FLUID-STRUCTURE SIMULATIONS OF A RUPTURED INTRACRANIAL ANEURYSM	63
<b>II</b>	<b>Cumulative Part - Segmentation and Simulation</b>	<b>71</b>
5	FROM IMAGING TO HEMODYNAMICS – HOW RECONSTRUCTION KERNELS INFLUENCE THE BLOOD FLOW PREDICTIONS IN INTRACRANIAL ANEURYSMS	73

6 SEMIAUTOMATIC NECK CURVE RECONSTRUCTION FOR INTRACRANIAL ANEURYSM RUPTURE RISK ASSESSMENT BASED ON MORPHOLOGICAL PARAMETERS 79

7 FLOW-SPLITTING-BASED COMPUTATION OF OUTLET BOUNDARY CONDITIONS FOR INTRACRANIAL ARTERIES 93

**III Cumulative Part - Visual Exploration and Evaluation 103**

8 COMBINING PSEUDO CHROMADEPTH ENHANCEMENT AND PARAMETER MAPPING FOR VASCULAR SURFACE MODELS 105

9 THE FAUST FRAMEWORK: FREE-FORM ANNOTATIONS ON UNFOLDING VASCULAR STRUCTURES FOR TREATMENT PLANNING 115

10 GUIDELINES FOR QUANTITATIVE EVALUATION OF MEDICAL VISUALIZATIONS ON THE EXAMPLE OF 3D ANEURYSM SURFACE COMPARISONS 127

11 EXPLORATIVE BLOOD FLOW VISUALIZATION USING DYNAMIC LINE FILTERING BASED ON SURFACE FEATURES 141

12 RUPTURE STATUS CLASSIFICATION OF INTRACRANIAL ANEURYSMS USING MORPHOLOGICAL PARAMETERS 155

13 MULTIPLE ANEURYSMS ANATOMY CHALLENGE 2018 (MATCH)—PHASE II: RUPTURE RISK ASSESSMENT 161

A APPENDIX 171

A.1 Contribution 171

A.2 List of Further Research Papers 174

BIBLIOGRAPHY 177

---

## COMPUTER SUPPORT FOR INTRACRANIAL ANEURYSMS

---

The presented postdoctoral thesis introduces methods for the computer-supported improvement of interventional neuroradiology and neurosurgery with focus on intracranial aneurysms (IAs). This chapter serves as an introduction to this cumulative thesis including the explanation of previous studies at the Otto-von-Guericke University of Magdeburg especially at the Visualization group, its embedding in computer visualistics as well as an overview about the state of the art. This overview also incorporates the discussion of the publications forming the subsequent cumulative Parts [I](#), [II](#), and [III](#).

### 1.1 PREVIOUS STUDIES REGARDING INTRACRANIAL ANEURYSMS AT THE OTTO-VON-GUERICKE UNIVERSITY AND THE VISUALIZATION GROUP

The model-based evaluation and hemodynamic simulation of intracranial aneurysms started in 2007 within the interdisciplinary federal research project MOBESTAN (Modellierung und Beeinflussung von Strömungen in Aneurysmen) as joint cooperation between Prof. Martin Skalej, clinical director of the Neuro-radiology Department of the University hospital Magdeburg, Prof. Georg Rose, chair of Medical Engineering, Prof. Dominique Thévenin, chair of Fluid Dynamics and Technical Flows, Prof. Klaus Tönnies, chair of Image Processing and Image Understanding, and Prof. Bernhard Preim, chair of Visualization. First steps were taken to carry out segmentations of these pathologies to allow for the computational approximation of the intracranial blood flow (Bade et al., 2007) which paved the way for two phd theses in the visualization group. Mathias Neugebauer and Rocco Gasteiger further refined the processing steps and include a visualization of the simulated blood flow based on specific cases. Hence, the focus lies on the individual evaluation of single cases due to the highly complex postprocessing. As a result, the geometrical postprocessing and the interactive visual exploration was presented by Neugebauer (2014). In addition, Gasteiger presented additional visual exploration concepts, without the focus on geometrical processing steps but rather including the evaluation of aortic blood flow visualization approaches

as well (Gasteiger, 2014). Recently, Monique Meuschke accomplished her phd thesis about the medical visualization of cerebral aneurysms as well presenting complex interactive visualization and exploration techniques for the blood flow and blood flow patterns (Meuschke, 2019). Due to the interdisciplinarity of this challenging topic, further phd projects were conducted, including the computer-aided detection of cerebral aneurysms in angiographics (Hentschke, 2013) in the image processing group or the CFD-based evaluation of patient-specific intracranial hemodynamics (Berg, 2015) in the fluid dynamics group. In addition, the visualization and visual exploration of simulated and often time-dependent flow data was evaluated within further studies of the visualization group and yielded substantial research results that were incorporated in the habilitation theses of Steffen Oeltze-Jafra and Kai Lawonn (Lawonn, 2017; Oeltze-Jafra, 2017). Both focused on various aspects of the visualization of the simulated blood flow, the major differences to previous theses were the inclusion of different virtual treatment outcomes (Oeltze-Jafra, 2017) or the focus on animated blood flow visualization and the aneurysm wall (Lawonn, 2017). My first research concerning intracranial aneurysms benefited from the already available knowledge about segmentation of suitable surface models or the visualization of the simulated blood flow. In contrast to the early results of the MOBESTAN project as well as the introduced theses, I put the focus on three aspects:

1. As induced by the state-of-the-art, intracranial aneurysms are pathological dilations of the vessel wall, thus the vessel wall should be considered accordingly. Due to the missing imaging modality of the vessel wall, comprehensive experiments were conducted, including the artificial generation of a porcine aneurysm, the usage of intravascular imaging methods (i.e., intravascular ultrasound and intravascular optical coherence tomography) and the evaluation of histological imaging on a cellular level. Furthermore, based on the cooperation with the Forensic Institute of the University hospital of Magdeburg, an analysis of intracranial aneurysms and their wall from human cadavers could be carried out. This also served as base for my approved German Research Foundation proposal GEPARD (Gefäßwandsimulation und -visualisierung zur patientenindividualisierten Blutflussvorhersage für die intrakranielle Aneurysmamodellierung) in cooperation with Dr.-Ing. Philipp Berg.
2. Rather than solely focusing on the visualization of the blood flow, many aspects of my work cover image processing methods as well. For example, the influence of different reconstruction kernels and the influence of voxel size on images as well as the subsequent segmentations and hemodynamic simulations were analysed. Also, a comprehensive postprocessing of the extracted surface meshes in order to extract morphological parameters, rupture risk predictors or additional information for a more realistic hemodynamic simulation was conducted.

3. Finally, the ultimate goal of intracranial aneurysm research is the rupture risk prediction. In order to increase the predictive power, it is of utmost interest to collect as many datasets as possible. Starting with roughly 20 datasets in 2014, I built up a database of intracranial aneurysms in collaboration with the medical experts that currently covers approx. 300 cases, which are carefully categorized and stored together with the simulated blood flow information and the additionally extracted information (e.g., reconstruction parameters, derived morphological parameters, treatment and treatment outcome information). The database is continuously growing and helped to select suitable subgroups for the various studies presented in this thesis.

## 1.2 EMBEDMENT IN COMPUTATIONAL VISUALISTICS

The interdisciplinary Computational Visualistics degree programme at the Otto-von-Guericke University of Magdeburg focuses on computer-based image generation and analysis. Major application subjects include medicine, biology, image information technology, construction and design as well as material science. Thus, this postdoctoral thesis is an example for such an interdisciplinary research focus. The cumulative Part I comprises studies focusing on the analysis of medical image data, i.e., the analysis of histologic data, intravascular data and computer tomographic data. Afterwards, Part II consists of studies focusing on the segmentation of 3D surface models and their subsequent evaluation w.r.t. the medical application scenario as well as analysis of computer-based hemodynamic simulations of cerebral blood flow. Thus, classical image processing was employed as well as techniques that were developed within the fluid dynamics research area. The last Part III covers a framework to support treatment planning. Furthermore, a classification approach to provide the medical experts with quantitative results as well as advanced visualization concepts for qualitative blood flow information is presented. This is completed by a presentation of guidelines that support the quantitative evaluation of medical visualization concepts.

## 1.3 MEDICAL BACKGROUND

Within the last decades, the young field of interventional neuroradiology has undergone a rapid and notable improvement (Higashida, 2000). The first milestone was set in 1960 by the American neurosurgeon Luessenhop, who placed silastic beads into an arteriovenous malformation directly into the larger neck arteries and thus conducted an intravascular embolization (Luessenhop & Spence, 1960). 14 years later, the Russian neurosurgeon Serbinenko employed a detachable latex ballon in order to treat intracranial aneurysms (IAs) and carotid fistulas (Serbinenko, 1974). These techniques were refined over the next years until Guglielmi

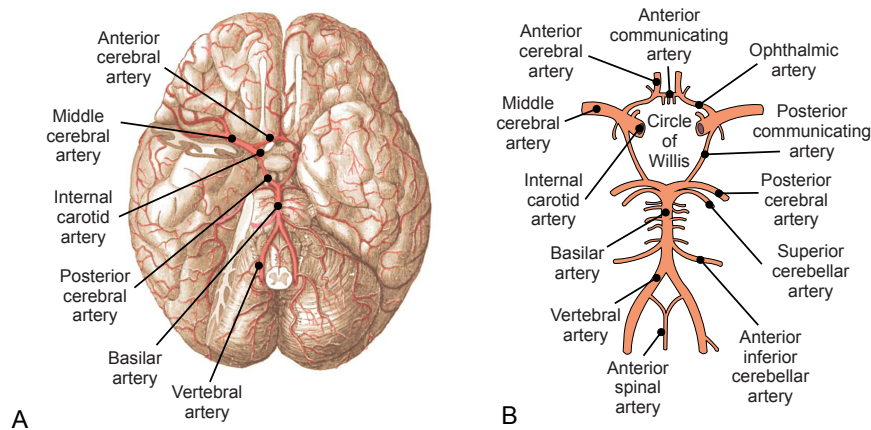


Figure 1.1: The blood supply of the brain is maintained by the anterior and the posterior cerebral circulation (a) and the Circle of Willis (b) as backup circulation (adapted from illustrations from (Gray, 2000)).

et al. (Guglielmi et al., 1991a; Guglielmi et al., 1991b) presented a detachable coil system for IAs, which eventually gained the approval of the Food and Drug Administration in the United States in 1995. Thus, the way was paved for highly skilled interventional neuroradiologists for treating surgically difficult or inoperable IAs. In the following section, a short medical background of the intracranial arteries including their pathologies with focus on IAs is provided. Afterwards, clinical treatment is briefly described.

### 1.3.1 Intracranial Arteries

The human brain is the organ with the highest demand for blood and oxygen and thus is requiring sufficient arterial supply. Its arteries are illustrated in Figure 1.1 and can be divided into the anterior and the posterior cerebral circulation. The anterior cerebral circulation is built up by the right and left internal carotid artery (ICA) branching from the left and right common artery. The ophthalmic artery supplying the eye and parts of the nose, the face and the meninges stems from the ICA. Next, each ICA is divided into the middle cerebral artery and the anterior cerebral artery. Inbetween the anterior cerebral arteries, the anterior communicating artery forms a connection. Together, they supply the lateral and medial parts of the brain. The basilar artery at the back of the brain originates from the left and right vertebral artery. In combination with their branches, they form the posterior cerebral circulation and supply the brain stem and the cerebellum. From the basilar artery, the two posterior cerebral arteries arise, which supply the occipital lobe. Inner parts of the brain, like basal ganglia and thalamus, are supplied by both the anterior and the posterior cerebral circulation.

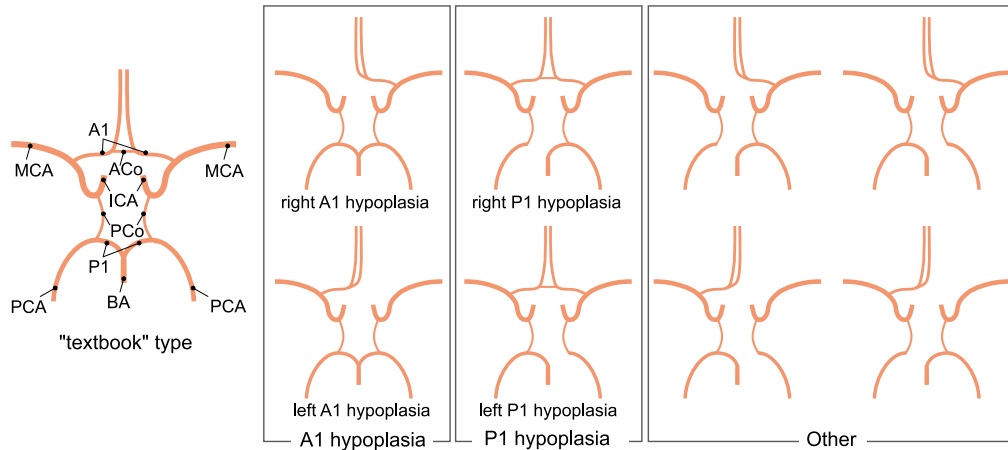


Figure 1.2: Variations of the arteries of the Circle of Willis, adapted from (Tanaka et al., 2006). The variations are presented for the main arteries: middle cerebral artery (MCA), internal carotid artery (ICA), anterior communicating artery (Acom), A1 segment between ICA and MCA of the anterior cerebral artery (A1), basilar artery (BA), posterior cerebral artery (PCA), P1 segment of the posterior artery between BA and PCA (B1) and the posterior communicating artery (PCom).

Since the basilar artery is connected via the bilateral posterior communicating arteries to the ICAs on each side, a circle is formed, the *Circle of Willis* named after Thomas Willis (1621-1675), “one of the greatest neuroanatomists of all time” (Ustun, 2004). This arterial circle serves as backup circulation to cope with a hampered blood supply, e.g., if one of the supplying arteries is occluded or even missing. Hence, a large variety of patient-specific manifestations exists, ranging from underdeveloped or even missing communicating arteries as well as a different number of branching arteries (Kayembe et al., 1984), see also the illustration in Figure 1.2.

### 1.3.2 Intracranial Aneurysms

Pathologic arteries are often characterized by arteriosclerosis, leading to a thickening and loss of elasticity of the arterial wall due to the accumulation of cellular wastes, see the illustration provided in Figure 1.3. Arteriosclerosis and its complications are currently the leading cause of death in industrialized countries (Osborn et al., 2013). The weakened vessel wall is prone to further pathologies, including aneurysms - a dilatation of the vessel wall. Aneurysms may occur at different arteries throughout the human body. Hence, aneurysms located at arteries in the skull, i.e., *intracranial aneurysms* (IAs), require special care due to the more difficult access route and their risk of rupture that may yield to injuries of brain tissue or brain vessels or even hemorrhagic strokes.

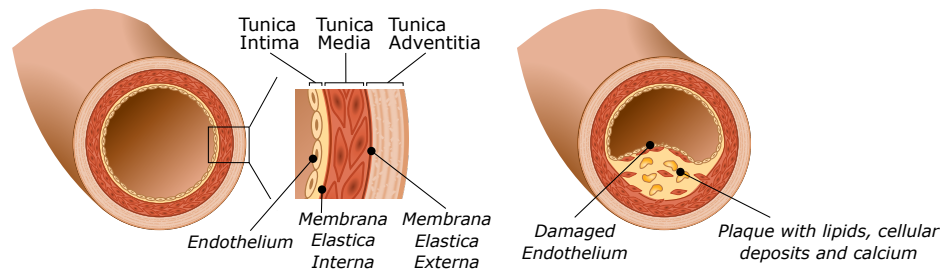


Figure 1.3: Illustration of a healthy vessel wall and its membranes (left) and a vessel wall narrowing due to arteriosclerosis (right).

Aneurysms present strong variations in their shape, where the most common type of IAs is called a saccular aneurysm with a narrow stem, see Figure 1.4(A-B). In contrast, a spindle-shaped aneurysm, i.e., a fusiform aneurysm, is characterized by a dilation of the whole vessel cross-section and an aneurysm neck is not present (Wanke & Dörfler, 2008), see Figure 1.4(C). These aneurysms affect all of the three vessel layers: tunica intima, tunica media and tunica externa. In contrast, a dissecting aneurysm only involves a single vessel wall layer that is splitted, see Figure 1.4(D). Hence, blood is intruding through a defect of the intima between the vessel wall layers. Blood-filled hematoma at an artery are called aneurysm spurium or aneurysm falsum.

In IA patients, approx. 30 % suffer from multiple aneurysms (Juvela, 2011) and approx. 9 % exhibit mirror aneurysms, i.e., a second aneurysm located directly opposite to the first one (Cebal & Raschi, 2012). Due to their position directly at a bifurcation or simply at the vessel wall, they are often divided into sidewall and bifurcation aneurysms, recall Figure 1.4.

The IA rupture is one of the most common causes of hemorrhagic strokes due to a subarachnoid bleeding (SAB), resulting in dramatic limitations of the patient's cognitive and motor skills, and thus it also represents a major financial burden on the healthcare system (Suarez et al., 2006). Due to the increasing number of acquired clinical images, the detection rate increases as well, with only a small part of the aneurysms even being at risk of rupture. Hence, prevalence of up to 6 % is relatively high compared to the incidence of aneurysmal SAB with up to 22 cases per 100,000 inhabitants (Alsheklee et al., 2010; Frösen et al., 2012; Ingall et al., 2000). As a result, most IAs are incidentally discovered. And due to the increased number of medical image acquisitions, the number of these *innocent aneurysms* rises (Etminan, 2015). A meta-analysis reports an annual IA rupture risk of 0.6 %-1.3 % where the asymptomatic aneurysms reportedly were 4 to 5 time less likely to rupture than the symptomatic ones (Wermer et al., 2007).

Although there are good and established surgical and endovascular treatment options, they have a residual complication risk and are associated with financial

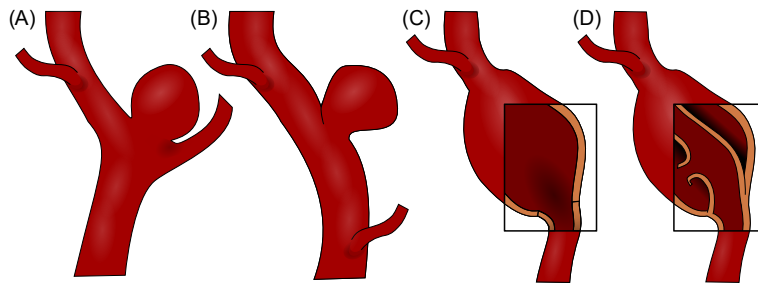


Figure 1.4: Illustration of saccular aneurysms (A-B), a fusiform aneurysm (C) and a dissecting aneurysm (D). Whereas the first three aneurysms (A-C) affect all three vessel wall layers, the dissecting aneurysm (D) is characterized by a split of a single wall layer yielding a false lumen. In addition, the first aneurysm is a representative for a bifurcation aneurysm (A) and the second one for a sidewall aneurysm (B).

expenses. Once an asymptomatic IA is associated with a high rupture risk or a symptomatic IA is present, therapy should necessarily be given because of the high clinical consequence of SAB. The problem, however, is that there is currently no way to determine the rupture risk of a patient precisely enough. Furthermore, aneurysm-specific attributes (e.g., location of the aneurysms determines the access path and thus different therapies) have to be considered as well.

Nevertheless, guidelines or scores exist. Presumably the most common is the PHASES (i.e., a score considering the attributes Population, Hypertension, Age, Size of aneurysm, Earlier SAB from another aneurysm, and Site of aneurysm) score presented by a study that pooled the analyses of six prospective cohort studies (Greving et al., 2014). It was reported that the patient's geographic region, hypertension status, age, IA size, history of SAB, and the IA location were independent predictors of IA rupture. However, the usefulness of this score is controversially discussed in clinical practice (Bijlenga et al., 2017; Hilditch et al., 2018). Hence, the score has not been validated on an independent large cohort. Furthermore, aneurysm growth within a possible follow-up study is not considered yet.

In consequence, IA rupture risk prediction is an active research area which will be discussed in more detail in Section 1.4.4.

Now that cardiac arteriosclerosis has been extensively researched and clinical guidelines are established, cerebral plaques still have many unanswered questions about optimal clinical care due to the more difficult access route and the different structural organization of the vessels (Subcommittee on Arteriosclerosis: Andrus et al., 2015).

### 1.3.3 *Treatment of Intracranial Aneurysms*

Treatment of IAs comprises surgery, i.e., neurosurgical clipping, and endovascular treatment apart from the wait-and-see strategy, i.e., monitoring the aneurysm (Seibert et al., 2011).

#### *Neurosurgical Clipping*

Neurosurgical clipping is a highly invasive procedure, where a surgical clip is carefully placed around the IA's neck to separate the aneurysm from blood supply, see Figure 1.5. Advantageously, the neurosurgeon can directly assess the aneurysm including the aneurysm wall and can possibly resolve complications of previous interventions, e.g., detachments of coils or stents, and aneurysm recanalization. Furthermore, the freshly closed aneurysm sac can be directly resected in favor of subsequent research and analysis. In addition, the intraoperative views can be employed to identify different aneurysm regions based on their visual appearance in order to evaluate the correlation of hemodynamics and aneurysm wall (Cezbral et al., 2019). However, the invasive surgical process involves cutting and removing a bone flap of the skull and brain tissue could be destroyed.

#### *Endovascular Treatment*

Endovascular treatment comprises catheter-based techniques to place implants into the aneurysm sac in order to cause a closure or to redirect the blood flow in the parent artery in favor of an aneurysm closure. These techniques comprise coiling, stenting or a combination thereof, recall Figure 1.5. Furthermore, an implantation of flow diverters can be carried out (Seibert et al., 2011). During coiling, a coil is placed inside the aneurysm to cause its closure. Various configuration and sizes are available which are selected based on the aneurysm size and volume. Stents, i.e., typically a metal mesh or metal braid, are often previously placed in case of broad aneurysm necks to support the coils (Fiorella et al., 2005). In addition, flow diversion devices (i.e., flow diverters) divert or redirect the flow away from the IA causing a closure of the IA based on blood stasis and thrombus formation without requiring a coiling at all (Fiorella et al., 2008). In some cases, the vascular deformation induced by the implant, i.e., a straightening of the vessel, further strengthens the flow redirection and thus improving IA closure.

#### *Monitoring of IAs*

The monitoring of IAs, i.e., the wait-and-see strategy is especially favorable in case of asymptomatic IAs that are furthermore associated with a low rupture risk. As it was discussed in the study of Bijlenga et al. (2017), the average rupture risk of unruptured incidentally found IAs can be estimated between 0.3% and >15% per 5 years, and for IAs smaller than 7 mm between 0.4% and 0.6%,

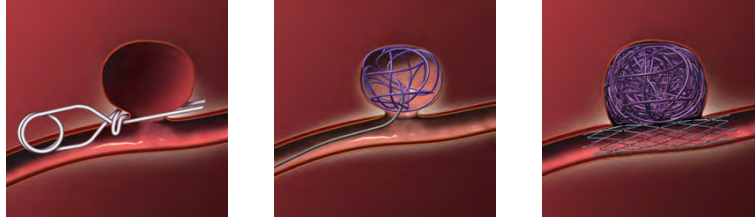


Figure 1.5: Illustration of a neurosurgical clipping (left), coiling (center) and stent-assisted coiling (right). (Image Courtesy Michigan Health System)

respectively (Etminan & Rinkel, 2016). In comparison, a preventive treatment was associated with an estimated risk of 1% mortality and approx. 5% morbidity, and for IAs smaller than 7 mm with a <0.1% mortality and <3% morbidity (Bruneau et al., 2015; Naggara et al., 2010; Rinaldo et al., 2017). However, patients often choose an interventional treatment over a conservative monitoring due to psychological factors, i.e., the high psychological burden.

#### *Treatment Strategy*

It is important to consider the substantial change of treatment strategy during the past two decades. Presumably motivated by the International Subarachnoid Aneurysm Trial (ISAT) (Molyneux, Kerr, International Subarachnoid Aneurysm Trial (ISAT) Collaborative Group, et al., 2002) that demonstrated reduced mortality rates at one year in patients undergoing endovascular treatment compared to microsurgical clipping, the first treatment strategy is carried out more often. In contrast, long-term results of the ISAT as well as the later conducted Barrow Ruptured Aneurysm Trial (BRAT) (Spetzler et al., 2019) report similar results for both treatment strategies. Hence, different aspects have to be considered (Etminan et al., 2015). For example, wide-necked IAs of the anterior circulation benefit from microsurgical clipping (Mascitelli et al., 2018). Furthermore, ruptured aneurysms at the middle cerebral artery with intracerebral hemorrhage significantly benefit from microsurgical treatment (Bohnstedt et al., 2013; Lee et al., 2012).

Finally, a decrease in microsurgical clipping for treatment of IAs is reported (Qureshi et al., 2011), resulting in two major aspects: First, a reduced number of clipped IAs hardens the training of future neurosurgeons based on a long-term assistance and the highest possible number of cases. Second, the remaining IAs required to be clipped are characterized by increased complexity (e.g., large neck areas, ruptured IAs), which further hardens the neurosurgical training. In essence, there is a lack of “easy” cases that would be beneficial for learning neurosurgeons.

As a result, the best treatment for unruptured and asymptomatic IAs remains ongoing research. Their therapy may lead to complications as well, whereas the rupture rates of asymptomatic IAs are reportedly equalled or exceeded by the

mortality rate associated with treatment (Wiebers, 2003). Thus, a computer support including the integration of blood flow information and the approximation of rupture risk can greatly improve the decision making for these IAs.

#### 1.3.4 *Medical Imaging in the Clinical Practice*

Medical imaging to detect and characterize IAs and the intracranial vessels includes tomographic imaging, i.e., computer tomography (CT), magnetic resonance imaging (MRI), 2D and 3D digital subtraction angiography (DSA) and 3D rotational angiography (RA) (Brisman et al., 2006; Kouskouras et al., 2004). For the tomographic imaging modalities, a contrast agent is intravenously applied yielding CT angiography and MR angiography data, respectively. For MRI, time-of-flight sequences exist as well, which do not require contrast agents and are thus suitable for patients with impaired renal functions. Due to its advantages for intervention and increased spatial resolution, Dyna CT angio suites are the preferable imaging modality. A C-arm rotates around the patient, see Figure 1.6. For the acquired X-ray projections, i.e., the rotational angiography dataset, a 3D tomographic scan is reconstructed. By starting a scan without contrast agent followed by a contrast-enhanced scan, digital subtraction can be carried out yielding the 3D DSA image data sets. The system also allows 2D X-ray scans with high spatial resolution as well as a time series of these 2D scans to analyze the contrast agent distribution. During intervention, the neuroradiologist follows the path of the catheters, guide wires and implants. The typical extent of tomographic image data is  $512 \times 512 \times 256$  voxels in clinical practice. The spatial resolution depends on the imaging modality and varies between  $\approx 0.2 - 0.5$  mm in the image plane with a slice distance of  $\approx 0.25 - 0.5$  mm.

In summary, the non-invasive imaging modalities may achieve similar sensitivity and specificity regarding the detection of IAs (Romijn et al., 2008), but DSA is considered as gold standard due to the increased resolution in combination with its interventional use (Geers et al., 2009; Tomycz et al., 2011).

### 1.4 COMPUTER SUPPORT FOR TREATMENT AND THERAPY PLANNING

The treatment of IAs can be simplified to the pipeline presented in Figure 1.7. This thesis comprises various approaches where this pipeline can be supported, and an extended illustration is provided in Figure 1.8. In the following, each step of the pipeline will be discussed in more detail. Embedded in the discussion of these steps and integrated in Figure 1.8 are my own research papers; whereas the selection forming the cumulative part of this thesis is highlighted, e.g. (Glaßer et al., 2017), and further studies I contributed to are less attenuated in the text, e.g., (Hoffmann et al., 2016).

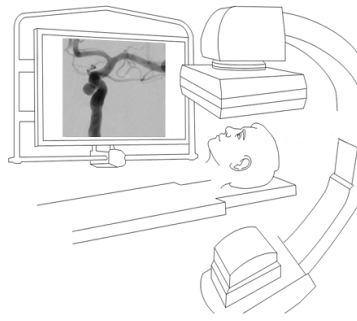


Figure 1.6: Illustration of a C-Bogen system (Image courtesy of T. Hoffmann, Otto-von-Guericke University of Magdeburg, Germany).

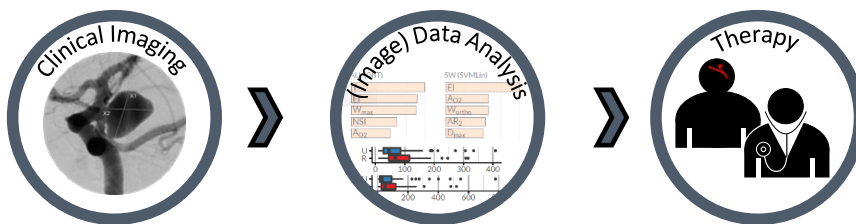


Figure 1.7: A simplified pipeline for IA treatment comprising the clinical imaging, an analysis of the medical image data and subsequent therapy.

Special attention must be paid to the large gap between clinical research and clinical practice. As it will be described in the following, clinical research comprises manifold tools and applications to not only characterize the intracranial vessel wall but even to predict the IA rupture risk. To close this gap, projects and applications from research tracks have to be translated into practice including a discussion of possible error sources and parameter choices as well as applying them to a large number of datasets. The translation into clinical practice is not only a matter of personal importance, but should also be a focus of more studies to finally improve the intervention and thus the patient's health itself.

#### 1.4.1 *Medical Imaging in Clinical Research*

Arteriosclerosis and subsequent vessel diseases manifest in the vessel wall and one of the main research directions is the imaging of the vessel wall. This is very similar to cardiac applications where cardiac arteriosclerosis has been extensively researched. Hence, the cerebral plaques still raise many unanswered questions about optimal clinical care due to the more difficult access route and the different structural organization of the vessels (Subcommittee on Arteriosclerosis: Andrus et al., 2015). Furthermore, neurosurgeons report a relationship between wall thickness and risk of IA rupture. Since currently no in vivo imaging technique

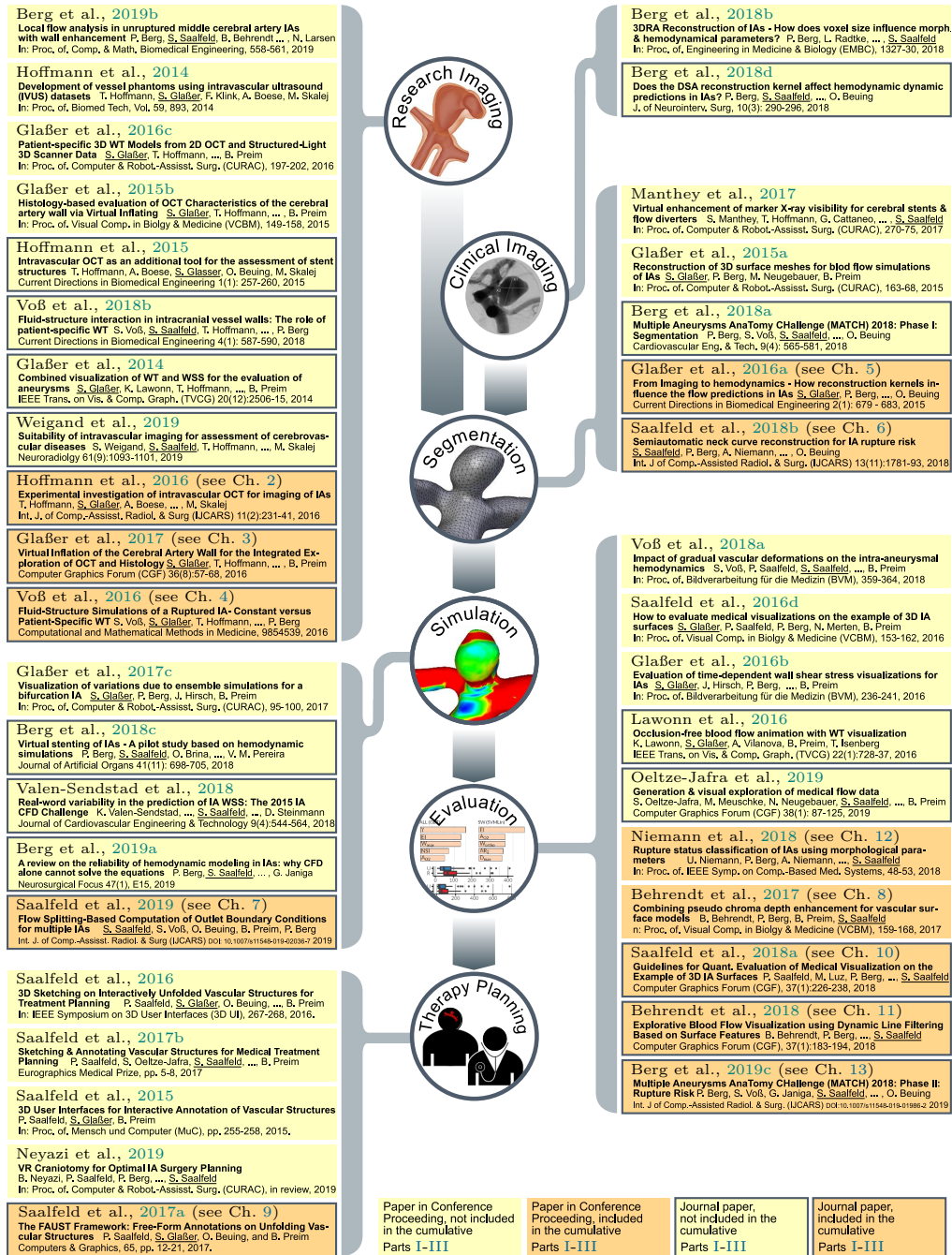


Figure 1.8: Classification of research papers and their relation to the pipeline. Evaluation covers visual exploration, visual analysis and rupture risk assessment. In case a paper contributes to several aspects, the most prominent aspect was chosen. Title of papers might be shortened due to limited space, WT is the abbreviation for wall thickness.

is available in the clinical practice (apart from highly invasive intra-operative views during surgery), this relationship is poorly documented. However, studies that evaluated resections acquired during neurosurgical clipping report an increased rupture risk for very thin or very heterogeneous IA walls (Frösen et al., 2004). Furthermore, histological and intraoperative observational studies characterized these walls as a highly variable region (with a thickness from 16 to 400  $\mu\text{m}$ ) containing areas with thick, intermediate and super-thin translucent tissue (Kadasi et al., 2013). For comparison, our recent study revealed an average wall thickness of 344  $\mu\text{m}$  of healthy intracranial vessel walls measured in histology data (Weigand et al., 2019).

### *Intravascular Imaging*

For clinical research, intravascular imaging, e.g., intravascular ultrasound (IVUS) and recently optical coherence tomography (OCT), is able to assess the vessel wall's morphology. Both intravascular imaging methods are routinely employed in clinical cardiac practice to assess stenoses and plaques with a superior image resolution compared to tomographic imaging. In consequence, several studies tried to assess their potential of characterizing arteriosclerotic plaque in intracranial vessels.

When comparing IVUS and OCT, the first has a larger penetration depth, i.e., approx. 20 mm and 4  $\mu\text{m}$  spatial resolution, but the latter exhibits higher spatial resolution, i.e., approx. 10 mm penetration depth and 15  $\mu\text{m}$  spatial resolution (Tsakanikas et al., 2012). Hence, IVUS is well suited for the evaluation of coronary arteries. The studies by Katouzian and colleagues (Katouzian et al., 2012a; Katouzian et al., 2012b) correlate IVUS with histological imaging based on a cage fixture setup for an in vitro experiment. Balzani et al. (2012) introduced a 3D reconstruction of geometrical models of atherosclerotic arteries (i.e., vessel walls with atherosclerotic plaque burden) based on multimodal image acquisition including IVUS, virtual histology data and angiographic X-ray images. IVUS was also successfully employed for imaging of the intracranial wall (Majidi et al., 2013). We further analysed the suitability of intravascular imaging for intracranial arteries. As starting point and for the extraction of intravascular vessel wall models, we employed IVUS to develop vessel phantoms (Hoffmann et al., 2014) as well as to probe an artificial IA. Therefore, a porcine artery was dissected and closed to form an aneurysm. The dataset was segmented and underwent CFD simulation. Afterwards, a combined visualization of the wall thickness and hemodynamic surface parameters (Glaßer et al., 2014) and blood flow animations (Lawonn et al., 2016) was generated.

OCT imaging was successfully conducted for the larger carotid arteries (Yoshimura et al., 2012) as well as for animal studies (van der Marel et al., 2014) or ex vivo studies (Lopes et al., 2012; Mathews et al., 2011). For a more dedicated application to human intracranial vessels, the probing of human Circles of Willis

was conducted, which were explanted post-mortem (Hoffmann et al., 2016). Hence, OCT was also analyzed w.r.t. its ability to evaluate IAs, which were provided as silicon phantom models based on the post-mortem extracted vessels. The study underpins the great potential of OCT to characterize the intracranial walls but also reveals limitations in larger aneurysms due to the limited penetration depth of max. 10 mm. Furthermore, we could show that OCT was able to assess stent structures of neurovascular implants (Hoffmann et al., 2015). Patel et al. 2013 were able to conduct the first in vivo human study and evaluate a left vertebral artery stent in a patient with vertebral artery stenosis. As summarized by Chen et al., OCT data is able to provide high-resolution images of vessel lumen and the wall including possible intraluminal thrombi and allows for aneurysm wall assessment with good correlation with histological sections (Chen et al., 2018). It also is suitable to evaluate the stent malapposition, locate perforating arteries, and accurately evaluate vessel diameters. Disadvantageously, intraluminal blood causes artifacts and, thus, clearance of blood and a flushing of the vessels is required, which is difficult for pathologies like IAs. More severe, the limited penetration depth of current OCT catheters hampers their suitability for larger IAs (Hoffmann et al., 2015; Chen et al., 2018). Hence, OCT data typically exhibits a spatial resolution of  $\approx 15 \mu\text{m}$  with a limited penetration depth of 10 mm which in turn often is further reduced to 3-4 mm due to signal attenuation inside the vessel, whereas tomographic images are limited to 0.2 mm spatial resolution. Finally, the required catheters are suited for the larger coronary arteries, but they might not be small and flexible enough for a safe navigation in the tortuous intracranial vasculature (Chen et al., 2018). Hence, restrictions of the medical board prevent the use in vivo.

### *Histological Analysis*

For preparation of a ground truth, histological analysis can provide the required information about vessel wall morphology and pathologic changes. We combined our studies about OCT in post-mortem intracranial vessels (Hoffmann et al., 2016) with hematoxylin and eosin (H&E) staining. The H&E staining is one of the most often used stains in medical image analysis, where the hematoxylin yields a blue coloring (and thus high contrast) of the cell nuclei and the eosin causes the reddish staining of the extracellular matrix and the surrounding tissue (Titford, 2005). Thus, arteriosclerosis or wall thickening of intracranial vessel walls can be evaluated with H&E stainings of the vessel cross-section.

For further co-registration of the deflated post-mortem vessels, the virtual inflation approach was developed (Glaßer et al., 2015b), (Glaßer et al., 2017). Virtual inflation refers to the process of virtually inflating the vessel cross-sections in order to compare OCT and histology globally and locally, see Figure 1.9. Hence, the user can define a brush in one modality and link it

to the second one. Furthermore, automatically extracted information about pathologies based on clustering of the nuclei and extraction of their characteristic shapes highlights pathologic vessel wall parts, e.g., an inflammatory region. This study is included in the cumulative Part I. Recently, a comprehensive investigation of intravascular imaging and histologic analysis was carried out (Weigand et al., 2019), yielding a statistically significant shrinkage of the vessel’s diameter, but in contrast a good agreement of their pathologies like atherosclerotic plaque.

A shortcoming of the intravascular imaging approaches is the missing 3D information. For example, conventional OCT scanners provide a stack of 2D slices which can be stacked and reformatted into a longitudinal vessel view, but the vessel centerline is assumed to be straight since no 3D information about the catheter’s path is available. Therefore, experimental results combined OCT data with a structured light scanner to obtain the 3D orientation (Glaßer et al., 2016c). Additionally, X-ray images of the catheter’s path were extracted and combined with the OCT data of an intracranial vessel bifurcation to improve the simulation of the internal blood flow (Voß et al., 2018b). Hence, the vessel walls were also virtually inflated by adaption of our previous method (Glaßer et al., 2017). Nowadays, commercial solutions aim at a combination of OCT with the angiography suite to combine bi-plane image data for the catheter path (i.e., to reconstruct the catheter’s 3D position) with the OCT data in an automated manner. In addition, Gounis et al. (2019) recently introduced the high-frequency (HF) OCT and a prototype, which is already in preclinical testing. Their system was specifically designed for use in tortuous neurovasculature and exhibits a larger field of view compared to conventional OCT. In addition, a spatial resolution approaching  $10 \mu m$  is reported (Gounis et al., 2019). Hopefully, HF OCT will be in clinical use in the near future.

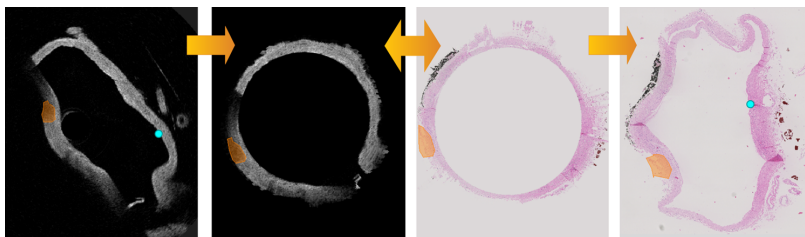


Figure 1.9: Illustration of the virtual inflation for an OCT slice (left) and corresponding histology slice (right). The user can define a brush in the first modality (orange polygon) that is linked to the second modality.

### *Vessel Wall MR Imaging*

In addition to the MR imaging in clinical practice, Matouk et al. (2012) used high-resolution MR vessel wall imaging (MR-VWI) in patients with multiple IAs to investigate the aneurysmal subarachnoid hemorrhage. Recently, Larsen et al.

(2018) studied unruptured middle cerebral artery aneurysms via MR-VWI and histology. As a result, MR-VWI is reportedly associated with inflammatory cell invasion, neovascularization, and the presence of vasa vasorum. They combined it with CFD and applied local flow analysis based on advanced filtering techniques to improve the understanding of vessel wall enhancement. Xiao et al. (2018) associate wall enhancement in MR-VWI with low wall shear stresses. We could confirm these findings in a recent study (Berg et al., 2019b). In addition, our work revealed a perpendicular direction to the main flow, see the exemplary cases provided in Figure 1.10. Thus, high resolution MR-VWI yields promising results for imaging of instable plaques and IAs with high risk of rupture (de Havenon et al., 2016), but the clinical use is still limited to specialized clinical centers.



Figure 1.10: Illustration of flow patterns associated with enhanced vessel wall regions (Berg et al., 2019b). The pink patches (arrow) show regions characterized by enhancement in the MR-VWI data and the presented streamlines represent the corresponding flow passing by these regions.

### *Enhancement of 3D RA*

Apart from these additional imaging techniques like intravascular imaging or MRI, the 3D RA itself can be improved. Hence, the process from generating a 3D tomographic dataset from the projections of the 3D RA datasets is called reconstruction. In IA research studies, this process is scarcely recognized when putting the focus on segmentation or CFD simulation. Often, clinical researchers provide the already reconstructed 3D DSA dataset for further analysis.

However, these C-arm CT images are frequently affected by motion artefacts which could be compensated with a geometric optimization algorithm (Frysch & Rose, 2015). Typically, the redundancies in the projection images are exploited (Meng et al., 2013). In addition, artifacts like beam hardening can be reduced during the reconstruction process (Abdurahman et al., 2018). Since these techniques achieved higher quality phantom datasets and were able to reduce the artifacts, an improvement for IA datasets is expected as well.

Apart from improving the reconstruction process based on research applications, the available clinical work stations bear potential for improvement or

could induce errors in the subsequent steps. Therefore, the influence of the chosen reconstruction kernel was analyzed yielding the rejection of smooth kernels for the application scenario of segmentation and CFD simulation for IAs (Glaßer et al., 2016a), (Berg et al., 2018d).

#### 1.4.2 *Segmentation of Vessel Surface Models*

Due to its high clinical importance, the segmentation of vessels and their pathologies is of utmost importance and a dominant research area. The following aspects are discussed:

- segmentation for vessel surface models,
- remeshing of surface models,
- and standardized analysis of segmentations.

##### *Segmentation for Vessel Surface Models*

In favor of reproducible results and a reduction of the clinicians' workload, automatic segmentations are desired but not always possible. In consequence, a wide variety of mesh segmentations exists (Shamir, 2008) and numerous approaches have been specifically proposed for the vessel lumen (Lesage et al., 2009). Data-based approaches, such as thresholding, are fast and immediately provide the segmentation result. Disadvantageously, they are affected by image artifacts caused for example by inhomogeneous contrast agent distribution or the partial volume effect. Furthermore, the resulting binary voxel mask has to be transferred into a geometrical surface model, e.g., by applying the Marching Cubes algorithm (Lorenson & Cline, 1987). In contrast, model-based approaches, such as level sets, are less sensitive to artifacts and can provide a segmentation at sub-voxel level. On the other hand, they are computationally expensive and the parametrization may be non-intuitive and challenging. Jerman et al. 2015 introduce an image analysis framework that includes a detection of aneurysms based on random forests and a grow-cut segmentation of the aneurysm and its parent vessel. The vascular modeling toolkit VMTK provides freely available tools for the 3D reconstruction, geometric analysis, mesh generation and surface data analysis for image-based modeling of blood vessels (Antiga et al., 2008; "The Vascular Modeling Toolkit website", 2019). Hence, a gradient-based level set segmentation is included.

##### *Remeshing of Surface Models*

Especially for interventional use, e.g., a stent-assisted coiling, the physicians often generate a 3D model of the patient for the current treatment and they

require instant feedback how the parameter changes are influencing the resulting 3D representation, i.e., the surface mesh. In contrast, segmentations for research projects must yield so-called waterproof surface meshes, i.e., the segmented aneurysm and its parent vessel must be transferred into a polygonal surface mesh with no holes and high triangle quality, i.e., equilateral triangles. A remeshing of these surfaces often aims at improvement of the quality of mesh elements, which is crucial for the robustness and numerical stability for CFD simulations (Alliez et al., 2008). Simplification of surface meshes reduces the complexity of meshes, i.e., the number of vertices and faces, or optimizes the vertex distribution (Gotsman et al., 2002). For improvement of aneurysm surfaces, previous studies (Moench et al., 2011; Glaßer et al., 2015a) employed an advancing front approach that accounts for regions of strong local curvature at the aneurysm neck by employing smaller triangles in areas with strong underlying curvature (Schöberl, 1997). However, recent CFD applications, e.g., STAR-CCM+ 11.06 (Siemens Product Lifecycle Management Software Inc., Plano, TX, USA 75024), already provide commercial remeshing approaches as a preprocessing step in order to create the volume grid required for the simulation. The interested reader is also referred to the survey of Oeltze-Jafra et al., where the segmentation and extraction of surface models for the simulation of medical flow data is discussed (Oeltze-Jafra et al., 2019).

#### *Standardized Analysis of Segmentations*

In addition to providing more information about the IAs and allow for subsequent blood flow simulations, the segmentation of IAs also induced further variations in the data and thus, limits the standardized evaluation. Hence, a standardized analysis of IAs can be provided by using digital video sequences to allow for inter-patient or inter-study comparisons (Iserhardt-Bauer et al., 2002) without any segmentation or user interaction. In order to increase the clinical acceptance of the computer support for IAs, further studies directly aim at the comparison of segmentations, similar to challenges for brain tumor segmentations (Menze et al., 2015) or liver tumors (Bilic et al., 2019).

The Multiple Aneurysms AnaTomy CHallenge (MATCH) was announced to evaluate state-of-the-art segmentation approaches for IAs (Berg et al., 2018a). The challenge received contributions of 26 participating groups from 13 countries and provides an overview of segmentation methodologies for IAS. The provided 3D DSA datasets comprised five IAs in the left and right anterior and the posterior circulation. We carefully selected the patient data, in close discussion with our interdisciplinary team especially the neuroradiologists. Due to the multiple aneurysms of a single patient, the influence of patient-specific factors such as further diseases, alcohol abusius etc. can be neglected. Based on the iterative closest point algorithm, a co-registration of the submitted segmentations was carried out (Besl & McKay, 1992; Chen & Medioni, 1992). When analyzing the applied

segmentation algorithms, most groups (11 groups) used a threshold-based approach, followed by level-set methods (10 groups) as well as region growing (4 groups) and a watershed algorithm (1 group). Special attention should be paid to the fact that further correction steps such as smoothing, cropping or artifact elimination were reported by almost all groups. A more detailed description of these postprocessing steps can be found in (Glaßer et al., 2015a). In summary, no consensus regarding segmentation software or underlying algorithms for IAs could be identified.

### 1.4.3 *Simulation of the Intracranial Blood Flow*

Based on the extracted 3D models of IAs, hemodynamic simulations are increasingly used to approximate the intracranial blood flow yielding the blood flow velocity and pressure. These results are employed to assess the rupture risk (Cebal et al., 2011a; Cebal et al., 2015; Valen-Sendstad & Steinman, 2014) or support the treatment planning of IAs (Cebal et al., 2011b; Janiga et al., 2015; Ma et al., 2014), (Berg et al., 2018c). This thesis does not focus on the hemodynamical simulation itself, but rather on its clinical benefits. Therefore, a focus is put on possible error sources as well as the limitations of the CFD. To be more precise, the following topics are discussed:

- importance of spatial resolution and boundary conditions,
- validation to increase the clinical acceptance,
- a standardized analysis of CFD results.

**SPATIAL RESOLUTION AND BOUNDARY CONDITIONS** Subsequent to the segmentation, a volume grid for the simulation is extracted. Hence, sufficient spatial resolution must be ensured (Berg et al., 2018b). Furthermore, realistic boundary conditions and appropriate simulation settings must be selected. For example, the velocity and the modelling of the blood flow at the vessel inlets have to be defined. A possible approximation of the inflow was extracted from a healthy volunteer 4D PC-MRI data Berg et al., 2014. Valen-Sendstad et al., 2015 studied the influence of scaled inflow waveforms. They concluded that a square law depending on the vessel inlet diameter leads to most physiological flow patterns. Further boundary conditions cover the modeling of the wall (rigid vs. non-rigid) or the blood flow behaviour at the vessel outlets. In Figure 1.11, an overview of these conditions is provided based on our recent review article (Berg et al., 2019a). The validation of the assumed or experimental determined approximations is mostly conducted either in vitro, i.e., based on comparisons in phantom models (Liang et al., 2016; Roloff et al., 2019) or in vivo, i.e., using 4D PC-MRI or other noninvasive imaging techniques (Berg et al., 2014).

Specifically, boundary conditions determine the flow split at vessel bifurcations and thus strongly influence the hemodynamical simulation result. For outlet boundary conditions, the most common zero-pressure strategy assigns constant zero pressure to the model outlets and has the advantage of numerical simplicity. However, it lacks a physiological basis. In contrast, a flow splitting based on Murray's law (Murray, 1926) accounts for the vessel diameters and models the flow proportional to the outlet diameter. Disadvantageously, the simulation results strongly depend on the truncation of the segmented vessel model. Chnafa et al. (2017) analyzed the energy loss at vascular bifurcations that describes the splitting of flow depending at a bifurcation considering the bifurcation angles and diameters of daughter branches. They also showed that the cerebrovascular simulations strongly depend on the outflow splitting strategy and hence require careful treatment (Chnafa et al., 2017; Chnafa et al., 2018). Their approach suggests to adapt the flow splitting at vessel bifurcations depending on the vessel's cross-sectional area, but they only consider circular vessel cross-sections. Finally, our study (Saalfeld et al., 2019) further improves the flow splitting by incorporating the actual vessel diameter including anatomical, i.e., arbitrary-shaped, vessel cross-sections. Especially elliptical cross-sections are better modeled. Furthermore, we were able to select and segment cases with multiple aneurysms (each patient suffered from four aneurysms) and a large vascular domain (first patient's vessel tree had twelve outlets, second patient's vessel trees had seven and eight outlets, respectively). The study is included in the cumulative part of this thesis in Part III.

VALIDATION IN ORDER TO INCREASE THE CLINICAL ACCEPTANCE  
To increase the clinical acceptance, in vivo and in vitro validation studies are essential (Berg et al., 2014; Bouillot et al., 2014; Bouillot et al., 2015; Liang et al., 2016). However, one limitation will remain: mostly, the CFD studies use rigid vessel walls, since the imaging modalities can only depict the vessel lumen. A fluid-structure simulation would be more realistic, especially when considering that aneurysm motion can be observed in the time-dependent 2D DSA images and is associated with rupture (Vanrossomme et al., 2015). Cebra and colleagues constructed 3D models from surgically treated aneurysms and identified five different wall regions according to their appearance in the surgical intraoperative videos. They concluded that local flow conditions yield a local remodeling of the aneurysm wall, e.g., low flow conditions characterized by low and oscillatory shear stress correlated with atherosclerotic and hyperplastic wall changes and high flow conditions with higher and less oscillatory WSS correlated with local wall thinning (Cebra et al., 2019). In summary, the vessel wall modeling needs further research and wall information is highly desirable. Therefore, we investigated a post-mortem Circle of Willis with a ruptured IA at the anterior communicating artery and scanned it with an industrial computed tomography system (Nanotom S 180, GE Measurement & Control, Fairfield, Connecticut,

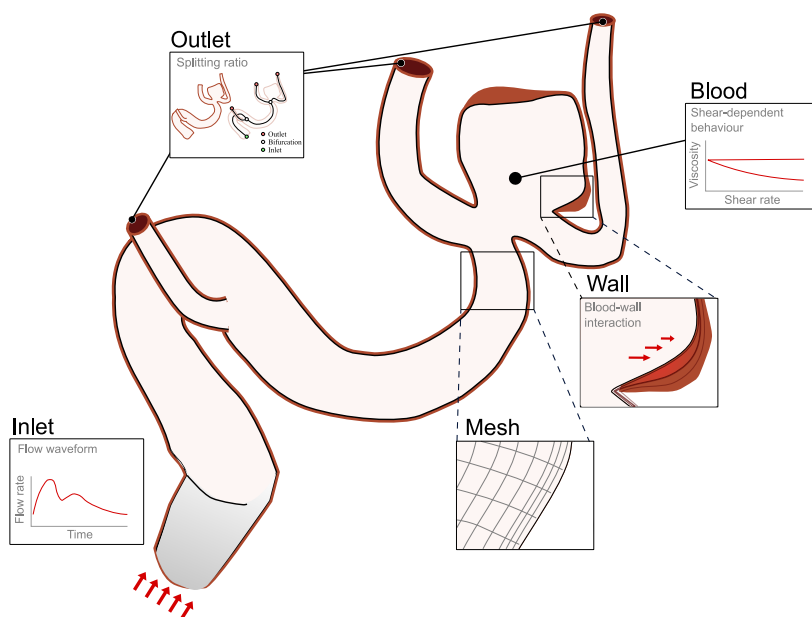


Figure 1.11: Illustrative depiction of relevant impact factors and boundary conditions for CFD of IAs: the volumetric mesh defining the spatial discretization of the flow domain; (time-dependent) inlet and outlet boundary conditions; the approximation of the wall as rigid or flexible and the approximation of blood as Newtonian or non-Newtonian fluid (Berg et al., 2019a).

USA) (Voß et al., 2016). This allowed for the extraction of the wall thickness and thus a segmentation of the inner and outer vessel wall. As a result, we could determine that only assuming a constant wall thickness might lead to wrong conclusions when compared to patient-specific vessel wall thickness. Although the averaged WSS values over the whole aneurysm sac were in very good agreement, large differences were found at the location of rupture.

**STANDARDIZED ANALYSIS OF CFD RESULTS** Similar to the segmentation of the IAs, a standardized analysis of CFD results for IAs is desirable. Radaelli et al. (2008) started one of the first CFD and IA-related challenges, the Virtual Intracranial Stenting Challenge (VISC) in 2007 to demonstrate the predictive potential of CFD for commercial available intracranial stents. In addition, the International Aneurysm CFD Challenge 2015 was announced by Valen-Sendstad et al. (2018), and the organizers compared rupture prediction between the CFD teams and clinicians yielding a benefit of the CFD analysis. In a second phase of the most recent MATCH challenge (Berg et al., 2018a), we compared the image-based hemodynamic simulations that were carried out to identify the ruptured aneurysm (Berg et al., 2019c). As a result, the majority of the 26 groups falsely selected the largest aneurysm as being the ruptured one and only four of the participating groups were able to correctly select the

ruptured aneurysm. Hence, the successful selections integrated clinically relevant information, e.g., aneurysm site, and advanced rupture probability models including morphological parameters and quantification of inflow jets as well as the identification of multiple vortices.

#### 1.4.4 *Computer-Supported Evaluation*

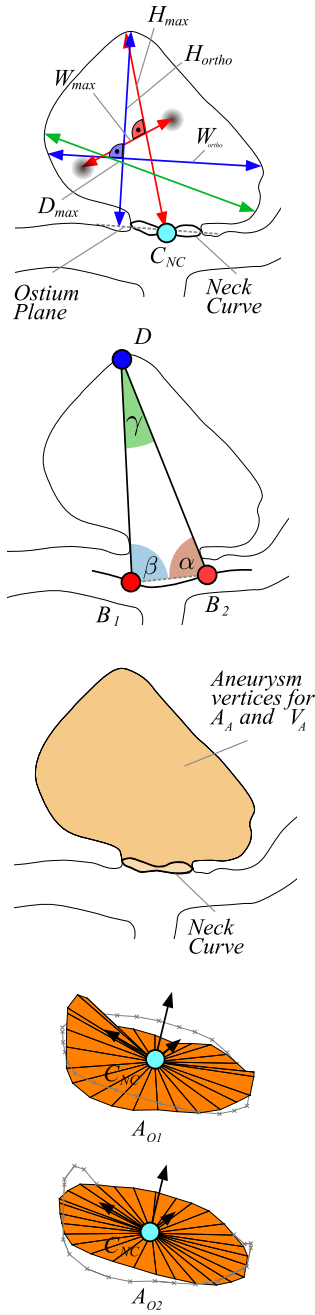
The computer-supported evaluation of IAs comprises the analysis of IA shape and shape-based parameters as well as the assessment of intracranial blood flow including hemodynamical parameters. Finally, a qualitative evaluation w.r.t. extracted properties of IAs is briefly discussed.

##### *Evaluation of Morphological Parameters*

As it was introduced in Section 1.3.2, rupture risk assessment of intracranial aneurysms is an active clinical research area, since a mismatch between treated aneurysms and actual aneurysms at risk occurs.

Therefore, a substantial amount of studies correlated the rupture risk of IAs with their morphological shape. In clinical practice, 2D measurements, e.g., ostium size or the dome-to-neck-ratio, are extracted from the 2D angiographies as rupture risk indicators (Backes et al., 2014; Weir et al., 2003). Although they are easily accessible within the clinical workflow, the extraction is highly user- and image-dependent based on the viewing angle for the 2D projections (Wong et al., 2012). The study concludes that 3D shape parameters of IAs yield a more standardized analysis. Furthermore, a considerable number of studies introduced 3D shape parameters of IAs and their correlation with rupture risk (Dhar et al., 2008; Lauric et al., 2012; Lv et al., 2016; Raghavan et al., 2005; Varble et al., 2017; Xiang et al., 2011). An illustration of morphological parameters is provided in Figure 1.12.

In more detail, Raghavan et al. (2005) evaluated five size and eight shape indices concluding that only five shape indices reached statistical significance when comparing the ruptured and unruptured aneurysm group. In contrast, Xiang et al. (2011) identified the size ratio, i.e., the ratio between maximum aneurysm height and averaged diameter of the parent vessel, as independent significant factor, but reported a significant difference of shape complexity parameters such as undulation index, ellipticity index, and nonsphericity index between the ruptured and the unruptured aneurysm group. Furthermore, special attention was paid on the aneurysm location. The study presented by Lv et al. (2016) was based on 129 IAs on the posterior communicating artery and their morphological discriminants. They reported that the size of aneurysm dome, the aspect ratio, the size ratio (i.e., the ratio of the maximum perpendicular height to the mean neck diameter) as well as the dome-to-neck ratio were statistically significant between ruptured and unruptured aneurysms. However, as it was presented



$A_A$	Area of the aneurysm surface
$V_A$	Volume of the aneurysm sac
$OA_1$	Area of the the ostium
$OA_2$	Area of the ostium, projected onto a plane
$D_{max}$	Max. diameter of the aneurysm
$H_{max}$	Max. height of the aneurysm
$W_{max}$	Max. width perpendicular to $H_{max}$
$H_{ortho}$	Max. height perpendicular to the ostium center
$H_{ortho2}$	Same as $H_{ortho}$ but no intersections with the aneurysm wall are allowed
$W_{ortho}$	Max. width parallel to the projected ostium plane
$N_{max}$	Maximum ostium diameter
$N_{avg}$	Average ostium diameter
$AR_1$	Aspect ratio: $H_{ortho}/N_{max}$
$AR_2$	Aspect ratio: $H_{ortho}/N_{avg}$
$SR$	Size ratio: $H_{max}/$ average vessel diameter
$V_{CH}$	Volume of the convex hull of the aneurysm sac
$A_{CH}$	Area of the convex hull of the aneurysm sac
$EI$	Ellipticity index; $EI = 1 - (18\pi)^{\frac{1}{3}} V_{CH}^{\frac{2}{3}} / A_{CH}$
$NSI$	Non-sphericity index; $NSI = 1 - (18\pi)^{\frac{1}{3}} V^{\frac{2}{3}} / A$
$UI$	Undulation index; $UI = 1 - V/V_{CH}$
$\alpha$	Smaller angle between centerline and dome
$\beta$	Larger angle between centerline and dome
$\gamma$	Angle at aneurysm dome

Figure 1.12: Illustration of morphological parameters that were automatically extracted based on a given neck curve and its center  $C_{NC}$ , see also (Niemann et al., 2018; Saalfeld et al., 2018b) for more details.

by Varble et al. (2017), the location of the IA influences results of the morphological (and hemodynamical) parameters. They analyzed 311 unruptured aneurysms and concluded that aneurysms at the internal carotid artery are subject to less rupture-prone morphological characteristics in comparison to other locations of the intracranial vasculature.

The presented studies exhibit two major drawbacks. On the one hand, some studies only consider a limited number of IAs, e.g., Raghavan et al. (2005) evaluated 27 cases or Dhar et al. (2008) evaluated 45 cases. On the other hand, the separation of the IA from the parent vessel uses planar cut planes (Lauric et al., 2012; Raghavan et al., 2005; Xiang et al., 2011), which is not justified for the highly variational shapes of IAs, see also the example in Figure 1.13.

To overcome this issue, a standardized neck curve for separation of aneurysm and parent vessel on a larger set of aneurysm data is required. A semi-automatic neck curve extraction was proposed by Neugebauer et al. (2010), but their approach was only tested on seven aneurysms and was not applicable to aneurysms with large or irregular blebs as well as strongly lobulated ones, see the examples in Fig. 1.13. This approach was extended by Meuschke et al. (2018), but it was only tested for ten datasets. A more analytical approach was presented by Jerman et al. (2015) who employed a raytracing approach for the determination of the ostium similar to (Neugebauer et al., 2010). We refined the approach of Neugebauer including a determination of the characteristic dome point angle (Saalfeld et al., 2018b). Our approach is applied to 3D segmentations of 100 IAs and a comparison with 100 manually drawn neck curves by a clinical expert is included. Since initial results indicate a high predictive power of the newly defined characteristic dome point angle, we carried out a statistical analysis to identify relevant shape parameters to differentiate between ruptured and unruptured aneurysms (Niemann et al., 2018). This study further affirmed the potential of this parameter. Both studies are included in the cumulative part of this thesis, see Chapters 6 and 12.

The recently proposed model of Detmer et al. (2018) combines and internally validates a model for aneurysm rupture risk prediction based on hemodynamic and geometric parameters, aneurysm location, and patient gender and age for characterization of 1631 aneurysms. Regarding aneurysm cases and the model's predictive power, they raised the bar considerably. Hence, future work should extend this model with the dome point angle parameter and include longitudinal data for clinical validation.

### *Evaluation of Hemodynamical Parameters*

A major aspect regarding the access to hemodynamical parameters is the CFD simulation that requires dedicated hardware in addition to software tools and skilled employees. Apart from the hardware requirements, a lot of parameter choices hamper the clinical acceptance.

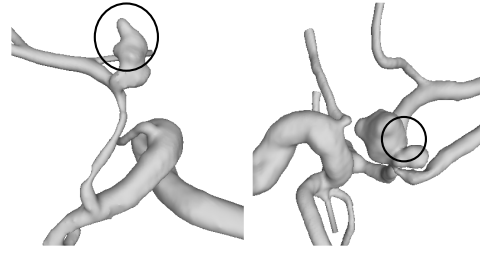


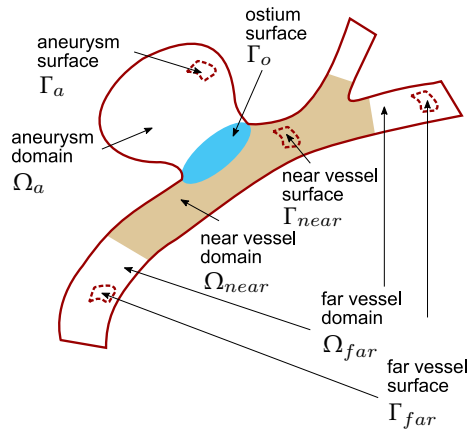
Figure 1.13: Depiction of two patient-specific aneurysm surface models from our IA database with irregular blebs or strongly lobulated aneurysm heads, see circles.

Similar to morphological parameters, a significant amount of studies analyzed hemodynamical parameters and their correlation with IA rupture risk (Byrne et al., 2014; Chung et al., 2017; Doddasomayajula et al., 2017; Jou et al., 2008; Lou et al., 2016; Miura et al., 2013; Takao et al., 2012; Xiang et al., 2011). In Figure 1.14, the most important ones are illustrated based on the study presented by Cebal et al. (2011a). Given the blood flow velocity  $u$ , the wall shear stress  $WSS$  can be extracted as friction against the vessel wall. As explained by Cebal et al. (2011a), a partitioning of the vascular models into different geographic regions can be conducted yielding the aneurysm separated by the ostium from the parent vessel and a further subdivision of the remaining vessel region into two subregions, i.e., the *near vessel* and *far vessel* regions with corresponding distances to the ostium surface less than or larger than 1.0 cm, respectively. Derived from the partitioning, the following parameters can be extracted. MWSS is the maximum  $WSS$  computed over the aneurysm region. The shear concentration index (SCI) measures the ratio of shear forces of the aneurysm in relation to the parent vessel, and the inflow concentration index (ICI) denotes the inflow of the blood from the parent vessel into the aneurysm. Both indices are reported to be larger for ruptured than for unruptured aneurysms (Cebal et al., 2011a).

The study presented by Xiang et al. (2011) showed that the average WSS, the maximum intra-aneurysmal WSS, the low WSS area, the average OSI, the number of vortices, and the relative resident time achieved statistical significance for the prediction of the rupture status.

In summary, rupture prediction models including morphological and hemodynamical parameters in addition to the clinical ones achieved considerably good rupture prediction rates (Detmer et al., 2018). The systematic review of Liang et al. (2019) identified 46 studies out of 231 studies reported in literature about aneurysm rupture prediction and concluded that aspect ratio, aneurysm size, low wall shear stress area, average wall shear stress, and size ratio correlate most strongly with IA rupture.

Mostly, for the extraction of these parameters, a separation of the aneurysm from the parent vessel mesh is necessary. While many approaches only apply a planar cut plane (Berg et al., 2019c), an anatomical ostium extraction as



$u$  flow velocity field  
 $\mu$  blood viscosity  
 $\rho$  blood density  
 $\tau$  WSS vector,  
 $\tau = \frac{\sigma u_t}{\sigma n}$ , with  
 $u_t$  is velocity at wall in  
 tangential direction, and  
 $n$  is normal to the wall)

$MWSS$  maximum WSS over  
 aneurysm region  $A_a$ ,  
 $MWSS = \max_{A_a} (|\tau|)$

$Q_{in}$  inflow rate into aneurysm

$Q_v$  flow rate in parent artery

$A_{in}$  area of inflow region

$A_o$  the ostium surface area

$ICI$  inflow concentration index

$$ICI = \frac{Q_{in}/Q_v}{A_{in}/A_a}$$

$SCI$  shear concentration index \*

$LSA$  low shear area in percentage  
 of aneurysm area \*

$LSI$  low shear index \*

$LSI$  low shear index \*

$KER$  kinetic energy ratio \*

$VDR$  viscous dissipation ratio \*

\*see (Cebal et al., 2011a) for details

Figure 1.14: Illustration of hemodynamical parameters including the required subdivision of the volumetric vascular domain adapted from (Cebal et al., 2011a).

described in our study (Saalfeld et al., 2018b) would improve the standardized evaluation and better account for irregularly shaped aneurysms.

### Visual Exploration

Beyond the parameter-based evaluation of the shape and blood flow information of intracranial aneurysms, the visual exploration of the IA shape as well as the simulated vector fields has great potential to explore, understand and evaluate the cerebral hemodynamics. Numerous studies deal with this interdisciplinary and fascinating research area, in this thesis, the focus is set on the following subtopics:

- visual exploration of medical flow data in combination with surface presentation and surface feature extractions,
- filtering of the flow information in order to reveal flow characteristics,
- uncertainty visualization for IA hemodynamics, and

- quantitative evaluation of medical visualizations.

VISUAL EXPLORATION OF INTRAANEURYSMAL FLOW DATA A general overview for visual exploration of medical flow data was recently presented by Oeltze-Jafra et al. (2019). When visualizing medical image data, usually complex 3D shapes are depicted which are often combined with additional parameters, e.g., aneurysm shape and internal blood flow. Hence, a careful adaption to shape or depth perception based on special color scales is recommended in the survey by Preim, Baer, Cunningham, Isenberg, and Ropinski (2016). Unfortunately, scalar wall parameters like WSS or OSI are often mapped to the vessel wall model via color-coding as well and thus also require appropriate color-coding. Therefore, we developed a framework that combined additional visualization techniques to increase the depth perception. As a result, surface parameters can be mapped to the vessel wall by utilizing the Fresnel effect (Behrendt et al., 2017). For this approach, we do use the full range of colors visible to the human eye, since the pseudo chromadepth approach only employs a gradient from red (low depth) to blue (high depth). This work was inspired by the study of Ropinski et al. (2006) who showed that angiography images could benefit from color-encoded depth information. They introduced the pseudo chromadepth approach based on the chromadepth technique (Steenblik, 1987) that employs color to create the illusion of depth in an otherwise flat image. The study presented by Ritter et al. (2006) enhanced depth relations in complex vascular structures with hatching to simulate a shadow. This approach was extended by depth-dependent halos and support lines to convey the depth of a complex 3D model in a static 2D image (Lawonn et al., 2015).

Our study (Behrendt et al., 2017) and the adaption of the Fresnel effect to adapt the vessel surface's opacity was motivated by the work of Gasteiger et al. (2010). They introduced the *Ghosted View* where the vessel front-facing part is rendered with Fresnel shading and thus allows to visualize the inner blood flow. A subsequent study conducted by Baer et al. (2011) showed the superiority of the ghosted view technique compared to a semi-transparent visualization indicating the potential of such smart visibility techniques. Hence, our study including IVUS-based aneurysm and aneurysm wall thickness models combined with hemodynamic surface parameters adapts the Fresnel effect for the aneurysm wall as well (Glaßer et al., 2014).

FILTERING FOR VISUALIZATIONS OF INTRAANEURYSMAL FLOW DATA A drawback of these approaches is that the blood flow is often globally presented or that a specific combination between wall and underlying flow is not supported. In order to account for the near-wall hemodynamics and also combine it with the surface features, we developed a system for explorative blood flow visualization based on surface features including dynamic line filtering (Behrendt et al., 2018). Thus, our system effectively copes with visual

clutter in 3D blood flow visualizations that include the vascular surface models as well as stream- or pathlines. Further approaches have been developed to apply filtering or clustering of important flow structures such as vortices. Related to this work, Neugebauer et al. (2013) presented the *Amni-Vis* system, where the clinical expert can explore the *near-wall hemodynamics*. This approach can be extended such that surface parameters like WSS not only guide the selection of blood flow but can be utilized to automatically generate surface patches. However, They did not include non-geometric, flow-based indicators (e.g. WSS or OSI) for the automatic selection of region of interest. Furthermore, the visualization of pathlines is restricted to the region of interest.

The approach presented by Van Pelt et al. (2010) employed an implicit filtering technique based on the selection of vessel cross-sections used as seeding planes to evaluate the flow. A color-coding of flow velocity is integrated. The *Flow Lens* is a focus-and-context approach presented by Gasteiger et al. (2011) that allows the user to clip away the vessel surface to reveal the underlying blood flow. Hence, the filtering is carried out in screen space, a 3D exploration would change the focal region and the flow cannot be traced in other interesting areas outside the lens. Lee et al. (2011) analyzed screen-space entropy and occlusion to filter the pathlines. Another approach used automatic cut-away techniques based on animated blood flow (Lawonn et al., 2016). Although the entire flow course cannot be displayed, a combination with vessel surface parameters can be carried out. The clustering of blood flow in IAs introduced by Oeltze et al. (2014) showed single cluster representatives instead of filtering the pathlines. They extended this approach by dynamic seeding capabilities to explore complex flow structures such as embedded vortices (Oeltze-Jafra et al., 2016). Hence, a combination with vessel surface parameters was not possible. Meuschke et al. (2017) combined the visualization of hemodynamic flow and vessel surface information with a focus on near-wall flow by mapping the vessel surface onto a 2D plane alongside the 3D view. Thus, multiple surface parameters, e.g., WSS and wall thickness, can be correlated, but the user cannot directly extract flow bundles corresponding to local surface features. Tailored to specific flow structures in IAs, Gasteiger et al. further developed a technique to show the inflow jet and impingement zone (Gasteiger et al., 2012) as well as the resulting inflow jets of different virtual stent configurations (van Pelt et al., 2014).

When discussing filtering techniques of blood flow in medical applications, line predicates can be considered as well. They have been successfully adapted by Born et al. (2013) to explore cardiac blood flow of 4D PC-MRI data. The user can then utilize the predicates to detect flow structures such as vortices, and to detect flow that originates in a certain anatomical area. Hence, a local correlation of particular surface features and underlying blood flow is limited. Broos et al. (2016) determined seeding positions for pathlines within the context of flow visualization of cardiac 4D PC-MRI data. They provided derived flow features, e.g., magnitude or curl, and a combination of user-defined transfer functions

serves as weighting of these features to determine possible seed points. Köhler et al. (2013) utilized line predicates to globally extract vortices in these data sets without the possibility to locally correlate the vessel surface with these blood flow structures. More information about cardiac 4D PC-MRI data processing is provided in the survey by Köhler et al. (2017).

UNCERTAINTY IN VISUALIZATIONS OF INTRAANEURYSMAL FLOW DATA These highly complex visualization and analysis tools have great potential for use in clinical practice, but their acceptance is limited due to the required preprocessing as well as possible artifacts, i.e., noisy data or no patient-specific CFD simulations. In order to increase the clinical acceptance, the sources of errors should be included in these visualization systems. A first step is provided in (Saalfeld et al., 2017c), where variations based on ensemble simulations for a bifurcation IA are presented with a direct volume rendering approach. In addition, the visualization of time-dependent wall shear stress of IAs was evaluated (Glaßer et al., 2016b). These initial studies have potential for improvement and the error sources should be systematically incorporated. The survey presented by Potter et al. (2012) provides further information about uncertainty visualization approaches in general.

QUANTITATIVE EVALUATION OF MEDICAL VISUALIZATIONS When analyzing the suitability of medical visualizations itself, a lack of quantitative studies can be observed. More general, Isenberg et al. 2013 provide a systematic review of the evaluation practices in visualization and conclude that the qualitative result inspection was most often used by all reviewed papers. To overcome this issue, we developed a thorough evaluation of medical visualizations on the example of 3D aneurysm surfaces (Glaßer et al., 2016d). In a subsequent step, we extract and postulate guidelines to increase the amount of quantitative evaluations in medical visualizations (Saalfeld et al., 2018a). In the critical analysis of the evaluation practice in medical visualizations, Preim and colleagues (2018) conclude that the lack of realistic evaluations might increase the gap between medical visualization research and actual use of visualization techniques in medical research and clinical practice. They also argue to use the whole spectrum of qualitative and quantitative methods for the development and evaluation of medical visualizations.

#### 1.4.5 *Therapy Planning*

For clinical treatment planning w.r.t IAs, the clinician could greatly benefit from the various studies presented in literature. This regards the following application areas:

- Therapy planning in order to train the IA treatment.

- A rupture risk assessment for IAs.
- Virtual treatment planning to identify the most suitable implant as well as a treatment support.
- The patient-specific evaluation of the vascular domain.

These areas are explained in more detail in the following.

It must be noted that these therapy planning methods are not possible for emergency patients, e.g., in case of a subarachnoidal hemorrhage where treatment has to be immediately carried out. The discussed approaches aim at improvement of treatment of patients with innocent aneurysms or patients who do not immediately require a treatment.

#### *Training of Intravascular Aneurysm Treatment*

The structural change in IA therapy, with a shift to more endovascular interventions and less microsurgical clippings (recall Sec. 1.3.3) (Qureshi et al., 2011) yields a shortcoming of easy-to-treat cases which could serve for training of neurosurgeons. To overcome these limitations, training systems could provide training environments.

Although several virtual reality simulations exist for neurosurgical training, the real-life translation is not satisfying (Konakondla et al., 2017). Usually, virtual reality programs related to this application area allow for an interactive exploration of the intracranial vasculature, but not for an interaction with the skull (Ong et al., 2018). Further approaches are developed for neurosurgery in general, but not specifically for aneurysm clipping (Bernardo, 2017). Therefore, a software prototype for training a craniotomy followed by microsurgical clipping was recently developed, see Figure 1.15 (Neyazi et al., 2019). Based on several IA configurations (e.g., an IA at the middle cerebral artery or at the posterior communicating artery), the inclination angle of the skull could be modified and the hole for the craniotomy could be positioned, see Figure 1.16 as well as the manuscript for more details (Neyazi et al., 2019).

#### *Virtual Treatment Planning and Treatment Support*

Virtual treatment studies aim at an automatic identification of the best therapy for the patient-specific vasculature and aneurysms without harming the patient. Within the focus of neuroradiological interventions of this thesis, special attention should be paid to virtual treatment planning tools to identify the most suitable implant w.r.t. the present vessel configuration (Cebal et al., 2011b).

To improve the clinical acceptance, CFD challenges are carried out, recall Section 1.4.3, where especially the *Virtual Intracranial Stenting Challenge* (VISC) yields a consistent quantifying of the performance of commercial intracranial stents (Radaelli et al., 2008) and an excellent agreement on the hemodynamic

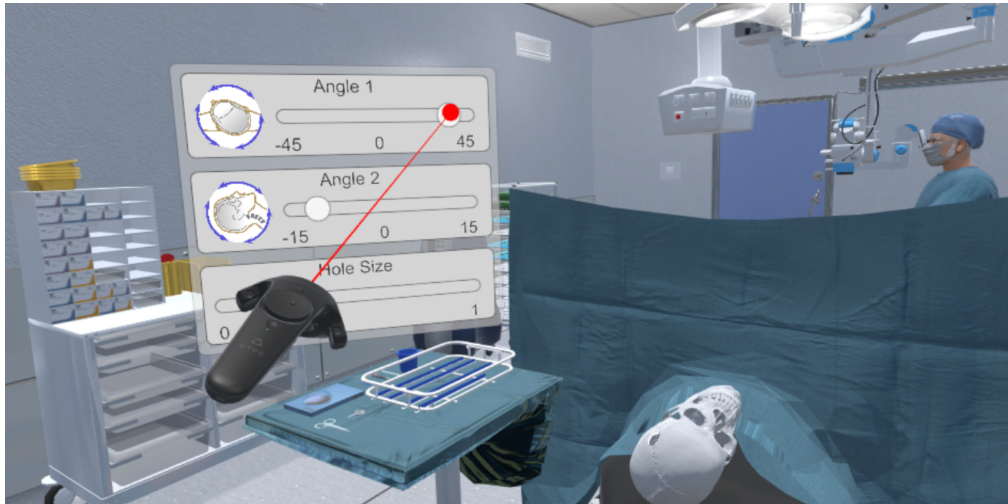


Figure 1.15: Depiction of the virtual environment for training of a craniotomy for IA clipping. Depicted is the user menu on the left and a rotatable 3D model of a skull representing the patient.

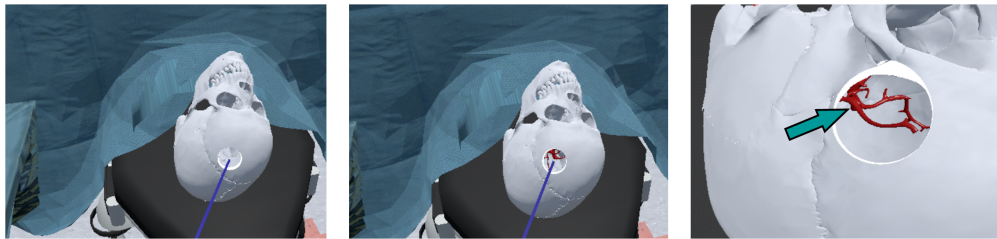


Figure 1.16: Illustration of the interactive hole definition with the software demonstrator. First, the neurosurgeon defines the skull's inclination angle. Second, the hole can be interactively dragged and resized. In the example, the trajectory successfully reveals the aneurysm at the anterior communicating artery (arrow). (Figure was adapted from (Neyazi et al., 2019) )

effect of different stent configurations compared to in vitro measurements (Cito et al., 2015). Potential improvements comprise already commercially available tools, such as the *ANKYRAS* system by Galgo Medical, Barcelona, Spain, for a personalized predictive simulation of braided stents (“ANKYRAS Product Website by GalgoMedical”, 2019). For these applications areas, it is important to also consider the flexibility of vessel walls. Since these implants have a certain stiffness, the vessel is changed accordingly, see the example in Figure 1.17. This information could be further exploited such that the implant is not only selected based on its hemodynamic consequences, but also on its stiffness and thus the expected vascular deformation (Voß et al., 2018a). Ideally, these tools could be simultaneously updated during intervention. A first idea was realized that highlights the stent markers (Manthey et al., 2017) to improve the stent deployment.

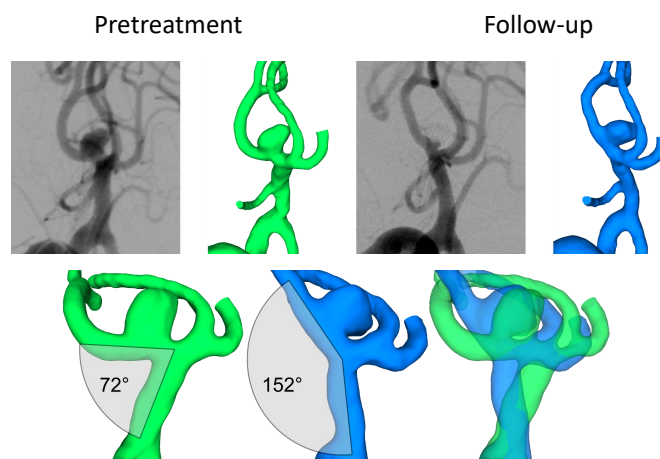


Figure 1.17: Patient data pre- (left, green surface mesh) and post-treatment (right, blue surface mesh). After the stent deployment, a strong change of the vessel course can be seen with a considerable change of the bifurcation angle. Image adapted from (Voß et al., 2017).

#### *Patient-Specific Rupture Risk Assessment for IAs*

As it was discussed in Section 1.4.4, the computer-based extraction of morphologic and hemodynamic information based on the conducted segmentation and CFD simulation is an important step for rupture risk assessment. First, more information could be provided in case of innocent aneurysms with a challenging access path, i.e., aneurysms that are at the peripheral arteries of the Circle of Willis. Second, for treatment of a patient harboring multiple aneurysms, the aneurysm with the highest rupture risk could be identified and treated first, see the example in Figure 1.18.

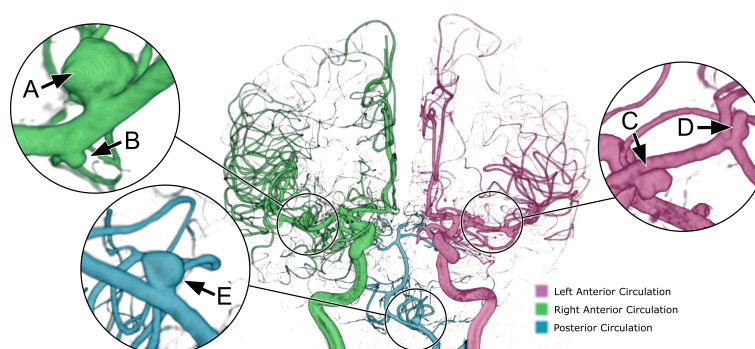


Figure 1.18: Illustration of a patient with five aneurysms, where the different circulation areas are color-coded. This dataset was also prepared for the MATCH challenge (Berg et al., 2018a).

Hence, various studies provide promising results, but there is still a mismatch between the clinical research and clinical practice. Ideally, the hospital would have a solution, comprising a segmentation and simulation suite that allows for extraction of all required information for the automatic rupture risk assessment. There exist clinical research prototypes, for example the research prototype from Siemens Healthcare GmbH. They allow for a fast segmentation and simulation based on a Lattice–Boltzmann solver (Berg et al., 2016), i.e., hemodynamic predictions could be created within several minutes at low spatial resolution. The study concludes that further in vivo validations are required to guarantee realistic predictions. Furthermore, such prototypes are not yet authorized. Given the ethical challenge (ruptured IAs are life-threatening and have to be treated always and as fast as possible under certain circumstances), a prospective study seems not realistic.

#### *The Patient-Specific Evaluation of the Vascular Domain*

For the evaluation of the patient-specific vascular domain, the clinical experts acquire a set of 2D DSA and often a 3D DSA dataset. Next, they analyze possible access paths and the presence or absence of vessels and pathologies.

Apart from commercial solutions, research projects for the evaluation of intracranial arteries and their pathologies tackle their challenging 3D shape and spatial orientation. Since the anatomical manifestation of the intravascular arteries underly strong, patient-specific variations with respect to shape and length (Kayembe et al., 1984), recall Section 1.3.1, the Circle of Willis is an excellent example for a challenging and complex 3D anatomy that benefits from computer-supported treatment planning. We developed the “Free-Form Annotations on Unfolding vascular Structures” (FAUST) framework for creating 3D annotations by freely sketching in the 3D environment (Saalfeld et al., 2017a) based on (Saalfeld et al., 2016; Saalfeld et al., 2015). Thus, the clinician can account for different stent configurations, coil lengths and access paths. Hence, an example case of an unruptured IA with increased neck size at a bifurcation is discussed. Due to the wide neck, the interventional therapy of plain or balloon-assisted coiling should be combined with a stenting. Even two stents may be necessary, i.e., a Y-, X- or T-stenting intervention, and special care is required to prevent hampering of the blood supply by blocking small branching arteries. Apart from the patient-specific treatment planning, a further study of the anatomy is possible which is supported by an interactive unfolding, see Figure 1.19 (Saalfeld et al., 2017b). The survey on virtual human anatomy education systems (Preim & Saalfeld, 2018) presents further studies dealing with computer-supported anatomy education.

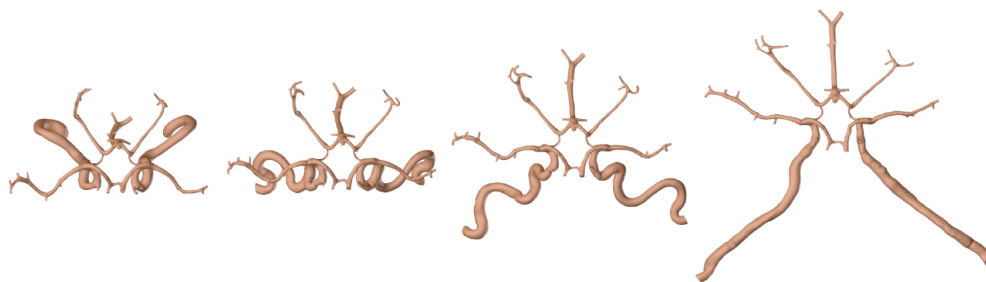


Figure 1.19: Illustration of the interactive unfolding of the Circle of Willis model. Image adapted from (Saalfeld et al., 2017a).

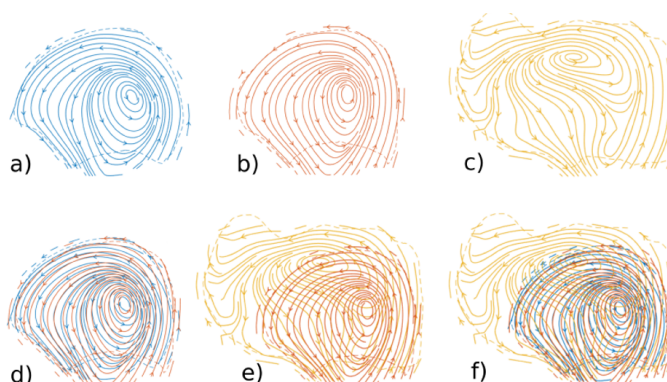


Figure 1.20: Illustration of the intra-aneurysmal hemodynamics, depicted with stream slices, see (Mittentzwei, 2019) for more information. The patient underwent three scans in 54 months, resulting in the first time step (a), a second time step (b) and the last one after rupture (c). A comparative visualization of (a) and (b) is presented in (d), of (b) and (c) in (e) and of all time steps in (f). Image is adapted from (Mittentzwei, 2019).

## 1.5 OUTLOOK

The presented pipeline (recall Fig. 1.8) provides an overview of the attached publications in the cumulative part of this thesis. It also indicates the different steps of treatment of IAs that benefit from computer-based evaluation and support tools.

When dealing with computer support for IAs, especially when comparing clinical research and clinical practice, several shortcomings can be identified:

1. The division of IAs in ruptured and unruptured aneurysms is unfortunate, since each unruptured aneurysm could hypothetically rupture on the next day. Hence, a division in stable vs. unstable aneurysms as well as more longitudinal studies should be carried out. First studies already divide into stable and unstable, e.g., Brinjikji et al. (2017) defined an aneurysm

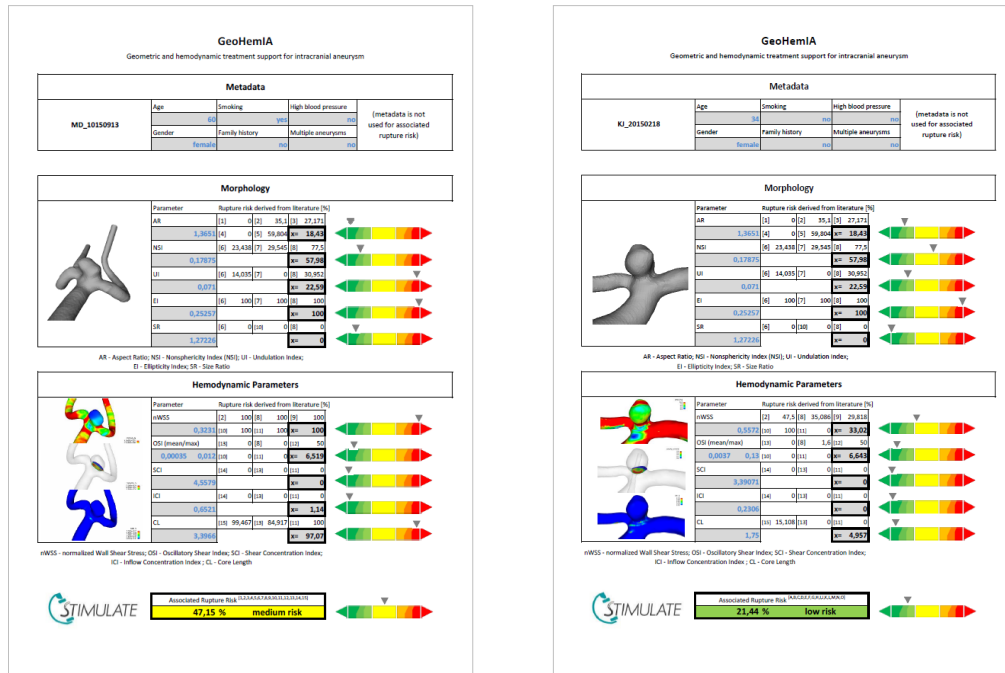


Figure 1.21: Evaluation of two clinical datasets with the *GeoHemIA* initiative. The clinician transferred two anonymized 3D DSA datasets and we applied our methods to extract morphological and hemodynamical parameters. A score is applied based on studies from literature.

as stable if its size match was within a 10% interval based on two 3D RA scans with at least 12 months apart.

2. Based upon this issue, a further need for the evaluation of longitudinal studies is present. Only longitudinal studies could provide further insight about the aneurysm growth and their change of intracranial hemodynamics, as we recently examined (Mittenentzwei, 2019); see Figure 1.20.
3. A missing imaging of the vessel wall hampers CFD simulation as well as thorough evaluation of aneurysms and cerebrovascular diseases. Hopefully, intravascular imaging methods will be available in the near future in clinical practice. Ideally, this will be combined with further information, e.g., specific patient parameters regarding the velocity of inflowing blood.
4. Although a wide variety of rupture risk studies exists with quite reasonable predictive power, the clinical acceptance is still limited. Hence, the following issues have to be tackled:
  - A systematic inclusion of possible error sources comprising the imaging, segmentation, CFD simulation and evaluation should be carried out and presented to the clinical expert. Thus, a confidence interval rather than a single score or parameter value should be presented. We

summarized these influences in the recently published review article about the reliability of hemodynamic modeling (Berg et al., 2019a).

- A standardized pre- and postprocessing of the medical image data should be conducted. Further guidelines have to be established, which in turn reduce the number of error sources. Nevertheless, apart from the medical image data, patient-specific diseases, life style, genetic factors and other aspects influence the rupture risk as well.
5. The required resources for the clinical research projects, i.e., skilled engineers that conduct segmentation, simulation and classification tasks, as well as hardware equipments, have to be available in broad public. With increasing digitalization, a distant service based on the standardized processing of the previous issue could solve this problem.

To tackle the last issue, we founded the *GeoHemIA* (geometrical and hemodynamical intracranial aneurysm rupture risk assessment) initiative, where anonymized medical 3D DSA datasets can be uploaded and the segmentation and CFD simulations are applied. As a result, the clinical expert will get a standardized single sheet document, where common rupture risk parameters from the literature are listed, see the example provided in Figure 1.21.

Advantageously, the computationally expensive operations can be carried out at a remote site and the clinicians just get the summarized lab reports, similar to a blood analysis at a general practitioner's. In 2017, we submitted this concept to the Hugo-Junkers Competition ("Hugo Junkers Competition", 2019), a local competition that encourages founders of companies and start-ups as well as scientists and inventors to submit their ideas for research and innovation. The *GeoHemIA* project was amongst the finalists, but not under the top three winners. Since similar approaches have been reported recently, this concept may be hopefully come true in the near future.

# Part I

## Imaging

This part of the postdoctoral thesis covers important aspects regarding the imaging of intracranial arteries and their pathologies, like IAs, and cumulates the following publications:

- Chapter 2 (see page 39): Hoffmann, T., Glaßer, S., Boese, A., Eppler, E., Kalinski, T., Beuing, O., & Skalej, M. (2016). Experimental investigation of intravascular OCT for imaging of intracranial aneurysms. *International Journal of Computer-Assisted Radiology and Surgery (IJCARS)*, 11(2), 231–41
- Chapter 3 (see page 51): Glaßer, S., Hoffmann, T., Boese, A., Voß, S., Kalinski, T., Skalej, M., & Preim, B. (2017). Virtual inflation of the cerebral artery wall for the integrated exploration of oct and histology data. *Computer Graphics Forum*, 36(8), 57–68
- Chapter 4 (see page 63): Voß, S., Glaßer, S., Hoffmann, T., Beuing, O., Weigand, S., Jachau, K., Preim, B., Thévenin, D., Janiga, G., & Berg, P. (2016). Fluid-Structure Simulations of a Ruptured Intracranial Aneurysm - Constant versus Patient-Specific Wall Thickness. *Computational and Mathematical Methods in Medicine*, 9854539

*The typesetting of the manuscripts has not been modified. No changes have been made to the texts and illustrations of these peer-reviewed submissions. Only header, footer, and page numbers were removed and replaced by a chapter header and a running number.*



## Experimental investigation of intravascular OCT for imaging of intracranial aneurysms

Thomas Hoffmann<sup>1</sup> · Sylvia Glaßer<sup>2</sup> · Axel Boese<sup>3</sup> · Knut Brandstädter<sup>4</sup> · Thomas Kalinski<sup>5</sup> · Oliver Beuing<sup>1</sup> · Martin Skalej<sup>1</sup>

Received: 13 January 2015 / Accepted: 22 July 2015  
© CARS 2015

### Abstract

**Purpose** Rupture risk assessment of an intracranial aneurysm (IA) is an important factor for indication of therapy. Until today, there is no suitable objective prediction method. Conventional imaging modalities cannot assess the IA's vessel wall. We investigated the ability of intravascular optical coherence tomography (OCT) as a new tool for the characterization and evaluation of IAs.

**Materials and methods** An experimental setup for acquisition of geometrical aneurysm parameters was developed. Object of basic investigation was a silicone phantom with six IAs from patient data. For structural information, three circle of Willis were dissected and imaged postmortem. All image data were postprocessed by medical imaging software.

**Results** Geometrical image data of a phantom with six different IAs were acquired. The geometrical image data showed a signal loss, e.g., in aneurysms with a high bottleneck ratio. Imaging data of vessel specimens were evaluated with respect to structural information that is valuable for the characterization of IAs. Those included thin structures (intimal flaps), changes of the vessel wall morphology (inti-

mal thickening, layers), adjacent vessels, small vessel outlets, arterial branches and histological information.

**Conclusion** Intravascular OCT provides new possibilities for diagnosis and rupture assessment of IAs. However, currently used imaging system parameters have to be adapted and new catheter techniques have to be developed for a complete assessment of the morphology of IAs.

**Keywords** Intracranial aneurysm wall · Optical coherence tomography (OCT) · Rupture risk · Intracranial arterial wall

### Introduction

An intracranial aneurysm (IA) is a saccular or fusiform dilation of intracranial arteries, mainly of those forming the circle of Willis and bifurcations of nearby cerebral arteries. In 6–10/100,000 inhabitants per year, an IA ruptures, which leads in the majority of cases to a subarachnoid hemorrhage (SAH) [1]. Approximately half of the patients die during the first 30 days after SAH and up to 50 % of the surviving patients suffer from permanent neurological and psychological deficits [2].

In contrast to the low incidence of aneurysm rupture, the prevalence of IAs is high with 3–6 % in most Western countries [3]. Due to the widespread use of magnetic resonance imaging (MRI) and computed tomography (CT) as diagnostic tools, many IAs are incidentally detected during examinations conducted for other reasons [4]. Thus, the physician is frequently facing the decision, whether the treatment—with the risk of severe complications—of such an unruptured IA is necessary to prevent SAH and its consequences, or whether observation suffices. The rupture rates of asymptomatic IAs are reportedly equaled or exceeded by

✉ Thomas Hoffmann  
t.hoffmann@ovgu.de

<sup>1</sup> Institute of Neuroradiology, Otto-von-Guericke University, Magdeburg, Germany

<sup>2</sup> Department of Simulation and Graphics, Otto-von-Guericke University, Magdeburg, Germany

<sup>3</sup> Department of Medical Engineering, Otto-von-Guericke University, Magdeburg, Germany

<sup>4</sup> Institute of Forensic Medicine, Otto-von-Guericke University, Magdeburg, Germany

<sup>5</sup> Institute of Pathology, Otto-von-Guericke University, Magdeburg, Germany

the mortality rate associated with treatment [5]. But up to date, no criteria exist that allow a reliable estimation of the rupture risk. Decision for treatment is mainly based on morphological aspects such as size, shape and location. Other factors, especially thickness and histological characteristics of the aneurysm wall, cannot be satisfactorily assessed. On the other hand, such information might change the strategy and result in fewer, potentially dangerous, therapeutic interventions. Intravascular optical coherence tomography (OCT) provides the possibility to assess vessel wall thickness as well as morphological and structural properties. To evaluate the potential of OCT to overcome this clinical problem, we investigated patient-specific aneurysms as a silicon model and the ability to illustrate aneurysm-specific structural parameters.

### Intravascular OCT

OCT is an established diagnostic method in cardiology for the assessment of atherosclerotic plaques and stent appositions. The diagnostic benefit has been documented in several trials and clinical studies [6–11].

Current systems are based on the spectral-domain imaging. A swept source semiconductor laser generates near-infrared light with a wavelength of 1300 nm (near-infrared light). The swept source technique enables imaging in real time. Caused by the wavelength, a spatial resolution of less than 15  $\mu\text{m}$  can be reached with good soft tissue contrasts [12]. The technique is based on a Michelson interferometer.

Near-infrared light is highly absorbed and scattered by blood. For imaging of the arterial wall, blood has to be replaced by a translucent fluid. Current systems use a liquid flush injection without occluding the vessel.

Tissue has a low absorption and scattering of near-infrared light (“near-infrared window”) [13]. Thus, a tissue penetration depth of 1–3 mm is possible with this non-ionizing radiation.

Current intravascular OCT systems create two-dimensional cross-sectional images of the vessel wall. A pullback of the catheter shaft has to be started to generate volume datasets along the catheter axis.

### Clinical workflow

The workflow of a cardiac OCT catheter intervention consists of eight different steps, as shown in Fig. 1. First, different system parameters must be set. Those include, e.g., the type of flush solution (saline or contrast agent), the pullback length and velocity and a manual or automatic pullback start of the catheter shaft. Next, all instruments (guide wire, guide catheter and imaging catheter) must be positioned. The location depends on the prior defined parameters. The imaging catheter is pushed through the lumen of the guide catheter and placed more distal to the pathology in the coronary artery.

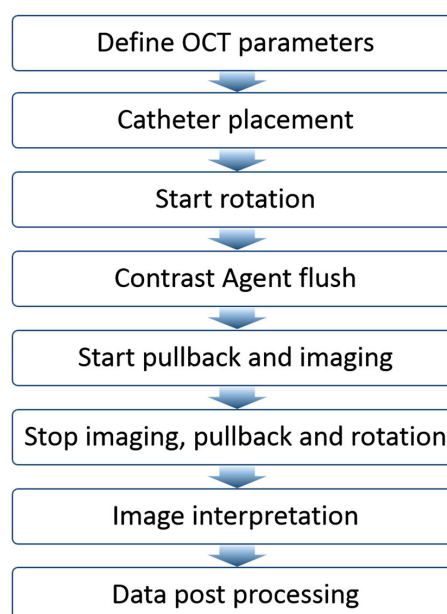


**Fig. 1** Clinical workflow of an OCT catheter intervention

A guide wire with a rapid exchange system in the catheter tip can be used for an easier positioning of the OCT catheter.

In a next step, the rotation of the catheter shaft must be started and an injection of flushing solution is triggered. Using contrast agent as a flushing solution enables simultaneous C-arm angiographic imaging during the OCT pullback. The pullback and image recording start automatically, after the vessel segment is free of blood. Liquid volume and injection speed depend on the vessel under investigation.

After complete coverage of the target structure, imaging, pullback and rotation of the catheter shaft will be stopped. After postprocessing, information such as vessel diameter, thickness and composition of plaques or intima dissections can be quantified with the system.

For imaging and characterization of IA walls, the OCT parameters have to be adapted. In contrast to coronary plaque assessment or stent apposition, IAs are accompanied with different requirements and challenges for a valid characterization.

Figure 2 illustrates the adaption of OCT imaging to aneurysm walls. The thickness, borders, intramural deposits and intraluminal thrombi must be imaged. From the signal characteristics of the OCT image, information about structural differences between the normal arterial and the aneurysm wall—such as intramural hematoma, lipid content or calcified areas—should be derived.

Aneurysms show more complex geometries than healthy vessels. We describe the geometry, as illustrated in Fig. 2, by

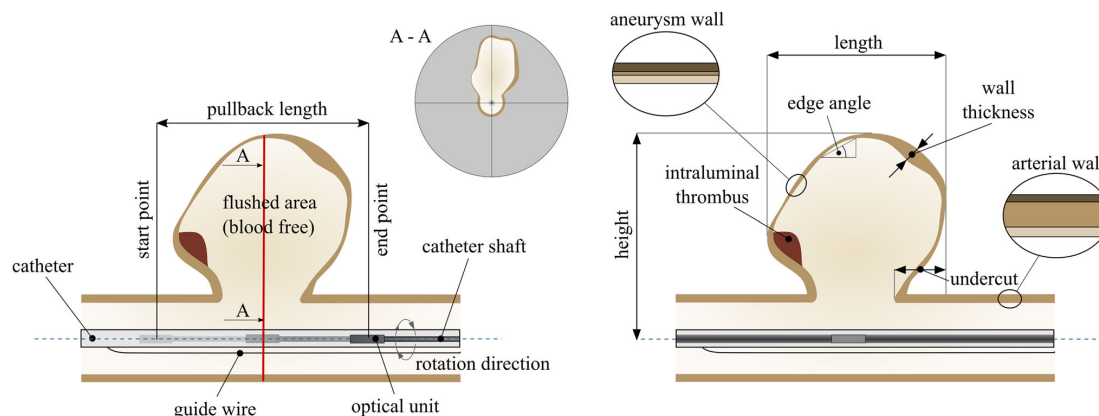


**Fig. 2** Principle, requirements and parameters for catheterized OCT probing of cerebral aneurysms. *Left* schematic overview of OCT data image acquisition. The catheter shaft with probe is rotating. A pullback starts after a saline or contrast agent injection is done. The probe is pulled back from the start point (see the *light gray shape*) to the end point. The

red line shows an example of an OCT image plane. The corresponding cross-sectional OCT image is illustrated in A–A. *Right* characteristics of the aneurysm and vessel wall, which have to be considered while the imaging process

the following parameters: “aneurysm undercut” which means a vessel wall area which is located behind another vessel wall. The “edge angle” can be described as the angle between two adjacent points connected by a straight line referred to the horizontal axis. If the slope of the straight line is positive, it is named rising edge, it is called falling edge if the slope is negative. The “bottleneck value” is the ratio between maximum ostium diameter and neck diameter and is an indicator for undercuts.

The aim of our study is to examine whether intravascular OCT is suitable to provide this information.

### State of the art

There is a great need for *in vivo* detection of degenerative changes of the vessel wall that arise during the development of aneurysms [14], as they may represent an important indicator of impending rupture. OCT is rated as a promising method to yield such structural information, which cannot be acquired by conventional imaging methods due to their limited spatial resolution or poor soft tissue contrast.

Nowadays, intravascular OCT is limited to applications in cardiac and peripheral vessels due to restrictions of the medical board. For neurovascular applications, only a few experimental and clinical trials were conducted in the past years.

Thorell et al. [15] created artificial coil embolized aneurysms in a canine model. OCT was used to image the aneurysm neck. The acquired images were correlated with histological findings. They concluded that OCT may be a

valuable method for follow-up studies and provides better understanding of tissue healing.

Mathews et al. [16, 17] developed an endovascular OCT catheter with a time-domain system for imaging of intracranial vessels. The study was done in animal and human vessels after explantation postmortem. A clinical trial was carried out with the healthy internal carotid artery of three patients. They showed that OCT is feasible for clinical use and can detect arterial structures. The understanding of pathologic OCT image signals allows optical biopsies of vascular tissue.

Lopes et al. [18] first imaged stent struts and arterial perforators, which could not be seen in angiography. They used a conventional OCT system and inserted the catheter by a femoral access in a human cadaver. In a second step, the brain and intracranial vessels were removed and imaged. They concluded that OCT imaging may aid in the treatment of neurovascular diseases.

Another work deals with the imaging of flow diverter struts in canine models with artificial sidewall aneurysms [19]. They conclude that OCT with its superior high spatial resolution has the ability to image malappositions.

A method to characterize mechanical properties of vessels can be done by motion estimation [20]. OCT is already able to depict dynamic processes to create elastographic investigations of plaques for the determination of their composition and mechanical properties [21].

### Material and methods

In this section, the OCT system, catheter and experimental setup are described.

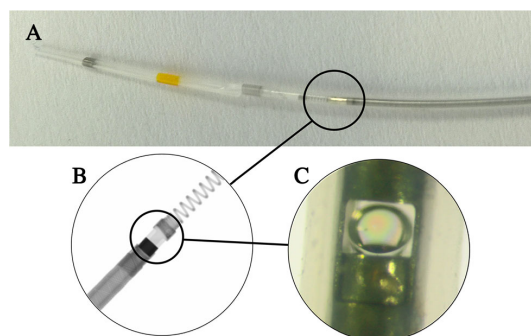


**Fig. 3** TERUMO Fastview™2.6F catheter. **a** Catheter tip with rapid exchange system and optical unit (*circle*). **b** Micro-CT image of the catheter tip with lens and prism. A spring is located on top of the probe. **c** Microscopic view of the probe

### OCT system

All measurements were carried out with a TERUMO LUNAWAVE™console (Terumo Corporation, Shibuya, Japan). The system is equipped with a near-infrared laser light source in the spectral domain. A maximum pullback length of 150 mm can be realized in 3.75 s. The pullback speed can be reduced stepwise from 40 to 0 mm/s. The system is real-time capable with a rate of 158 frames per second.

### OCT catheter

A TERUMO Fastview™2.6F catheter was used for all measurements. It contains an optical fiber, which is rotating inside the catheter. The fiber is connected to a lens and a prism in the distal end; see Fig. 3. A linear motor in a unit, which is connected to the catheter, can pullback the fiber without changing the location of the catheter tip. A rapid exchange system at the distal end of the catheter enables the use of a guide wire.

### Setup 1: Aneurysm form

We developed an individual silicone phantom to evaluate the ability to image whole aneurysms. This phantom was created using 3D angiographic datasets of patients harboring an aneurysm. From these data, sidewall and bifurcation aneurysms were segmented and analyzed. The aneurysm geometries were virtually separated from their parent vessel and added to a 175-mm-long cylinder with a diameter of 4 mm (see Fig. 4). This model was 3D printed in wax first and casted with silicone afterward.

To assess the general suitability of OCT for the imaging of IAs, we selected IAs with a wide geometrical range. The aneurysm volumes range from 8.78 mm<sup>3</sup> for the smallest one

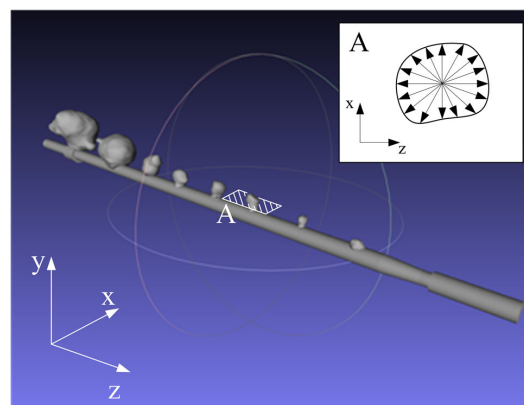


**Fig. 4** Virtual cylinder with eight IAs, segmented from patient data. **a** Illustration of the measuring method for determination of dome and neck diameter. A layer with the highest diameter in  $x$ - $z$  plane was selected. Eight circumferential measurements were carried out. In a postprocessing step, the arithmetic mean was calculated

**Table 1** Extracted geometrical properties of eight selected IAs (increasing size)

Aneurysm (-)	Mean volume (mm <sup>3</sup> )	Mean height (mm)	Aspect ratio (-)
1	8.78	2.43	0.95
2	9.24	2.66	1.34
3	26.79	4.25	1.63
4	42.99	4.07	1.33
5	54.39	5.05	1.58
6	158.77	9.02	2.09
7	946.67	11.74	1.73
8	1573.78	14.79	2.38

All measured values are mean values of 3 different measurements. Aspect ratio classification [22]: <1.6—low risk of rupture; 1.6–2.2—borderline risk; >2.2 high risk

up to 1.57 cm<sup>3</sup> for the largest one. More parameters are displayed in Table 1. The aspect ratio (dome height/maximum neck width), which is an accepted parameter for aneurysm status, was calculated additionally. The aneurysms 3, 6 and 7 were classified as borderline risk of rupture (aspect ratio: 1.6–2.2). Aneurysm 8 was classified as high risk (aspect ratio: >2.2). Aneurysms 1, 2, 4 and 5 were assigned to a low risk of rupture [22]. All IAs were unruptured at the time of diagnostic imaging.

The experimental setup was built up in an angiography laboratory. The OCT catheter was inserted into the phantom. Afterward, model and catheter were put into a saline solution. Measurements were carried out for aneurysms 1–6, which have sufficient geometries to evaluate the imaging method. To check the pullback process of the catheter shaft, all trials were

done under fluoroscopic imaging. OCT system parameters were set to an automatic pullback of 130 mm with a velocity of 20 mm/s.

The acquired datasets were analyzed and postprocessed with the freely available software MeVisLab (MeVis Medical Solutions AG, Bremen, Germany). The postprocessing included a semiautomatic segmentation of the aneurysm contour, with a primitive thresholding and a region growing techniques. A marching cubes triangulation algorithm of the segmented 2D data stack was applied to generate a 3D mesh model of the IA. The extracted 2D and 3D image data were analyzed by experienced neuroradiologists.

For measuring the parameters neck diameter and dome diameter, a single  $x$ - $z$  plane was selected and eight diameters were measured with MeVisLab (see Fig. 4a). The maximum, minimum and mean were extracted from those values. Height was determined by selecting a  $y$ - $z$  plane with maximum height of the dome. Measurement was carried out from ostium to dome. Furthermore, the bottleneck (dome diameter/neck diameter) ratios of six aneurysms were calculated.

## Setup 2: Structural information

In addition to the geometrical information, structural information is an indicator for the risk of rupture of an IA [14]. To check the ability of OCT to assess vascular structures, three human circle of Willis were explanted postmortem. All investigations were performed in accordance with the local ethic committee. The specimens were investigated for pathological changes of the vessel wall, e.g., plaque and aneurysms. After explantation, the preparations were flushed with saline and placed in 4 % formaldehyde. For the following OCT imaging, the preparations were fixed on a silicone plate with cannulae and embedded into a container with saline. To enter the vessel lumen with the OCT catheter, a guide wire was inserted and carefully pushed through the vessel. The OCT catheter was then advanced over the guide wire and placed in the correct position to image the selected vessel. To avoid artifacts, the guide wire was removed before imaging. For the inflation of arteries, a 5F guide catheter was placed in one of the vessels of the circle of Willis and then connected to an injector filled with saline. Flow rate was adjusted for an inflation of the current vessel of interest (4–20 ml/s). OCT system parameters were individually selected depending on the vessel length and region of interest.

Arteries with a smaller diameter than the OCT catheter were examined by positioning the catheter beside the vessel. With this technique, it was possible to image all segments of the circle of Willis (Fig. 5). The analysis of the generated datasets was carried out with MeVisLab. To validate detected abnormalities in the signal characteristics of the vessel wall, a histological investigation of the segment was done. Therefore, the preparation was embedded into paraffin and

cut into 3  $\mu$ m slices. The distances of the slices were individually selected, depending on extent of the pathology and virtual slice thickness of the OCT images. A hematoxylin and eosin (HE) stain was used. The slices were scanned with a high-resolution slide scanner (NanoZoomer, Hamamatsu Photonics, Hamamatsu, Japan).

## Results

As described before, all datasets were analyzed with respect to the feasibility of probing IAs and gaining morphological information with the OCT technology.

### Geometrical parameters of phantom scans

It was possible to probe and completely image aneurysms 1 and 2, as it can be seen in Fig. 6. The parameters height and diameter could be measured as well (see Table 2).

For aneurysms 3–6, it was not possible to measure the maximum height due to the limited OCT imaging diameter of 9 mm. The neck diameter could be measured for all aneurysms.

The 3D views in Fig. 6 show that the resolution in  $z$  direction, i.e., the slice distance, is not high enough to seamlessly reconstruct the aneurysm surface. Due to the pullback length and velocity, a slice thickness of 127  $\mu$ m was reached. For aneurysm number 1 and 2 were 27 and 25 slices acquired, respectively. In cases of a high gradient of the aneurysm wall along the  $z$  axis (large edge angle, see Fig. 2) and resulting high tissue thickness perpendicular to the catheter axis, it is not possible to depict the whole geometrical information.

We were able to visualize undercuts of aneurysm neck and wall in the translucent silicone phantom. An indicating parameter for undercuts is the previously described bottleneck ratio. Therefore, we measured those diameters in the image data. As shown in Table 3, the ratio varies between 1 and 1.20. For aneurysms 3–6, we measured only the maximum dome diameter which could be determined in the OCT data.

### Structural information

Analysis of the ex vivo acquired datasets of intracranial vessels (Fig. 5) showed typical morphological information as described in the following. The evaluation of data was done with respect to parameters that are critical for the assessment of the rupture risk of IAs.

### Intimal detachments

The ex vivo imaging of the vertebral artery showed intimal flaps in some areas. The reasons for that are unknown to us. It was probably caused by the insertion of the OCT catheter

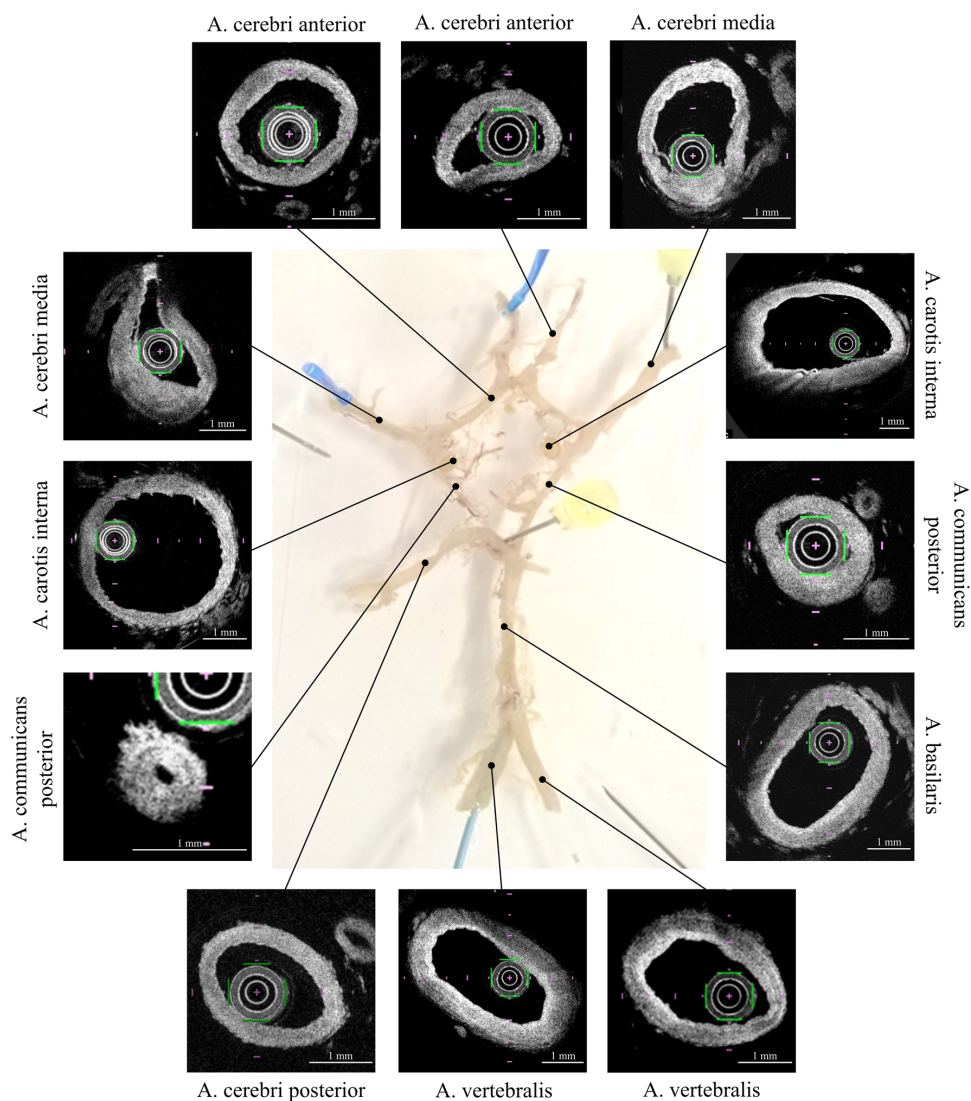


**Fig. 5** Postmortem preparation of the circle of Willis. The fixated preparation is inserted in saline and attached with cannulae to a silicone plate. An OCT catheter was inserted in the vessel of interest. A

guide catheter was inserted in an adjacent vessel to flush and inflate the arteries. OCT images show the morphology of probed vessels

and the guide wire. The detached intima layer had a thickness of about  $67 \mu\text{m}$  (Fig. 7).

#### Intimal thickening

OCT images allow for a clear assessment of differences in intimal thickness (Fig. 8). A thickened intima was observed at branches in all imaged vessels.

#### Perforators

Perforating arteries could be identified ex vivo (Fig. 9). A 3D image of the artery segment shows the ability of the OCT system to image the perforator through the wall of the vertebral artery, but details of the perforator wall are lost.

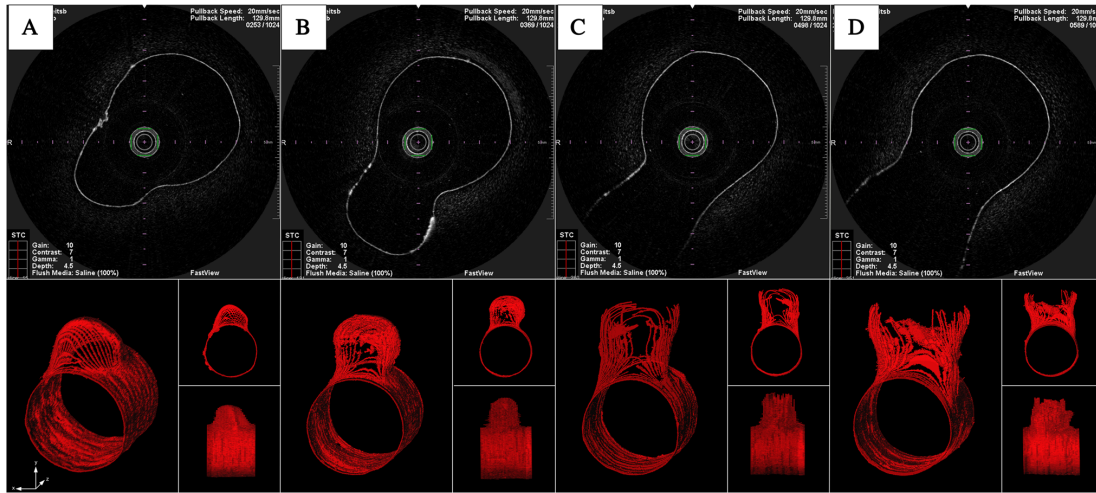


**Fig. 6** OCT images (top) and 3D reconstructions (bottom) of the aneurysm silicone phantom in different views. **a, b** Acquired OCT image data of aneurysms 1 and 2 show the inner surface of the phantom. It can be seen that a loss of information is given at strongly rising and falling edges. **c, d** The maximum image diameter of the OCT system

was exceeded. The aneurysm dome could not be depicted completely. Additionally, a loss of information at areas of thick tissue (rising and falling edges) occurs. Aneurysm neck and undercuts of the dome are shown

**Table 2** Geometrical parameters of six probed IAs

Aneurysm (-)	Height (mm)	Ostium diameter (mm)	Dome diameter (mm)
1	2.26	3.14	-
2	2.78	2.48	2.71
3	3.38 (max.)	2.99	3.36
4	3.58 (max.)	3.46	4.16
5	3.14 (max.)	3.93	4.40
6	3.13 (max.)	5.26	5.76

For aneurysms 3–6, the real height could not be measured caused by the maximum imaging diameter of the OCT system

**Table 3** Maximum bottleneck ratios (BN) of aneurysms 1–6

Aneurysm	Aneurysm					
	1	2	3	4	5	6
BN (-)	1	1.09	1.12	1.20	1.12	1.10

For aneurysm 1, the ratio is calculated to a value of 1, because maximum dome diameter was identical to ostium diameter

**Layered structures**

As documented in literature, OCT imaging is able to depict all three layers of an artery wall. In our investigation, we were able to visualize the layered structures of all intracranial vessel preparations (see Figs. 5, 10).

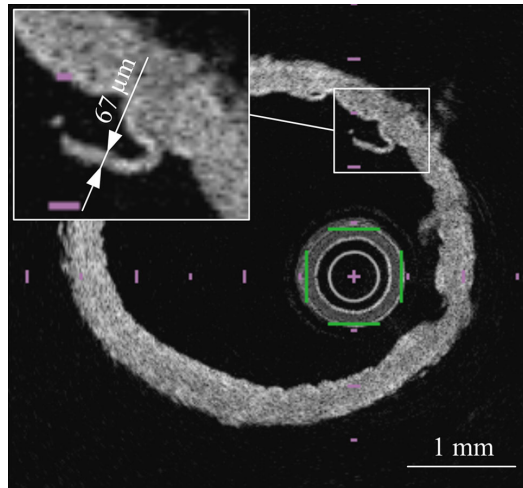


**Fig. 7** OCT image of a vertebral artery shows an intimal flap with a thickness of 67  $\mu\text{m}$

**Branches**

The visualization of different branches with the OCT system was possible. A 3D imaging of the middle cerebral artery (MCA) shows a branch from the M1 segment to the M2 segment. As shown in Fig. 11, it is not possible to show a detailed view of the vessel wall of the adjacent vessel, caused

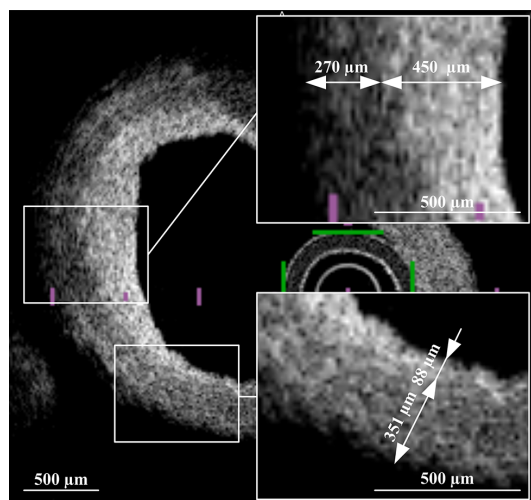


**Fig. 8** Cross-sectional OCT image of a vertebral artery. A changing intima thickness from 88  $\mu\text{m}$  to 450  $\mu\text{m}$  can be observed

by a signal reduction through the wall of the parent vessel. It was possible to image the arterial wall in the area of the branches.

#### Histological information

OCT provides the possibility to differentiate normal from pathological tissue.

In our case, we investigated the generated datasets of the circle of Willis for pathological changes in the vessel wall. One internal carotid artery showed changes in the area of the intimal layer with signal loss behind. A histological investigation of the artery demonstrated a fibrous plaque with a thickness of about 500  $\mu\text{m}$  (Fig. 12).

#### Discussion

The assessment of the rupture risk of incidentally detected IAs is of huge clinical interest, as current therapies all may lead to devastating complications. To date, the risk of future rupture of an aneurysm cannot be reliably predicted, even if several morphological parameters have been found useful by some authors. All these parameters focus on size and ratios of measured diameters, but for the estimation of the rupture risk it seems crucial to gain information about the aneurysm wall strength and intramural pathologic changes. Intravascular OCT has a very high spatial resolution and is frequently used in cardiology. Several studies proved that cardiovascular pathologies, e.g., plaques, can be well assessed by OCT, which in turn improves patient care.

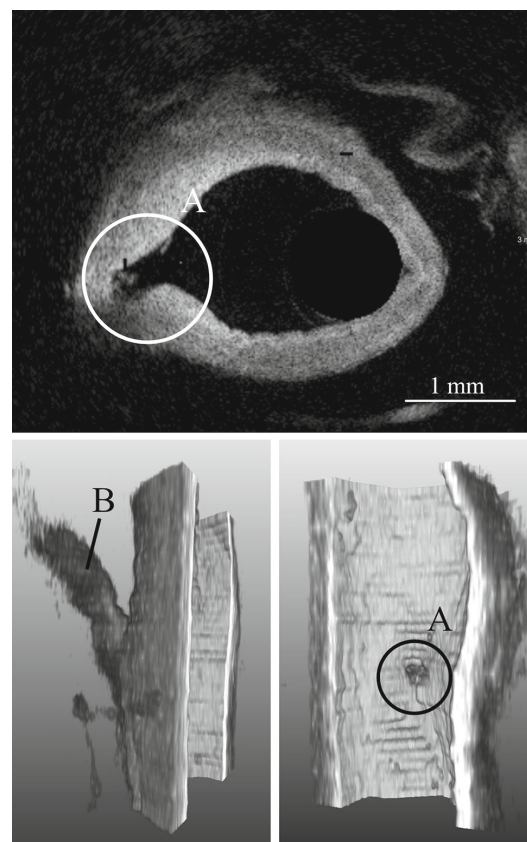


**Fig. 9** Cross section and 3D illustration of a vertebral artery segment in half section. **a** Outgoing area of an arterial perforating branch. **b** Perforating vessel with lower signal and less geometrical information compared with parent vessel

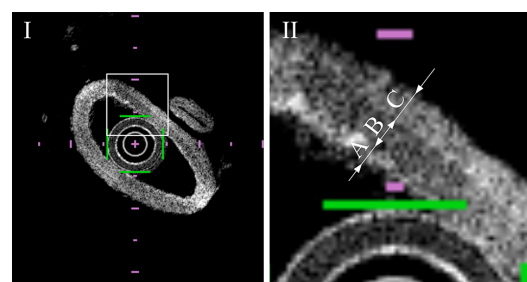


**Fig. 10** Cross section of an intracranial artery. **I** Total view of the artery with discernible vessel wall layers. **II** Enlargement of a wall section from **I** (square) with tunica intima (**A**), tunica media (**B**) and tunica adventitia (**C**)

The advantage of extraordinary high spatial resolution and sufficient soft tissue contrast might be a crucial factor for an objective assessment of IAs. The imaging method pro-

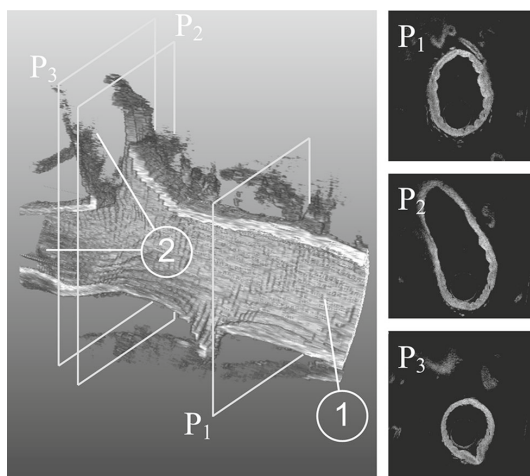


**Fig. 11** Cross-sectional 2D OCT and 3D illustrations of an MCA branch. 1—Middle cerebral artery M1 segment. 2—Middle cerebral artery M2 segment. P1–P3 show cross-sectional planes of the OCT images

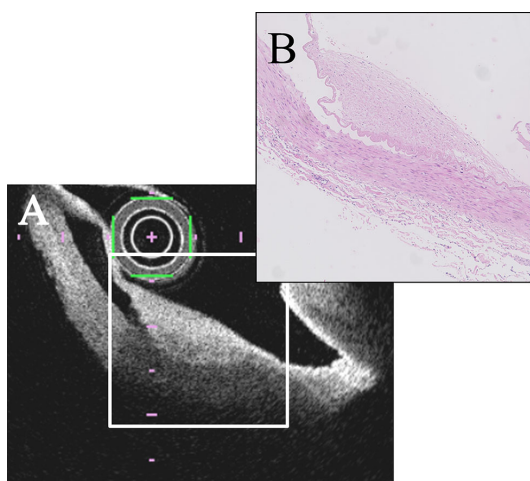


**Fig. 12** OCT image of a fibrous plaque located at the internal carotid artery (ICA) communicating segment (C7). An OCT catheter is inside the vessel. Intimal detachments can be seen. Plaque structure leads to signal attenuation in the area behind. **a** Histological view of the plaque area (**a**, white square). Intimal detachments and fibrous plaque structure are observable

vides information about the vessel wall and can be used to distinguish different vessel structures. But imaging of IAs is challenging, mainly due to their complex geometry and the difficult access. Our study investigated the abilities of a current OCT system for detailed intravascular examinations of aneurysms. Focus areas were the acquisition of the correct geometry and its structural composition. Another issue,

which was not considered in our study, is the absence of blood in the aneurysms while probing. The flushing of the aneurysm might be more complex and dangerous than flushing a vessel segment for the probing of plaques. In contrast to a selected vessel segment with one major direction of blood flow, an aneurysm has a pathologic topology with irregular and complex blood flow conditions. Furthermore, aneurysms can be localized at a side wall or at a bifurcation. This fact influences the contrast flush with respect to volume and duration. Those aspects have to be further investigated.

### Imaging of geometry and structure

The aim of our study was to prove the ability of probing IAs with current OCT systems, primarily used in cardiology. Therefore, the results of this study must be understood within this context.

We were able to completely image the geometry of two IAs with different shapes and sizes in a silicone phantom. The ability to capture the whole aneurysm geometry depends mainly on the catheter position in the parent vessel, the aneurysm diameter and the diameter of the ostium. The investigated silicone IAs with a maximum height of less than 4 mm showed a bottleneck ratio of maximum 1.20. Hence, it was possible to image aneurysm geometry with small undercuts from the parent vessel. Aneurysms with larger undercuts will suffer from a signal loss at the aneurysm wall caused by the absorption and scattering of the parent vessel wall. Moreover, a steep rise of the aneurysm wall (large edge angle) leads to a thicker tissue. This means that the absorption of the tissue raises and that a signal loss occurs. Thus, a correct imaging of the aneurysm geometry is impossible.

Our investigations of the ability of OCT to image arterial wall structures can be applied to IAs. We were able to image and distinguish the vessel wall layers tunica intima, tunica media, and tunica adventitia. In those layers occur the pathological changes, which lead to the formation of IAs. Thus, it is essential to assess the changes of the aneurysm wall layers to predict the rupture status of an IA. We could show that OCT enables a depiction of wall changes, i.e., an intimal thickening, an apposition of collagen and intimal flaps.

Furthermore, it is possible to visualize thin wall structures with OCT. We were able to image an intimal detachment of  $67\ \mu\text{m}$ . The extraordinary high spatial resolution of an OCT system enables even an imaging of thinner structures.

The imaging of vessel branches provides some indication of the ability to probe larger aneurysms with undercuts. It was shown that in areas of undercuts a signal absorption of the parent vessel strongly attenuates a signal from the adjacent vessel. Thus, information of the aneurysm vessel wall will not be visible in such cases.

### Comparison with conventional imaging techniques

None of the currently established imaging modalities (e.g., CT, MRI) provide sufficient detail of aneurysm walls because of their low spatial resolution or soft tissue contrast.

Three-dimensional angiography of intracranial vessels shows only the blood flow and the inner contour of the aneurysm without information about wall thickness and structure.

MRI has the ability to show good soft tissue contrasts. Indeed, the imaging process is slower than CT and OCT depending on spatial resolution, sequence and more parameters. Current approaches with ultrahigh field MRI systems increase spatial resolution, but are not widely used in clinical routine [23].

As a result of the limited spatial resolution of current CT and MRI systems, it is not possible to generate detailed images of IAs. Signal information blur in partial volume effect with structures directly beside the aneurysm.

OCT generates more detailed images than CT and MRI but is limited in penetration depth. OCT and MRI are using non-ionizing radiation compared with CT. However, OCT catheterization is an invasive procedure which can harm the patient. Therefore, its diagnostic benefit has to be proven.

### Clinical scope

The depiction of the cerebral vessel wall and its different layers offers new horizons in diagnosis and therapy of IAs. For the first time, structural information of the pathologic vessel and aneurysm wall could be potentially used for an objective diagnosis of the patient. OCT contains the possibility for a better understanding of the formation and growth of IAs. There might be new information for the decision of therapy or decision against endovascular therapy. Prior to a patient study, safety aspects of catheterization of neurovascular structures have to be examined.

### Technical scope

The use of OCT as a modality for imaging aneurysms contains new focus areas in data processing, visualization and simulation. Combining angiographic data and OCT data will improve the correct imaging of the vessel morphology. This might be a basis for the extension of computational fluid dynamics (CFD) with methods of structure mechanics. A more realistic simulation of individual flow conditions and mechanical load of the aneurysm wall can help to find an objective computer-based rupture criteria.

### Technical adjustments

For the implementation of those new opportunities in computer-assisted radiology and intervention, first the existing OCT systems have to be adapted to the new requirements of those pathologies. This comprises the technical revisions of the OCT catheters. Current systems are only suitable for side wall aneurysms. This is due to the fact that the laser perpendicularly probes to the catheter axis during pullback. In most cases, an IA is located at a bifurcation of a vessel. The successful application of an OCT catheter would require a pullback through the adjacent distal and the proximal parent vessel. There might be a strong signal loss while passing the wall of the parent vessel and tissue structures which are located between the parent vessel and the outer aneurysm wall. Thus, it is necessary to adapt and optimize OCT catheters for aneurysm imaging. Main focus is the design of the catheter probe; for example, for bifurcation aneurysms a forward looking OCT probe would be beneficial for imaging the ostium.

System parameters such as pullback speed and pullback length have to be adjusted to create a detailed image of the aneurysm wall.

Another important fact is the amount and volume flow of contrast agent to flush an aneurysm. Today's systems work with non-occlusive techniques. The blood flow is suppressed by the contrast agent flow. For intracranial vessels, those parameters have to be carefully examined, because changes in pressure might induce stress to the aneurysm wall and cause a rupture. In the beginnings of intravascular OCT imaging, occlusive techniques were used to suppress the blood from the region of interest. This could be an opportunity to carefully suppress blood inside the aneurysm with contrast agent. To avoid reflow from connecting vessels in the area of the circle of Willis, a balloon occlusion proximal and distal to the aneurysm could be done. Indeed, high stresses can be generated in the vessel wall which may lead to a rupture. Further investigations have to be carried out.

### Conclusion

We examined the suitability of OCT to image IAs from phantom and specimen data and successfully extracted geometrical and structural properties.

Current OCT systems are able to visualize the morphology of IAs. The size and shape of the aneurysms influenced the imaging process. For side wall aneurysms, whose maximum height is less than the maximum imaging diameter of the OCT system with respect to catheter diameter, current OCT systems provide additional information of the aneurysm wall. Hence, the clinician can integrate the vessel wall thickness

and morphology in the approximation of the rupture risk and future therapy decision.

For bifurcation and larger aneurysms with a high bottleneck ratio, current OCT systems have to be technically adapted. As presented in our study, intravascular OCT shows great potential for assessing the patient-specific risk of IA rupture.

**Acknowledgments** This work was partly funded by the Federal Ministry of Education and Research (BMBF) and Saxony-Anhalt within the Forschungscampus STIMULATE (13GW0095A; I60).

**Compliance with ethical standards**

**Conflict of interest** There is no conflict of interest in this study.

## References

- Forsting M, Wanke I (2008) Intracranial vascular malformations and aneurysms. Springer, Berlin
- Keedy A (2006) An overview of intracranial aneurysms. *McGill J Med* 9(2):141
- Mueller OM, Schlamann M, Mueller D, Sandalcioglu IE, Forsting M, Sure U (2011) Intracranial aneurysms: optimized diagnostic tools call for thorough interdisciplinary treatment strategies. Therapeutic advances in neurological disorders, pp. 1756285611415309
- Vernooij MW, Ikram MA, Tanghe HL, Vincent Arnaud JPE, Hofman A, Krestin GP, Niessen WJ, Breteler Monique MB, van der Lugt A (2007) Incidental findings on brain MRI in the general population. *N Engl J Med* 357(18):1821–1828
- Wiebers DO (2003) Unruptured intracranial aneurysms: natural history, clinical outcome, and risks of surgical and endovascular treatment. *Lancet* 362(9378):103–110
- Tearney GJ, Jang I-K, Bouma BE (2006) Optical coherence tomography for imaging the vulnerable plaque. *J Biomed Opt* 11(2):021002-021002-10
- Prati F, Regar E, Mintz GS, Arbustini E, Di Mario C, Jang I-K, Akasaka T, Costa M, Guagliumi G, Grube E (2010) Expert review document on methodology, terminology, and clinical applications of optical coherence tomography: physical principles, methodology of image acquisition, and clinical application for assessment of coronary arteries and atherosclerosis. *Eur Heart J* 31(4):401–415
- Murata A, Wallace-Bradley D, Tellez A, Alviar C, Aboodi M, Sheehy A, Coleman L, Perkins L, Nakazawa G, Mintz G (2010) Accuracy of optical coherence tomography in the evaluation of neointimal coverage after stent implantation. *JACC Cardiovasc Imaging* 3(1):76–84
- Kang S-J, Mintz GS, Akasaka T, Park D-W, Lee J-Y, Kim W-J, Lee S-W, Kim Y-H, Lee CW, Park S-W (2011) Optical coherence tomographic analysis of in-stent neointimal hyperplasia after drug-eluting stent implantation. *Circulation* 123(25):2954–2963
- Farooq MU, Khasnis A, Majid A, Kassab MY (2009) The role of optical coherence tomography in vascular medicine. *Vasc Med* 14(1):63–71
- Standish BA, Spears J, Marotta TR, Montanera W, Yang VX (2012) Vascular wall Imaging of vulnerable atherosclerotic carotid plaques: current state of the art and potential future of endovascular optical coherence tomography. *Am J Neuroradiol* 33(9):1642–1650
- Fujimoto JG, Pitris C, Boppart SA, Brezinski ME (2000) Optical coherence tomography: an emerging technology for biomedical imaging and optical biopsy. *Neoplasia* 2(1):9–25
- Smith AM, Mancini MC, Nie S (2009) Bioimaging: second window for in vivo imaging. *Nat Nanotechnol* 4(11):710–711
- Frösen J, Tulamo R, Paetau A, Laaksamo E, Korja M, Laakso A, Niemelä M, Hernesniemi J (2012) Sacular intracranial aneurysm: pathology and mechanisms, (eng). *Acta Neuropathol* 123(6):773–786
- Thorell WE, Chow MM, Prayson RA, Shure MA, Jeon SW, Huang D, Zeynalov E, Woo HH, Rasmussen PA, Rollins AM (2005) Optical coherence tomography: a new method to assess aneurysm healing. *J Neurosurg* 102(2):348
- Mathews MS, Su J, Heidari E, Levy EI, Linskey ME, Chen Z (2011) Neuroendovascular optical coherence tomography imaging and histological analysis. *Neurosurgery* 69(2):430
- Mathews MS, Su J, Heidari E, Linskey ME, Chen Z (eds) (2011) Neuro-endovascular optical coherence tomography imaging: clinical feasibility and applications. SPIE BiOS. International Society for Optics and Photonics, pp 788341-1–788341-7
- Lopes DK, Johnson AK (2011) Evaluation of cerebral artery perforators and the pipeline embolization device using optical coherence tomography. *J Neurointerv Surg* neurintsurg-2011-010102
- van der Marel K, Gounis M, King R, Wakhloo A, Puri A (2014) P-001 high-resolution optical and angiographic CT imaging of flow-diverter stents for assessment of vessel wall apposition, (eng). *J Neurointerv Surg* 6(Suppl 1):A21
- Costalat V, Sanchez M, Ambard D, Thines L, Lonjon N, Nicoud F, Brunel H, Lejeune JP, Dufour H, Bouillot P (2011) Biomechanical wall properties of human intracranial aneurysms resected following surgical clipping (IRRAs Project). *J Biomech* 44(15):2685–2691
- Sun C, Standish B, Yang VXD (2011) Optical coherence elastography: current status and future applications. *J Biomed Opt* 16(4):043001-043001-12
- Lall RR, Eddleman CS, Bendok BR, Batjer HH (2009) Unruptured intracranial aneurysms and the assessment of rupture risk based on anatomical and morphological factors: sifting through the sands of data. *Neurosurg Focus* 26(5):E2
- Kleinloog R, Korkmaz E, Zwanenburg JJ, Kuijff HJ, Visser F, Blankena R, Post JA, Ruigrok YM, Luijten PR, Regli L, Rinkel GJ, Verweij BH (2014) Visualization of the aneurysm wall: a 7.0-tesla magnetic resonance imaging study. *Neurosurgery* 75(6):614–622



# Virtual Inflation of the Cerebral Artery Wall for the Integrated Exploration of OCT and Histology Data

S. Glaßer<sup>1</sup>, T. Hoffmann<sup>2</sup>, A. Boese<sup>3</sup>, S. Voß<sup>4</sup>, T. Kalinski<sup>5</sup>, M. Skalej<sup>2</sup> and B. Preim<sup>1</sup>

<sup>1</sup> Department of Simulation and Graphics, Otto-von-Guericke University, Magdeburg, Germany

<sup>2</sup> Institute of Neuroradiology, Otto-von-Guericke University, Magdeburg, Germany

<sup>3</sup> Department of Medical Engineering, Otto-von-Guericke University, Magdeburg, Germany

<sup>4</sup> Department of Fluid Dynamics and Technical Flows, Otto-von-Guericke University Magdeburg, Germany

<sup>5</sup> Joint Practice for Pathology, Hamburg, Germany

---

## Abstract

*Intravascular imaging provides new insights into the condition of vessel walls. This is crucial for cerebrovascular diseases including stroke and cerebral aneurysms, where it may present an important factor for indication of therapy. In this work, we provide new information of cerebral artery walls by combining ex vivo optical coherence tomography (OCT) imaging with histology data sets. To overcome the obstacles of deflated and collapsed vessels due to the missing blood pressure, the lack of co-alignment as well as the geometrical shape deformations due to catheter probing, we developed the new image processing method virtual inflation. We locally sample the vessel wall thickness values based on the (deflated) vessel lumen border instead of the vessel's centerline. Our method is embedded in a multi-view framework where correspondences between OCT and histology can be highlighted via brushing and linking yielding OCT signal characteristics of the cerebral artery wall and its pathologies. Finally, we enrich the data views with a hierarchical clustering representation which is linked via virtual inflation and further supports the deduction of vessel wall pathologies.*

Categories and Subject Descriptors (according to ACM CCS): Computer Graphics [I.3.3]: Picture/Image Generation—Image Processing and Computer Vision [I.4]: Applications—Computer Applications [J.3]: Life and Medical Sciences—

---

## 1. Introduction

With an increased rate of cerebrovascular diseases in the Western civilized countries, the need for an advanced vessel wall analysis increases as well. Usually, the contrast-enhanced vessel lumen data is acquired to provide information about possible vessel stenoses or pathologies such as cerebral aneurysms. However, the disease is often manifested in the vessel wall causing a pathologic weakening or thickening including arteriosclerotic plaque deposits. For clinical research, intravascular imaging, e.g., intravascular ultrasound (IVUS) and recently optical coherence tomography (OCT), provides new insights into the morphology of the wall and possible pathologic changes. IVUS and OCT are employed in clinical routine for cardiology to assess stenoses and plaques with superior image resolution compared to tomographic imaging. OCT data exhibits a spatial

resolution of less than 15  $\mu\text{m}$  with a limited penetration depth of 3 - 4 mm, whereas tomographic images are limited to 0.2 mm spatial resolution. Due to restrictions of the medical board, i.e., the catheters might not be small and flexible enough to guarantee a safe use in cerebral vessels in vivo, an adequate imaging modality for cerebral pathologic vessel wall changes is still missing.

To assess the potential of characterizing cerebral arteriosclerotic plaque, OCT studies have been successfully carried out for the larger carotid arteries [YKYea12] as well as for animal studies or ex vivo studies [MSH\*11]. Due to its ability to characterize pathological vessel wall changes and its spatial resolution superior to other intravascular imaging methods [TMF\*12], it is expected that OCT imaging of the cerebral vessels will be employed and allowed for interventional use in the near future.

Our work focuses on the *ex vivo* evaluation of the Circle of Willis (CoW), the cerebral arterial circle that supplies the brain with blood. We correlate OCT imaging of the CoW containing plaque with histologic imaging. The combination is hampered by a deflation or collapse of the vessels due to the lack of an intact blood cycle (see Fig. 1). Due to the CoW's numerous and particularly small branchings, a sufficient flushing is not applicable. Further changes of the vessel shape are caused by the *ex vivo* OCT catheter probing (small vessels are reshaped due to the catheter's size and stiffness) and by the sectioning of the preparations for histologic imaging. To overcome these limitations, we combine both image data modalities via virtual inflation.

The virtual inflation method is embedded in a multi-view framework for the interactive and simultaneous exploration of OCT and histology data. To assess the accuracy of the combination, we provide a quantitative evaluation based on a finite-element simulation creating a deformed virtual vessel wall model. Furthermore, we provide a clustering of the cell nuclei in the histological image data set for an adapted cluster visualization. We then combine the OCT characteristics via brushing and linking with the features extracted from histology. Finally, we transfer the cluster visualization to the OCT data and provide novel information about the vessel wall composition. This work is an extension of our previous work [GHB\*15]. The additional contributions of this paper are:

- We extend the virtual inflation framework by combining it with a visual representation of clustered cell nuclei to allow for an improved evaluation of OCT image data. We are able to define and extract the spatial connectivity of the nuclei and identify and automatically derive important attributes for a dedicated visual representation. Thus, we can even transfer more information from the histologic data to the OCT image.
- Based on the newly available information, we provide medical findings which were extracted via combining OCT and histology.
- For an improved evaluation of our method, we refine previously developed virtual vessel phantoms and include a Poisson-disk sampling for a quantitative evaluation.

## 2. Related Work

A lot of effort was spent in recent years on the visualization of vascular structures [OP05, AMB\*13, KGPS13]. These methods focused on the visualization of vessel walls by means of polygonal meshes aiming at watertight surfaces, continuity and accuracy. For the visualization of vascular pathologies manifested in the vessel wall, these methods are not applicable. Direct volume rendering with appropriate transfer functions [GOH\*10] enabled the simultaneous visualization of plaques, stents and vessel walls and thus, better serves diagnostic purposes. In contrast to the methods

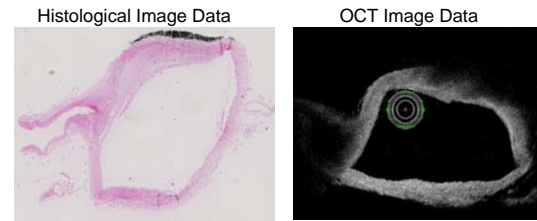


**Figure 1:** *Ex vivo* histology and OCT slice depicting the same vessel part with varying shapes due to deflation.

directly operating on tomographic radiological image data, we consider intravascular imaging.

An intravascular imaging-based evaluation of the arterial wall is mainly carried out in cardiology. Katouzian et al. [KKSea12] correlated IVUS with histological imaging. They created a cage fixture setup for an *in vitro* experiment. Also intended for the cardiological use, Balzani et al. [BBBea12] introduced a 3D reconstruction of geometrical models of arteriosclerotic arteries based on multimodal imaging including IVUS, virtual histology data and angiographic X-ray images. The reconstructed 3D model comprises the inner wall with color-coded parameters describing stress distributions, and a transparently rendered outer wall. In contrast, we are focusing on cerebral arteries. Thus, we deal with many particularly small vessel bifurcations yielding deflated vessels in the *ex vivo* imaging.

The analysis and the visualization of the vessel wall for cerebrovascular diseases, including aneurysms, is a novel research area, mainly motivated by intravascular imaging. Glaßer et al. [GLH\*14] prepared an artificial porcine aneurysm, probed it with IVUS and provided a visual representation of hemodynamic information as well as the wall thickness. The flat map [NGB\*09] visualized near wall flow data which is mapped onto the cerebral aneurysm surface. Instead of hemodynamic information, our virtual inflation method allows for the mapping of histological information onto the vessel wall.

Related to our analysis of the cerebral vessel wall, the curvicircular feature aggregation [MMVe13] samples information around the vessel's centerline to provide pathologic changes of blood vessels as an alternative to the curved planar reformation technique [KFW\*02]. The curvicircular features allow for an expressive visualization of vessels and highlight stenoses. Born et al. [BSRea14] present the 2D stent map for aortic valve stenosis analysis, where generalized cylindrical coordinates are extracted from the vessel centerline to create a mapping of different stent parameters, e.g., radial force or compression level. In contrast to these approaches, we do not sample around the vessel's centerline but rather along the inner vessel wall. Their work is also based on *in vivo* CT (angiography) imaging without

S. Glaßer et al. / Virtual Inflation of the Cerebral Artery Wall

deflated vessels. We developed the virtual inflation method to overcome the limitation of collapsing vessels, which is distantly related to the active contour and the balloon force concept [Coh91]. However, the active contour is allowed to move, i.e., it is attracted towards features such as edges. Our approach assumes a fixed length of the contour.

Similar to our work, virtual inflation can be applied to organic tissue instead of blood vessels. Such approaches were developed for endoscopic views, where a virtual view is generated from a tomographic image dataset. Bartroli et al. [BWK01] introduced a virtual colon unfolding based on nonlinear ray casting and a nonlinear 2D scaling algorithm. The latter compensates distortions due to the unfolding of the colon similar to the nonlinear magnification fields used in information visualization. Hong et al. [HGQ\*06] presented the conformal virtual colon flattening including a topological denoising to cope with high genus surface meshes. Zeng et al. [ZMG\*10] applied a harmonic map registration to the conformal virtual colon flattened images to co-register supine and prone colon. Furthermore, the landmark-driven optimal quasiconformal mapping presented in [ZY14] straightens the main anatomical landmark curves of the colon. For future work, an adaption for the whole vessel, i.e., a virtual vessel flattening would be interesting.

Also related to our method is the medial axes approach, which can be applied to measure the thickness of medical structures, e.g., the corpus callosum [HKW12]. In contrast, we focus on a thickness measurement originating at the inner vessel wall and directed to the outer vessel wall.

The evaluation of hematoxylin and eosin (H&E) stained data is the standard method in histopathology and enables the pathologist to recognize tissue alterations, e.g., diagnosis and grading of cancer. Major trends for nuclei detection, segmentation, feature computation and classification techniques in digital histology data were presented in the exhaustive overview by Irshad et al. [IVRR14]. For the delineation of touching nuclei, the watershed approach has been successfully adapted for H&E data [LSP03, AM12]. Sertel et al. [SCSG09] also applied the watershed algorithm and reduced staining variations with anisotropic diffusion. Naik et al. [NDA\*08] automatically segmented nuclear and glandular structures in H&E data based on three information levels: low-level information based on pixels, high-level information based on relationships between pixels for object detection and domain-specific information based on relationships between histological structures. Our approach includes pixel information as well as high-level information such that a neighborhood for each nucleus is determined and integrated in the clustering. For a more general system dealing with various histologically stained image data, Kårsnäs et al. [KSD\*15] provided a comprehensive software tool for extracting and quantifying sub-cellular data. They especially account for biological and staining-induced variations.

Multi-view frameworks are often employed in medical vi-

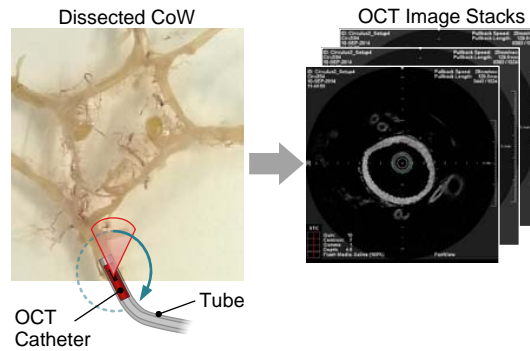


**Figure 2:** Illustration of the intravascular OCT image acquisition based on the post-mortem dissected CoWs preparation yielding the 2D OCT image stacks.

ualization and analysis for data exploration [GRW\*00]. Our prototype comprises two synchronized views of the cerebral vessels in a multi-view framework. Our work includes brushing and linking, a concept that was initially developed for highlighting data in scatterplots [BC87], to combine both views.

### 3. Image Data Acquisition

This section explains the image acquisition of the OCT data sets. Afterwards, the histology-based data sets are described.

#### 3.1. OCT Image Acquisition

Three human CoWs were explanted post-mortem, fixated with formalin and probed with OCT aiming at the characterization of vascular wall structures (see Fig. 2). All investigations were performed in accordance with the local ethics committee. The specimens were examined for pathological changes of the vessel wall, e.g., plaque and aneurysms. The CoW preparations were flushed with isotonic saline solution. They were fixated with needles on a silicon pad in a container filled with saline solution for OCT image acquisition with a TERUMO LUNAWAVE<sup>TM</sup> console (Terumo Corporation, Shibuya, Japan). The system is equipped with a near infrared laser light source in the spectral domain. The OCT system's pullback speed was 20 mm/s over an average distance of 130 mm yielding 1024 slices with a pixel size of  $15 \mu\text{m} \times 15 \mu\text{m}$ .

During image acquisition, a constant saline flush of the CoW was started with an injector system. It reduced the deflation of the vessels, but it could not be prevented completely due to small outlets of the circle. Since only parts of the CoW could be acquired with one setup, i.e., with one placement of the OCT catheter, different OCT imaging setups were carried out for each preparation. As a result, we obtain a set of OCT image series for each vessel part of the

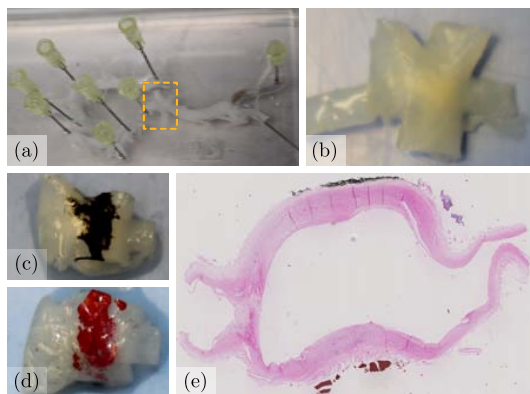


**Figure 3:** From a dissected CoW (a), a specimen was taken, see inlet (b). Black and red ink is employed for later co-registration with OCT data (c-d). In the digitized H&E stained slice the red and black ink is still visible (e).

CoW that exhibits vessel diameters large enough for catheter probing. Further information of the OCT imaging setup can be found in [GHB\*15, HGBea16].

### 3.2. Histologic Image Acquisition

To assess vessel wall pathologies, we select certain vessel parts with arteriosclerotic plaque as well as prominent bifurcations for orientation purposes (see Fig. 3). Additionally, the specimen was marked lengthwise doublesided with black and red ink. After paraffin embedding, cross-sections of the specimen were cut using a microtome with a thickness of  $2\mu\text{m}$  and a slice gap of  $50\mu\text{m}$ . The sections were transferred to standard glass slides, H&E stained and coverslipped. The slides were digitized using a Hamamatsu Nanozoomer (Hamamatsu Photonics, Hamamatsu, Japan) with a resolution of  $.23\mu\text{m}$  per pixel. The original proprietary file was formatted to JPEG2000 [KZSea08] and stacked into a volume for the processing with our framework. The original data comprise approx.  $11,000 \times 8,000$  pixels per slice with a resolution of  $.92\mu\text{m}$  per pixel.

## 4. Virtual Inflation for the Combined Evaluation of OCT and Histology Data

In this section, we describe our workflow (see Fig. 4), starting with the virtual inflation method. Afterwards, the clustering of the nuclei and our framework are presented.

### 4.1. Virtual Inflation

The virtual inflation method allows for the inflation of deflated vessels. It can be applied to OCT and histology data

since only the contours of the vessel walls are required. The process is subdivided in three steps (see Fig. 4a).

#### Step 1: Extraction of equidistantly sampled contours.

First, the contours of the vessel lumen, i.e., the inner wall, and the vessel-surrounding border, i.e., the outer wall, are required. We use manually segmented binary masks and process each wall separately. From the binary mask, all foreground pixels are selected forming a point set. Then, an arbitrary starting point is chosen and its closest, yet not visited, point is iteratively added to obtain a sorted list of contour points. Next, the list is equidistantly resampled. The amount of sample points is a user-defined parameter. Empirically determined default values are 400 for an OCT slice with  $600 \times 600$  pixels and 1600 for a histology slice with approx.  $11,000 \times 8,000$  pixels. The overall length of the contour is divided by the number of sampling points yielding a contour segment length. Then, new sampling points are extracted as intersection points with the connected contour list such that the distance between two subsequent sample points equals the contour segment length.

**Step 2: Extraction of normals and wall thickness.** For each point  $p_i$  of the inner vessel wall, the normal vector  $\vec{n}_i$  perpendicular to the line spanned by  $p_{i-1}$  and  $p_{i+1}$  is extracted (see Fig. 4a). The normals are iteratively averaged as long as they intersect each other. We approximate the wall thickness  $t_i$  at  $p_i$  as distance to the outer wall by intersecting it with a ray originating at  $p_i$  in direction  $\vec{n}_i$ .

**Step 3: Transformation of vessel walls and sampling of intensities.** We virtually inflate the inner wall by projecting the  $n$  equidistantly sampled inner wall points  $p$  onto a circle with center  $m$  and radius  $r$ . Hence,  $m$  equals the mean of the points  $p$ . We extract  $r = c/(2\pi)$ , where  $c$  is the circumference of the inner wall. Approximating  $p'_i$  via:

$$p'_i = m + r \cdot \begin{pmatrix} \cos \alpha_i \\ \sin \alpha_i \end{pmatrix} \quad (1)$$

ensures equidistant points onto the circle, where  $\alpha_i = i * 2\pi/n$  and  $i = 1..n$ . We remodel the outer wall by adding the stored values for  $t_i$  to  $p'_i$  in the direction  $\vec{m}\vec{p}'_i$ . As a result, we obtain the virtually inflated vessel walls. With linear interpolation, we can create intermediate steps. For example, we translate the point  $p_i$  only half the distance between  $p_i$  and  $p'_i$  of the virtually inflated circular inner vessel wall (see the illustration for Step 3 in Fig. 4a). The interpolated virtual inflation is presented in Fig. 5. It allows the clinical expert an interactive inflation and exploration of the data. The transition from original data to virtually inflated data can be also visualized in an animated manner. The user defines how many intermediate stages should be created. For the translation of intensity values from the original image data to the virtually inflated image, the rays  $\vec{n}_i$  are sampled (see Fig. 6). We acquire a list of samples for each pixel of the virtual inflated images (if  $k$  rays cover the pixel, then  $k$  samples are obtained) and interpolate the pixel's intensity by averaging over the samples. If a pixel  $x$  with no samples exists, the

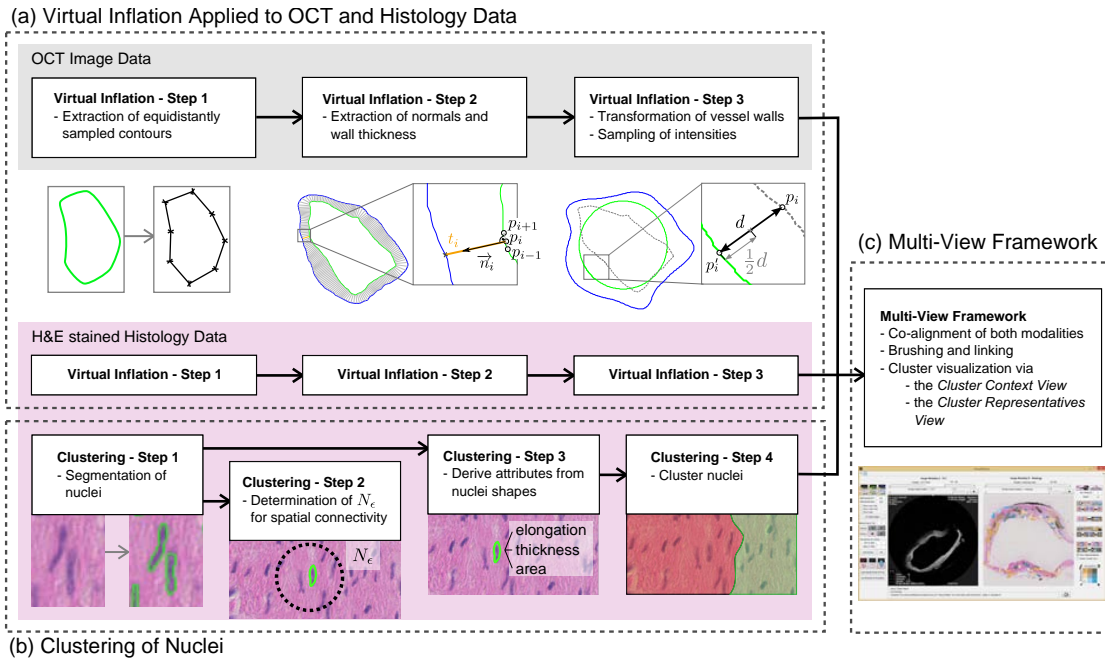


**Figure 4:** Illustration of the proposed framework for exploration of the cerebral vessel wall with virtual inflation. The virtual inflation of the OCT image data is depicted which comprises three steps (a). These steps are repeated for the histology data. The four steps for clustering the histology data are depicted at the bottom (b). The virtually inflated images of OCT and histology data as well as the clustering result serve as input for the interactive exploration within our multi-view framework (c). It allows for co-alignment of both modalities as well as brushing and linking, which can be further combined with the cluster context view or the cluster representatives view.

pixel's intensity value  $I(x)$  is interpolated from its neighborhood  $N$  (see Fig. 6c):

$$I(x) = \sum_{q \in N} \frac{1}{w_q} * I(q). \quad (2)$$

The sum of weights  $\sum w$  drops below 1 if more than one pixel is missing. In this case, we leave the missing pixels out and divide the sum of the remaining pixels by  $\sum w$ . To exploit as many samples as possible, we first create a ranking of the pixels, based on their number of missing neighbors. Then, we interpolate all pixels with one neighbor missing, followed by pixels with two neighbors missing and so on. The interpolation is restricted to vessel wall pixels with a point-in-polygon test based on the two walls. We empirically set the step size for the sampling to .2 of the pixel's width. Larger step size values would gather less samples with more missing pixels. Smaller values would result in more samples per pixel and slightly increased computation time.

The runtime of the virtual inflation step depends on the number of intermediate images. For the presented OCT data, the sampled intensities are extracted in 0.5 s. The creation of

the single virtually inflated circular cross-section from the sampled intensities costs 3.7 s whereas the creation of 10 intermediate images costs 35.4 s on a desktop PC with 8 GB RAM and an Intel(R) Core i5 CPU (3.20 GHz).

#### 4.2. Hierarchical Clustering of Nuclei

For the evaluation of vessel wall pathologies, the most important information extracted from the H&E stained histological image data is the presence, arrangement and shape of nuclei. The nuclei shape allows for a rough classification of cell types, e.g., elongated nuclei often correspond to mesenchymal cells. Inflammations are characterized by infiltrates of different types of cells, e.g., lymphocytes with small round nuclei. The clinical expert also takes additional information into account, e.g., composition of the walls by analyzing tissue types. Based on discussions with our pathological cooperation partners, we decided to focus on cell nuclei with round and elongated shapes. A further requirement was the clustering of similar, spatially connected nuclei and thus, to provide a quick overview representation. Therefore,

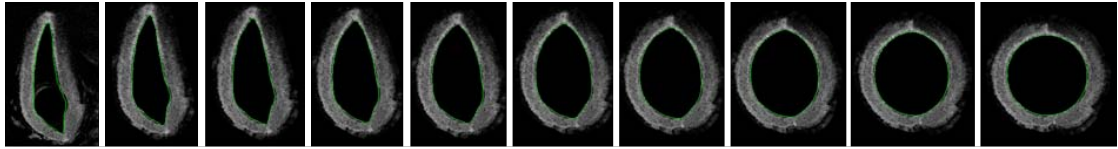


**Figure 5:** Result (right) of the virtual inflation and the sampling of intensity values applied to a deflated vessel OCT cross-section view (left). Intermediate steps are based on the linearly interpolated inner vessel wall points.

we developed an extraction of clusters (recall the clustering steps depicted in Fig. 4b).

**Step 1: Segmentation of nuclei.** For the nuclei segmentation, we convert the colored H&E stained histology image into a gray image and invert it subsequently. To account for variations of intensities and colors due to scanning, non-uniform illumination and staining, we apply a contrast-limited adaptive histogram equalization which works on small regions rather than on the entire image [Zui94]. Next, we automatically separate the nuclei from the background with Otsu’s method [Ots79] which calculates an optimal threshold by minimizing the intraclass variances of the foreground and background class. Foreground objects smaller than ten pixels are removed. As suggested in [SCSG09], we apply anisotropic diffusion filtering [PM90] to smooth the histologic image data while preserving the edge information. Finally, we apply the watershed transform for a delineation of nuclei. This approach defines a group of basins in the image domain such that ridges in between these basins can be employed as borders to isolate the nuclei from each other. Based on the borders, a binary mask is created which holds the estimated boundaries for the nuclei.

**Step 2: Determination of spatial connectivity.** We determine the position of each nucleus as mean of the associated pixels’ positions. Next, we approximate a neighborhood size  $N_\epsilon$  for the nuclei depending on a user-defined minimum number of neighbors *MinPoints*. Here, a default value of 5 yields suitable results for all tested histological data sets. We

build the  $k$ -distances graph (also called elbow function) for the given *MinPoints* value, as suggested in [EKSSX96]. The graph maps the distance of each nucleus to its  $k$  next neighbors (with  $k = \text{MinPoints}$ ). A well-suited  $N_\epsilon$  can be automatically detected at the elbow point. Nuclei with an Euclidean distance smaller than  $N_\epsilon$  are neighbored.

**Step 3: Extraction of attributes from nuclei shapes.** We want to differentiate between long, elongated nuclei and smaller, round nuclei, e.g., from inflammatory cells. Therefore, we derive the following attributes (see Fig. 7):

- the *elongation* is a customized parameter for characterization of the roundness of the nucleus,
- the *thickness* describes the nucleus’ thickness, i.e., the number of erosion steps (with a  $3 \times 3$  rectangular kernel element) necessary to completely remove the object, and
- the *area* describes the nucleus’ size, i.e., the number of pixels.

We extract the *elongation*  $e$  with a principal component analysis and subsequent evaluation of the eigenvalues  $\lambda_1$  and  $\lambda_2$  (see Fig. 7). We normalize  $\lambda_1$  and  $\lambda_2$  with  $l_1 = \lambda_1/(\lambda_1 + \lambda_2)$ ,  $l_2 = \lambda_2/(\lambda_1 + \lambda_2)$  and extract  $e$ :

$$e = \max(l_1, l_2) - \min(l_1, l_2) \quad (3)$$

The main advantage of this measure compared to more conventional parameters, such as compactness, is its direct extraction and robustness. Since nuclei pixel positions are stored as binary masks, we do not have round shapes or smooth boundaries. Hence, a time-consuming extraction of the required information, e.g., the perimeter, the minimum bounding box or the longest chord, would be necessary. Especially if the pixel masks are incomplete due to noise, our

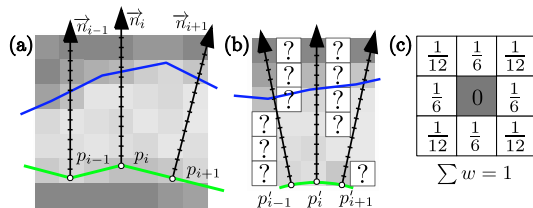


**Figure 6:** Illustration of intensity value sampling. Depiction of the original image with the inner (green) and outer (blue) vessel wall (a). The samples are accumulated along the rays to interpolate values (b). If no sample value was assigned, the intensity is interpolated with the depicted filter (c).

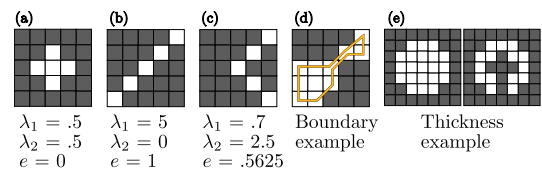


**Figure 7:** Examples of segmented nuclei pixels and their elongation  $e$  (a-c). Next, a pixel set with its boundary (orange) is presented (d). Two pixel sets are shown yielding similar values for  $e$  but with distinct thickness values (e).

S. Glaßer et al. / Virtual Inflation of the Cerebral Artery Wall

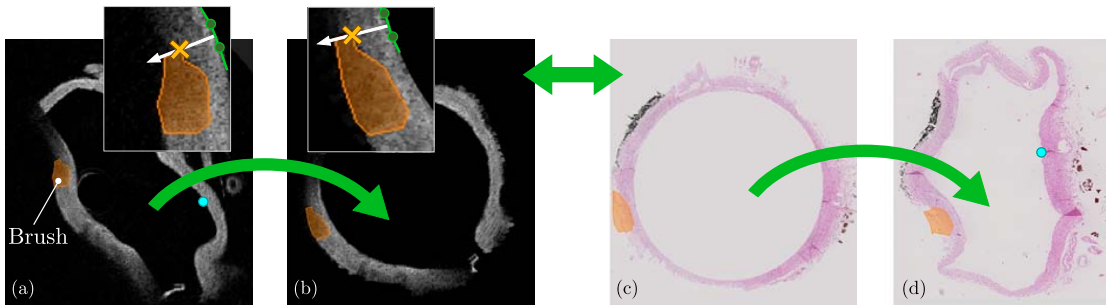


**Figure 8:** Illustration of brushing and linking. Corresponding OCT and histology slices and their virtually inflated images are depicted. When the user defines a brush (a), it is automatically converted to the inflated view (b), based on the distance of the vertices of the brush and their distance to the vessel-lumen border (see inlets). The virtually inflated images of OCT and histology can be correlated (b-c). Analogously, the brush can be translated from the inflated to the original image (d).

*elongation* measure yields satisfying results. In case of round nuclei, we can separate round shapes from curved objects with the thickness parameter (see Fig. 7e).

**Step 4: Clustering of nuclei.** We employ an agglomerative hierarchical clustering. Similar to region merging, each nucleus is forming its own cluster at the beginning. Each cluster is neighbored to clusters of corresponding nuclei within the distance  $N_\epsilon$ . Then, the most similar neighbored clusters are merged into a new cluster and the neighbor list is built up from the merged clusters. The similarity is defined as Euclidean distance between the feature vectors, where each cluster has a feature vector that contains the mean values of the cluster pixel's attributes. Prior to clustering, z-scoring is applied to each attribute. From the cluster hierarchy we obtain cluster results based on two parameters: the minimum cluster size and the  $\epsilon$ -value that defines the cluster division. We substitute the first one with the *MinPoints* parameter, since the spatial connectivity is already adapted to this value. The  $\epsilon$ -value is empirically set to 1.0, but can be adapted to obtain a coarser or finer cluster division.

### 4.3. Framework

First, we describe the multi-view framework and second, we explain the included cluster views.

**The multi-view framework.** The virtual inflation and the clustering are combined into a multi-view framework implemented in MATLAB (MathWorks, Natick, USA) for the interactive exploration of the OCT and histological data (recall Fig. 4c). The implementation is sped up by using vectorized data structures leveraging MATLAB's implicit multithreading capabilities as well as explicit parallel computing techniques and GPU computing. The *gpuArray* command transfers data to the GPU memory. Subsequent image processing methods are performed on the GPU and the results are transferred back using the *gather* command. Furthermore,

the *parfor* command distributes independent loop iterations across multiple MATLAB sessions using a multi-core CPU.

An initial correlation of the vessels is carried out with two landmarks, e.g., a vessel bifurcation, to determine a corresponding slice in both modalities. Next, the data sets are co-aligned based on the known slice distance of the OCT and histology data. If the user scrolls to a slice in one view, the other view is updated accordingly. For inspection of the data, virtual inflation is separately carried out for the OCT image data and the H&E stained histology data (recall Fig. 4a). The user can qualitatively explore the vessel wall and choose between different interpolation steps (see Fig. 5). Thus, the clinician can work with an intermediate image instead of the completely virtually inflated one.

Based on the virtual inflation results, our framework allows for brushing and linking for an interactive exploration (see Fig. 8). The user selects a set of points forming a polygonal region of interest (ROI) – the brush. This brush is translated for each interpolation step of the virtual inflation. Finally, a correlation between a brush from the virtually inflated OCT image to the virtually inflated histology image (or vice versa) is carried out. As a prerequisite, the user selects two corresponding landmarks on the inner vessel wall of the virtually inflated images, e.g., the small vessels (see cyan circles) in Fig. 8. The brush from the virtually inflated histology image is translated to the original histology image. Thus, a ROI defined in the original OCT image will be linked to its corresponding ROI in the original histology image (or vice versa). The clinician can correlate the image characteristics of a specific vessel wall part. Our collaboration partners preferred the evaluation in the original images by restricting the histology information to the brush.

**The cluster views.** We included two cluster views in our framework: a color coding of the clusters for context information – the *cluster context view* – and the adapted visual-

ization of the cluster representatives – the *cluster representatives view*.

The cluster context view maps the cluster average attributes (i.e., the average attributes of all cluster elements) to color with a bivariate color map (see Fig. 9a-c). We employ orange and blue to achieve a visual separation from the H&E stained image data. The complementary colors work with red-green color blindness and allow for an intuitive highlighting of the different shaped nuclei. For all segmented nuclei positions, we carry out a Delaunay triangulation. Next, we identify inner triangles, i.e., triangles connecting only nuclei included in the cluster. In addition, edges of the Delaunay triangulation which do not belong to inner triangles but are spanned between two cluster elements, are selected. Inner triangles and the selected edges are color-coded (see Fig. 9c). To avoid visual clutter, the cluster context visualization can be switched off and replaced by the cluster representatives view (see Fig. 9d).

The cluster representatives view shows color-coded glyphs representing the cluster attributes inspired by choropleth maps. For the initial positioning, we employ the position of the most likely cluster element compared to the cluster's attributes. For the extraction of the glyph's shape, we transfer the assigned pixel map of the most likely cluster element into a polygon and slightly smooth the polygon's outline. We employ the bivariate color map and add a silhouette with a slightly darkened color for an improved visual separation from the remaining image. These glyphs are enlarged and mapped at the cluster representatives' positions.

Cluster representatives may overlap which hampers the visualization result (see Fig. 9d). Since the overlap-free positioning problem of these cluster representatives is not deterministically solvable in polynomial time (NP-hard) [MS93], we developed a fast approximation consuming only a few seconds. We use an image buffer with reduced size for the adaption of cluster representatives' positions. For the employed histological data, we achieved satisfying results with a reduction factor of 1/30 yielding an image buffer of  $370 \times 300$  pixels. Then, we mask the corresponding pixels of the downscaled cluster representatives at its initial position in the image buffer. If no overlap occurs, we store this position and proceed with the next cluster. Otherwise, we move the pixel mask in the image buffer one pixel to the left, right, top, and bottom yielding four altered image buffers. Then, we select the image buffer where the Hausdorff distance to the original position increased and the smallest amount of overlapping pixels occurs. This prevents cyclic translations. We repeat this procedure until no pixels overlap and store the translation. In peripheral areas, no valid position may be found due to limited space. Hence, we stop the rearrangement of the current cluster representative, if we reach the image buffer's boundaries or if the current translation exceeds a previously defined threshold (e.g., a Hausdorff distance of 100 pixels in the image buffer). In this case,

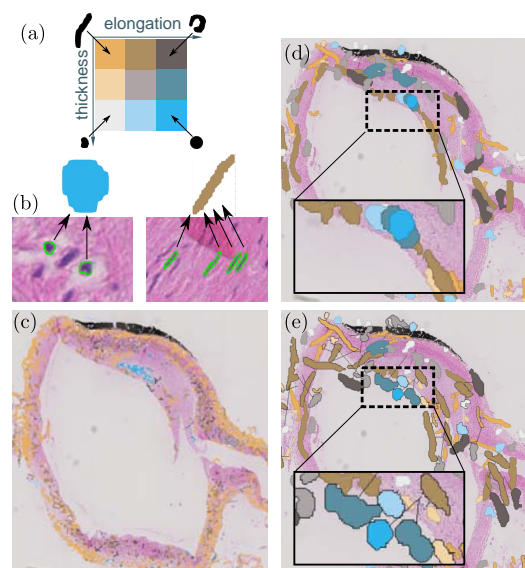


**Figure 9:** The bivariate colormap is used for the color-coding of clusters (a). Examples of two clusters and their cluster representatives (b). The cluster context view provides context information but visual clutter as well (c). The cluster representatives view yields a sparse visualization (d), which will be further improved with the adjusted positions (e).

we place the cluster representative at its original position, accepting an overlap. In Fig. 9e, the adapted cluster representatives' positions are presented. Lines connect adjusted cluster representatives to their initial position in the original image (see inlets of Fig. 9d-e).

When employing the cluster result as brush, the clusters can be linked to the OCT view. Therefore, the set of nuclei and their positions are interpreted as points of the polygonal brush and transferred to the OCT data. Furthermore, the cluster view can be restricted to clusters covered by the polygonal brush.

## 5. Evaluation

Our method is tailored to deflated vessels in OCT and histology data. Due to the novelty of the medical application, a ground truth is not available. To overcome this limitation, we designed a software phantom (see Fig. 10a), and applied two deformation configurations via finite-element simulations yielding detailed positions and displacements of the discrete elements. The finite-element method is widely used to numerically simulate the relation of deformation, mechanical strain and stress, based on the conservation of the momentum, which is solved locally for each finite element. Based on this, we can conduct an evaluation taking into

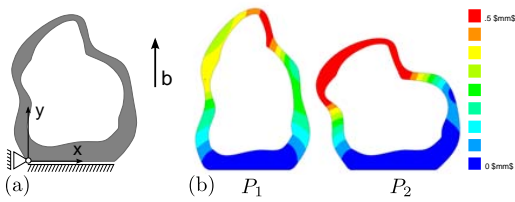


**Figure 10:** Depiction of the software phantom in the initial, stress-free state (a). The local coordinate system is shown at the bottom. The application of the load  $b$  yields  $P_1$  and  $P_2$ , while the bottom is fixated to prevent rigid body motion. Contour plots of the vector displacement magnitudes for software phantoms  $P_1$  and  $P_2$  (b).

account the material behavior in combination with known locations of each discrete element. The static simulations considering large deflections and small strains were carried out with ANSYS Mechanical (ANSYS, Inc., Canonsburg, USA).

The initial 2D model with a circular cross-section [GHB\*15] was extended to a more realistic one. The dimensions are carefully matched to the properties of cerebral vessels, with an inner radius of 2.2 mm and a heterogeneous vessel wall of 0.3 mm. The wall thickness variations serve as anatomical landmarks for the virtual inflation step. The numerical model consists of 96,000 tetrahedral elements with quadratic basis functions to obtain high accuracy. To induce deformation, a load  $b$  is applied as body force in positive and negative  $y$ -coordinate direction, yielding the software phantoms  $P_1$  and  $P_2$ , see Fig. 10b). Fixating the displacement in  $y$ -direction at the bottom edge and in  $x$ -direction at the bottom left vertex prevents rigid body motion. The load causes mechanical stress in the model's inside and results in deformation depending on the specified linear elastic material model. For investigation of the movement of the cerebral vessel walls, the Young's modulus is 1 MPa, the Poisson's ratio is 0.45 and the density is  $1,000 \text{ kg/m}^3$  [BHZea10].

The displacement of  $P_1$  and  $P_2$  ranges up to 0.5 mm.  $P_1$  and  $P_2$  consist of 195,000 indexed vertices, where the world coordinates and displacements for each vertex are stored and employed as ground truth. We build two DICOM files based on  $P_1$  and  $P_2$ . We employ an image size of  $500 \times 500$  pixels, where 1 pixel covers  $0.01 \text{ mm} \times 0.01 \text{ mm}$ . The  $x$ -coordinates of  $P_1$  range from  $-0.26 \text{ mm}$  to  $3.00 \text{ mm}$  and the  $y$ -coordinates from  $0 \text{ mm}$  to  $4.62 \text{ mm}$ . For  $P_2$ ,  $x$ -coordinates range from  $-0.96 \text{ mm}$  to  $3.15 \text{ mm}$  and  $y$ -coordinates from  $-0.01 \text{ mm}$  to  $3.76 \text{ mm}$ . We extract for each vertex of  $P_1$  and  $P_2$  its pixel position by translating the origin in the bottom left of the bounding box yielding the images  $I_1$  and  $I_2$ .

We load  $I_1$  and  $I_2$  into our framework and carry out brushing and linking. Originally, we brushed 3 polygons as well as

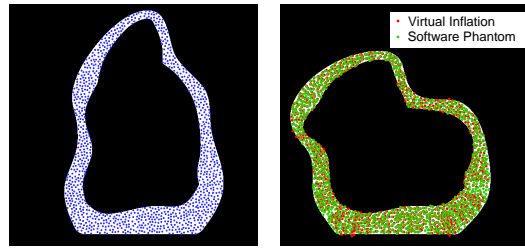


**Figure 11:** Depiction of the binarized images  $I_1$  and  $I_2$  and the Poisson disk sample set. Via virtual inflation followed by brushing and linking, the corresponding positions (red) were extracted and compared with the ground truth (green).

a random point set comprising 100 points to compare the virtual inflation results with the ground truth [GHB\*15]. However, some of the randomly placed points were too tightly packed together or too sparsely distributed. We improved this quantitative evaluation by scattering 1,000 points which are Poisson disk sampled on the foreground object of  $I_1$  forming our sample set, see Fig. 11. Therefore, we adapted the approach in [Tul08], which is based on [Bri07]. With the Poisson disk sampling, a more homogeneously scanning of the vessel wall is ensured.

For the quantification of displacement errors induced by the virtual inflation, we compare the pixel coordinates of the corresponding brushes obtained via brushing and linking with the coordinates directly extracted from  $P_1$  and  $P_2$ . Therefore, we carry out the following steps:

1. Extract the pixel coordinates for each sample point in  $I_1$ .
2. Select the corresponding world coordinates of  $P_1$ , i.e., transpose the pixel coordinates into world coordinates.
3. Derive the corresponding world coordinates of these vertices in  $P_2$  (known from the finite-element simulation).
4. Convert the vertices from  $P_2$  into pixel coordinates of  $I_2$ .
5. Compare these pixel coordinates with the pixel coordinates from  $I_2$  extracted via brushing and linking.

The resulting average displacement of the sample set compared to the ground truth is  $61.94 \mu\text{m}$ . This error is slightly larger than for the initial, more circle-like software phantom [GHB\*15]. Reasons might be the more complex phantom as well as Poisson disk sampling that yields many points close to the border of the outer vessel wall. However, the result is satisfying. In relation to the image size of  $500 \times 500$  pixels, the displacement of 6.19 pixels equals 1.24%. Although the small displacement rate depends on the perfectly matched software phantom and may differ for real preparations, the virtual inflation allows for linking of a defined brush in one image to the other image.

## 6. Medical Findings

We applied the virtual inflation to several OCT data sets of the CoW and their corresponding histological images, including the basilar artery with arteriosclerotic plaque. We discussed the results with a neuroradiologist and a pathologist and provide the most important findings in Fig. 12.

In Fig. 12a, the histologic evaluation revealed a fibrotic plaque deposit in the pathologically thickened intima, i.e., the inner vessel wall layer. When brushing the deposits, the linking to the OCT slice reveals an area with dense plaque accumulation, see the dense tissue parts with high attenuation (marked with \*) yielding the low attenuated areas behind. These findings are reflected by the clustering with blueish, circular shaped cluster representatives indicating inflammatory areas compared to orange-colored cluster representatives in healthy tissue.

In Fig. 12b, the brush covers an accumulation of mucoid plaque, which is typically loose. As it can be seen in the OCT image, the brushed region is part of the plaque area with low signal and low attenuation, but no specific differences can be extracted. The cluster view restricted to the brush in the histology image does not highlight any conspicuous nuclei shapes.

In Fig. 12c, a small area with inflammatory cells, characterized by sharp, round cell nuclei, was selected. Inflammations often vary and a precise prediction concerning their density values is not possible. This is reflected in the small brush in the OCT image (Fig. 12c, right), which reveals a small, heterogeneous area. Hence, the cluster view, restricted to the brush that was linked to the OCT image, comprises a sharp, round, blueish nucleus shape as well.

The brush in Fig. 12d covers a part of the vessel wall which was conspicuous during histology evaluation due to its increased thickness. However, the analysis of the histologic image does not confirm a plaque deposit. Probably, this area is caused by a cutting-artifact. In accordance, no change in the signal characteristics of the OCT data occurs. This is also reflected by the clustering view that is restricted to the brush. Hence, it does not contain any conspicuous nuclei shapes.

The virtual inflation correlates the fibrotic plaque deposit to a homogeneous signal-rich region in the OCT data which matches findings in literature [KBBa06]. In case the vessels exhibit ellipsoidal cross-sections as well as various elongated cross-sections due to pathologies, an evaluation of the slightly virtually inflated vessel was beneficial, recall Fig. 5.

## 7. Discussion

The proposed virtual inflation supports a combined analysis of OCT and histologic image data. The spatial differences between a brush and the corresponding brush in the second modality were evaluated based on finite-element simulations

yielding a sufficient precision. For the medical image data, the co-alignment could be further improved by implanting some markers, e.g., a small thread, in the preparations. Our data sets were probed ex vivo. Thus, a detachment of the intima emerged, which typically occurs during decomposition. Hence, a larger study could provide more information about artifacts such as conservation-based shrinking.

The pathologic expert rated the cluster primitives, especially their accordance with the underlying morphologic features, as very useful extension for a quick overview of nuclei shapes especially in the OCT slices. Once an interesting vessel part was detected, the original histologic data set was evaluated for an in-depth analysis. The combination of the ex vivo OCT and histologic properties provides new information about the cerebral vessel wall morphology and its corresponding OCT imaging. Such findings can form the basis for a solely radiology-based OCT image evaluation.

## 8. Summary and Future Work

In this paper, we presented a virtual inflation of ex vivo vessel parts probed with OCT and acquired with histology to analyze characteristics of the cerebral vessel wall. Our prototype requires manual segmentation of the vessel-lumen and the vessel-surrounding borders. It is adapted to intravascular imaging of the cerebral vasculature. Our framework comprises multiple coordinated views, which allows for brushing and linking between the OCT image and the histological image. Our work provides basic information for the radiologic evaluation of OCT signal characteristics which are almost unknown for cerebral artery walls.

Future work should include automatically segmented vessel walls of the OCT data [TSDS\*11]. We are also particularly interested in a setup similar to the cage fixture [KKSea12] for an in vitro setup. However, their work is based on IVUS, whereas OCT would require different adaptations. Also, an analytic representation of the inner vessel wall and the wall thickness values could be developed to avoid averaging steps and reduce the calculation time. Finally, our work has great importance for the fluid-structure interaction regarding vessel wall and blood flow. The new wall information based on virtually inflated images currently serves our cooperation partners to examine the effect of wall thickness on the hemodynamic simulation.

**Acknowledgements** This work was partly funded by the German Federal Ministry of Education and Research within the Forschungscampus *STIMULATE* (grant number: 13GW0095A).

## References

- [AM12] ALI S., MADABHUSHI A.: An Integrated Region-, Boundary-, Shape-Based Active Contour for Multiple Object Overlap Resolution in Histological Imagery. *IEEE Trans. Med. Imaging* 31, 7 (2012), 1448–1460. 3

S. Glaßer et al. / Virtual Inflation of the Cerebral Artery Wall

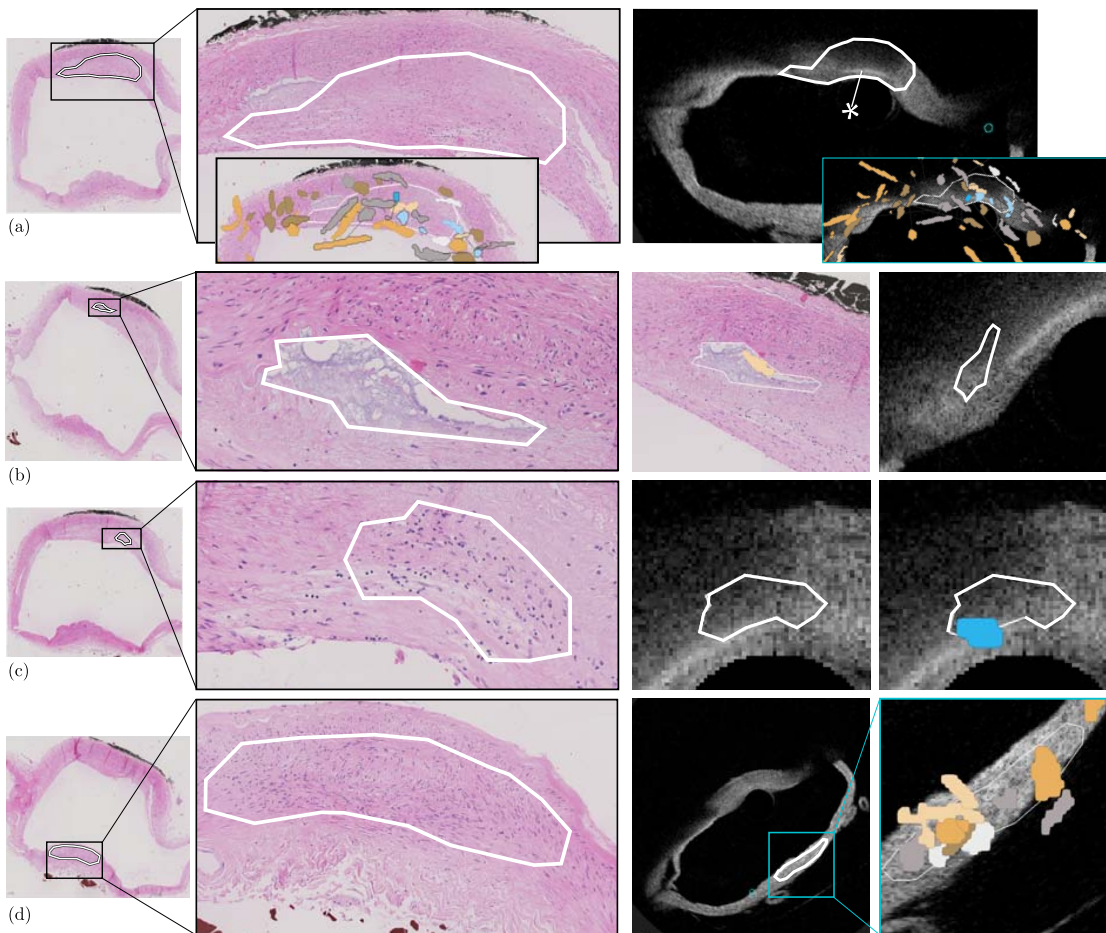


**Figure 12:** Examples for the correlation of histology and OCT images. For each example (a-d), the left and second from left columns represent the histologic image including an enlarged view of pathologies. Brushes were defined in the histologic view and linked to the OCT view via virtual inflation. The cluster representatives are shown for the whole vessel cross-sections (see inlays in a). The cluster view can be restricted to the histological brush (b), as well as to the linked brush in the OCT view (c-d).

[AMB\*13] AUZINGER T., MISTELBAUER G., BAČLIJA I., SCHERNTHANER R., KÖCHL A., WIMMER M., GRÖLLER M. E., BRUCKNER S.: Vessel Visualization using Curved Surface Refraction. *IEEE Trans. Vis. Comput. Graph.* 19, 12 (2013), 2858–2867. 2

[BBBea12] BALZANI D., BÖSE D., BRANDS D., ET AL.: Parallel Simulation of Patient-Specific Atherosclerotic Arteries for the Enhancement of Intravascular Ultrasound Diagnostics. *Engineering Computations* 29, 8 (2012), 888–906. 2

[BC87] BECKER R. A., CLEVELAND W. S.: Brushing Scatterplots. *Technometrics* 29, 2 (1987), 127–142. 3

[BHZeal0] BAZILEVS Y., HSU M.-C., ZHANG Y., ET AL.: A Fully-Coupled Fluid-Structure Interaction Simulation of Cerebral Aneurysms. *Comput Mech* 46, 1 (2010), 3–16. 9

[Bri07] BRIDSON R.: Fast Poisson Disk Sampling in Arbitrary Dimensions. In *ACM SIGGRAPH* (2007), p. 5. 9

[BSRea14] BORN S., SUNDERMANN S. H., RUSS C., ET AL.: Stent Maps - Comparative Visualization for the Prediction of Adverse Events of Transcatheter Aortic Valve Implantations. *IEEE Trans. Vis. Comput. Graph.* 20, 12 (2014), 2704–2713. 2

[BWKGO1] BARTROLÍ A. V., WEGENKITTL R., KÖNIG A., GRÖLLER E.: Nonlinear Virtual Colon Unfolding. In *Proc. of IEEE Visualization* (2001), pp. 411–420. 3

[Coh91] COHEN L. D.: On Active Contour Models and Balloons. *CVGIP: Image Understanding* 53, 2 (1991), 211–218. 3

[EK SX96] ESTER M., KRIEGEL H.-P., SANDER J., XU X.: A Density-Based Algorithm for Discovering Clusters in Large Spatial Databases with Noise. In *Proc. of Knowledge Discovery and Data Mining* (1996), pp. 226–231. 6

[GHB\*15] GLASSER S., HOFFMANN T., BOESE A., VOSS S.,

- KALINSKI T., SKALEJ M., PREIM B.: Histology-Based Evaluation of Optical Coherence Tomographic Characteristics of the Cerebral Artery Wall via Virtual Inflating. In *Proc. of Eurographics Workshop on Visual Computing for Biology and Medicine (VCBM)* (2015), pp. 149–158. 2, 4, 9
- [GLH\*14] GLASSER S., LAWONN K., HOFFMANN T., SKALEJ M., PREIM B.: Combined Visualization of Wall Thickness and Wall Shear Stress for the Evaluation of Aneurysms. *IEEE Trans. Vis. Comput. Graph.* 20, 12 (2014), 2506–2515. 2
- [GOH\*10] GLASSER S., OELTZE S., HENNEMUTH A., KUBISCH C., MAHNKEN A., WILHELMSSEN S., PREIM B.: Automatic Transfer Function Specification for Visual Emphasis of Coronary Artery Plaque. *Computer Graphics Forum* 29, 1 (2010), 191–201. 2
- [GRW\*00] GRESH D. L., ROGOWITZ B. E., WINSLOW R. L., SCOLLAN D. F., YUNG. C.: WEAVE: A System for Visually Linking 3-D and Statistical Visualizations, Applied to Cardiac Simulation and Measurement Data. In *Proc. of IEEE Visualization* (2000), pp. 489–492. 3
- [HGBea16] HOFFMANN T., GLASSER S., BOESE A., ET AL.: Experimental Investigation of Intravascular OCT for Imaging of Intracranial Aneurysms. *Int J Comput Assist Radiol Surg* 11, 2 (2016), 231–241. 4
- [HGG\*06] HONG W., GU X., QIU F., JIN M., KAUFMAN A.: Conformal virtual colon flattening. In *Proc. of the Symposium on Solid and Physical Modeling* (2006), pp. 85–93. 3
- [HKW12] HERRON T. J., KANG X., WOODS D. L.: Automated Measurement of the Human Corpus Callosum Using MRI. *PMC* 25, 6 (2012). 3
- [IVRR14] IRSHAD H., VEILLARD A., ROUX L., RAOCEANU D.: Methods for nuclei detection, segmentation, and classification in digital histopathology: a review – current status and future potential. *IEEE Rev. Biomed. Eng* 7 (2014), 97–114. 3
- [KBBea06] KAWASAKI M., BOUMA B. E., BRESSNER J., ET AL.: Diagnostic Accuracy of Optical Coherence Tomography and Integrated Backscatter Intravascular Ultrasound Images for Tissue Characterization of Human Coronary Plaques. *Journal of the American College of Cardiology* 48, 1 (2006), 81–88. 10
- [KFW\*02] KANITSAR A., FLEISCHMANN D., WEGENKITTL R., FELKEL P., GRÖLLER M. E.: CPR: Curved Planar Reformation. In *Proc. of IEEE Visualization* (2002), pp. 37–44. 2
- [KGPS13] KRETSCHMER J., GODENSCHWAGER C., PREIM B., STAMMINGER M.: Interactive Patient-Specific Vascular Modeling with Sweep Surfaces. *IEEE Trans. Vis. Comput. Graph.* 19, 12 (2013), 2828–2837. 2
- [KKSea12] KATOZIAN A., KARAMALIS A., SHEET D., ET AL.: Iterative Self-Organizing Atherosclerotic Tissue Labeling in Intravascular Ultrasound Images and Comparison With Virtual Histology. *IEEE Trans. Biomed. Eng.* 59, 11 (2012), 3039–3049. 2, 10
- [KSD\*15] KÄRSNÄS A., STRAND R., DORÉ J., EBSTRUP T., LIPPERT M., BJERRUM K.: A histopathological tool for quantification of biomarkers with sub-cellular resolution. *Computer Methods in Biomechanics and Biomedical Engineering: Imaging & Visualization* 3, 1 (2015), 25–46. 3
- [KZSea08] KALINSKI T., ZWÖNITZER R., SEL S., ET AL.: Virtual 3D Microscopy Using Multiplane Whole Slide Images in Diagnostic Pathology. *American Journal of Clinical Pathology* 130, 2 (2008), 259–264. 4
- [LSP03] LATSON L., SEBEK B., POWELL K. A.: Automated Cell Nuclear Segmentation in Color Images of Hematoxylin and Eosin-Stained Breast biopsy. *Analytical and Quantitative Cytology and Histology* 25, 6 (2003), 321–331. 3
- [MMVea13] MISTELBAUER G., MORAR A., VARCHOLA A., ET AL.: Vessel Visualization using Curvicircular Feature Aggregation. *Computer Graphics Forum* 32, 2 (2013), 231–240. 2
- [MS93] MARKS J., SHIEBER S.: *The Computational Complexity of Cartographic Label Placement*. Tech. Rep. TR-05-91, Center for Research in Computing Technology, Harvard University, 1993. 8
- [MSH\*11] MATHEWS M. S., SU J., HEIDARI E., LEVY E., LINSKEY M. E., CHEN Z.: Neuroendovascular Optical Coherence Tomography Imaging and Histological Analysis. *Journal of Neurosurgery* 69, 2 (2011), 430–439. 1
- [NDA\*08] NAIK S., DOYLE S., AGNER S., MADABHUSHI A., FELDMAN M., TOMASZEWSKI J.: Automated Gland and Nuclei Segmentation for Grading of Prostate and Breast Cancer Histopathology. In *Proc. of IEEE Symposium on Biomedical Imaging (ISBI): From Nano to Macro* (2008), pp. 284–287. 3
- [NGB\*09] NEUGEBAUER M., GASTEIGER R., BEUNG O., DIEHL V., SKALEJ M., PREIM B.: Map Displays for the Analysis of Scalar Data on Cerebral Aneurysm Surfaces. *Computer Graphics Forum* 28 (3) (2009), 895–902. 2
- [OP05] OELTZE S., PREIM B.: Visualization of Vascular Structures: Method, Validation and Evaluation. *IEEE Transactions on Medical Imaging* 25(4), 4 (2005), 540–549. 2
- [Ots79] OTSU N.: An Automatic Threshold Selection Method Based on Discriminate and Least Squares Criteria. *Denshi Tsushin Gakkai Ronbunshi* 63 (1979), 349–356. 6
- [PM90] PERONA P., MALIK J.: Scale-Space and Edge Detection Using Anisotropic Diffusion. *IEEE Trans. Pattern Anal. Mach. Intell* 12, 7 (1990), 629–639. 6
- [SCSG09] SERTEL O., CATALYUREK U. V., SHIMADA H., GURCAN M. N.: Computer-aided prognosis of neuroblastoma: Detection of mitosis and karyorrhexis cells in digitized histological images. In *Proc. of Conf. of IEEE Engineering in Medicine and Biology Society* (2009), pp. 1433–1436. 3, 6
- [TMF\*12] TSAKANIKAS V. D., MAICHALIS L. K., FOTIADIS D. I., NAKA K. K., BOURANTAS C. V.: *Intravascular Imaging: Current Applications and Research Developments*. IGI Global, 2012. 1
- [TSDS\*11] TUNG K.-P., SHI W.-Z., DE SILVA R., EDWARDS E., RUECKERT D.: Automatic Vessel Wall Detection in Intravascular Coronary OCT. In *Proc. of IEEE Symp. on Biomedical Imaging: From Nano to Macro* (2011), pp. 610–613. 10
- [Tul08] TULLEKEN H.: Poisson Disk Sampling. *Dev. Mag* 21 (2008), 21–25. 9
- [YKYea12] YOSHIMURA S., KAWASAKI M., YAMADA K., ET AL.: Visualization of Internal Carotid Artery Atherosclerotic Plaques in Symptomatic and Asymptomatic Patients: A Comparison of Optical Coherence Tomography and Intravascular Ultrasound. *American Journal of Neuroradiology* 33, 2 (2012), 308–313. 1
- [ZMG\*10] ZENG W., MARINO J., GURIJALA K. C., GU X., KAUFMAN A.: Supine and prone colon registration using quasi-conformal mapping. *IEEE Trans. Vis. Comput. Graph.* 16, 6 (2010), 1348–1357. 3
- [Zui94] ZUIDERVELD K.: Contrast Limited Adaptive Histogram Equalization. In *Graphics gems IV* (1994), Academic Press Professional, Inc., pp. 474–485. 6
- [ZY14] ZENG W., YANG Y.-J.: Colon flattening by landmark-driven optimal quasiconformal mapping. In *Proc. of Medical Image Computing and Computer-Assisted Intervention (MICCAI)* (2014), pp. 244–251. 3

## Research Article

# Fluid-Structure Simulations of a Ruptured Intracranial Aneurysm: Constant versus Patient-Specific Wall Thickness

**S. Voß,<sup>1</sup> S. Glaßer,<sup>2</sup> T. Hoffmann,<sup>3</sup> O. Beuing,<sup>3</sup> S. Weigand,<sup>3</sup> K. Jachau,<sup>4</sup> B. Preim,<sup>2</sup>  
D. Thévenin,<sup>1</sup> G. Janiga,<sup>1</sup> and P. Berg<sup>1</sup>**

<sup>1</sup>Department of Fluid Dynamics and Technical Flows, University of Magdeburg, Magdeburg, Germany

<sup>2</sup>Department of Simulation and Graphics, University of Magdeburg, Magdeburg, Germany

<sup>3</sup>Institute of Neuroradiology, University Hospital Magdeburg, Magdeburg, Germany

<sup>4</sup>Institute of Forensic Medicine, University Hospital Magdeburg, Magdeburg, Germany

Correspondence should be addressed to S. Voß; [samuel.voss@ovgu.de](mailto:samuel.voss@ovgu.de)

Received 20 May 2016; Accepted 31 July 2016

Academic Editor: Xinjian Yang

Copyright © 2016 S. Voß et al. This is an open access article distributed under the Creative Commons Attribution License, which permits unrestricted use, distribution, and reproduction in any medium, provided the original work is properly cited.

Computational Fluid Dynamics is intensively used to deepen the understanding of aneurysm growth and rupture in order to support physicians during therapy planning. However, numerous studies considering only the hemodynamics within the vessel lumen found no satisfactory criteria for rupture risk assessment. To improve available simulation models, the rigid vessel wall assumption has been discarded in this work and patient-specific wall thickness is considered within the simulation. For this purpose, a ruptured intracranial aneurysm was prepared *ex vivo*, followed by the acquisition of local wall thickness using  $\mu$ CT. The segmented inner and outer vessel surfaces served as solid domain for the fluid-structure interaction (FSI) simulation. To compare wall stress distributions within the aneurysm wall and at the rupture site, FSI computations are repeated in a virtual model using a constant wall thickness approach. Although the wall stresses obtained by the two approaches—when averaged over the complete aneurysm sac—are in very good agreement, strong differences occur in their distribution. Accounting for the real wall thickness distribution, the rupture site exhibits much higher stress values compared to the configuration with constant wall thickness. The study reveals the importance of geometry reconstruction and accurate description of wall thickness in FSI simulations.

## 1. Introduction

Although intracranial aneurysms have been intensively investigated within the last two decades [1], many open questions remain that require further research. Particularly numerical methods are increasingly used since they enable a highly detailed insight into disease processes at no risk for the individual patient. In this regard, Computational Fluid Dynamics (CFD), an established numerical method from classical engineering, was applied to model the blood flow in the human vasculature [2]. Several authors, who investigated patient-specific aneurysm models with regard to intra-aneurysmal flow patterns, identified risk factors for future rupture, but the results are inconsistent. For instance, Xiang et al. [3] associated low wall shear stress (WSS) with aneurysm bleeding, while Cebal et al. [4] detected high WSS

within their cohort of ruptured aneurysms. In a subsequent review article by Meng et al. [5], two possible pathways were postulated that assign both low and high WSS a crucial role regarding aneurysm growth and rupture. In addition, Cebal et al. [6] presented a relation between bleb formation and regions of high WSS as well as flow impaction zones.

However, due to patient-individual properties that are unknown (e.g., cerebral flow rates and vital parameters under activity) or due to the requirement of fast computations, all numerical studies are based on several model simplifications. The most severe but commonly used assumption is the treatment of the luminal vessel surface as a rigid, non-flexible wall with infinite resistance. Since three-dimensional segmentations of the diseased dilations are normally gained from contrast-enhanced imaging modalities, only the vessel lumen is represented; no information of the actual wall

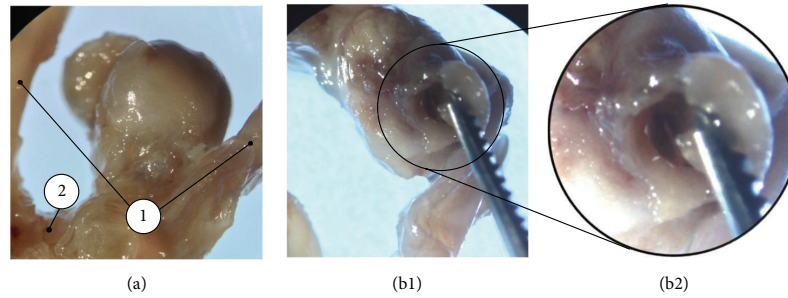


FIGURE 1: Specimen with Acom aneurysm and adjacent vessels (a). (1) Anterior cerebral arteries. (2) Anterior communicating artery. (b1) Rupture site with magnification (b2).

structure is obtained. However, a study by Frösen et al. [7] has demonstrated the heterogeneity of cerebral vessels, especially when diseases occur.

To extend previous numerical studies by considering mechanical exchanges between blood flow and the surrounding vessel tissue, fluid-structure interaction (FSI) simulations were carried out. Already in 2009 Bazilevs et al. [8] proposed a simple approach to construct vessels with variable wall thicknesses, depending on the radii of inlet and outlet. Cebra et al. [9] used the local WSS distribution of a rigid-wall simulation to estimate the wall thickness, since it induces several pathophysiological processes in the vessel wall. A correlation between the wall thickness as well as its stiffness and the rupture site was presented. The study of Raut et al. [10] focused on FSI simulations of the human aorta. They strongly recommended the use of patient-specific, regionally varying wall thicknesses as well, especially with regard to rupture risk assessment.

Although these studies are important steps towards realistic hemodynamic predictions and FSI simulations in intracranial aneurysms, none of them considered the patient-specific wall thickness. Therefore, the present study is, to the authors' knowledge, the first of its kind that incorporates the measured vessel wall thickness of a ruptured aneurysm into FSI computations. To evaluate the importance of patient-specificity, a simulation assuming constant walls is performed for comparison. The analyses of stress predictions within the complete aneurysm sac as well as at the particular rupture site address the question, whether patient-specific wall thickness is required in related simulations.

## 2. Materials and Methods

**2.1. Case Description and Preparation.** With approval of the local ethics committee, a complete Circle of Willis (CoW) of a 33-year-old male patient was investigated, which was explanted in the course of a forensic autopsy. Two intracranial aneurysms were found, one at the anterior communicating artery (Acom), the other at the carotid T. Death was caused by subarachnoid hemorrhage due to aneurysm rupture. The Acom aneurysm could be unambiguously identified as

the ruptured one, as it was enclosed in a large blood clot and the wall defect was clearly visible (see Figure 1).

To enable the further examination and imaging of the explant, the CoW was put into formaldehyde (4%) for fixation immediately after explantation. Then, the blood clot was carefully removed and the arteries were flushed with formaldehyde. For imaging of the ruptured aneurysm, the anterior cerebral arteries were dissected approximately 10 mm proximal and distal to the anterior communicating artery. After that, plastic tubes were inserted in the anterior cerebral arteries to avoid collapse of their lumen. Plastic was used, because it has a different X-ray density compared to biological tissue and consequently the following postprocessing steps, especially segmentation, are facilitated. The tubes were then stuck into a silicone block in such a way that the specimen had no contact to the silicone surface.

**2.2. Image Acquisition.** For image acquisition, an industrial computed tomography system (Nanotom S 180, GE Measurement & Control, Fairfield, Connecticut, USA) was selected. Despite its low contrast resolution—and thus the impossibility to distinguish different tissue layers of the vessel wall—the device was chosen because of the superior spatial resolution compared to clinical CT and MRI scanners. This allows for the accurate measurement of the wall thickness and visualization of the inner and outer boundary of the specimen. Imaging parameters were as follows: tube voltage of 50 kV, tube current of 150  $\mu\text{A}$ , and reconstructed voxel size of  $7.5 \times 7.5 \times 7.5 \mu\text{m}^3$ .

**2.3. Segmentation.** Two 3D surface meshes, one of the inner and one of the outer vessel wall, were extracted from the tomographic  $\mu\text{CT}$  data. Then, a separate segmentation of both walls was carried out. The workflow is derived from the pipeline for aneurysm surface extraction described in [11]. Initially, a threshold-based segmentation was applied in MeVisLab 2.8 (MeVis Medical Solutions AG, Bremen, Germany) [12]. The initial segmentation was manually corrected with MeVisLab due to the low contrast between vessel wall and vessel lumen of the  $\mu\text{CT}$  data as well as small artifacts, for example, detached tissue parts or blood clots,

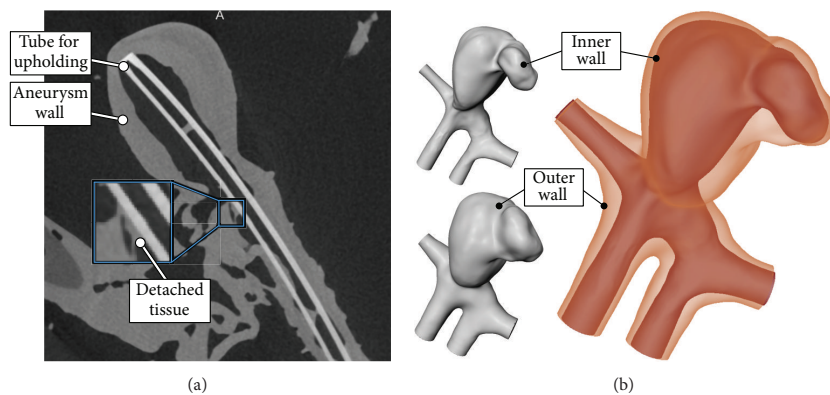


FIGURE 2: Slice image of the  $\mu$ CT data with the aneurysm wall (a). A detached tissue part of the ex vivo preparation is highlighted (see blue inlay). The resulting surface meshes for the inner vessel wall ((b) top left), the outer vessel wall ((b) bottom left), and the combination of both ((b) right) are illustrated.

due to the ex vivo preparation. In Figure 2(a), an example is provided, where small detached tissue parts inside the aneurysm are shown.

Next, surface meshes for the inner and outer vessel wall were extracted with Marching Cubes based on the segmentation masks in MeVisLab. Postprocessing of the surface meshes included the manual smoothing of small bumps and artifacts with Sculptris 1.02 (Pixologic, Los Angeles, USA). Furthermore, in- and outlets of the aneurysm were artificially extruded and perpendicularly cut with Blender 2.74 (Blender Foundation, Amsterdam, The Netherlands) to provide sufficiently long enough and straight vessel sections for the subsequent FSI simulation. The resulting 3D surface meshes are depicted in Figure 2(b).

**2.4. Fluid-Structure Simulations.** Since growth and rupture of an intracranial aneurysm are complex problems connecting blood flow and arterial wall behavior, FSI simulations were carried out. Therefore, the segmented aneurysm model was divided into two subdomains consisting of the fluid region and the solid region, respectively. The first was solved numerically using CFD based on a finite volume discretization, while the latter was treated as a structural problem using the finite element method. Both domains were coupled at the interface, the luminal surface. This coupling was implemented as data transfer, exchanging fluid pressure and WSS as well as wall displacement, respectively.

The fluid was modeled as incompressible, non-Newtonian (Carreau-Yasuda model:  $\eta_0 = 15.92$  mPa s,  $\eta_{\infty} = 4$  mPa s,  $\lambda = 0.08268$  s,  $a = 2$ , and  $n = -0.4725$ , parameters acquired in the local rheology lab) fluid with a density of  $1055$  kg/m<sup>3</sup>. The inflow conditions were obtained from a healthy volunteer using 7 T PC-MRI [13] and scaled according to the power law of Valen-Sendstad et al. [14]. No-slip conditions for all wall boundaries and zero-pressure outlets were defined. The vessel wall was deformable and coupled the fluid to the solid

TABLE 1: Spatial resolution of the FSI computations for the constant and the patient-specific wall thickness configuration.

	Cells in fluid domain	Elements in solid domain
Constant WT	1 206 806	63 072
Patient-specific WT	1 206 806	62 208

domain. The latter was assumed to be homogeneous and isotropic using a linearly elastic material model, considering density, Young's modulus, and Poisson's ratio of  $1050$  kg/m<sup>3</sup>,  $1$  MPa, and  $0.45$ , respectively [15, 16]. According to Torii et al. [17], this model is reasonable for investigating FSI in intracranial aneurysms. The wall thickness in the constant configuration was set to  $0.3$  mm according to the mean value for male patients in Costalat et al. [18] and obtained by normal extrusion of the luminal wall. In- and outlets of the solid domain were fixed; all other surfaces were free. The fluid domain was spatially discretized by polyhedral cells and five layers of prism cells at the wall, following the recommendations of Janiga et al. [19]. Regarding the solid domain, a structured mesh and hexahedral elements with quadratic basis function were used. Solvers were STAR-CCM+ 9.04 (CD-adapco, Melville, New York, USA) for the fluid and Abaqus FEA 6.14 (Dassault Systemes Simulia Corp., Providence, Rhode Island, USA) for the solid domain. Table 1 lists the number of discretization volumes, cells (for the fluid), and elements (for the solid); both are shown in Figure 3.

The time step size for the fluid domain was set to  $0.001$  s, while the variable time step for the solid domain was limited by the coupling time step of  $0.01$  s. Two cardiac cycles were simulated, but only the second one was postprocessed to avoid inaccuracies from initialization. The time-dependent FSI simulations were performed on a standard workstation, using four Intel Xeon E3 cores with  $3.3$  GHz and  $32$  GB RAM,

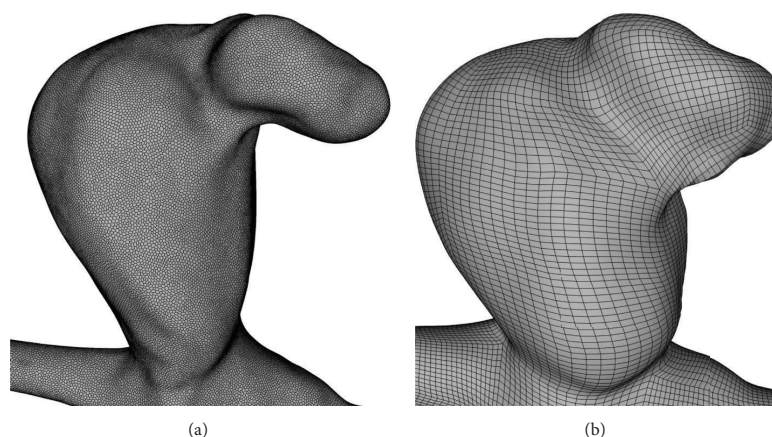


FIGURE 3: The fluid mesh consists of polyhedral and prism cells (a). Hexahedral finite elements are used for the solid domain (b).

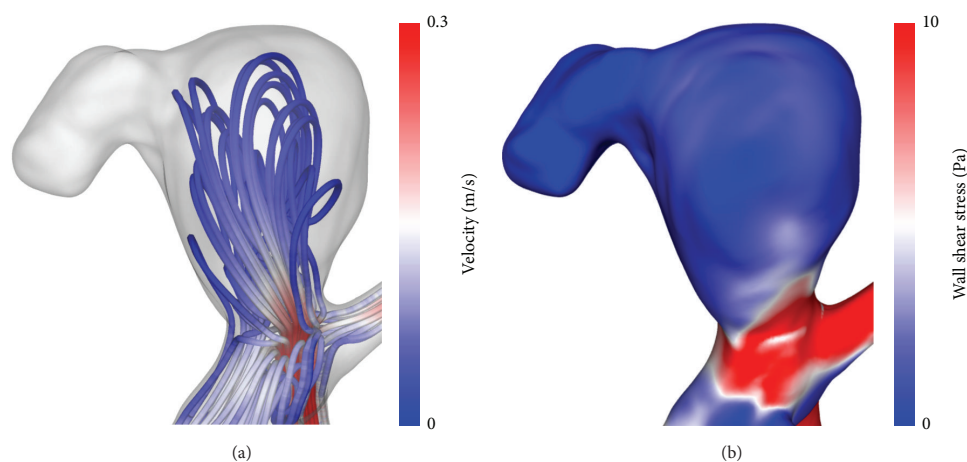


FIGURE 4: Visualization of the flow pattern (streamlines) and wall shear stresses of the patient-specific configuration at peak-systole.

resulting in calculation times of approximately 30 hours per case.

**2.5. Qualitative and Quantitative Analysis.** Both fluid and solid domain were considered in postprocessing. Streamlines and WSS are presented shortly to provide a qualitative impression of the hemodynamic flow pattern. However, the focus lies on the temporal-averaged stress distribution inside the aneurysm wall, which is initially shown on the inner and outer surface. To carry out a quantitative comparison, wall stress values were exported for two regions of interest: (a) the complete aneurysm sac (approx. 29,000 points) and (b) the rupture site (approx. 6,000 points), which is of particular interest due to its known location. Subsequently, for both regions of interest the spatial-average stress level was calculated and classified into bins of 500 Pa.

### 3. Results

**3.1. Qualitative Comparison.** As presented in Figure 4, the flow velocity inside the aneurysm remains small compared to the parent vessel. This results in low WSS over the entire aneurysm dome. Only in the neck region high values up to 25 Pa are present. Since the time-averaged deformations are below 1 mm, only the patient-specific configuration is shown here.

The main differences between both configurations concern the effective stress inside the aneurysm wall. Figures 5 and 6 compare the stresses on the outer and inner surface for the constant ((a) and (c)) and patient-specific configuration ((b) and (d)), respectively. Not only do stresses differ in level, but strong local variations are visible as well, leading to different structures. It is particularly interesting to note that the rupture site correlates with spots of high stresses when

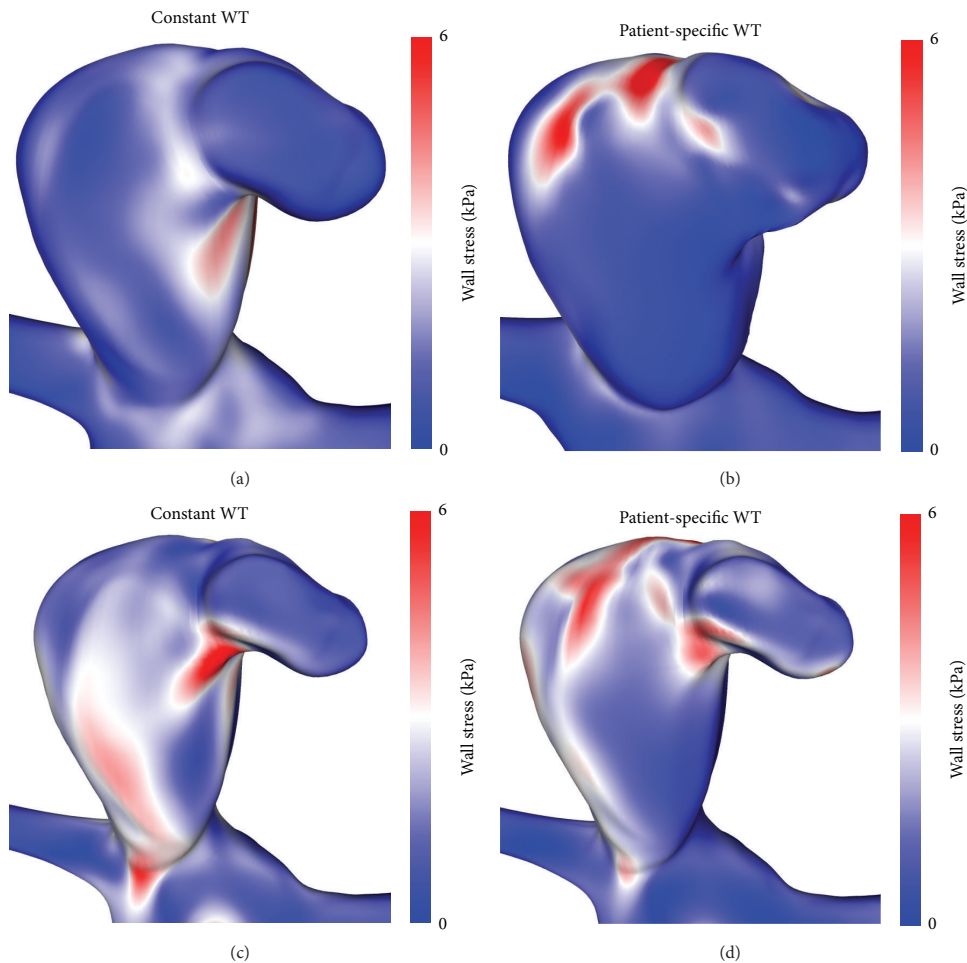


FIGURE 5: Front view of the effective stress at the outer ((a) and (b)) and inner ((c) and (d)) surface of the constant ((a) and (c)) and the patient-specific ((b) and (d)) wall thickness (WT) configuration, respectively.

using the patient-specific configuration (see Figures 6(b) and 6(d)), while nothing particular is observed in this region when a constant wall thickness is used for the computations.

**3.2. Quantitative Comparison.** Figure 7 illustrates the points that are associated with the complete aneurysm sac. Stress values are plotted as histogram plot using bins of 500 Pa. The dashed (constant wall thickness) and solid (patient-specific wall thickness) lines show the high similarity concerning the spatial-averaged stress level of both configurations, in spite of the large local variations. The difference between both approaches is only 3.8% concerning the average, which is not obvious considering only spatial plots.

To further investigate the aneurysm's rupture site, the quantitative comparison is now concentrated on a smaller region of interest, around the rupture site. Figure 8 shows

the selection of solid grid nodes that are considered for analysis. The histogram plot indicates that values in the constant wall thickness configuration are lower than 3 kPa, while for the patient-specific configuration they reach up to 6.5 kPa in the analyzed area. Likewise, the spatial-averaged stresses (dashed and solid line in Figure 8) reveal a relative difference of 55.2%.

#### 4. Discussion

Regarding realistic blood flow predictions in intracranial aneurysms, the reconstructed geometry has an essential impact [3]. In addition, Lee et al. [20] assume that aneurysm morphology is strongly related to aneurysm rupture. Building on these findings, the importance of an appropriate geometry reconstruction for aneurysmal wall mechanics is addressed

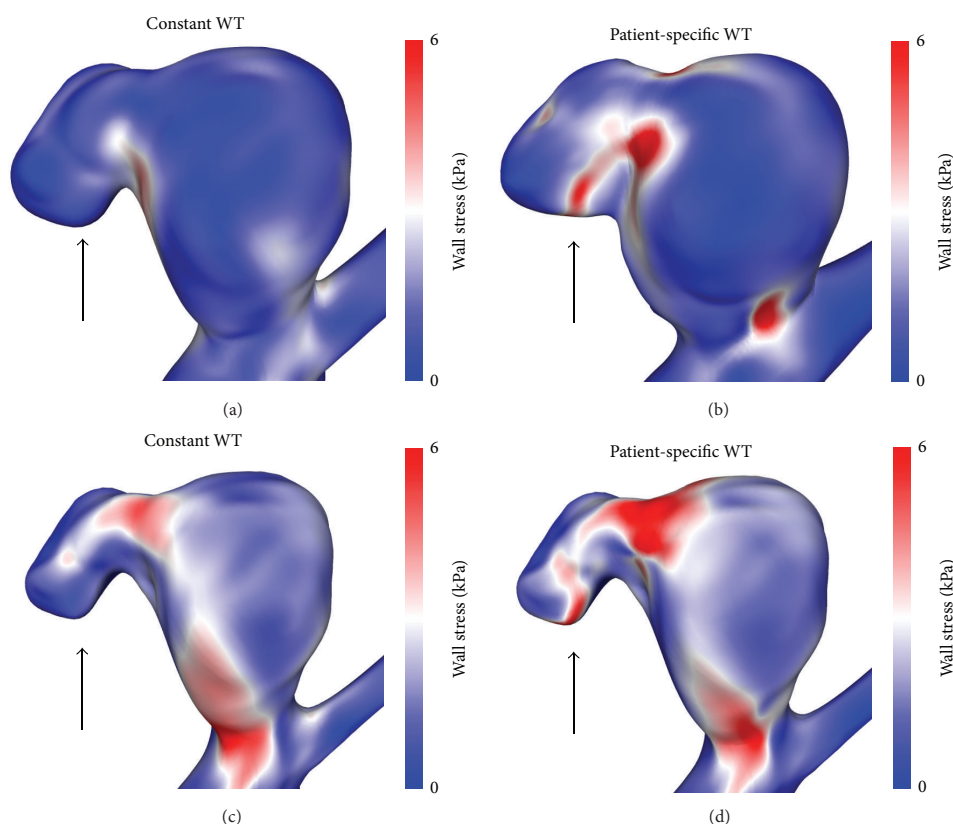


FIGURE 6: Second perspective of the effective stress at the outer ((a) and (b)) and inner ((c) and (d)) surface of the constant ((a) and (c)) and the patient-specific ((b) and (d)) wall thickness configuration, respectively. Very different stress levels are found at the location of the rupture site (indicated by the black arrow).

in the present study. In this regard, a variable vessel wall of a patient-specific intracranial aneurysm and a constant, virtually extruded wall thickness were both considered and compared using FSI simulation. Both investigated configurations are identical with respect to the fluid domain and its conditions. The only difference lies in the wall thickness treatment. This results in almost no differences in the hemodynamic parameters. Therefore, the study focuses on the wall mechanics and particularly on the wall stress, whose distribution varies strongly between both configurations, due to variations in local wall thickness. Consequently, it is suggested that the wall thickness is an important factor for FSI simulations, similar to the lumen morphology in the analysis of flow characteristics.

However, the use of patient-specific wall thickness is limited by the difficulties in acquisition, even *ex vivo*. This might be one reason for the fact that constant wall thickness is used in almost all similar studies of intracranial aneurysms. Nevertheless, promising models exist, which are related to wall mechanics, but do not take into account the wall thickness itself. Cebal et al. [9] used the value of local

WSS to manipulate the local wall thickness and stiffness, respectively. Based on the findings, thin and stiff wall regions in combination with abnormal high WSS correlate with the observed rupture sites. Sanchez et al. [21, 22] used fluid-structure simulations to quantify the volume variations over the cardiac cycle, assuming that material properties have a major impact. Accordingly, large volume variation is caused by weak walls, indicating an increased rupture risk. Still, the application of both approaches for the aneurysm presented in this study might be difficult, since neither the WSS is abnormally high inside the whole aneurysm, nor is it exposed to considerable deformation.

The main focus of the comparison lies in the known rupture site. For the patient-specific wall thickness configuration a good correlation with spots of high stresses is found, contrary to the constant wall thickness configuration. The latter shows a lower averaged stress of 55.2% in the area close to the rupture location. Taking the whole aneurysm into account, high similarity of both approaches in terms of average wall stress is present; the difference is only 3.8%. Accordingly, the choice of wall thickness for the artificial

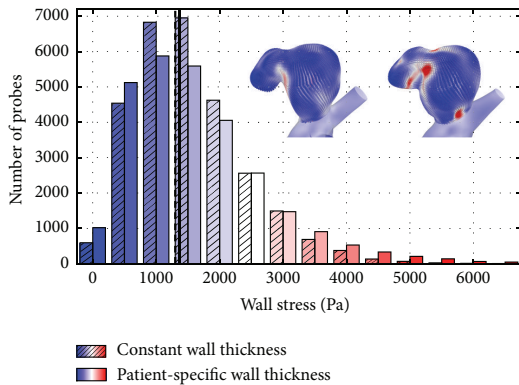


FIGURE 7: Histogram comparing wall stresses based on approx. 29,000 points in the aneurysm wall. The single bars indicate the number of points in a wall stress range of 500 Pa. As illustrated by the vertical lines, the average stress value obtained with the constant wall thickness configuration (dashed line) nearly matches the level obtained in the patient-specific configuration (solid line).

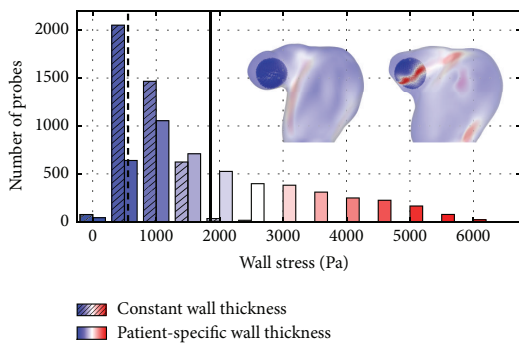


FIGURE 8: Histogram comparing wall stresses based on approx. 6,000 points around the rupture site. Bars of the constant WT configuration (indicated by the hatching) show a much lower stress level in the rupture zone, compared to the values found with patient-specific wall thickness. The dashed (constant WT) and solid (patient-specific WT) lines depict the mean stress found in the considered region of interest.

constant configuration is not responsible for the different stress level at the rupture site; it is a direct result of the patient-specific wall thickness. However, it needs to be pointed out that the rupture location does not correlate with the overall highest effective stress value. A reason for that might be the more complex structure of the aneurysm tissue or the surrounding vasculature, which was not considered during the modeling. There might be a general stress level that is dangerous, enabling rupture depending on the wall condition. However, this was not the objective of this study, which only aims at the comparison with constant wall thickness—a common assumption that is often used in FSI computations. Considering this particular case, obvious differences in

the local stresses are observed, pointing at limitations associated with the constant wall thickness approach.

Another interesting aspect with respect to the rupture site consists in its location at a daughter aneurysm revealing a bleb-like shape. Cebal et al. [6] investigated the relation between local hemodynamics in particular the WSS and the formation of blebs. According to the authors, blebs mostly occur at or adjacent to aneurysm regions near the flow impaction zone. This assumption is reasonable in this case as well; see Figure 4. In addition, the WSS decreased to a lower level compared to the main aneurysm, as observed by Cebal et al. In the frame of this study, only the final stage of the aneurysm geometry is known and the process of bleb growth remains unclear. However, the stress distribution inside the aneurysm wall may be related to bleb formation. Therefore, patient-specific wall thickness of aneurysm blebs may play an important role to deepen the understanding of this complex process and should be addressed in future studies.

In order to receive numerical predictions with reasonable computational effort, uncertainty and simplifications must be accepted and certainly influence the results. Concerning imaging, vessel position and arrangement as well as fixation differ from the in vivo setting. In addition, the resolution is limited, although  $\mu$ CT offers a good basis for a detailed segmentation process. However, it requires a lot of manual artifact elimination and local smoothing to provide appropriate vessel surfaces. Regarding the inflow condition and wall properties, a representative 7 T PC-MRI measurement and literature values, respectively, were used. It must be kept in mind that the homogenous, isotropic, linearly elastic material model used in this study is far from the real, complex tissue structure found in reality as function of age, activity, location, biological constitution, and so forth. However, Torii et al. [17] pointed out that linearly elastic models may be suitable for corresponding computations.

Future work should take into account a more detailed numerical description of the aneurysm geometry and material. This can be achieved by adding additional information obtained from histology, for example, the distinction between vessel layers and pathologies. The surrounding tissue might play an important role as well and could be considered by specified solid boundary conditions. Finally, a higher number of cases must be included, even if acquiring the real wall thickness is a difficult and time-consuming task.

### 5. Conclusion

The findings of this study highlight the importance of proper geometry reconstruction and accurate description of local wall thickness regarding hemodynamic FSI simulations. The patient-specific wall thickness seems to play an important role for the prediction of stress distributions inside aneurysm walls. While the spatial-averaged wall stresses of the complete aneurysm sac show almost no difference (only 3.8%) compared to those obtained with a constant wall thickness, high differences (55.2%) are observed around the known rupture site. Despite many simplifications, the presented results are a consequent step towards a deeper understanding

of aneurysmal wall behavior. Future research is required and should include more cases as well as a more advanced modeling of the wall mechanics.

### Competing Interests

The authors declare that there are no competing interests regarding the publication of this paper.

### Acknowledgments

The authors warmly acknowledge PD Dr. Elisabeth Eppler (University Hospital Magdeburg, Germany) for her support and fruitful discussions regarding histological examination. This work was partly funded by the Federal Ministry of Education and Research in Germany within the Research Campus STIMULATE under Grant no. 13GW0095A.

### References

- [1] B. Chung and J. R. Cebral, "CFD for evaluation and treatment planning of aneurysms: review of proposed clinical uses and their challenges," *Annals of Biomedical Engineering*, vol. 43, no. 1, pp. 122–138, 2015.
- [2] P. Berg, C. Roloff, O. Beuing et al., "The computational fluid dynamics rupture challenge 2013—phase II: variability of hemodynamic simulations in two intracranial aneurysms," *Journal of Biomechanical Engineering*, vol. 137, no. 12, p. 121008, 2015.
- [3] J. Xiang, S. K. Natarajan, M. Tremmel et al., "Hemodynamic-morphologic discriminants for intracranial aneurysm rupture," *Stroke*, vol. 42, no. 1, pp. 144–152, 2011.
- [4] J. R. Cebral, F. Mut, J. Weir, and C. Putman, "Quantitative characterization of the hemodynamic environment in ruptured and unruptured brain aneurysms," *American Journal of Neuro-radiology*, vol. 32, no. 1, pp. 145–151, 2011.
- [5] H. Meng, V. M. Tutino, J. Xiang, and A. Siddiqui, "High WSS or Low WSS? Complex interactions of hemodynamics with intracranial aneurysm initiation, growth, and rupture: toward a unifying hypothesis," *American Journal of Neuroradiology*, vol. 35, no. 7, pp. 1254–1262, 2014.
- [6] J. R. Cebral, M. Sheridan, and C. M. Putman, "Hemodynamics and bleb formation in intracranial aneurysms," *American Journal of Neuroradiology*, vol. 31, no. 2, pp. 304–310, 2010.
- [7] J. Frösen, R. Tulamo, A. Paetau et al., "Saccular intracranial aneurysm: pathology and mechanisms," *Acta Neuropathologica*, vol. 123, no. 6, pp. 773–786, 2012.
- [8] Y. Bazilevs, M.-C. Hsu, D. J. Benson, S. Sankaran, and A. L. Marsden, "Computational fluid-structure interaction: methods and application to a total cavopulmonary connection," *Computational Mechanics*, vol. 45, no. 1, pp. 77–89, 2009.
- [9] J. R. Cebral, M. Vazquez, D. M. Sforza et al., "Analysis of hemodynamics and wall mechanics at sites of cerebral aneurysm rupture," *Journal of NeuroInterventional Surgery*, vol. 7, no. 7, pp. 530–536, 2015.
- [10] S. S. Raut, A. Jana, V. de Oliveira, S. C. Muluk, and E. A. Finol, "The importance of patient-specific regionally varying wall thickness in abdominal aortic aneurysm biomechanics," *Journal of Biomechanical Engineering*, vol. 135, no. 8, Article ID 081010, 2013.
- [11] S. Glaßer, B. Berg, M. Neugebauer, and B. Preim, "Reconstruction of 3D surface meshes for blood flow simulations of intracranial aneurysms," in *Proceedings of the Conference of the German Society for Computer and Robotic Assisted Surgery*, pp. 163–168, 2015.
- [12] F. Ritter, T. Boskamp, A. Homeyer et al., "Medical image analysis," *IEEE Pulse*, vol. 2, no. 6, pp. 60–70, 2011.
- [13] P. Berg, D. Stucht, G. Janiga, O. Beuing, O. Speck, and D. Thévenin, "Cerebral blood flow in a healthy circle of willis and two intracranial aneurysms: computational fluid dynamics versus four-dimensional phase-contrast magnetic resonance imaging," *Journal of Biomechanical Engineering*, vol. 136, no. 4, Article ID 041003, 2014.
- [14] K. Valen-Sendstad, M. Piccinelli, R. KrishnankuttyRema, and D. A. Steinman, "Estimation of inlet flow rates for image-based aneurysm CFD models: where and how to begin?" *Annals of Biomedical Engineering*, vol. 43, no. 6, pp. 1422–1431, 2015.
- [15] Y. Bazilevs, M.-C. Hsu, Y. Zhang et al., "A fully-coupled fluid-structure interaction simulation of cerebral aneurysms," *Computational Mechanics*, vol. 46, no. 1, pp. 3–16, 2010.
- [16] A. Valencia, D. Ledermann, R. Rivera, E. Bravo, and M. Galvez, "Blood flow dynamics and fluid-structure interaction in patient-specific bifurcating cerebral aneurysms," *International Journal for Numerical Methods in Fluids*, vol. 58, no. 10, pp. 1081–1100, 2008.
- [17] R. Torii, M. Oshima, T. Kobayashi, K. Takagi, and T. E. Tezduyar, "Fluid-structure interaction modeling of a patient-specific cerebral aneurysm: influence of structural modeling," *Computational Mechanics*, vol. 43, no. 1, pp. 151–159, 2008.
- [18] V. Costalat, M. Sanchez, D. Ambard et al., "Biomechanical wall properties of human intracranial aneurysms resected following surgical clipping (IRRA Project)," *Journal of Biomechanics*, vol. 44, no. 15, pp. 2685–2691, 2011.
- [19] G. Janiga, P. Berg, O. Beuing et al., "Recommendations for accurate numerical blood flow simulations of stented intracranial aneurysms," *Biomedizinische Technik*, vol. 58, no. 3, pp. 303–314, 2013.
- [20] C. J. Lee, Y. Zhang, H. Takao, Y. Murayama, and Y. Qian, "A fluid-structure interaction study using patient-specific ruptured and unruptured aneurysm: the effect of aneurysm morphology, hypertension and elasticity," *Journal of Biomechanics*, vol. 46, no. 14, pp. 2402–2410, 2013.
- [21] M. Sanchez, D. Ambard, V. Costalat, S. Mendez, F. Jourdan, and F. Nicoud, "Biomechanical assessment of the individual risk of rupture of cerebral aneurysms: a proof of concept," *Annals of Biomedical Engineering*, vol. 41, no. 1, pp. 28–40, 2013.
- [22] M. Sanchez, O. Ecker, D. Ambard et al., "Intracranial aneurysm pulsatility as a new individual criterion for rupture risk evaluation: biomechanical and numeric approach (IRRA Project)," *American Journal of Neuroradiology*, vol. 35, no. 9, pp. 1765–1771, 2014.

## Part II

# Segmentation and Simulation

This part of the postdoctoral thesis covers important aspects regarding the segmentation for the subsequent simulation of IAs, including important aspects such a morphological division based on extracted ostium neck curves or the flow splitting based on vessel diameters:

- Chapter 5 (see page 73): Glaßer, S., Berg, P., Voß, S., Serowy, S., Janiga, G., Preim, B., & Beuing, O. (2016a). From imaging to hemodynamics ? How reconstruction kernels influence the blood flow predictions in intracranial aneurysms. *Current Directions in Biomedical Engineering*, 2(1), 679–683,
- Chapter 6 (see page 79): Saalfeld, S., Berg, P., Niemann, A., Luz, M., Preim, B., & Beuing, O. (2018b). Semiautomatic neck curve reconstruction for intracranial aneurysm rupture risk assessment based on morphological parameters. *International Journal of Computer Assisted Radiology and Surgery (IJCARS)*, 13(11), 1781–1793
- Chapter 7 (see page 93): Saalfeld, S., Voss, S., Preim, B., Beuing, O., & Berg, P. (2019). Flow-splitting-based computation of outlet boundary conditions for improved cerebrovascular simulation in multiple intracranial aneurysms. *International Journal of Computer Assisted Radiology and Surgery (IJCARS)*. doi:<https://doi.org/10.1007/s11548-019-02036-7>

*The typesetting of the manuscripts has not been modified. No changes have been made to the texts and illustrations of these peer-reviewed submissions. Only header, footer, and page numbers were removed and replaced by a chapter header and a running number.*



Sylvia Glaßer\*, Philipp Berg, Samuel Voß, Steffen Serowy, Gabor Janiga, Bernhard Preim and Oliver Beuing

# From imaging to hemodynamics – how reconstruction kernels influence the blood flow predictions in intracranial aneurysms

DOI 10.1515/cdbme-2016-0148

**Abstract:** Computational fluid dynamics (CFD) is increasingly used by biomedical engineering groups to understand and predict the blood flow within intracranial aneurysms and support the physician during therapy planning. However, due to various simplifications, its acceptance remains limited within the medical community. To quantify the influence of the reconstruction kernels employed for reconstructing 3D images from rotational angiography data, different kernels are applied to four datasets with patient-specific intracranial aneurysms. Sharp, normal and smooth reconstructions were evaluated. Differences of the resulting 24 segmentations and the impact on the hemodynamic predictions are quantified to provide insights into the expected error ranges. A comparison of the segmentations yields strong differences regarding vessel branches and diameters. Further, sharp kernels lead to smaller ostium areas than smooth ones. Analyses of hemodynamic predictions reveal a clear time and space dependency, while mean velocity deviations range from 3.9 to 8%. The results reveal a strong influence of reconstruction kernels on geometrical aneurysm models and the subsequent hemodynamic parameters. Thus, patient-specific blood flow predictions require a carefully selected reconstruction kernel and appropriate recommendations need to be formulated.

\*Corresponding author: **Sylvia Glaßer**, Department of Simulation and Graphics, University of Magdeburg, Germany, E-mail: glasser@ovgu.de

**Philipp Berg, Samuel Voß and Gabor Janiga:** Department of Fluid Dynamics and Technical Flows, University of Magdeburg, Germany, E-mail: berg@ovgu.de (P. Berg); samuel.voss@ovgu.de (S. Voß); janiga@ovgu.de (G. Janiga)

**Steffen Serowy and Oliver Beuing:** Department of Neuroradiology, University Hospital Magdeburg, Germany, E-mail: serowy@med.ovgu.de (S. Serowy); beuing@med.ovgu.de (O. Beuing)

**Bernhard Preim:** Department of Simulation and Graphics, University of Magdeburg, Germany, E-mail: preim@ovgu.de

**Keywords:** Computational fluid dynamics; Hemodynamics; Intracranial aneurysm; Reconstruction.

## 1 Introduction

Within the last decades, computational fluid dynamics (CFD) has been increasingly used to predict blood flow in intracranial aneurysms (IAs). Studies of large cohorts of patient-specific dilatations mainly try to understand initiation, remodelling as well as rupture processes in order to assist physicians during therapy planning [1, 2]. However, due to several assumptions, which are required to receive numerical results in a feasible time frame, the acceptance of CFD remains limited in the clinical context.

Therefore, several groups mainly focused on the evaluation of the variability of hemodynamic predictions based on varying input parameters. Berg et al. [3] compared in a double-blinded, international CFD challenge numerical solutions of 28 participating groups for two patient-specific IAs under given boundary conditions. The results were in a good agreement with only few outliers due to invalidated solvers or inadvertence during post-processing. To quantify the impact of geometry, Szikora et al. [4] simulated the blood flow in 21 IAs. They concluded that IAs with a main axis parallel to the parent artery are more prone to rupture than those with a perpendicular axis. Geers et al. [5] compared computer tomographic angiography and 3D rotational angiography (RA) images to evaluate the reproducibility of computational hemodynamics in IAs. As a result, different imaging modalities lead to equivalent predictions of the main flow characteristics, but large discrepancies in quantitative measurements are present.

This study extends the usual workflow and incorporates the reconstruction process directly from the digital subtraction angiography (DSA) suite Artis Q (Siemens Healthcare GmbH, Forchheim, Germany). Four patient-specific IA data sets are reconstructed with six available kernels. Next, 24 configurations are segmented and

analysed regarding the IAs' morphology and the impact on blood flow prediction.

## 2 Material and methods

### 2.1 Case description

Four IAs in four female patients with mean age of 50 years (range 45–59 years) were investigated in this study. Three cases exhibit acute subarachnoid hemorrhage (SAH), and one aneurysm was incidentally found. Clinical condition was poor in two of the patients with acute SAH (grade IV according to Hunt and Hess), the other two patients had no significant neurologic deficits. One IA was located at the anterior communicating artery, one at the posterior communicating artery, one at the segment of the internal carotid artery, and one at the bifurcation of the middle cerebral artery. Their size varied from approximately 2.5 mm to 8.0 mm. All IAs were treated with endovascular coiling.

### 2.2 Reconstruction and segmentation

From the RA image data, 6 3D-DSA images were reconstructed per patient by using the kernels EE (edge enhanced) smooth, EE normal, EE sharp, Hounsfield unit (HU) smooth, HU normal and HU sharp. This results in a total number of 24 configurations.

For each patient, a threshold-based segmentation, as proposed in [6], was carried out for the HU normal reconstructed DSA image data. Next, the remaining reconstructions of the same patient were carried out such that they exhibit similar contours in a representative slice covering the aneurysm, see Figure 1. Based on each threshold, the iso-surface is extracted to obtain the triangle surface mesh.

### 2.3 Clinical research prototype

The hemodynamic simulations were carried out with a clinical research prototype. To define the cross-sections where in- and outflow boundary conditions are applied, the vessel surfaces were cropped. A time-dependent velocity profile corresponding to a measured flow curve was defined at the inlet and zero-pressure conditions were set at the outlet cross sections. All required settings of the Lattice-Boltzmann solver were pre-defined and could

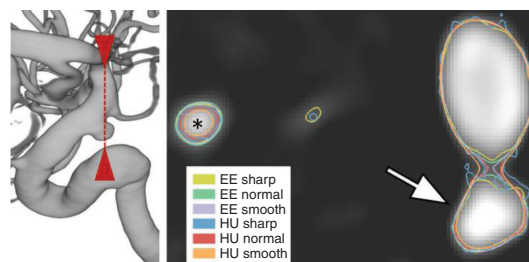


**Figure 1:** To provide comparable segmentations, a slice with the aneurysm of patient VA (indicated with arrowheads, left) is chosen. A threshold is selected such that similar IA segmentations are achieved (see arrow, right). The resulting segmentation masks are color-coded. The reconstruction kernels influence the extent of the segmentation, especially for peripheral vessels (see \*, right).

be adjusted by experienced users. Blood was treated as an incompressible ( $\rho = 1000 \text{ kg/m}^3$ ), Newtonian ( $\eta = 4 \text{ mPa}\cdot\text{s}$ ), laminar fluid and rigid walls were assumed. By default, two cardiac cycles were simulated, whereas only the second one was considered. To guarantee an appropriate mesh resolution, an element size of approximately 0.1–0.15 mm was chosen, yielding a coverage of the minimum ostium diameter by at least 20 voxels. Due to the efficient parallelization of the GPU-based solver, computational times of the unsteady simulations were approximately 30–45 min per case.

### 2.4 Qualitative and quantitative analyses

For a qualitative analysis of the segmented aneurysm models, a simultaneous view of all six surfaces was implemented in MeVisLab 2.8 (MeVis Medical Solutions AG, Bremen, Germany, [www.mevislab.de](http://www.mevislab.de)), a tool for medical image processing and visualization, see Figure 2. A transparent shading technique allows for an interactive and combined exploration of the vessel models.

Furthermore, the effect of different segmentations on the subsequent hemodynamic computations was evaluated using centrelines for the velocity fields. In this regard, spatial and temporal influences are considered and the variability of numerical predictions is quantified.

## 3 Results

### 3.1 Segmentation results

A 3D view of the segmented IA models is provided in Figure 2. The qualitative analysis revealed the missing

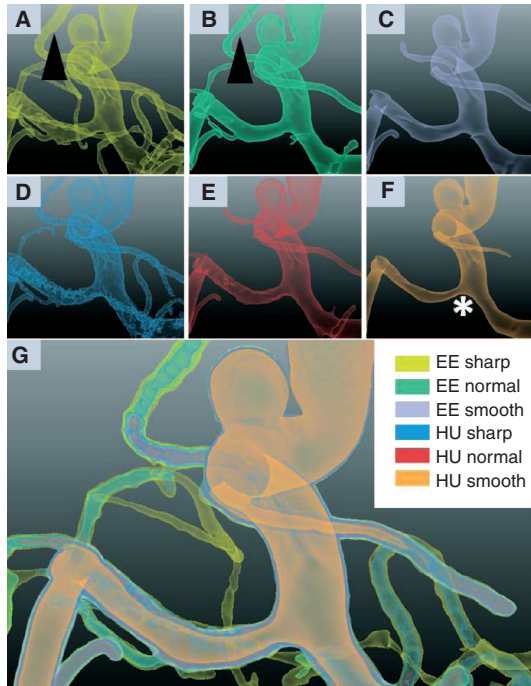


**Figure 2:** (A)–(F) Transparent, shaded 3D surface views for the six segmentation results for case EM including bifurcations (\*) and peripheral vessels (arrowheads). (G) Combined view of all segmentations.

of small vessels for smooth and normal reconstructions. Even for larger vessel parts, including the aneurysm neck, segmentations based on sharp reconstructions yield larger diameters. Although the segmentation threshold was carefully adapted such that similar aneurysm head segmentations were obtained, the aneurysm volume decreases from sharp to normal to smooth reconstructions.

Comparison of HU smooth and EE smooth indicates a slightly better result regarding bifurcations (see the example marked with \* in Figure 2E). Furthermore, branching vessels next to the aneurysm are better preserved in the EE-based segmentations (see arrowheads in Figure 2A and B).

For comparison of the aneurysm’s inflow zone, the ostium was approximated as intersecting plane dividing the aneurysm from the parent vessel. The resulting areas are compared in Figure 3. Hence, segmentations based on smooth reconstruction kernels yielded larger ostium areas, whereas segmentations based on sharp reconstruction kernels resulted in smaller ostium areas.

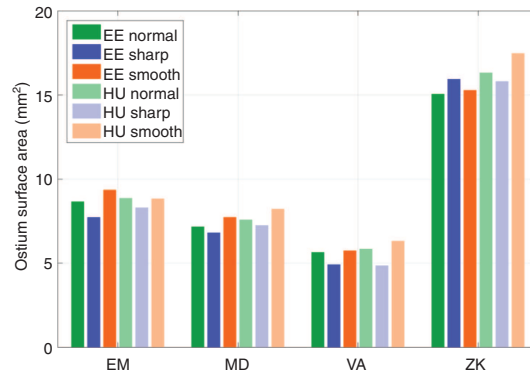


**Figure 3:** Ostium surface areas for the four patients and six segmentation results.

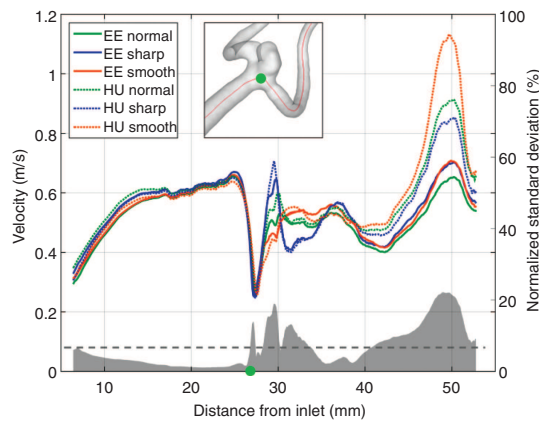


**Figure 4:** Velocity prediction along the centreline of case MD for the six different reconstruction kernels at one time step (top). Location-dependent normalized standard deviation (SD) illustrated in grey with the mean value presented by a dashed line (bottom).

### 3.2 Hemodynamic predictions

The effect of different reconstruction kernels on the hemodynamic predictions is exemplarily illustrated in Figure 4 for case MD. The velocity magnitude along the centreline shows a good agreement in the proximal part of the investigated domain. However, the numerical predictions strongly deviate in the distal part, especially between EE and HU. An equivalent behaviour is observed for the pressure predictions (not presented here).

To quantify the effect of time-dependency, Table 1 contains the standard deviations normalized to mean values for the four aneurysms at ten time steps over the cardiac cycle. It can be noticed that with increasing inflow

**Table 1:** Normalized standard deviation for centreline velocity at 10 time steps.

Case	Normalized standard deviation [%] over time									
EM	4.0	5.9	3.9	3.9	3.9	4.2	<b>5.2</b>	5.1	4.5	4.2
MD	6.1	6.0	5.8	5.7	5.9	6.4	<b>6.7</b>	6.5	6.2	6.1
VA <sup>a</sup>	6.5	5.9	5.5	5.3	4.6	5.8	7.3	<b>8.0</b>	7.0	6.7
ZK <sup>a</sup>	6.0	5.9	5.8	5.8	5.8	6.1	6.3	<b>6.4</b>	6.2	6.1

Highest values are bold. <sup>a</sup>indicates that EE sharp is not considered due to unsuccessful simulations.

velocity the deviations increase with the highest differences at peak-systole. However, the overall differences of the velocity results remain relatively low compared to the strong geometric deviations presented earlier.

## 4 Discussion

The qualitative comparison of the segmentations based on the six reconstruction kernels yields strong differences regarding branching vessels as well as vessel diameters. Sharp kernels tend to produce noisy surfaces, which are not well-suited for simulation. Smooth kernels yield smoother surfaces but are usually accompanied with smaller vessel cross-sections. Furthermore, segmentations based on EE kernels better comprise surrounding vessels and avoid a decrease in the vessel diameter at bifurcations. When analysing quantitative segmentation results, sharp kernels mostly lead to smaller and smooth kernels to larger ostium areas, respectively. Smooth kernels shrink elongated structures like small vessels, but flatten regions with high curvature, and thus increase the neck area. Sharp kernels yield opposite effects.

Equivalent observations are present with respect to the hemodynamic computations. Although the velocity values were in a good agreement in some vessel sections, other regions in the investigated domains clearly depend on the results of the reconstruction kernel. Hence, the results demonstrate how sensitive hemodynamic parameters depend on geometric variations. This awareness should lead to a careful selection of reconstruction kernels, if CFD computations and therefore patient-specific blood flow predictions are desired. As a result, we strongly recommend including the influence of reconstruction kernels into future CFD challenges like the challenge presented in [3].

Within this study the following limitations need to be mentioned: Firstly, the segmentations are based on a global threshold and a locally adapted segmentation may improve the quality of the 3D surface meshes. Secondly, the hemodynamic simulations assume rigid vessel walls without considering fluid-structure interactions. Thirdly, due to the lack of patient-specific boundary conditions, a representative flow curve was applied.

**Acknowledgment:** The authors warmly acknowledge Dr. Thomas Redel (Siemens Healthcare GmbH, Forchheim, Germany) for his support regarding the clinical research prototype. Further, we thank Marko Bögel (Friedrich-Alexander-University Erlangen-Nürnberg), who supported the segmentation process with fruitful discussions.

### Author's Statement

**Research funding:** This work was partly funded by the Federal Ministry of Education and Research in Germany within the Research Campus *STIMULATE* (grant no. 03FO16102A). **Conflict of interest:** Authors state no conflict of interest. **Material and Methods:** **Informed consent:** Informed consent has been obtained from all individuals included in this study. **Ethical approval:** The research related to human use complies with all the relevant national regulations, institutional policies and was performed in accordance with the tenets of the Helsinki Declaration, and has been approved by the authors' institutional review board or equivalent committee.

## References

- [1] Xiang J, Natarajan SK, Tremmel M, Ma D, Mocco J, Hopkins LN, et al. Hemodynamic-morphologic discriminants for intracranial aneurysm rupture. *Stroke*. 2011;42:144–52.
- [2] Cebal JR, Mut F, Weir J, Putman CM. Association of hemodynamic characteristics and cerebral aneurysm rupture. *Am J Neuroradiol*. 2011;32:264–70.
- [3] Berg P, Roloff C, Beuing O, Voss S, Sugiyama S, Aristokleous N, et al. The computational fluid dynamics rupture challenge 2013 – phase II: variability of hemodynamic simulations in two intracranial aneurysms. *J Biomech Eng*. 2015;137:121008.
- [4] Szikora I, Paal G, Ugron A, Naszstanovics F, Marosfoi M, Berentei Z, et al. Impact of aneurysmal geometry on intraaneurysmal flow: a computerized flow simulation study. *Interventional Neuroradiology*. 2008;50:411–21.
- [5] Geers AJ, Larrabide I, Radaelli G, Bogunovic H, Gratama van Andel HAF, Majoie CB, et al. Reproducibility of image-based

**DE GRUYTER**S. Glaßer et al.: From imaging to hemodynamics — **683**

computational hemodynamics in intracranial aneurysms: comparison of CTA and 3DRA. *Proceeding IEEE International Symposium on Biomedical Imaging: From Nano to Macro*; 2009. p. 610–3.

[6] Glaßer S, Berg P, Neugebauer M, Preim, B. Reconstruction of 3D surface meshes for blood flow simulations of intracranial aneurysms. *Proceeding of Computer- und Roboterassistierte Chirurgie (CURA)*; 2015. p. 163–9.





## Semiautomatic neck curve reconstruction for intracranial aneurysm rupture risk assessment based on morphological parameters

Sylvia Saalfeld<sup>1,4</sup> · Philipp Berg<sup>2,4</sup> · Annika Niemann<sup>1</sup> · Maria Luz<sup>1</sup> · Bernhard Preim<sup>1,4</sup> · Oliver Beuing<sup>3,4</sup>

Received: 10 January 2018 / Accepted: 14 August 2018  
© CARS 2018

### Abstract

**Purpose** Morphological parameters of intracranial aneurysms (IAs) are well established for rupture risk assessment. However, a manual measurement is error-prone, not reproducible and cumbersome. For an automatic extraction of morphological parameters, a 3D neck curve reconstruction approach to delineate the aneurysm from the parent vessel is required.

**Methods** We present a 3D semiautomatic aneurysm neck curve reconstruction for the automatic extraction of morphological parameters which was developed and evaluated with an experienced neuroradiologist. We calculate common parameters from the literature and include two novel angle-based parameters: the *characteristic dome point angle* and the *angle difference of base points*.

**Results** We applied our method to 100 IAs acquired with rotational angiography in clinical routine. For validation, we compared our approach to manual segmentations yielding highly significant correlations. We analyzed 95 of these datasets regarding rupture state. Statistically significant differences were found in ruptured and unruptured groups for maximum diameter, maximum height, aspect ratio and the characteristic dome point angle. These parameters were also found to statistically significantly correlate with each other.

**Conclusions** The new 3D neck curve reconstruction provides robust results for all datasets. The reproducibility depends on the vessel tree centerline and the user input for the initial dome point and parameters characterizing the aneurysm neck region. The characteristic dome point angle as a new metric regarding rupture risk assessment can be extracted. It requires less computational effort than the complete neck curve reconstruction.

**Keywords** Intracranial aneurysm · Neck curve · Morphological parameters · Rupture risk assessment

### Introduction

Rupture risk assessment for intracranial aneurysms (IAs) remains challenging, since vascular malformations are highly individual with respect to their shape and underlie varying hemodynamic conditions [1]. 2D measurements (e.g., ostium size, dome-to-neck ratio and aspect ratio) are carried out and

are used as rupture risk indicators in clinical routine [2, 3]. However, these measurements are highly user—as well as image-dependent, and the viewing angle for the 2D projections influences the resulting parameter values [4].

To overcome this problem, several studies considering 3D shape parameters of IAs were carried out during the last years [5–10]. Raghavan et al. [9] compared five size and eight shape indices with respect to the rupture status. They showed that none of the size parameters were significantly different between the ruptured and unruptured group, while five shape indices reached significance. A total of 119 aneurysm models were analyzed by Xiang et al. [11]. They identified the size ratio as the only independently significant factor in their morphology model. However, shape complexity parameters such as undulation index, ellipticity index and non-sphericity index were also significantly different between ruptured and unruptured aneurysms. Lv et al. [7] focused on morphological discriminants for the rupture

✉ Sylvia Saalfeld  
sylvia.saalfeld@ovgu.de

<sup>1</sup> Department of Simulation and Graphics, Otto-von-Guericke University of Magdeburg, Magdeburg, Germany

<sup>2</sup> Department of Fluid Dynamics and Technical Flows, Otto-von-Guericke University of Magdeburg, Magdeburg, Germany

<sup>3</sup> Department of Neuroradiology, University Hospital of Magdeburg, Magdeburg, Germany

<sup>4</sup> Research Campus STIMULATE, Magdeburg, Germany

status of posterior communicating artery aneurysms. They evaluated 129 cases, and their univariate analysis revealed that the size of aneurysm dome, the aspect ratio, the size ratio as well as the dome-to-neck ratio were significantly associated with rupture. Recently, Varble et al. [10] used a database of 311 aneurysms to quantify morphological characteristics of patient-specific IAs. They could demonstrate that only the size ratio was different between internal carotid artery (ICA) aneurysms, middle cerebral artery aneurysms and anterior/posterior communication artery aneurysms. Furthermore, they concluded that ICA aneurysms are subject to less rupture-prone morphological characteristics in comparison with other locations within the Circle of Willis.

Overall, it can be noticed that several drawbacks occur. First, some studies considered only a low number of aneurysms (e.g., 27 IAs in [9] and 45 IAs in [5]). Additionally, the separation of the aneurysm from the healthy parent vessel is often realized using a (planar) cut-plane [6, 9, 11] instead of an anatomical neck curve (NC) that also accounts for the highly variational aneurysm shapes including possible bulges. Furthermore, the influence of imaging parameters like reconstruction kernels also influences the morphology [12].

As a consequence, relevant parameters such as diameters, surfaces, volumes as well as derived ratios can be clearly over- or underestimated compared to the actual situation leading to wrong conclusions with respect to the rupture risk assessment.

The recent study addresses those issues and provides an analysis, which is based on high-quality data. Specifically, 3D segmentations of 100 IAs were carried out based on extensive technical experience [13–16]. We present a semiautomatic NC reconstruction that allows for automatic extraction of the morphological parameters. An evaluation is carried out based on 100 manually drawn NCs. Finally, a statistical analysis identifies relevant shape parameters to differentiate between ruptured and unruptured aneurysms.

## Materials and methods

In this section, we describe the acquired datasets and the semiautomatic NC reconstruction. Afterward, the extraction of morphological parameters is described.

### Data acquisition and segmentation

The datasets included in this study comprise 100 IA datasets from 70 patients (age: 33–93 years, 14 male and 56 female). The maximum height of the aneurysms ranged from 1.63 to 11.72 mm, with a mean value of 5.12 mm and a median value of 4.69 mm. The maximum diameter of the aneurysms ranged from 2.29 to 15.60 mm with a mean value of 6.58 mm and

a median value of 5.86 mm. Fifty-three of these aneurysms were ruptured, whereas 42 aneurysms were not ruptured. The status of the remaining five aneurysms was unclear since they were acquired during clinical routine. All patients included in this study underwent digital subtraction angiography (DSA) at the University Hospital Magdeburg, Germany, because of ruptured or incidentally discovered aneurysms. The examinations were part of the necessary clinical work-up and were performed on an Artis Q (Siemens Healthineers, Forchheim, Germany). The imaging protocol included a 3D rotational angiography (3D RA) in each patient, which is considered the gold standard in diagnostics and post-processing due to its high resolution. The 3D vascular trees were reconstructed from the data of the 3D RA using a threshold-based segmentation as proposed in [17], and then converted into a 3D triangulated surface mesh. Based on the surface mesh, the vessel's centerline was semi-automatically extracted with the vascular modeling toolkit (VMTK, [vmtk.org](http://vmtk.org)) [18]. Hence, the user manually selects the seed points by selecting the inlet and all outlets. The use of the data and its analysis comply with the guidelines of the local ethics committee.

For the evaluation of our approach, a manual NC segmentation for each of the 100 IAs was acquired by an experienced neuroradiologist. Each IA surface model was loaded into Blender 2.74 (Blender Foundation, <https://www.blender.org/>), and the NC was manually placed using the “knife” tool. The user can arbitrarily place lines onto the surface mesh which were manually corrected to obtain a closed NC. The obtained NCs were interpreted as gold standard for the evaluation of our approach.

### Semiautomatic neck curve reconstruction

Our framework is implemented in MATLAB (MathWorks, Natick, USA). Thus, the implementation is speed up by using vectorized data structures as well as MATLAB's Parallel Computing Toolbox, which supports image processing operations on the GPU.

For the automatic NC extraction, we discussed basic requirements for the resulting curves based on manually drawn NC from clinical experts. Inspired by the approach of Neugebauer et al. [19] and our discussions, we aim at an ostium plane that is roughly bent around the centerline of the parent vessel. Hence, we decide to employ the two nearest vessel branches to the aneurysm itself. Compliant to this approach, we also extract two points on the parent vessel surface that are located before ( $P_1$ ) and after ( $P_2$ ) the bulging of the aneurysm (between centerline and dome), since these points were always crossed by the manual NCs.

To describe the bending of the NC, we require two additional points  $P_3$  and  $P_4$ . The bending of the NC depends on the vessel radius and the aneurysm shape. The connected points yield the NC. Since the neck is the smallest part at

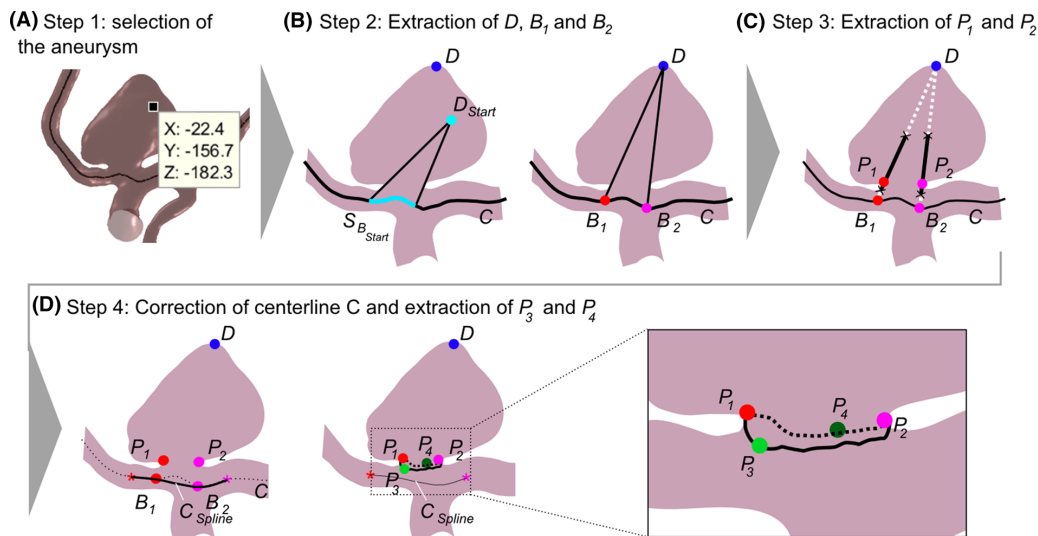


**Fig. 1** Pipeline for the semiautomatic NC reconstruction. First, the user clicks in the scene on the aneurysm to define  $D_{Start}$  (a).  $D_{Start}$  is used to extract  $S_{B_{Start}}$  on the centerline  $C$  and the dome  $D$ . Next, the base points

$B_1$  and  $B_2$  are extracted (b). Afterward,  $P_1$  and  $P_2$  are determined (c).  $C$  is replaced with a spline-based corrected centerline  $C_{Spline}$ .  $P_3$  and  $P_4$  are reconstructed (d), which are connected to the NC (see inlay)

the transition from parent vessel to aneurysm, the connection of these points is restricted to shortest paths on the aneurysm surface. Although the work by Neugebauer et al. [19] used these four characteristic points as well, we use different extraction methods as well as a modified connection approach for them.

The workflow is illustrated in Fig. 1 and comprises four steps:

- **Step 1** One-click selection of the aneurysm (see Fig. 1a).
- **Step 2** Extraction of the dome point  $D$  and base points  $B_1$  and  $B_2$  (see Fig. 1b).
- **Step 3** Extraction of  $P_1$  and  $P_2$  at the aneurysm surface (see Fig. 1c).
- **Step 4** Extraction of  $P_3$  and  $P_4$  to reconstruct the NC (see Fig. 1d).

#### Step 1: One-click selection of the aneurysm

In Step 1, the user selects the aneurysm with a single click which also initializes our method. We refer with  $D_{Start}$  to the selected position (recall Fig. 1a).  $D_{Start}$  should be near the actual dome point  $D$ . The dome point  $D$  refers to the aneurysm point with largest distance to the parent vessel. To speed up the subsequent steps, only parts of the surface mesh and centerline within 15 mm distance to  $D_{Start}$  are used. The user can increase or decrease this value.

#### Step 2: Extraction of the dome point $D$ and the base points $B_1$ and $B_2$

In Step 2, the base points  $B_1$  and  $B_2$  and the dome point  $D$  are extracted (see Fig. 1b). First, the set of points  $S_{B_{Start}}$  is determined, where  $S_{B_{Start}}$  comprises all points  $B_i$  of the centerline such that the vector  $\overrightarrow{B_i D_{Start}}$  does not intersect the triangle mesh (recall Fig. 1b). We set  $D$  to  $D_{Start}$ . If any neighbored vertex  $N_i$  of  $D$  exhibits a larger average distance to  $S_{B_{Start}}$ , we set  $D = N_i$  and iteratively repeat this process until  $D$  is the most distant point to  $S_{B_{Start}}$ . Two vertices are neighbored if they share an edge on the triangle mesh. We extract  $S_B$  comprising all points  $B_i$  of the centerline, where  $\overrightarrow{B_i D}$  does not intersect the triangle mesh.

Next,  $B_1$  and  $B_2$  are extracted from  $S_B$ , see Fig. 2. To account for bifurcation aneurysms including branching centerlines, three points  $T_1$ ,  $T_2$  and  $T_3$  are extracted.  $T_1$  and  $T_2$  form the pair of points from  $S_B$  with the maximum possible distance to each other.  $T_3$  is the point with maximum distance to  $T_1$  and  $T_2$ . If  $T_1$ ,  $T_2$  and  $T_3$  form a non-degenerated triangle,  $B_1$  and  $B_2$  are selected as the two points from  $T_1$  to  $T_3$  with shortest distance to  $D$  (recall Fig. 2). Otherwise,  $B_1$  and  $B_2$  are set to the points with largest distance to each other. We empirically define  $T_1$ ,  $T_2$  and  $T_3$  to form a degenerated triangle if the longest triangle edge  $e_1$  and the remaining edges  $e_2$  and  $e_3$  fulfill  $0.8 \times e_1 < e_2 + e_3 < 1.2 \times e_1$ .

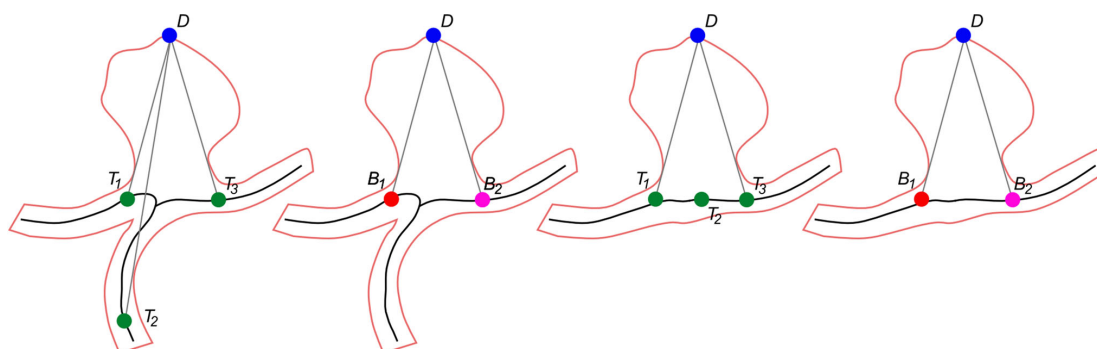


**Fig. 2** Extraction of  $B_1$  and  $B_2$  from  $T_1, T_2$  and  $T_3$  for two aneurysms. For bifurcation aneurysms,  $T_1, T_2$  and  $T_3$  form a triangle and  $B_1$  and  $B_2$  exhibit smallest distances to  $D$  (left). For sidewall aneurysms,  $T_1, T_2$  and  $T_3$  form a thin and degenerated triangle (right)

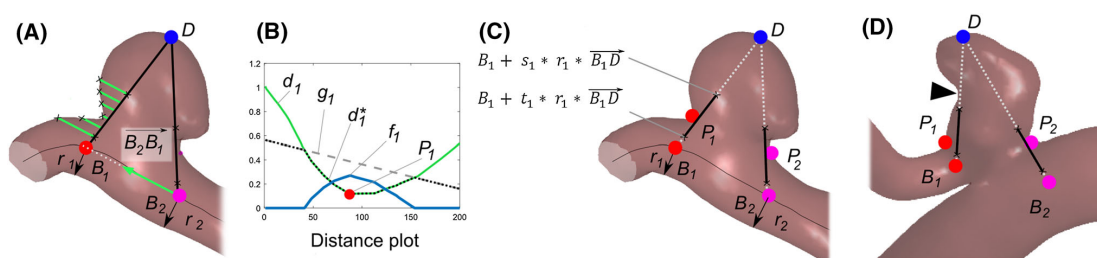


**Fig. 3** Extraction of  $P_1$  and  $P_2$ . The distances to the surface mesh starting at segment  $\overline{B_1D}$  in direction  $\overline{B_2B_1}$  are extracted as intersection points (a). They are plotted in the distance plots as  $d_1$  from which  $g_1, d_1^*$  and  $f_1$  are extracted (b). The maximum of  $f_1$  defines the position

of  $P_1, P_2$  is extracted accordingly. As a result,  $P_1$  and  $P_2$  are depicted with the original mesh (c). Example case where a false position (see arrowhead) has the shortest distance to  $\overline{B_1D}$  (d). With the restriction to the aneurysm neck region based on  $t_1, s_1$  and  $r_1, P_1$  is correctly determined

**Extraction of  $P_1$  and  $P_2$  at the aneurysm surface**

In Step 3, points  $P_1$  and  $P_2$  are extracted (see Fig. 1c).  $P_1$  and  $P_2$  are located at the aneurysm neck along the parent vessel. They are characterized by minimum distances to the segments  $\overline{B_1D}$  and  $\overline{B_2D}$  near the aneurysm neck region.

For the calculation of  $P_1$ , we cast rays in direction  $\overline{B_2B_1}$  by sampling the segment  $\overline{B_1D}$  and determine the distances  $d_1$  to the intersections with the surface, see Fig. 3. Possible neck points are characterized by a local minimum of  $d_1$  near the aneurysm neck region. To determine this region, only points originating between  $t_1 \times r_1$  and  $s_1 \times r_1$  on the segment  $\overline{B_1D}$  are considered, where  $r_1$  is the vessel radius at  $B_1$ . For the vessel radii extraction, rays are cast perpendicular to the centerline at  $B_1$  and the median distance to the surface is assigned to  $r_1$ . We empirically set  $t_1 = 0.5$  and  $s_1 = 2.0$ . These parameters can be adapted by the user since it may occur that the vessel radii cannot be correctly determined due to the large variations considering the aneurysm shapes.

As a result,  $d_1$  is restricted to the aneurysm neck region. We plot  $d_1$  in a distance plot (see Fig. 3b). We fit a line through  $d_1$  yielding  $g_1$ . Since we are only interested in minima, we

set all values  $d_1(x) < g_1(x)$  to  $g_1(x)$  and obtain  $d_1^*$ . The position of  $P_1$  is defined at the maximum position of  $f_1(x)$ , where  $f_1(x)$  provides the shortest distance for each point  $(x; d_1^*)$  to the line defined by  $g_1$ . Once we obtained  $x$ , we extract the corresponding intersection point with the surface mesh and obtain  $P_1$  (see Fig. 3c).

This method works well for large variations of aneurysm shapes. For example, the specific aneurysm shape yields various minimum distances to  $\overline{B_1D}$  in Fig. 3d. In particular, a location near the dome would result in a false candidate for  $P_1$  (see arrowhead, Fig. 3d). Due to the restriction to the aneurysm neck region (based on parameters  $t_1$  and  $s_1$ ), this candidate is not considered for  $P_1$ .

Analogously, we repeat this procedure for  $B_2$  to obtain  $d_2$  and finally  $P_2$ .

**Extraction of  $P_3$  and  $P_4$  of the neck curve**

In Step 4, we extract  $P_3$  and  $P_4$  as the last two sample points for the NC. The centerline is distorted caused by the aneurysm sac. To compensate for this distortion, we gather points of the centerline of  $B_1$  and  $B_2$  from the outside, i.e.,

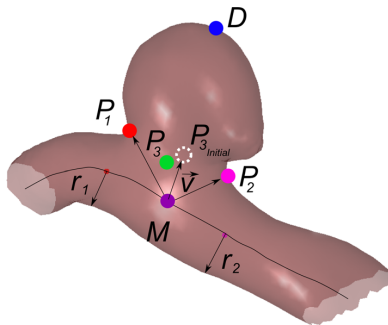


**Fig. 4** Illustration of the extraction of  $P_3$ :  $P_{3\text{initial}}$  is determined inside the aneurysm (see dashed circle), and  $P_3$  is identified as nearest surface point to  $P_{3\text{initial}}$

which are not in between them. We employ these sample points to fit a cubic spline curve and replace centerline points between  $B_1$  and  $B_2$  with the corresponding spline points (see Fig. 1d). Thus, we interpolate the points in between assuming continuity in the curve and its gradient direction.

Next, the initial position of  $P_3$  is extracted. Therefore, we determine the point  $M$  which is equidistant to  $B_1$  and  $B_2$  and lies on the centerline, see Fig. 4. The initial position of  $P_3$  is denoted as  $P_{3\text{initial}}$  and interpolated by  $P_{3\text{initial}} = M + \frac{1}{2}(r_1 + r_2) * \vec{v}$ , where  $\vec{v}$  is the normalized vector of  $\vec{MP_1} + \vec{MP_2}$ . Then,  $P_3$  is identified as nearest surface point to  $P_{3\text{initial}}$ .

To obtain the shortest NC, we iteratively move  $P_3$  along the surface mesh, in case one of its neighbors yields a shorter

NC than the initial position. That means, we extract for each neighbor  $N_i$  of  $P_3$  the shortest paths from  $P_1$  to  $N_i$  and from  $N_i$  to  $P_2$ . If we obtain a shorter path, we set  $P_3 = N_i$  and repeat the procedure. For finding the shortest connections, we interpret the surface mesh as graph structure and use MATLAB's *shortestpath()* function based on [20].

$P_4$  is extracted by rotating the vector  $\vec{MP_3}$  around the axis  $\vec{B_2B_1}$  with an angle in between  $180^\circ$  and  $270^\circ$ . We empirically set this angle to  $220^\circ$ . In accordance to  $P_3$ ,  $P_4$  is moved as long as a neighbor exists that yields a shorter path from  $P_1$  to  $P_2$  containing this point. However, the large variations of aneurysm anatomies lead to cases where the NC is defined under the parent vessel, see Fig. 5. To overcome this problem, we automatically extract exclusion points. We determine  $P'_1$  and  $P'_2$  opposite  $P_1$  and  $P_2$ .  $P'_1 = C_{P_1} - \vec{C_{P_1}P_1}$  and  $P'_2 = C_{P_2} - \vec{C_{P_2}P_2}$ , where  $C_{P_1}$  and  $C_{P_2}$  are nearest points on the centerline to  $P_1$  and  $P_2$ . We then exclude all surface mesh points within 1 mm distance to  $P'_1$  and  $P'_2$  for the shortest path search. We furthermore extract the closest pair of points  $Q_1$  and  $Q_2$  (where  $Q_1$  is within 1 mm distance to  $P'_1$  and  $Q_2$  is within distance to  $P'_2$ ), extract the shortest path between these points and add the path vertices to the exclusion points. Thus, the NC cannot intersect with these paths. The final NC is provided by the shortest paths from  $P_1$  to  $P_3$ ,  $P_3$  to  $P_2$ ,  $P_2$  to  $P_4$  and  $P_4$  to  $P_1$  (recall Fig. 1d).

Although our approach works for a wide variety of saccular and bifurcation IAs, it requires a pronounced neck curve. Very small aneurysms may not exhibit a visible distinguish-

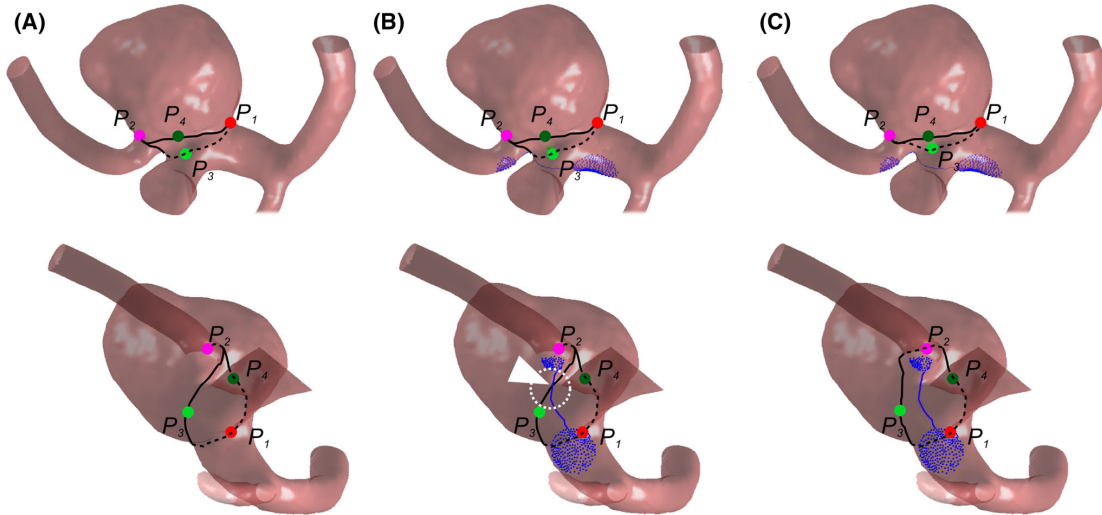


**Fig. 5** Example of an aneurysm at the posterior communicating artery from the front (top row) and the bottom (bottom row). The neck curve without exclusion points would be found under the parent vessel (a).

The excluded vertices and the excluded path are illustrated in blue (b). The excluded path intersects with the shortest path from  $P_3$  to  $P_2$  (see arrowhead). After exclusion, the correct neck curve is extracted (c)

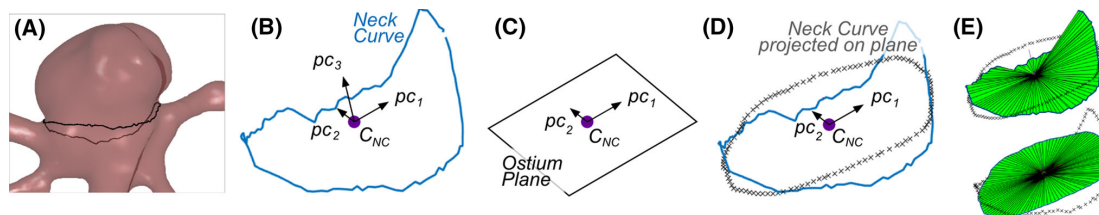


**Fig. 6** Extraction of the ostium plane for a basilar artery aneurysm (a). From the NC points, the mean  $C_{NC}$  and the principal components  $pc_1$ ,  $pc_2$  and  $pc_3$  are extracted (b). The ostium plane is defined by  $C_{NC}$ ,  $pc_1$

and  $pc_2$  (c). The NC can be projected on this plane (d). Triangulation of the NC and the projected NC yields two surfaces (e)

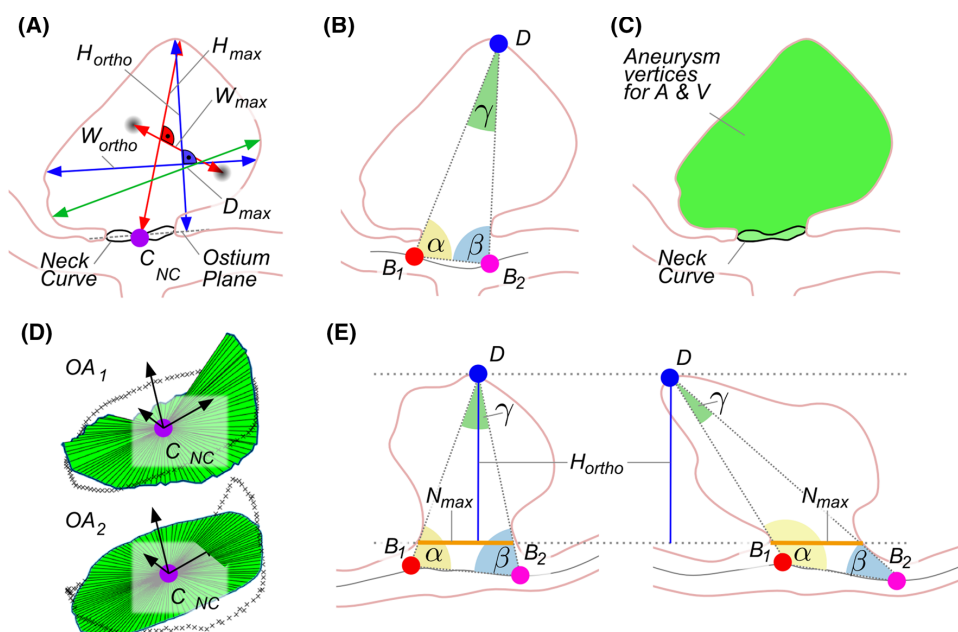


**Fig. 7** Illustration of the morphological parameters  $H_{max}$ ,  $W_{max}$ ,  $H_{ortho}$ ,  $W_{ortho}$  and  $D_{max}$  (a), as well as the angles  $\alpha$ ,  $\beta$  and  $\gamma$  between the base points  $B_1$  and  $B_2$  and the dome  $D$  (b). The NC separates the aneurysm vertices from the parent mesh to approximate  $A$  and  $V$  (c). The surface

area of the ostium is extracted for the reconstructed NC ( $OA_1$ ) as well as for the projected NC ( $OA_2$ ) (d). The angle-related parameters account for the tilting of the aneurysm (e). Here, the aspect ratio is identical, but  $\gamma$  and  $\Delta_{\alpha\beta}$  differ

able neck yet. For these cases, the user can manually place  $P_3$  and  $P_4$  on the surface and the final NC is again provided by the shortest paths from  $P_1$  to  $P_3$ ,  $P_3$  to  $P_2$ ,  $P_2$  to  $P_4$  and  $P_4$  to  $P_1$ . For all cases of the presented study,  $P_3$  and  $P_4$  were automatically determined.

### Morphological analysis

With the extracted NC, we can automatically and robustly determine common morphological parameters [5, 9]. Since many parameters from the literature require a planar ostium plane, we provide this plane as well. We denote the center

of the neck curve, i.e., the mean of all neck curve points using  $C_{NC}$ . Next, we employ a principal component analysis (PCA) to all neck curve points yielding principal component vectors  $\vec{pc}_1$ ,  $\vec{pc}_2$ , and  $\vec{pc}_3$ , see Fig. 6. First, we define the ostium plane as plane through  $C_{NC}$  with the plane vectors  $\vec{pc}_1$  and  $\vec{pc}_2$ . Second, we project each NC point onto this plane by determining the intersection point in direction of  $\vec{pc}_3$ , which equals the plane's normal (recall Fig. 6).

We extract the following 20 parameters, which are illustrated in Fig. 7.

- $A$  the area of the aneurysm (without the ostium), i.e., the surface area of all triangles separated by the neck curve.
- $V$  the volume of the aneurysm (the NC is triangulated by connecting all neck curve points with  $C_{NC}$ ).
- $OA_1$  area of the ostium (the NC is triangulated by connecting all neck curve points with  $C_{NC}$ ).
- $OA_2$  area of the ostium with the NC projected onto a plane.
- $D_{max}$  maximum diameter of the aneurysm, i.e., the distance of the two most distant points of the aneurysm.
- $H_{max}$  maximum height, i.e., maximum distance of an aneurysm point to  $C_{NC}$ .
- $W_{max}$  maximum width of the aneurysm perpendicular to  $H_{max}$ . This distance is obtained by connecting  $C_{NC}$  with the point corresponding to  $H_{max}$  and sampling rays perpendicular to this connection.
- $H_{ortho}$  height of the aneurysm approximated as length of the ray perpendicular to the ostium plane starting from  $C_{NC}$ .
- $W_{ortho}$  maximum width parallel to the projected ostium plane.
- $N_{max}$  maximum NC diameter, i.e., the maximum possible distance of two NC points.
- $N_{avg}$  average NC diameter, i.e., the mean distance of  $C_{NC}$  to the NC points.
- $AR_1$  the aspect ratio:  $H_{ortho}/N_{max}$ .
- $AR_2$  the aspect ratio:  $H_{ortho}/N_{avg}$ .
- $V_{CH}$  volume of the convex hull of the aneurysm vertices.
- $A_{CH}$  area of the convex hull of the aneurysm vertices.
- $EI$  the ellipticity index:  $EI = 1 - (18\pi)^{1/3} V_{CH}^{2/3} / A_{CH}$ .
- $NSI$  the non-sphericity index:  $NSI = 1 - (18\pi)^{1/3} V^{2/3} / A$ .
- $UI$  the undulation index:  $UI = 1 - \left(\frac{V}{CHV}\right)$ .
- $\Delta_{\alpha\beta}$  absolute value of difference between the angles  $\alpha$  (i.e., the angle between  $\overrightarrow{B_1D}$  and  $\overrightarrow{B_1B_2}$ ) and  $\beta$  (i.e., the angle between  $\overrightarrow{B_1B_2}$  and  $\overrightarrow{DB_2}$ ).
- $\gamma$  angle at  $D$ , i.e., between  $\overrightarrow{DB_1}$  and  $\overrightarrow{DB_2}$ .

It must be noted that all of these parameters can be automatically extracted based on a given NC and no manual user interaction is necessary. Furthermore, parameters except  $\Delta_{\alpha\beta}$  and  $\gamma$  were already introduced in the literature. During the NC detection development, the parameters  $\Delta_{\alpha\beta}$  and  $\gamma$  were identified as well suited to characterize tilted aneurysms with respect to their parent arteries. In contrast to  $AR_1$  and  $AR_2$ ,  $\gamma$  describes the height and width ratio of aneurysms and their tilting at the same time (recall Fig. 7e). Furthermore,  $\Delta_{\alpha\beta}$  provides information about the tilting itself. We carried out statistical evaluation to assess whether ruptured and unruptured aneurysms differ w.r.t. their morphological parameters. All tests were carried out with SPSS 22.0 (IBM, New York, USA).

## Evaluation

Our semiautomatic NC reconstruction was applied to all 100 datasets, and we could automatically extract the morphological parameters for each aneurysm. First, the comparison of the semiautomatic NC to the manually drawn curves is carried out. Afterward, the results of the morphologic parameter extraction w.r.t. rupture state are presented.

### Comparison of semiautomatic and manual NC approach

We compared the semi-automatically determined NC ( $NC_{new}$ ) to the manually segmented one ( $NC_{manual}$ ) for each aneurysm. Therefore, we employ the average distance and standard deviation between two NCs presented by Cárdenes et al. [21]. The resulting average distances are provided in the box plot (Fig. 8), with a median value of 1.35 mm. In Fig. 9, the average distances w.r.t. the maximum aneurysm diameter are depicted separately. We use the result of this metric to identify the three cases with lowest and highest average differences, recall Fig. 8. Comparison of the average distances of the manual and semiautomatic NC to the individual aneurysm's maximum diameter yields the following results: 25% of the cases exhibit errors smaller than 14%, 50% smaller than 25% and 75% smaller than 36% of the maximum diameter.

The clinician requested similar results concerning the morphological parameters based on  $NC_{manual}$  and  $NC_{new}$ . We conducted a correlation analysis based on the Pearson correlation coefficient (PCC) for the parameters  $A$ ,  $V$ ,  $OA_1$ ,  $OA_2$ ,  $D_{max}$ ,  $H_{max}$ ,  $W_{max}$ ,  $H_{ortho}$ ,  $W_{ortho}$ ,  $N_{max}$  and  $N_{avg}$  since these are most often used in clinical practice.

Our analysis yields significant correlations with  $p < 0.001$  for all parameters:  $PCC(A) = 0.974$  (i.e., the  $PCC(A)$  denotes the PCC for parameter  $A$  based on  $NC_{manual}$  and  $A$  based on  $NC_{new}$ ),  $PCC(V) = 0.940$ ,  $PCC(OA_1) = 0.971$ ,  $PCC(OA_2) = 0.961$  ( $p = 0.000$ ),  $PCC(D_{max}) = 0.934$ ,  $PCC(H_{max}) = 0.960$ ,  $PCC(W_{max}) = 0.962$ ,  $PCC(H_{ortho}) = 0.951$ ,  $PCC(W_{ortho}) = 0.947$ ,  $PCC(N_{max}) = 0.938$  and  $PCC(N_{avg}) = 0.963$ . As a result, we can conclude that  $NC_{manual}$  and  $NC_{new}$  yield significantly correlating parameter values for the morphologic parameters and the usage of our semiautomatic NC approach is justified.

### Results of morphological parameter analysis

For the statistical evaluation, we only used 95 aneurysms with clear rupture state. Unclear rupture states arise if a patient suffered from multiple aneurysms and the ruptured one could not be clearly identified. First, an analysis for normal distribution was carried out; the Kolmogorov–Smirnov test did

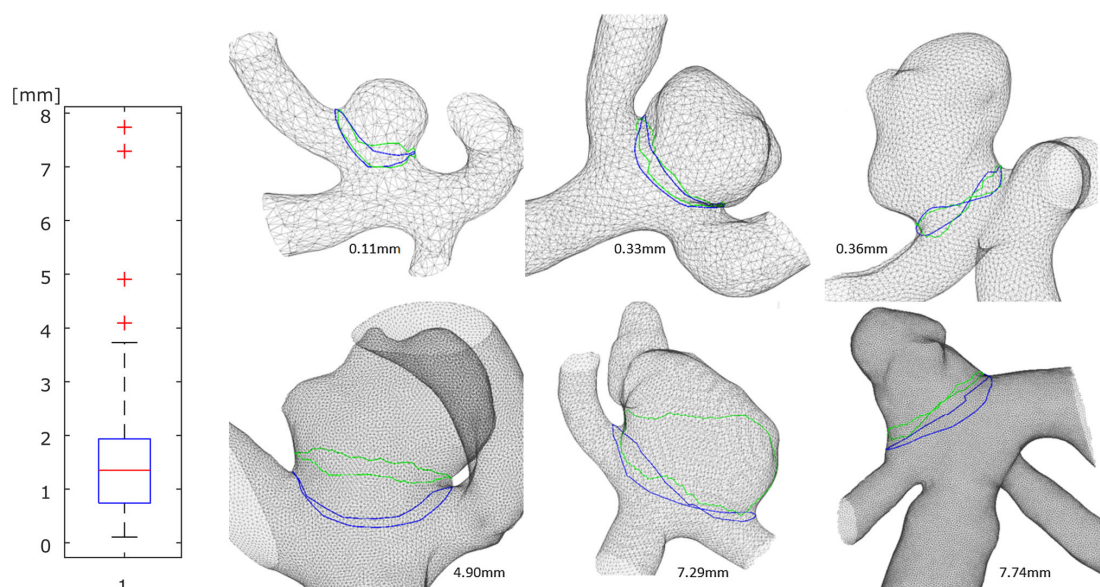


**Fig. 8** Boxplot of the extracted averaged distances (in mm) between manual and semiautomatic NCs for the 100 tested datasets (median = 1.53 mm, 25th percentile = 0.74 mm, 75th percentile = 1.94 mm, left). Depiction of the semiautomatic NC results for the three best (right, top

row) and three worst (right, bottom row) datasets with respect to average differences between semiautomatic NC (green) and manual NC (blue). The average differences are provided for each of the cases in the figure

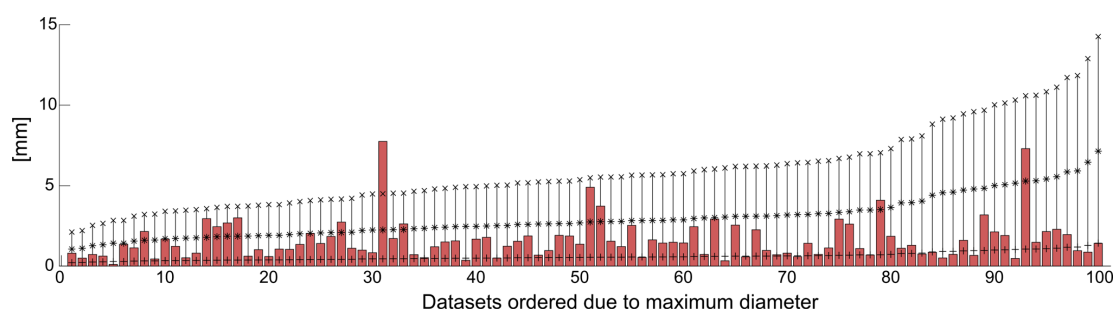


**Fig. 9** Bar plot of the average distance between manual and semiautomatic NC for all 100 datasets in relation to the maximum aneurysm diameter: the markers +, \* and x refer to 10%, 50% and 100% of the maximum aneurysm diameter, respectively

not show normal distributed data for each of the provided parameters.

Therefore, the nonparametric Mann–Whitney– $U$  test was applied for each parameter, see Table 1. The ruptured and unruptured aneurysms significantly differ regarding the parameters  $D_{\max}$ ,  $H_{\max}$ ,  $AR_1$ ,  $AR_2$  and  $\gamma$ . Mean value and standard deviation are provided in Table 2, and box plots are depicted in Fig. 10. The box plots for the unruptured and ruptured IAs present the parameter distribution based on  $NC_{\text{manual}}$  and  $NC_{\text{new}}$ . Subsequently, we calculated the correlation between these parameters based on the Pearson correlation coefficient (PCC). Interestingly, all of these five parameters significantly correlate with

each other:  $PCC(D_{\max}; H_{\max}) = 0.972$ ,  $PCC(D_{\max}; AR_1) = 0.473$ ,  $PCC(D_{\max}; AR_2) = 0.498$ ,  $PCC(D_{\max}; \gamma) = -0.343$ ,  $PCC(H_{\max}; AR_1) = 0.646$ ,  $PCC(H_{\max}; AR_2) = 0.662$ ,  $PCC(H_{\max}; \gamma) = -0.500$ ,  $PCC(AR_1; AR_2) = 0.980$ ,  $PCC(AR_1; \gamma) = -0.822$ , and  $PCC(AR_2; \gamma) = -0.812$ , with  $p < 0.01$  for all tests.

## Discussion

This study introduces a new approach to semi-automatically reconstruct the neck curve of patient-specific IAs. It was adapted to 100 IAs with varying sizes, locations and type

**Table 1** Result of the nonparametric Mann–Whitney-*U* (MWU) test for the morphological parameters

Parameter	MWU	Z	<i>p</i>
<i>A</i>	867	-1.803	0.071
<i>V</i>	903	-1.533	0.125
<i>OA</i> <sub>1</sub>	990	-0.879	0.379
<i>OA</i> <sub>2</sub>	992	-0.864	0.388
<i>D</i> <sub>max</sub>	845	-1.969	0.049*
<i>H</i> <sub>max</sub>	795	-2.344	0.019*
<i>W</i> <sub>max</sub>	916	-1.435	0.151
<i>H</i> <sub>ortho</sub>	854	-1.901	0.057
<i>W</i> <sub>ortho</sub>	934	-1.300	0.194
<i>N</i> <sub>max</sub>	1031	-0.571	0.568
<i>N</i> <sub>avg</sub>	985	-0.917	0.359
<i>AR</i> <sub>1</sub>	785	-2.419	0.016*
<i>AR</i> <sub>2</sub>	771	-2.525	0.012*
<i>V</i> <sub>CH</sub>	895	-1.593	0.111
<i>A</i> <sub>CH</sub>	890	-1.631	0.103
<i>EI</i>	930	-1.330	0.184
<i>NSI</i>	918	-1.420	0.156
<i>UI</i>	1061	-0.346	0.730
$\Delta_{\alpha\beta}$	869	-1.788	0.074
$\gamma$	734	-2.803	0.005**

\*\*Strongly significant correlation, double-sided, *p* < 0.01; \*significant correlation, double-sided, with *p* < 0.05

**Table 2** Mean values ( $\bar{x}$ ) and standard deviation (*s*) of the parameters *D*<sub>max</sub>, *H*<sub>max</sub>, *AR*<sub>1</sub>, *AR*<sub>2</sub> and  $\gamma$  extracted with the semiautomatic neck curve approach

	<i>D</i> <sub>max</sub> (mm)	<i>H</i> <sub>max</sub> (mm)	<i>AR</i> <sub>1</sub>	<i>AR</i> <sub>2</sub>	$\gamma$ (°)
<i>Ruptured aneurysms</i>					
$\bar{x}$	7.22	5.81	1.35	1.55	31.91
<i>s</i>	3.04	2.68	0.56	0.66	14.03
<i>Unruptured aneurysms</i>					
$\bar{x}$	6.13	4.64	1.08	1.22	44.25
<i>s</i>	2.74	2.37	0.47	0.53	19.14

(sidewall and bifurcation aneurysms). The presented method could extract *P*<sub>1</sub> and *P*<sub>2</sub> characterizing the transition from parent vessel to aneurysm between centerline and dome as well as *P*<sub>3</sub> and *P*<sub>4</sub> describing the bending of the NC. As illustrated in Fig. 10, the parameters extracted from the semiautomatic approach correlate well with those from the manually drawn curves. Largest differences are present for *AR*<sub>1</sub> which depends on *N*<sub>max</sub>. This might be caused due to different bendings of the neck curves at the parent vessel.

A 3D NC determination and subsequent parameter extraction is superior to 2D measurements [4, 22], where inadequate viewing directions for the 2D projections could hamper the result, see the example in Fig. 11a. The 2D projections

in clinical practice have to account for possible occlusions of surrounding vessels, and often a clear view on the parent vessel for subsequent endovascular treatment is required.

Extraction of ostium neck curves is challenging due to the wide variety of shape and size. Karmonik et al. [23] presented a 2D NC extraction which requires an analysis of vessel radius change opposite the aneurysm and could not produce the desired results for bifurcation aneurysms (see Fig. 11b). The estimation of Jerman et al. [24] is similar to our approach since ray tracing is also enabled to get the NC points. The approach by Cárdenes et al. [25] uses Voronoi diagrams for the NC extraction. Hence, a centerline inside the aneurysm is necessary.

Comparisons of the semiautomatic and manual NCs reveal a median error of 1.53 mm for the average displacements based on the metric introduced in [21]. Thus, our median average distance is definitely lower than the values reported in an additional study by Cárdenes et al. [21] comparing different neck curve extractions. They reported average median distances lower than 0.5 mm for automatic neck curve extraction methods based on deformable model extensions or geodesic curves with topological restrictions. For manual cutting plane placement, the average median distances are even lower than 0.37 mm. In consequence, these methods will yield better results w.r.t. average distance of neck curves than our approach. On the contrary, we strongly reject planar neck curves (see the example in Fig. 11d) and their dataset only comprised 26 cases.

Our approach was inspired by Neugebauer et al. [19], but we experienced several drawbacks of their method. First, the vessel radii of the parent vessel are often not identical (recall example in Fig. 11c), which caused problems for extraction of *P*<sub>1</sub> and *P*<sub>2</sub>. This step also suffers from thin and bulged aneurysm shapes, where a minimum distance between the centerline and a projected centerline has to be determined. We solved this problem by restricting the possible occurrences of *P*<sub>1</sub> and *P*<sub>2</sub> to the aneurysm neck region, recall Fig. 3d. In addition, the extraction of *P*<sub>3</sub> and *P*<sub>4</sub> might stuck at local minima, i.e., bulges of the aneurysm next to the centerline can be missed, see Fig. 11c. With our method, the extraction and adaption of *P*<sub>3</sub> and *P*<sub>4</sub> prevents this problem, see the result in Fig. 12. Nevertheless, their approach was tested on seven cases, while our method could only be developed based on the large variations in the 100 datasets. On the other hand, our approach requires a pronounced neck. Although a manual selection of *P*<sub>3</sub> and *P*<sub>4</sub> can be carried out to cope with very small aneurysms without a visible neck, this is a shortcoming of our approach. An approximation of the aneurysm neck with a 2D cutting plane (as suggested in [5, 6, 9]) introduces errors when evaluating morphological parameters, since the perfect position of this plane remains unclear in case of bulging aneurysms, recall Fig. 11d.

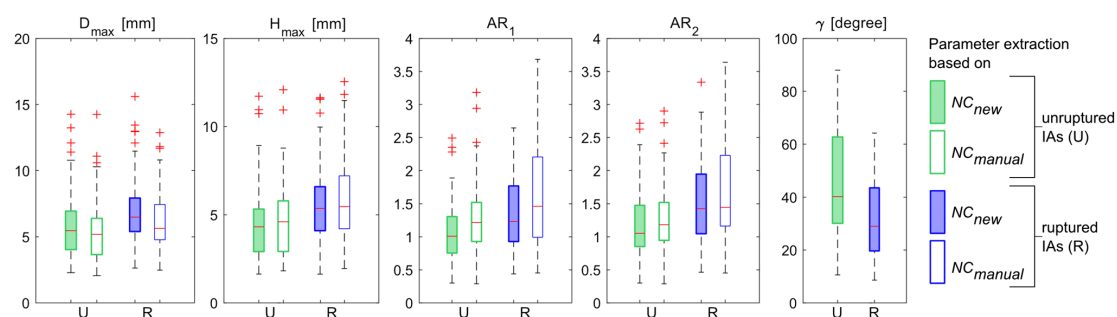


**Fig. 10** Box plots of the parameters  $D_{max}$ ,  $H_{max}$ ,  $AR_1$ ,  $AR_2$  and  $\gamma$  extracted based on the semiautomatic neck curve approach  $NC_{new}$  and the manually drawn neck curves  $NC_{manual}$ . Hence,  $\gamma$  is only available for  $NC_{new}$ . For each set of aneurysms (unruptured and ruptured), an individual box plot is provided

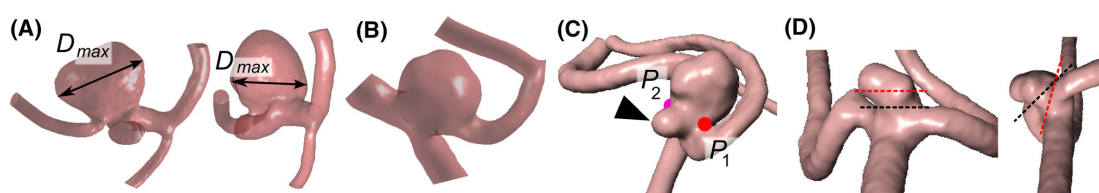


**Fig. 11** Drawbacks of various approaches and specific aneurysm cases. When extracting  $D_{max}$  in 2D, the view direction influences the result (a). Example of a bifurcation aneurysm (b). Example of an aneurysm with bulges (c). A shortest path starting from  $P_1$  may miss aneurysm

bulges with an arrowhead. The plane-based approximation of the ostium is error-prone for inclined aneurysms (d). It is not clear if the red or the black dashed cutting plane yields the better ostium plane

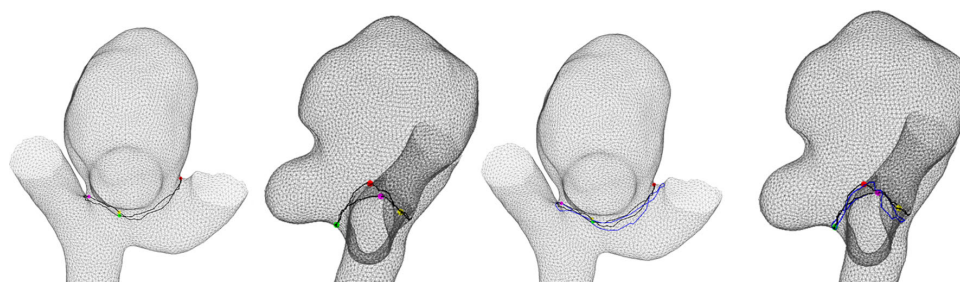


**Fig. 12** Result of our NC reconstruction algorithm for the case presented in Fig. 11c (left) including the manually drawn curve (right)

The statistical evaluation of morphological parameters reveals that  $D_{max}$ ,  $H_{max}$ ,  $AR_1$ ,  $AR_2$  and  $\gamma$  statistically significantly correlate with the aneurysm rupture status. This is especially remarkable, since we introduce  $\gamma$  as characteristic angle at the dome  $D$ . Although Dhar et al. [5] introduced angle-based parameters (*aneurysm inclination angle* and *vessel angle*), we do not rely on these parameters since they are only defined for sidewall IAs and depend on the direction from which the geometry is viewed. Furthermore, the viewing direction and thus the parameter extraction had to be manually carried out in their approach. We extracted  $\gamma$  for all 100 aneurysms (including sidewall and bifurcation IAs) independent on the viewing direction.

Comparing them with values reported in the literature yields the following results. Lauric et al. [6] pointed out the variations for AR in the literature, arising from different definitions of aneurysm height (orthogonal height, maximum height and “depth” height which is only defined inside the aneurysm sac) and aneurysm neck diameter (maximum, average or minimum). We obtain similar values for  $AR_1$ :  $1.35 \pm 0.56$  or 53 ruptured IAs and  $1.08 \pm 0.47$  for 42 unruptured IAs compared to their values:  $1.41 \pm 0.55$  for 60 ruptured and  $1.14 \pm 0.45$  for 74 unruptured IAs. Similar results are obtained for  $AR_2$ ; we obtain  $1.55 \pm 0.66$  for ruptured and  $1.22 \pm 0.53$  for unruptured IAs. Lauric et al. report  $1.62 \pm 0.74$  and  $1.27 \pm 0.51$ , respectively. The definition of

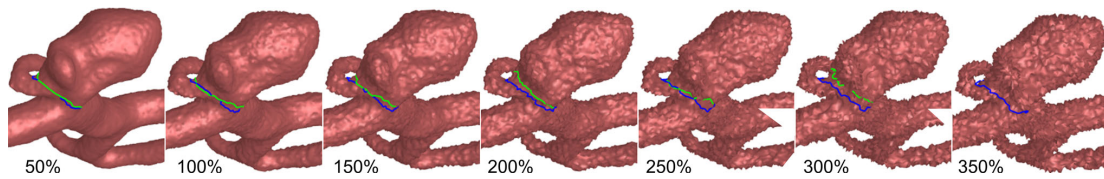


**Fig. 13** Extraction of the NC (green) for triangular meshes with random noise that displaces each vertex in direction of its normal. The manual NC (blue) is provided for comparison. The percentage describes the amount of maximum displacement w.r.t. the average edge length

the aspect ratio by Dhar et al. [5] matches  $AR_2$ . They reported a mean value of  $1.5 \pm 0.45$  for 25 ruptured and  $1.2 \pm 0.55$  for 20 unruptured aneurysms, which agrees very well with our results.

Lauric et al. [6] report  $D_{\max}$  mean values of  $9.05 \pm 4.00$  mm and  $H_{\max}$  mean values of  $7.41 \pm 3.55$  mm for 60 ruptured and  $D_{\max}$  mean values of  $6.9 \pm 2.78$  mm and  $H_{\max}$  mean values of  $5.36 \pm 2.37$  mm for 74 unruptured IAs. These trends are reflected by our results, where ruptured IAs exhibit larger mean values than unruptured ones, but we obtain slightly different values ( $D_{\max}^{\text{ruptured}} = 7.22 \pm 3.04$  mm,  $D_{\max}^{\text{unruptured}} = 6.13 \pm 2.74$  mm,  $H_{\max}^{\text{ruptured}} = 5.81 \pm 2.68$  mm,  $H_{\max}^{\text{unruptured}} = 4.64 \pm 2.37$  mm). In addition, mean values of  $6.76 \pm 2.03$  mm for 30 ruptured and  $4.6 \pm 2.85$  mm for 37 unruptured IAs were reported for a slightly different  $D_{\max}$  extraction in [26]. When comparing morphological measures, it must be noted that their predictive values regarding rupture risk also depend on the aneurysm location [10] and considerably variations exist regarding their definition [6]. We account for this problem by extracting different variations of the aspect ratio yielding  $AR_1$  and  $AR_2$  instead of a single parameter. Hence, future studies and clinical trials should provide information and standardized guidelines which method is preferable.

Due to the high correlations between the morphological parameters  $D_{\max}$ ,  $H_{\max}$ ,  $AR_1$ ,  $AR_2$  and  $\gamma$ , it may be not necessary to extract all of them. Future work should evaluate different classifiers based on different parameter sets w.r.t their discriminative power. Since extraction of  $\gamma$  does not require the complete NC but only  $D$ ,  $B_1$  and  $B_2$  (i.e., only Step 2 of our pipeline, depicted in Fig. 1b), a future classification approach could be speed up. Initial experiments identified  $\gamma$  and the  $EI$  as most important parameters based on our training dataset for a gradient-boosted tree classifier. Hence, a combination of parameters is superior to the usage of a single one. Future work can reveal which combination of the presented parameters yields best prediction results. Dhar et al. [5] also carried out multivariate logistic regression analysis stating that only two of their five parameters were identified as independently significant; the size ratio and the undulation index  $UI$ . Regarding the effect size of our approach, we achieved only a small effect [27] due to the large sample size.

We do not evaluate interaction effects yet. Although all significant parameters correlate with each other maybe interaction effects between nonsignificant parameters can be examined. This will be part of a subsequent analysis. In addition, a prospective study comprising untreated longitudinal IAs is of great interest, but these datasets are rare in clinical practice.

For the assessment of artifacts due to noise, we added artificial random noise to the triangle meshes inspired by [28]. An example for case 53 is provided in Fig. 13. Therefore, each vertex of the surface mesh was randomly displaced in direction of its surface normal. The maximum amount of the displacement for each step was determined by the percentage average edge length of the triangle mesh. With a noise level that randomly alters vertices up to 300% of the average edge length, the NC could still be successfully extracted. Only with a noise level of 350%, the identification of  $V_1$  and  $V_2$  was not possible anymore, see Fig. 13.

For the 100 aneurysms, no manual correction was required. The reproducibility of our method depends on the centerline,  $D_{\text{Start}}$  and parameters  $t$  and  $s$ . For centerline extraction, we employ an already well-established method [18].  $D_{\text{Start}}$  does not influence  $D$  in a mesh where  $D$  has the largest distance to the centerline. If there is noise present,  $D$  may be found at the local maximum. A post-processing step could further reduce this variability, by first separating the aneurysm from the parent vessel and then repeat the procedure but using the separated aneurysm for possible locations of  $D$  instead the neighbored surface vertices of  $D_{\text{Start}}$ . Parameters  $t$  and  $s$  do influence the result, but we provide default values such that the same NC is extracted.

A ground truth for neck curves is not available yet. Future work could include more manual drawn neck curves from more clinical experts; however, manual definition is a very time-consuming task. Furthermore, errors during manual drawing may occur as well especially for complex and irregularly shaped aneurysms.

Beside the precise morphological evaluation of the 3D aneurysm shape, an automatized ostium detection is highly beneficial for the quantification of hemodynamic flow simulations [29]. Particularly, since relevant blood flow parameters that are associated with rupture (e.g., normalized wall shear stress, shear concentration index, oscillatory shear

index [30]) need to be calculated with high accuracy, wrong aneurysm-vessel-separation or high user-dependency can lead to clear variations regarding the analysis.

## Conclusions

We presented a semiautomatic 3D NC reconstruction algorithm which yields reproducible results and was successfully applied to 100 IAs. The employed IA triangle surface meshes are based on segmented rotational angiography images. However, the approach is suitable for segmented CTA and MRA datasets as well. The NC reconstruction yields an anatomical shaped curve, i.e., the NC does not lie in a plane. It allows for automatic extraction of common morphological parameters as well as a newly introduced characteristic angle  $\gamma$  at the aneurysm's dome. Statistical evaluation yields statistical significant correlation of the morphological parameters  $D_{\max}$ ,  $H_{\max}$ ,  $AR_1$  and  $AR_2$  with rupture status which is in good agreement with the literature. Thus, the 3D NC reconstruction is well suited for further applications including the quantification of hemodynamic flow simulations. The newly introduced characteristic angle  $\gamma$  at the dome yields statistical significance as well and correlates with the other morphological parameters indicative for rupture status. Considering that  $\gamma$  can be extracted at a very early stage of our method relying on  $B_1$  and  $B_2$  but not on the complete NC, a benefit for future classifiers is expected.

**Acknowledgements** The work was funded by the Federal Ministry of Education and Research within the Forschungscampus *STIMULATE* under Grant No. "13GW0095A."

## Compliance with ethical standards

**Conflict of interest** The authors declare that they have no conflict of interest.

**Ethical approval** All procedures performed in studies involving human participants were in accordance with the ethical standards of the institutional and/or national research committee and with the 1964 Declaration of Helsinki and its later amendments or comparable ethical standards. For this type of study, formal consent is not required.

**Informed consent** Informed consent was obtained from all individual participants included in the study.

## References

- Meng H, Tutino VM, Xiang J, Siddiqui A (2014) High WSS or low WSS? complex interactions of hemodynamics with intracranial aneurysm initiation, growth, and rupture: toward a unifying hypothesis. *Am J Neuroradiol* 35(7):1254–1262
- Weir B, Amidei C, Kongable G, Findlay JM, Kassell NF, Kelly J, Dai L, Karrison TG (2003) The aspect ratio (dome/neck) of ruptured and unruptured aneurysms. *J Neurosurg* 99(3):447–451
- Backes D, Vergouwen MD, Velthuis BK, van der Schaaf IC, Bor ASE, Algra A, Rinkel GJ (2014) Difference in aneurysm characteristics between ruptured and unruptured aneurysms in patients with multiple intracranial aneurysms. *Stroke* 45(5):1299–1303
- Wong SC, Nawawi O, Ramli N, Kadir KAA (2012) Benefits of 3D rotational DSA compared with 2D DSA in the evaluation of intracranial aneurysm. *Acad Radiol* 19(6):701–707
- Dhar S, Tremmel M, Mocco J, Kim M, Yamamoto J, Siddiqui AH, Hopkins LN, Meng H (2008) Morphology parameters for intracranial aneurysm rupture risk assessment. *Neurosurgery* 63(2):185–196 (discussion 196–7)
- Lauric A, Baharoglu MI, Malek AM (2012) Ruptured status discrimination performance of aspect ratio, height/width, and bottleneck factor is highly dependent on aneurysm sizing methodology. *Neurosurgery* 71(1):38–45
- Lv N, Wang C, Karmonik C, Fang Y, Xu J, Yu Y, Cao W, Liu J, Huang Q (2016) Morphological and hemodynamic discriminators for rupture status in posterior communicating artery aneurysms. *PLoS ONE* 11(2):e0149906
- Miura Y, Ishida F, Umeda Y, Tanemura H, Suzuki H, Matsushima S, Shimosaka S, Taki W (2013) Low wall shear stress is independently associated with the rupture status of middle cerebral artery aneurysms. *Stroke* 44(2):519–521
- Raghavan ML, Ma B, Harbaugh RE (2005) Quantified aneurysm shape and rupture risk. *J Neurosurg* 102(2):355–362
- Varble N, Rajabzadeh-Oghaz H, Wang J, Siddiqui A, Meng H, Mowla A (2017) Differences in morphologic and hemodynamic characteristics for "PHASES-based" intracranial aneurysm locations. *Am J Neuroradiol* 38(11):2105–2110
- Xiang J, Natarajan SK, Tremmel M, Ma D, Mocco J, Hopkins LN, Siddiqui AH, Levy EI, Meng H (2011) Hemodynamic-morphologic discriminants for intracranial aneurysm rupture. *Stroke* 42(1):144–152
- Berg P, Saalfeld S, Voß S, Redel T, Preim B, Janiga G, Beuing O (2017) Does the DSA reconstruction kernel affect hemodynamic predictions in intracranial aneurysms? an analysis of geometry and blood flow variations. *J Neurointervent Surg*. <https://doi.org/10.1136/neurintsurg-2017-012996>
- Neugebauer M, Lawonn K, Beuing O, Berg P, Janiga G, Preim B (2013) AmniVis—a system for qualitative exploration of near-wall hemodynamics in cerebral aneurysms. *Comput Graph Forum* 32(3):251–260
- Janiga G, Berg P, Beuing O, Neugebauer M, Gasteiger R, Preim B, Rose G, Skalej M, Thévenin D (2013) Recommendations for accurate numerical blood flow simulations of stented intracranial aneurysms. *Biomed Eng* 58(3):303–314
- Saalfeld P, Luz M, Berg P, Preim B, Saalfeld S (2017) Guidelines for quantitative evaluation of medical visualizations on the example of 3D aneurysm surface comparisons. *Comput Graph Forum* 27(5):347
- Glaßer S, Berg P, Voß S, Serowy S, Janiga G, Preim B, Beuing O (2016) From imaging to hemodynamics—how reconstruction kernels influence the blood flow predictions in intracranial aneurysms. *Curr Dir Biomed Eng* 2(1):163
- Glaßer S, Berg P, Neugebauer M, Preim B (2015) Reconstruction of 3D surface meshes for blood flow simulations of intracranial aneurysms. In: *Proceeding of the computer- and robot-assisted surgery (CURAC)*, pp 163–168
- Antiga L, Piccinelli M, Botti L, Ene-Iordache B, Remuzzi A, Steinman DA (2008) An image-based modeling framework for patient-specific computational hemodynamics. *Med Biol Eng Compu* 46(11):1097–1112

19. Neugebauer M, Diehl V, Skalej M, Preim B (2010) Geometric reconstruction of the ostium of cerebral aneurysms. In: *Proceeding of the vision modeling visualization (VMV)*, pp 307–314
20. Dijkstra EW (1959) A note on two problems in connexion with graphs. *Numer Math* 1(1):269–271
21. Cárdenes R, Larrabide I, San Román L, Frangi AF (2013) Performance assessment of isolation methods for geometrical cerebral aneurysm analysis. *Med Biol Eng Compu* 51(3):343–352
22. Ma B, Harbaugh RE, Raghavan ML (2004) Three-dimensional geometrical characterization of cerebral aneurysms. *Ann Biomed Eng* 32(2):264–273
23. Karmonik C, Arat A, Benndorf G, Akpek S, Klucznik R, Mawad ME, Strother CM (2004) A technique for improved quantitative characterization of intracranial aneurysms. *Am J Neuroradiol* 25(7):1158–1161
24. Jerman T, Pernuš F, Likar B, Špiclin Ž (2015) Computer-aided detection and quantification of intracranial aneurysms. In: *Proceeding of the medical image computing and computer-assisted intervention (MICCAI). Lecture notes in computer science*, vol 9350, pp 3–10
25. Cárdenes R, Pozo JM, Bogunovic H, Larrabide I, Frangi AF (2011) Automatic aneurysm neck detection using surface Voronoi diagrams. *IEEE Trans Med Imaging* 30(10):1863–1876
26. Hoh BL, Siström CL, Firmont CS, Fautheree GL, Velat GJ, Whiting JH, Reavey-Cantwell JF, Lewis SB (2007) Bottleneck factor and height-width ratio: association with ruptured aneurysms in patients with multiple cerebral aneurysms. *Neurosurgery* 61(4):716–723
27. Cohen J (1988) *Statistical power analysis for the behavioral sciences*. Erlbaum, New York
28. Neugebauer M, Lawonn K, Beuing O, Preim B (2013) Automatic generation of anatomic characteristics from cerebral aneurysm surface models. *Int J Comput Assist Radiol Surg (JCARS)* 8(2):279–289
29. Berg P, Beuing O (2018) Multiple intracranial aneurysms: a direct hemodynamic comparison between ruptured and unruptured vessel malformations. *Int J Comput Assist Radiol Surg (JCARS)* 13(1):83–93
30. Cebal JR, Mut F, Weir J, Putman C (2011) Quantitative characterization of the hemodynamic environment in ruptured and unruptured brain aneurysms. *Am J Neuroradiol (AJNR)* 32(1):145–151





# Flow-splitting-based computation of outlet boundary conditions for improved cerebrovascular simulation in multiple intracranial aneurysms

Sylvia Saalfeld<sup>1,4</sup> · Samuel Voß<sup>2,4</sup> · Oliver Beuing<sup>3,4</sup> · Bernhard Preim<sup>1,4</sup> · Philipp Berg<sup>2,4</sup>

Received: 11 January 2019 / Accepted: 18 July 2019  
© CARS 2019

## Abstract

**Purpose** Image-based hemodynamic simulations have great potential for precise blood flow predictions in intracranial aneurysms. Due to model assumptions and simplifications with respect to boundary conditions, clinical acceptance remains limited.

**Methods** Within this study, we analyzed the influence of outflow-splitting approaches on multiple aneurysm studies and present a new outflow-splitting approach that takes the precise morphological vessel cross sections into account. We provide a detailed comparison of five outflow strategies considering eight intracranial aneurysms: zero-pressure configuration (1), a flow splitting inspired by Murray's law with a square (2) and a cubic (3) vessel diameter, a flow splitting incorporating vessel bifurcations based on circular vessel cross sections (4) and our novel flow splitting including vessel bifurcations and anatomical vessel cross sections (5). Other boundary conditions remain constant. For each simulation and each aneurysm, we conducted an evaluation based on common hemodynamic parameters, e.g., normalized wall shear stress and inflow concentration index.

**Results** The comparison of five outflow strategies for image-based simulations shows a large variability regarding the parameters of interest. Qualitatively, our strategy based on anatomical cross sections yields a more uniform flow rate distribution with increased aneurysm inflow rates. The commonly used zero-pressure approach shows the largest variations, especially for more distal aneurysms. A rank ordering of multiple aneurysms in one patient might still be possible, since the ordering appeared to be independent of the outflow strategy.

**Conclusions** The results reveal that outlet boundary conditions have a crucial impact on image-based blood flow simulations, especially for multiple aneurysm studies. We could confirm the advantages of the more complex outflow-splitting model (4) including an incremental improvement (5) compared to strategies (1), (2) and (3) for this application scenario. Furthermore, we discourage from using zero-pressure configurations that lack a physiological basis.

**Keywords** Outlet boundary condition · Computational fluid dynamics · Hemodynamic simulation · Intracranial aneurysms

## Introduction

It is estimated that intracranial aneurysms (IAs) occur in approximately 5–10% of the western population [14].

Rupture of IAs and a subsequent subarachnoid hemorrhage can lead to fatal consequences. Since treatment may cause severe complications as well, a reliable rupture risk assessment is required. Within the last decade, computer-assisted

✉ Sylvia Saalfeld  
sylvia.saalfeld@ovgu.de

Samuel Voß  
samuel.voss@ovgu.de

Oliver Beuing  
oliver.beuing@med.ovgu.de

Bernhard Preim  
bernhard.preim@ovgu.de

Philipp Berg  
philipp.berg@ovgu.de

<sup>1</sup> Department of Simulation and Graphics, Otto-von-Guericke University Magdeburg, Universitätsplatz 2, 39106 Magdeburg, Germany

<sup>2</sup> Department of Fluid Dynamics and Technical Flows, Otto-von-Guericke University Magdeburg, Universitätsplatz 2, 39106 Magdeburg, Germany

<sup>3</sup> University Hospital Magdeburg, Magdeburg, Germany

<sup>4</sup> Research Campus STIMULATE, Magdeburg, Germany

studies for IA characterization increased [10] and hemodynamic parameters such as wall shear stresses (WSS) or oscillatory shear can be associated with pathological effects [22]. However, the acceptance of numerical methods among neuroradiologists remains partly limited.

Reasons for this mistrust mainly result from the absence of patient-specific flow conditions. To analyze and evaluate the effect of such parameters, different studies focused on specialized questions: First, Valen-Sendstad et al. [19] investigated the effect of scaled inflow waveforms. They found that a square law with respect to the inlet diameter leads to most physiological flow patterns. Concerning the inlet condition type (plug flow, parabolic, Womersley), similar flow predictions were observed in the majority of cases for an international aneurysm rupture challenge [4] including 26 simulation groups.

Second, hemodynamic simulations mostly consider rigid vessel walls due to missing information about their thickness and stiffness. Sanchez et al. [18] examined the effect of aneurysmal pulsatility based on different wall stiffness values which yielded to elasticity and volume variations. Voß et al. [20] reported variations of the simulation outcome based on constant and variable vessel wall thicknesses of a patient-specific IA acquired using  $\mu$ CT.

Finally, outlet boundary conditions (BCs) were addressed by Chnafa et al. [8,9]. They concluded that the modeling of energy loss at vascular bifurcations can improve the simulation accuracy. Furthermore, it was demonstrated that cerebrovascular simulations strongly depend on the outflow-splitting strategy and hence require careful treatment.

The presented study also focuses on the specific choice of outlet BCs. Previous work often considered only a small vessel section proximal and distal to the aneurysm, where the complete blood flow was directed through one to three outlet cross sections. Here, an appropriate flow weighting or splitting was not required. However, with increasing computational resources, larger domains of the vasculature, as

depicted in Fig. 1, are taken into account enabling more precise analyses. To allow for an improved understanding of the effect of outlet BCs on subsequent hemodynamic simulations, four common approaches are compared with our advanced splitting technique.

## Methods

The combined steps to conduct the hemodynamic simulations are presented in Fig. 2 illustrating the structure of the subsequent sections.

### Medical imaging and vessel segmentation

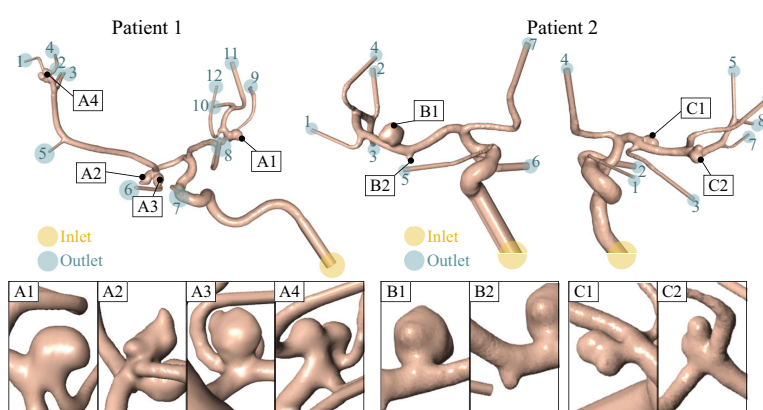
We provide examples of highly complex patient data sets acquired during clinical routine; recall Fig. 1. Aneurysms A1–A4 stem from a 65-year-old female patient and aneurysms B1, B2, C1 and C2 from a 56-year-old female patient. The second case was presented and analyzed in more detail in the multiple aneurysms anatomy challenge (MATCH) [6].

Both patients underwent digital subtraction angiography (DSA) with an Artis Q Angiography Suite with a spatial resolution of  $0.28 \times 0.28 \times 0.28$  mm. From the DSA datasets, the vascular trees harboring the aneurysms were segmented with thresholding in MeVisLab 2.8 [17] (MeVis Medical Solutions AG, Bremen, Germany). For the subsequent simulations, vessel outlets were cut and extruded about five times of the vessel diameter to avoid reverse flows and possible blending artifacts were removed [12].

### Extraction of vessel diameters and cross-sectional areas

Afterward, the vessel's centerline was extracted with the vascular modeling toolkit (VMTK) [2]; see Fig. 2c. Hence, the

**Fig. 1** Illustration of complex vascular domains represented by 3D surface models with eight intracranial aneurysms from two patients. The first case exhibits four aneurysms (A1–A4) at a single vessel tree with twelve vessel outlets. The second case also exhibits four aneurysms (B1 and B2; and C1 and C2) in the anterior circulation with seven and eight vessel outlets, respectively



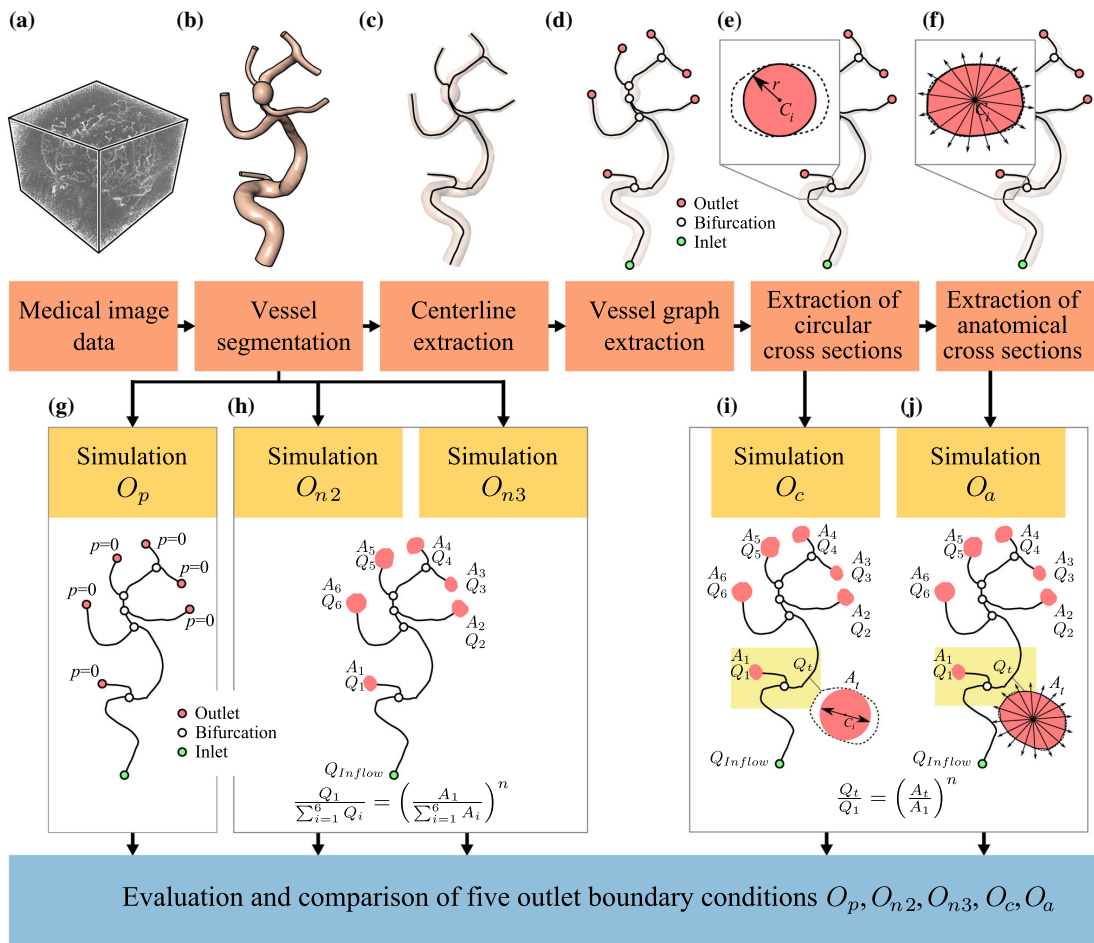


**Fig. 2** Illustration of our workflow for outlet BC comparison for an exemplary dataset: from the medical image data (a), the vessel tree is segmented (b) and its centerline (c) is converted into a vessel graph (d). Based on maximum inscribed spheres, the circular vessel cross sections are stored (e). Anatomical vessel cross sections based on polygonal cut

areas are extracted as well (f). Simulations with outlet BCs  $O$  are carried out: zero-pressure configuration (g), flow splitting inspired by Murray’s law with power coefficients  $n = 2$  and  $n = 3$  (h) and flow divisions based on circular cross sections (i) and anatomical cross sections (j). An evaluation is conducted for all outlet BCs

user manually selects the inlet and all outlets. During this step, vessel diameters for each centerline point were provided based on maximum inscribed spheres. From the vessel’s centerline, a graph representation was extracted. Iteratively, we analyzed each centerline segment from each outlet to the inlet and split it when different segments were intersecting. Only unique segments were kept. Next, a vessel graph was gathered from the segments which can be represented as tree structure; see Fig. 2d.

For the extraction of circular cross sections for each centerline segment, i.e., edge in the vessel graph, we employed the vessel diameters provided by VMTK. However, they under-

estimate the vessels cross-sectional area in case of elliptic shapes; see Fig. 2e. Therefore, we also extract the anatomical cross sections. We cast rays for each centerline point  $C_i$  perpendicular to the centerline and determined their intersections with the surface mesh. These intersection points form the polygonal cut surface at  $C_i$ , and the surface area is stored for subsequent steps; see an illustration in Fig. 2f.

**Outlet boundary conditions**

In order to evaluate their impact on hemodynamic parameters, we considered the following outlet BCs  $O$ :

- (1) zero-pressure outflow condition:  $O_p$ ,
- (2) a flow weighting inspired by Murray's law but with power exponent  $n = 2$ :  $O_{n2}$ ,
- (3) and with the power of  $n = 3$ :  $O_{n3}$ ,
- (4) a flow splitting including vessel bifurcations based on circular vessel cross sections  $O_c$ , and
- (5) a flow splitting including vessel bifurcations based on anatomical vessel cross sections  $O_a$ .

**Simulation with BC  $O_p$**  The most commonly used zero-pressure configuration assigns a constant zero pressure at all outlets. It is numerically simple but lacks a physiological basis.

**Simulation with BC  $O_{n2}$  and  $O_{n3}$ .** Murray's law [15] is based on a more general principle that a vessel's flow rate  $Q$  is proportional to the vessel's diameter  $D$  to the power of  $n$ . Subsequently, the flow rate  $Q_i$  of the  $i$ th outlet with diameter  $D_i$  can be described as:

$$\frac{Q_i}{\sum Q_i} = \left( \frac{D_i}{\sum D_i} \right)^n. \quad (1)$$

Murray's law refers to  $n = 3$ , but as commonly practiced in hemodynamic simulations, outlet flow splitting is carried out with  $n = 2$  as well, yielding outlet BCs  $O_{n2}$  and  $O_{n3}$ ; see also Fig. 2h. Thus, these BCs strongly depend on the vessel model's truncation.

**Simulation with BC  $O_c$ .** To compensate these drawbacks, Chnafa et al. [8] adapt this power law relationship locally to each vessel bifurcation; see Fig. 2i. For example, a bifurcation with two daughter branches with diameters  $D_1$  and  $D_2$  yields a flow division  $Q_1/Q_2$ :

$$\frac{Q_1}{Q_2} = \left( \frac{D_1}{D_2} \right)^n. \quad (2)$$

The outflow division is propagated for each bifurcation until the segmentation model outlets are reached yielding the proportional inflow for each outlet. We set  $n = 2$  as proposed by Chnafa et al. [8]. The vessel diameters are extracted based on the maximum inscribed spheres, and thus, non-circular vessel cross sections are underestimated; recall Fig. 2e.

**Simulation with BC  $O_a$ .** We extend the previous approach by including the anatomical vessel cross sections instead of a radius based on minimum inscribed spheres. We extract the polygonal surface cut area for each point  $C_i$  on the centerline. Adapting Eq. 2 with  $n = 2$ , an  $A \propto D^2$  yields:

$$\frac{Q_1}{Q_2} = \frac{A_1}{A_2}, \quad (3)$$

where  $Q_1/Q_2$  describes the flow division at a bifurcation with two daughter branches with cross-sectional areas  $A_1$  and  $A_2$ .

For both strategies  $O_a$  and  $O_c$ , the vessel diameter and the vessel area along a vessel segment that is not an outlet are modeled based on the Hagen–Poiseuille equation to account for pressure losses according to the vessel segment's length. Hence, the pressure loss depends on the power of 4 or the power of 2 for diameter or cross-sectional area, respectively.

## Simulation settings

To evaluate the variability due to different outlet BCs, image-based blood flow simulations were carried out using STAR-CCM+ 11.06 (Siemens Product Lifecycle Management Software Inc., Plano, TX, USA 75024). Firstly, the segmented datasets were spatially discretized using polyhedral and prismatic elements with a base size of  $\Delta x = 0.1$  mm and four prism layers resulting in a total number of elements ranging from 2.7 to 2.9 million for the three vessel trees. Secondly, a time-dependent waveform based on flow measurements of a healthy volunteer using 7T phase-contrast magnetic resonance imaging was applied at the inlet cross Sect. [5]. Furthermore, all vessel walls were assumed to be rigid due to the lack of information with respect to the wall thickness and wall properties. The outlet boundary conditions were defined using flow split ratios based on the model predictions described in Sect. 2.3. Blood considered as an incompressible ( $\rho = 1055$  kg/m<sup>3</sup>), Newtonian ( $\eta = 4$  mPa s) fluid and laminar flow was assumed.

The outflow boundary conditions were imposed by defining the individual splitting fraction at each outlet section depending on the strategy, i.e., outflow BCs were predicted and equally to the actual fluxes.

In total, three cardiac cycles with a time step size of  $\Delta t = 0.001$  s were considered for each simulation. The described settings remained constant except for the outlet BCs described above.

For the analysis of hemodynamic parameters, only the last cardiac cycle was considered. Here, normalized time-averaged wall shear stress (nAWSS), inflow concentration index (ICI) and neck inflow rate are evaluated, respectively [7].

## Results

The results of the hemodynamic simulations for the eight aneurysms are illustrated in Figs. 3 and 4. The outflow rates for each vessel tree are provided in Table 1. In addition, the accumulated flow split values are provided in Table 2 to analyze the flow rate proximal to the aneurysms.

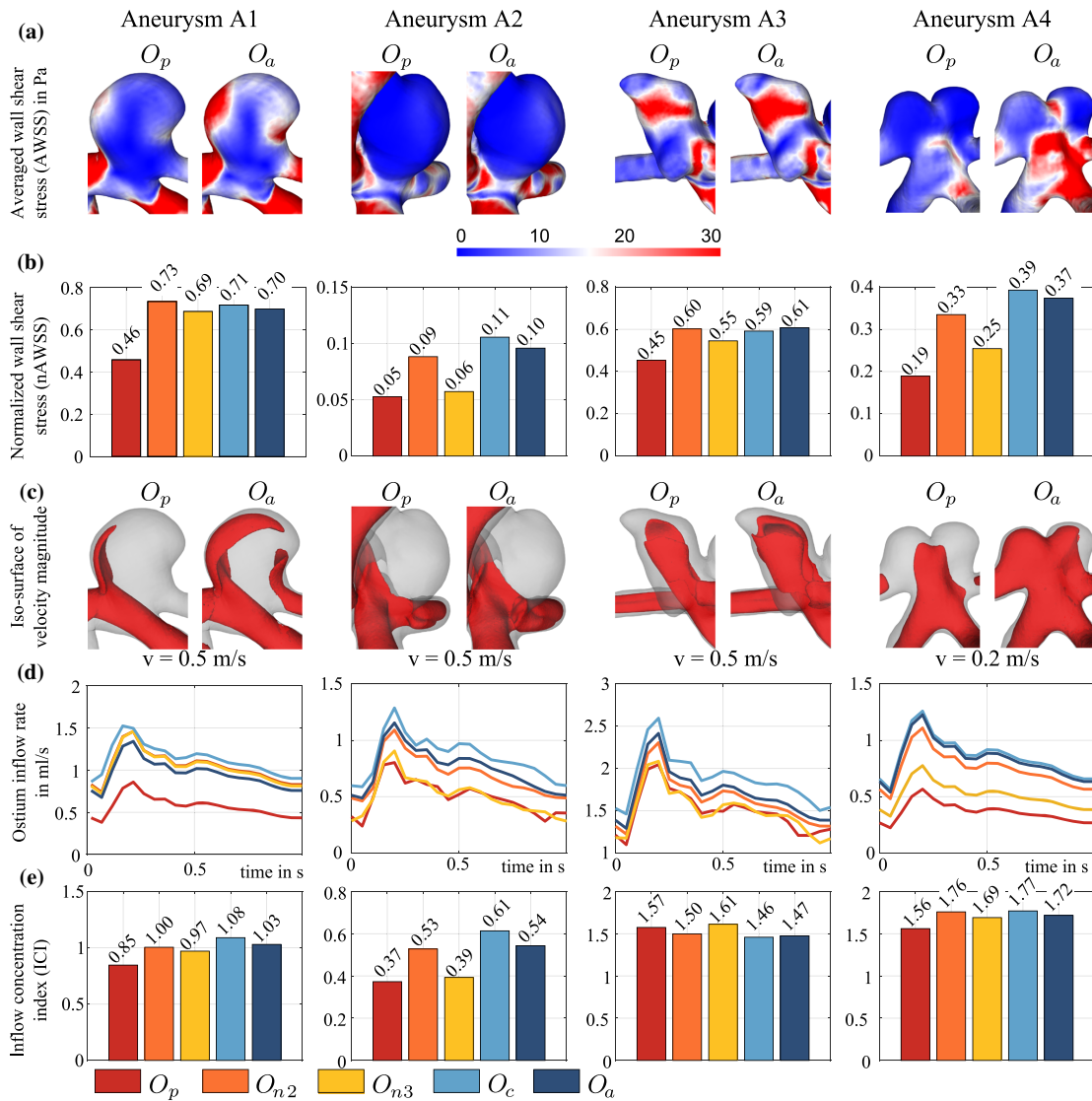


**Fig. 3** Comparative presentation of simulation results with outlet BCs  $O_p$ ,  $O_{n2}$ ,  $O_{n3}$ ,  $O_c$  and  $O_a$  for aneurysms A1-A4. In **a**, color-coded AWSS representations for  $O_p$  and  $O_a$ , which often exhibit the largest variations, are shown. In **b**, the nAWSS is presented (normalization is carried out with AWSS of the parent artery). In **c**, iso-surfaces highlight

variations of resulting blood flow velocity. In **d**, the ostium inflow rate for each aneurysm is depicted over time. In **e**, the ICI values are illustrated. For nAWSS and ICI, local scales are used to highlight differences

Strong variations are present, e.g., when comparing nAWSS and iso-surfaces of the velocity magnitude; see Figs. 3a, c and 4a, c. A qualitative evaluation indicates that the most commonly used  $O_p$  differs most from all other strategies and large variations are visible, especially for the aneurysms A1, A4, B1, B2, C1 and C2. The aneurysms A2 and A3 do not

exhibit these variations regarding AWSS and velocity magnitude, but they are also more proximal than the remaining ones, i.e., there are only two vessel bifurcations proximal to A2 and A3 but at least three proximal to the other aneurysms. Furthermore, for aneurysm A2, fewer variations are perceivable since this aneurysm seems to be not affected by irregular

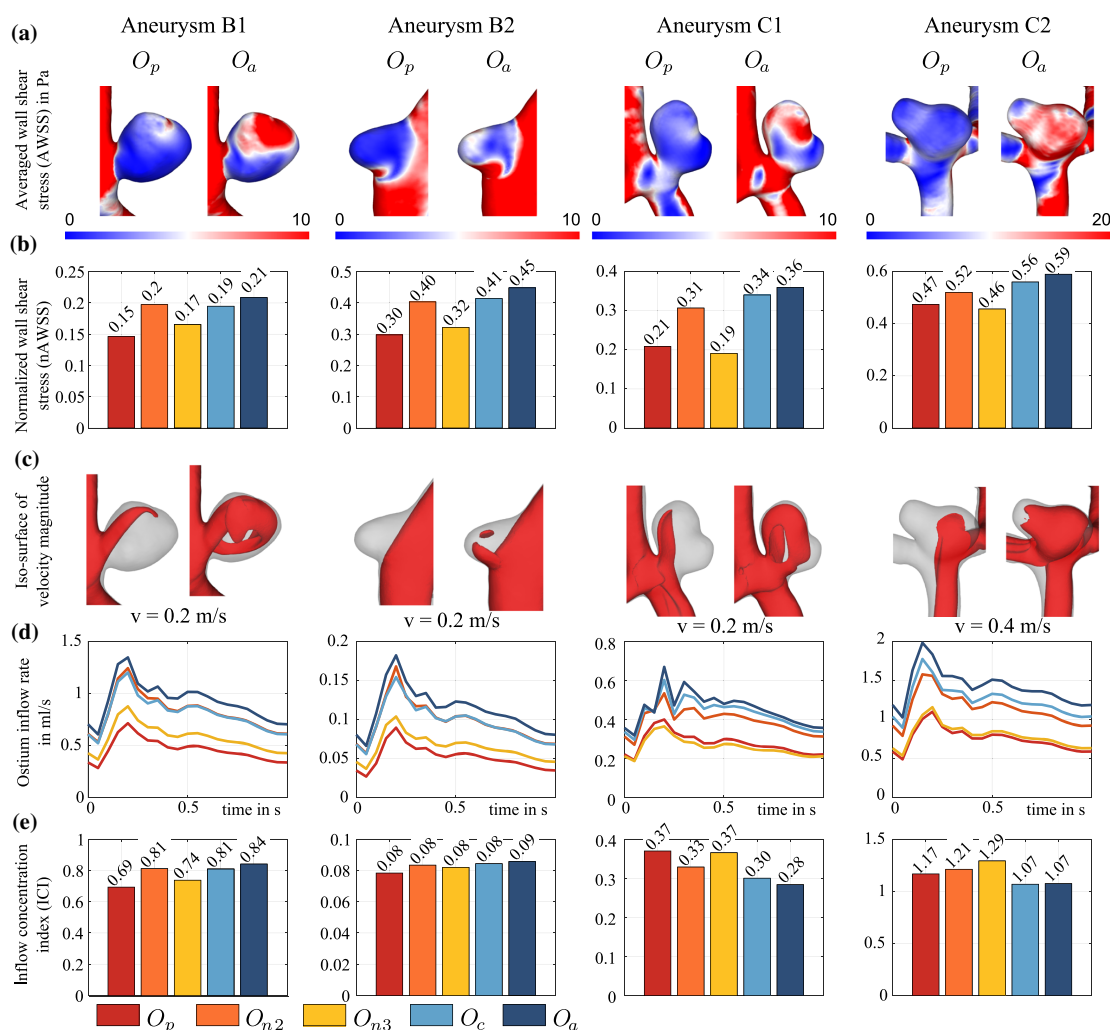


**Fig. 4** Comparative presentation of simulation results with outlet BCs  $O_p$ ,  $O_{n2}$ ,  $O_{n3}$ ,  $O_c$  and  $O_a$  for aneurysms B1, B2 and C1 and C2. In **a**, color-coded AWSS representations for  $O_p$  and  $O_a$ , which often exhibit the largest variations, are shown. In **b**, the nAWSS is presented. (Normalization is carried out with AWSS of the parent artery.) In **c**,

iso-surfaces highlight variations of resulting blood flow velocity. In **d**, the ostium inflow rate for each aneurysm is depicted over time. In **e**, the ICI values are illustrated. For nAWSS and ICI, local scales are used to highlight differences

or complex flow. Based on the qualitative inspection of the presented results in Figs. 3b, e and 4b, e more advanced approaches such as  $O_c$  and  $O_a$  are in better agreement.

When comparing the inflow rates in Figs. 3d and 4d,  $O_c$  and  $O_a$  yield the largest inflow rates and  $O_p$  the lowest. The finding for  $O_p$  is also reflected by the lowest percentage values for the accumulated flow split proximal to the aneurysms in Table 2.

Based on the results provided in Table 1, a pairwise comparison of outlet flow rates with the root-mean-square error

(RMSE) identifies  $O_p$  as outlet strategy that differs most from the remaining strategies (sum of RMSE for  $O_p$  and the remaining strategies yields 1.55; for  $O_{n2}$  1.05; for  $O_{n3}$  1.32; for  $O_c$  1.19; and for  $O_a$  1.28).

Although clear quantitative differences among the chosen outflow strategies occur, one can notice that the rank ordering appears to be independent of the applied method. Exemplarily, aneurysm A1 always possesses the largest normalized AWSS, while all simulation results yield the lowest ICI values for aneurysm A2.

**Table 1** Final outflow rates in mL/s for all aneurysms and their vessel trees

Vessel tree	Outlet no.	Outlet flow rates				
		$O_p$	$O_{n2}$	$O_{n3}$	$O_c$	$O_a$
Patient 1	1	0.1234	0.2917	0.1936	0.3540	0.3666
	2	0.3339	0.4071	0.3185	0.3764	0.5125
	3	0.2880	0.4249	0.3387	0.3206	0.4057
	4	0.2443	0.4077	0.3167	0.4862	0.3893
	5	0.4169	0.3727	0.2790	0.4590	0.3675
	6	1.0034	0.8410	0.9409	1.0936	0.8523
	7	1.5862	0.7112	0.7329	0.9771	0.7509
	8	1.3927	1.1215	1.4479	1.5412	1.1720
	9	0.2715	0.5918	0.5563	0.2879	0.5652
	10	0.5843	0.5807	0.5398	0.3278	0.5545
	11	0.6488	0.9572	1.1445	0.4753	0.7754
	12	0.2336	0.3314	0.2328	0.3399	0.3253
Patient 2 right	1	0.3258	0.3858	0.2186	0.2968	0.2605
	2	2.6497	2.0980	2.7657	1.9739	1.6874
	3	0.5576	0.6531	0.4811	0.6458	0.6582
	4	2.0416	1.7467	2.1017	1.5488	1.5254
	5	0.4010	0.4767	0.3006	0.7339	0.7709
	6	0.4473	0.7446	0.5861	0.6620	0.7490
	7	0.1719	0.3826	0.2160	0.3808	0.4843
	8	0.5266	0.5636	0.3863	0.8067	0.9113
Patient 2 left	1	0.2733	0.4566	0.2666	0.4841	0.5353
	2	0.8637	1.0812	0.9693	1.0669	1.2054
	3	0.4451	0.7568	0.5684	0.6597	0.8476
	4	0.2090	0.4831	0.2898	0.4840	0.4469
	5	0.2557	0.5871	0.3884	0.4426	0.5581
	6	4.0316	2.5852	3.5750	2.3783	2.1232
	7	1.0421	1.1145	1.0139	1.5490	1.3455

**Table 2** Accumulated flow split proximal to aneurysms' parent vessels for all eight aneurysms

Vessel tree	Aneurysm	Accumulated flow split					$\frac{(\max - \min)}{\min}$
		$O_p$	$O_{n2}$	$O_{n3}$	$O_c$	$O_a$	
Patient 1	A1	0.242	0.356	0.358	0.357	0.323	47.934
	A2	0.337	0.396	0.346	0.396	0.417	23.739
	A3	0.337	0.396	0.346	0.396	0.417	23.739
	A4	0.052	0.098	0.072	0.098	0.106	103.846
Patient 2 right	B1	0.252	0.394	0.297	0.383	0.431	71.032
	B2	0.252	0.394	0.297	0.383	0.431	71.032
Patient 2 left	C1	0.296	0.401	0.280	0.460	0.508	81.429
	C2	0.217	0.308	0.212	0.368	0.415	95.755

A value of 0.242 indicates that 24.2% of the inflow arrives in the parent vessel of the a given aneurysm

**Discussion**

With increasing computational resources, hemodynamic simulations become more and more realistic and can be applied to improve the rupture risk assessment or treatment planning of IAs. However, due to missing information

with respect to patient-individual flow that could be used as boundary condition for the computations, the integration into clinical practice is limited.

One important aspect regarding the quality of blood flow simulations is the choice of an appropriate segmentation approach. Recently, intensive comparisons among

existing strategies were carried out in the frame of an international challenge [6,13,21]. It turned out that state-of-the-art segmentation methods can lead to inaccurate representations of the real aneurysm anatomy and hence to false blood flow predictions. Furthermore, the lack of a ground truth still leaves open questions, and hence, further efforts toward improved segmentation assessment are required.

Besides the generation of reliable vascular models, the selection of an appropriate outlet BC becomes more and more crucial for the outcome of the simulation. Since early studies considered only small vessel sections proximal and distal to the aneurysm with mostly two similar outlets, the selection of a realistic outflow splitting had minor impact. However, due to the consideration of larger vascular domains containing multiple aneurysms and outlet cross sections, its importance increases with respect to the precise calculation of relevant hemodynamic parameters. This finding is supported by the values listed in Table 2. Hence, strongest variations occur for aneurysm A4 where the corresponding location at the vessel tree is distal to four vessel bifurcations. In contrast, aneurysms A2 and A3 exhibit the lowest variations but are located distal to only two vessel bifurcations. Hence, the influence of the outlet BC strategy is smaller.

This study has several limitations. Firstly, only eight aneurysms were compared in three datasets and the findings cannot be generalized at this stage. However, the complex cases with the presence of multiple outlet cross sections highlight the occurring effects due to outflow variations. Secondly, a ground truth, which serves as a reference, is missing, since precise intracranial flow measurements were not possible in the considered patients. In this regard, *in vivo* measurement techniques based on phase-contrast MRI are desirable in the future, which can be used to improve the knowledge of the individual flow splitting [1,16]. Hence, future work contains the application of our approach to further patient-specific cases. Additionally, *in vivo* as well as *in vitro* validation experiments based on 4D phase-contrast MRI measurements are ongoing work to build up a reference database.

Another issue is presented by bifurcation losses, which were successfully included by Chnafa et al. [9] for their reduced-order modeling of cerebrovascular flow distribution, i.e., their reduced-order representation of the vascular network. Hence, their work accounted for bifurcation resistances by including the underlying vessel geometry w.r.t. bifurcation angles based on the decomposing of bifurcating vessels developed by Antiga and Steinman [3]. Thus, the pressure drop was not only extracted based on the hydraulic resistance, i.e., based on the length and cross sections of the vessel parts, but on the bifurcation resistance as well. Since a very good agreement is reported between the reduced-

order modeling and the CFD with flow splitting based on the hydraulic resistance [9], we can assume that the outlet BCs are sufficient without integration of bifurcation losses. Nevertheless, the results of our study based on outlet BC strategy  $O_a$  present an (albeit minor) improvement of the outlet BC  $O_c$  strategy. Furthermore, we presented the influence of flow splitting for multiple aneurysm cases and large vascular domains. Finally, we further confirm the strong need for alternative flow splitting methods as presented by Chnafa et al. [8] and strengthen their claim to omit the zero-pressure strategy.

Finally, the evaluation revealed a positive finding regarding multiple aneurysm patients. Our analysis comprised three vessel trees with multiple aneurysms. It was observed that the qualitative assessment of hemodynamic parameters appears to be independent of the outflow strategy. Specifically, a rank ordering of multiple aneurysms in one patient might still be possible, even if quantitative inaccuracies can occur. Hence, if physicians are rather interested in a relative information, e.g., which aneurysm is the most endangered from a hemodynamical point of view, the type of outflow splitting might have secondary importance. However, in case a quantitative assessment of the individual blood flow behavior is desired, e.g., to apply advanced rupture risk models as presented by Detmer et al. [11], a careful selection of an appropriate splitting approach is suggested.

## Conclusion and outlook

In this work, we presented a comparison of different flow splitting strategies and highlight the impact of outlet BCs on the subsequent simulation results for complex multiple aneurysm studies. Our evaluation reveals large differences of the commonly used zero-pressure outlet BC and minor differences for complex strategies based on circular or anatomical vessel cross sections. Thus, we further discourage the employment of this strategy. Particularly, when aneurysm-specific rupture risk assessment is desired, such numerical variations might lead to wrong conclusions. Hence, we motivate the use of advanced flow splitting approaches based on Chnafa et al. [8], which is already available within the VMTK toolkit [2]. Our methodology extends this approach by incorporating anatomical cross sections. Since rank ordering of multiple aneurysms in the same patient appears to be independent of the chosen outflow strategy, qualitative results can be beneficial for clinicians to decide, which aneurysm requires treatment first.

**Acknowledgements** This work is partly funded by the Federal Ministry of Education and Research within the Forschungscampus *STIMULATE* (13GW0095A, 13GW0095B) and the German Research Foundation (SA 3461/2-1, BE 6230/2-1).

### Compliance with ethical standards

**Ethic approval** All procedures performed in studies involving human participants were in accordance with the ethical standards of the institutional and/or national research committee and with the 1964 Helsinki Declaration and its later amendments or comparable ethical standards. For this type of study, formal consent is not required.

**Conflict of interest** The authors Sylvia Saalfeld, Samuel Voß, Oliver Beuing, Bernhard Preim and Philipp Berg declare that they have no conflict of interest.

**Informed consent** Informed consent was obtained from all individual participants included in the study.

### References

- Adib MAHM, Ii S, Watanabe Y, Wada S (2017) Minimizing the blood velocity differences between phase-contrast magnetic resonance imaging and computational fluid dynamics simulation in cerebral arteries and aneurysms. *Med Biol Eng Comput* 55(9):1605–1619
- Antiga L, Piccinelli M, Botti L, Ene-Iordache B, Remuzzi A, Steinman DA (2008) An image-based modeling framework for patient-specific computational hemodynamics. *Med Biol Eng Comput* 46(11):1097
- Antiga L, Steinman DA (2004) Robust and objective decomposition and mapping of bifurcating vessels. *IEEE Trans Med Imaging* 23(6):704–713
- Berg P, Roloff C, Beuing O, Voss S, Sugiyama S, Aristokleous N, Anayiotos AS, Ashton N, Revell A, Bressloff NW, Brown AG, Chung BJ, Cebal JR, Copelli G, Fu W, Qiao A, Geers AJ, Hodis S, Dragomir-Daescu D, Nordahl E, Suzen YB, Khan MO, Valen-Sendstad K, Kono K, Menon PG, Albal PG, Mierka O, Münster R, Morales HG, Bonnefous O, Osman J, Goubergrits L, Pallares J, Cito S, Passalacqua A, Piskin S, Pekkan K, Ramalho S, Marques N, Sanchi S, Schumacher Kristopher R, Sturgeon J, vSvihlová H, Hron J, Usera G, Mendina M, Xiang J, Meng H, Steinman DA, Janiga G (2015) The computational fluid dynamics rupture challenge 2013—phase II: variability of hemodynamic simulations in two intracranial aneurysms. *J Biomech Eng* 137(12):121008/1–13
- Berg P, Stucht D, Janiga G, Beuing O, Speck O, Thévenin D (2014) Cerebral blood flow in a healthy circle of willis and two intracranial aneurysms: computational fluid dynamics versus four-dimensional phase-contrast magnetic resonance imaging. *J Biomech Eng* 136(4):041003
- Berg P, Voß S, Saalfeld S, Janiga G, Bergersen A, Valen-Sendstad K, Bruening J, Goubergrits L, Spuler A, Cancelliere NM, Steinman DA, Pereira VM, Chiu TL, Tsang AC, Chung BJ, Cebal JR, Cito S, Pallares J, Copelli G, Csippa B, Paal G, Fujimura S, Takao H, Hodis S, Hille G, Karmonik C, Elias S, Kellermann K, Khan MO, Marsden AL, Morales HG, Piskin S, Finol EA, Pravdivtseva M, Rajabzadeh-Oghaz H, Paliwal N, Meng H, Seshadhri S, Howard M, Shojima M, Sugiyama S, Niizuma K, Sindeev S, Frolov S, Wagner T, Brawanski A, Qian Y, Wu Y, Carlson K, Dragomir-Daescu D, Beuing DO (2018) Multiple aneurysms anatomy challenge 2018 (MATCH): phase I: segmentation. *Cardiovasc Eng Technol* 9(4):565–581
- Cebal JR, Mut F, Weir J, Putman C (2011) Quantitative characterization of the hemodynamic environment in ruptured and unruptured brain aneurysms. *Am J Neuroradiol* 32(1):145–151
- Chnafa C, Brina O, Pereira VM, Steinman DA (2018) Better than nothing: a rational approach for minimizing the impact of outflow strategy on cerebrovascular simulations. *Am J Neuroradiol* 39(2):337–343
- Chnafa C, Valen-Sendstad K, Brina O, Pereira VM, Steinman DA (2017) Improved reduced-order modelling of cerebrovascular flow distribution by accounting for arterial bifurcation pressure drops. *J Biomech* 51:83–88
- Chung B, Cebal JR (2015) CFD for evaluation and treatment planning of aneurysms: review of proposed clinical uses and their challenges. *Ann Biomed Eng* 43(1):122–138
- Detmer FJ, Chung BJ, Mut F, Slawski M, Hamzei-Sichani F, Putman C, Jiménez C, Cebal JR (2018) Development and internal validation of an aneurysm rupture probability model based on patient characteristics and aneurysm location, morphology, and hemodynamics. *Int J Comput Assist Radiol Surg* 13(11):1767–1779
- Glaßer S, Berg P, Neugebauer M, Preim B (2015) Reconstruction of 3D surface meshes for blood flow simulations of intracranial aneurysms. In: *Proceedings of computer- and robot-assisted surgery (CURAC)*, pp 163–168
- Goubergrits L, Hellmeier F, Bruening J, Spuler A, Hege HC, Voss S, Janiga G, Saalfeld S, Beuing O, Berg P (2019) Multiple aneurysms anatomy challenge 2018 (match)—uncertainty quantification of geometric rupture risk parameters. *BioMed Eng OnLine* 18(1)(35):1–16, 03
- Linn FHH, Rinkel GJE, Algra A, Van Gijn J (1996) Incidence of subarachnoid hemorrhage: role of region, year, and rate of computed tomography: a meta-analysis. *Stroke* 27(4):625–629
- Murray CD (1926) The physiological principle of minimum work: I. The vascular system and the cost of blood volume. *Proc Natl Acad Sci USA* 12(3):207
- Onishi Y, Aoki K, Amaya K, Shimizu T, Isoda H, Takehara Y, Sakahara H, Kosugi T (2013) Accurate determination of patient-specific boundary conditions in computational vascular hemodynamics using 3D cine phase-contrast mri. *Int J Numer Methods Biomed Eng* 29(10):1089–1103
- Ritter F, Boskamp T, Homeyer A, Laue H, Schwier M, Link F, Peitgen H-O (2011) Medical image analysis. *IEEE Pulse* 2(6):60–70
- Sanchez M, Ecker O, Ambard D, Jourdan F, Nicoud F, Mendez S, Lejeune J-P, Thines L, Dufour HH, Brunel MP, Lobotesis K, Bonafe A, Costalat V (2014) Intracranial aneurysmal pulsatility as a new individual criterion for rupture risk evaluation: biomechanical and numeric approach (IRRAS project). *Am J Neuroradiol* 35(9):1765–1771
- Valen-Sendstad K, Piccinelli M, Krishnankutty KRR, Steinman DA (2015) Estimation of inlet flow rates for image-based aneurysm CFD models: where and how to begin? *Ann Biomed Eng* 43(6):1422–1431
- Voß S, Glaßer S, Hoffmann T, Beuing O, Weigand S, Jachau K, Preim B, Thevenin D, Janiga G, Berg P (2016) Fluid-structure simulations of a ruptured intracranial aneurysm—constant versus patient-specific wall thickness. *Comput Math Methods Med*. <https://doi.org/10.1155/2016/9854539>
- Voss S, Janiga G, Beuing O, Berg P (2019) Multiple aneurysms anatomy challenge 2018 (match) phase IB: Effect of morphology on hemodynamics. *PLOS ONE* page accepted for publication, 05
- Xiang J, Natarajan SK, Tremmel M, Ma D, Mocco J, Hopkins LN, Siddiqui AH, Levy EI, Meng H (2011) Hemodynamic-morphologic discriminants for intracranial aneurysm rupture. *Stroke* 42(1):144–152

**Publisher's Note** Springer Nature remains neutral with regard to jurisdictional claims in published maps and institutional affiliations.



# Part III

## Visual Exploration and Evaluation

This part of the postdoctoral thesis covers important aspects regarding the visual exploration and evaluation of the acquired medical image data, the segmented 3D IA surface models and the hemodynamic information to better understand, explore and characterize the intracranial vessels and their pathologies. Furthermore, the rupture risk assessment is approximated based on the extracted information. The following papers are included:

- Chapter 8 (see page 105): Behrendt, B., Berg, P., Preim, B., & Saalfeld, S. (2017). Combining pseudo chroma depth enhancement and parameter mapping for vascular surface models. In *Proc. of Eurographics Workshop on Visual Computing for Biology and Medicine (VCBM)* (pp. 159–168)
- Chapter 9 (see page 115): Saalfeld, P., Glaßer, S., Beuing, O., & Preim, B. (2017a). The FAUST framework: Free-form annotations on unfolding vascular structures for treatment planning. *Computers & Graphics*, 65, 12–21
- Chapter 10 (see page 127): Saalfeld, P., Luz, M., Berg, P., Preim, B., & Saalfeld, S. (2018a). Guidelines for quantitative evaluation of medical visualizations on the example of 3d aneurysm surface comparisons. *Computer Graphics Forum*, 37(1), 226–238
- Chapter 11 (see page 141): Behrendt, B., Berg, P., Beuing, O., Preim, B., & Saalfeld, S. (2018). Explorative blood flow visualization using dynamic line filtering based on surface features. *Computer Graphics Forum*, 37(3), 183–194
- Chapter 12 (see page 155): Niemann, U., Berg, P., Niemann, A., Beuing, O., Preim, B., Spiliopoulou, M., & Saalfeld, S. (2018). Rupture status classification of intracranial aneurysms using morphological parameters.

In *Proc. of IEEE Int. Symposium on Computer-Based Medical Systems (CBMS)* (pp. 48–53)

- Chapter 13 (see page 161): Berg, P., Voß, S., Janiga, G., Saalfeld, S., Bergersen, A. W., Valen-Sendstad, K., Bruening, J., Goubergrits, L., Spuler, A., Chiu, T. L., Tsang, A. C. O., Copelli, G., Csippa, B., Paál, G., Závodszy, G., Detmer, F. J., Chung, B. J., Cebal, J. R., Karmonik, C., Elias, S., Cancelliere, N. M., Najafi, M., Steinman, D. A., Pereira, V. M., Piskin, S., Finol, E. A., Pravdivtseva, M., Velvaluri, P., Rajabzadeh-Oghaz, H., Paliwal, N., Meng, H., Seshadhri, S., Shojima, M., Sindeev, S., Frolov, S., Qian, Y., Wu, Y.-A., Carlson, K. D., Kallmes, D. F., Dragomir-Daescu, D., & Beuing, O. (2019c). Multiple aneurysms anatomy challenge 2018 (MATCH): Phase II: Rupture risk assessment. *International Journal of Computer Assisted Radiology and Surgery (IJCARS)*. doi:[10.1007/s11548-019-01986-2](https://doi.org/10.1007/s11548-019-01986-2)

*The typesetting of the manuscripts has not been modified. No changes have been made to the texts and illustrations of these peer-reviewed submissions. Only header, footer, and page numbers were removed and replaced by a chapter header and a running number.*

# Combining Pseudo Chroma Depth Enhancement and Parameter Mapping for Vascular Surface Models

B. Behrendt<sup>1</sup> & P. Berg<sup>2</sup> & B. Preim<sup>1</sup> & S. Saalfeld<sup>1</sup>

<sup>1</sup>Dept. of Simulation and Graphics, University of Magdeburg, Germany

<sup>2</sup>Dept. of Fluid Dynamics and Technical Flows, University of Magdeburg, Germany

---

## Abstract

*The presence of depth cues in a visualization can be a great aid in understanding the structure and topology of a vessel tree. Pseudo Chromadepth is a well-known technique for enhancing depth perception in vascular 3D models. Since it strongly relies on the color channel to convey its depth cues, it is traditionally not suited for combined visualizations comprising color-encoded surface parameters.*

*In this paper, we present and evaluate the use of a modified form of Pseudo Chromadepth that supports displaying additional surface parameters using the color channel while still increasing depth perception. This technique has been designed for the visualization of cerebral aneurysm models. We have combined a discretized color scale to visualize the surface parameter with the Pseudo Chromadepth color scale to convey depth using a Fresnel-inspired blending mask.*

*To evaluate our approach, we have conducted two consecutive studies. The first was performed with 104 participants from the general public and the second with eleven experts in the fields of medical engineering and flow simulation. These studies show that Pseudo Chromadepth can be used in conjunction with color-encoded surface attributes to support depth perception as long as the color scale is chosen appropriately.*

Categories and Subject Descriptors (according to ACM CCS): I.3.7 [Computer Graphics]: Three-Dimensional Graphics and Realism—Color, shading, shadowing, and texture I.4.8 [Image Processing and Computer Vision]: Scene Analysis—Depth cues

---

## 1. Introduction

A large set of vessel visualization techniques have been developed, including surface and volume rendering, illustrative techniques and model-based techniques. Some of these techniques are carefully adapted to shape or depth perception by using special color scales [PBC\*16]. The downside of relying on color scales to convey depth is that they often prevent the color channel from being used to visualize parameters on the vessel wall.

Studying vascular diseases, such as plaques and abdominal or cerebral aneurysms, involves the evaluation of both morphology and hemodynamic parameters. Morphologic parameters of objects can usually be directly inferred from the visualization (such as the position in the vessel tree) or determined by using measuring tools (such as size or aspect ratio). Hemodynamic parameters are either measured or derived with a computational fluid dynamic simulation and either conveyed in the form of stream or path lines (to display blood flow patterns) or by mapping information directly onto the vessel surface using a color scale (such as pressure or wall shear stress). Using colors to encode the information onto the vessel surface is a common technique and well accepted by physicians.

In this paper, we will examine if this type of encoding can be combined with additional visualization techniques to increase depth perception. We present a framework for the improved visualization of vessels that features enhanced depth perception in addition to allowing surface parameters to be mapped to the vessel wall using color scales. Our approach uses different color scales on the vessel surface to create separate visualizations for depth and surface parameters, which are then combined using a blending mask. The generation of this mask is inspired by the Fresnel effect, which describes the reflection of a surface based on the viewing angle.

An important application for such a technique is supporting the understanding of cerebral aneurysms. Cerebral aneurysms show a high prevalence in the western population (3-5%) [BSB06], while their annual risk of rupture is below 1% [MKH\*12]. On the one hand, the bleeding caused by a rupture can have fatal consequences. On the other hand, the treatment procedure itself is risky and can lead to severe complications. Especially in the case of small, asymptomatic cerebral aneurysms, the mortality rate of the treatment may exceed the risk of rupture [Wie03].

Therefore it is vital to assess its risk of rupture to devise an optimal, patient-specific treatment plan. This is especially true for pa-

tients with multiple aneurysms that may require several treatment sessions. Each aneurysm has its own individual risk of rupture, and each separate treatment session increases the overall procedural risk. To minimize the risk of both treatment and incidence of a rupture, the physicians need to identify and treat the aneurysms with the highest risk of rupture and keep the rest under observation.

## 2. Related Works

There are various ways to enhance the perception of both depth and shape in computer-generated 3D images [BCFW08, PBC\*16]. In this paper, we focus on the use of color to increase the perception of depth.

Rheingans and Ebert used distance color blending, a combination of intensity depth cueing and color modulation, to increase depth perception in volume models [RE01]. This approach mimics the light-scattering effect of the atmosphere by reducing color intensity of more distant objects and adding a slightly blue tint to them. Joshi et al. later validated this method specifically for enhancing depth perception in vessel visualization [JQD\*08].

Another method to convey depth by emulating real-world optical effects is depth of field (DoF), where objects are gradually blurred depending on their distance to a focal plane. Without using eye tracking, this focal plane needs to be positioned manually or using heuristics [RSH06]. Grosset et al. evaluated the effectiveness of various DoF techniques in a study with 25 participants [GSBH13]. They found that DoF only supports depth perception when the focal plane is placed in the front of the scene. A general problem of DoF is that it is not possible to focus on two objects at the same time unless they have a similar distance to the viewer.

Ritter et al. employed hatching to visualize depth relations in complex vascular structures [RHD\*06]. Whenever two sections of the anatomy were overlapping, the posterior structure was hatched to simulate a shadow. The size of the hatched area directly corresponded to the distance between the two structures. In a study with 160 participants, Ritter et al. were able to show that their approach significantly increased depth perception when compared to Gouraud shading. Lawonn et al. presented a combination of depth-dependent halos, support lines and the illustrative shadows by Ritter et al. to improve perceptibility of depth [LLPH15]. These support lines are cast from manually selected points of the vessel onto a plane, creating an effect similar to beams holding the model up. They could successfully convey the depth of a complex 3D model in a static 2D image, although it does not allow for a free rotation of the vessel.

Pseudo Chromadepth (PCD) was introduced by Ropinski et al. [RSH06]. It is based on the idea of enhancing depth perception in 3D visualizations of angiography datasets by mapping the depth of each point on the surface to a color gradient. PCD was derived from the chromadepth technique [Ste87], which follows a similar idea. Due to the fact that light with different wavelengths is refracted at different angles in the lens of the eye, color can be used to create the illusion of depth in an otherwise flat image. This does not necessarily require any special type of surface, glasses or other additional devices, although the effect can be strongly enhanced by diffraction grating glasses [BC98].

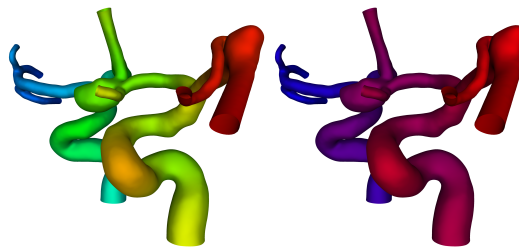


**Figure 1:** Comparison of the chromadepth (left) and pseudo chromadepth (right) color scales applied to a cerebral vessel.

Instead of using the full range of colors visible to the human eye. Pseudo Chromadepth only uses a gradient from red (low depth) to blue (high depth). A wide range of hues might distract from the shading used to convey shape. The chroma depth color scale may work well for geometric objects or shapes with low complexity, such as an organ surface, but it is inappropriate for such complex shapes as vessels. A comparison between both techniques can be seen in Figure 1.

The colors red and blue were chosen due to their high difference in wavelength to maximize their chromadepth effect. Additionally, red is attention-grabbing and intuitively perceived as foreground, whereas blue – the color of the sky – is perceived as background. In a study with 14 participants, Ropinski et al. showed that angiography images could benefit from color-encoded depth information [RSH06]. Additional studies confirmed this effect [KOCC14].

The Fresnel effect has previously been used to integrate additional information into vessel visualizations. Gasteiger et al. introduced Ghosted Views, which use an approximation of the Fresnel effect to modulate the opacity of vessel surfaces [GNKP10]. This method allows to show the blood flow inside of a vessel without removing the entire front-facing part of the surface, thus increasing shape perception of the vessel. In a subsequent study, Baer et al. showed that this approach allowed for a more accurate analysis of the aneurysm and its flow patterns [BGCP11]. Glaßer et al. presented a similar technique, which uses the Fresnel effect to highlight vessel boundaries [GSB\*16]. They also used discrete color scales to visualize surface attributes on the vessel surface, but did not combine this directly with their boundary-enhanced view.

## 3. Method

The idea of both chromadepth and PCD is based on the fact that the color channel of the image does not contain any relevant information and can therefore be fully utilized to increase depth perception [RSH06]. While this is true for angiography images, it cannot be generalized for any kind of medical visualization task.

When analyzing vascular pathologies, physicians are often interested not only in the vessel shape, but also in functional parameters, such as pressure or wall shear stress on the vessel wall. An appropriate visualization should therefore convey the general shape and depth of the vessel model, but simultaneously encode the aforementioned functional parameters as well. The physician should be able

B. Behrendt & P. Berg & B. Preim & S. Saalfeld / Combining PCD and Parameter Mapping for Vascular Surface Models

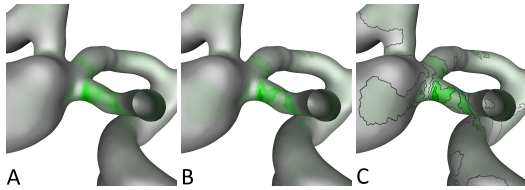


**Figure 2:** Comparison of a smooth color scale (A), discrete color scale (B) and discrete color scale with additional boundaries (C) when visualizing wall shear stress on a vessel.

to compare different regions on the vessel wall regarding their spatial relation and parameter values without having to switch between different types of shading.

These requirements prevent the application of traditional chromadepth or PCD shading, as it would conflict with the parameter information encoded into the color channel. A likely result would be a slower analysis with increased risk of errors and mental load for the physician. In contrast, we present a technique that allows the use of PCD in addition to mapping data to the surface color of a model, which is described in the following.

### 3.1. Surface Visualization

The vessel surface models are generated from 3D digital subtraction angiography data with cerebral aneurysms by applying a threshold-based segmentation. The iso-surface is extracted and converted into a triangle mesh. This mesh is then visualized as a 3D surface model and illuminated using Phong Shading with a single headlight.

For the extraction of hemodynamic parameters, such as pressure and wall shear stress, the surface mesh is employed for computational fluid dynamic simulations. We realized two approaches: the parameters are mapped to a color scale ranging from white to orange for a pilot study and to a color scale from white to green for the final study. We decided against using hatching to convey the additional information, as it may also interfere with the Phong-based lighting we use to convey the shape of the vessels. Furthermore, hatching is not well suited to highlight small areas of interest.

When analyzing surface parameters on a vessel, physicians often look for "hot spots". These are small areas with very high values, which can be perceived pre-attentively when they are encoded with color. To highlight regions with particularly high or low parameter values, we have chosen to discretize the color scale to five different shades (Fig. 2B). To make these shades even more distinct, a black outline has been added to mark the transition line between shades (Fig. 2C).

### 3.2. Fresnel-Inspired PCD

Traditionally, PCD occupies the entire color channel. This mostly prevents additional information from being shown on the objects surface. Since the green color channel is not occupied by PCD, a trivial solution would be to map information to that specific color

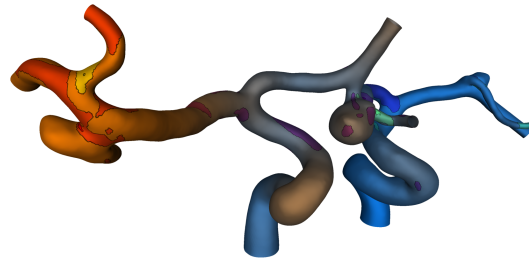


**Figure 3:** PCD shading where the depth is continuously mapped to the red and blue color scale and the scalar parameter is mapped to the green color channel using a discrete scale.

channel only. Such a visualization (Fig. 3) would be unsatisfactory, since it is very difficult for humans to mentally disassemble a color into their respective channels. The same parameter value can have widely different hues depending on its location on the model's surface. As a result, the interpretation of such a visualization is very challenging.

Our method displays the PCD color scale on the edges of the 3D model only, based on the current viewing direction. This type of shading is inspired by the Fresnel effect, which describes the amount of reflection and refraction of light on a surface in relation to the viewing angle. A flatter viewing angle on a surface increases the amount of light that is reflected, resulting in the surface appearing brighter when lighted (Fig. 4A).

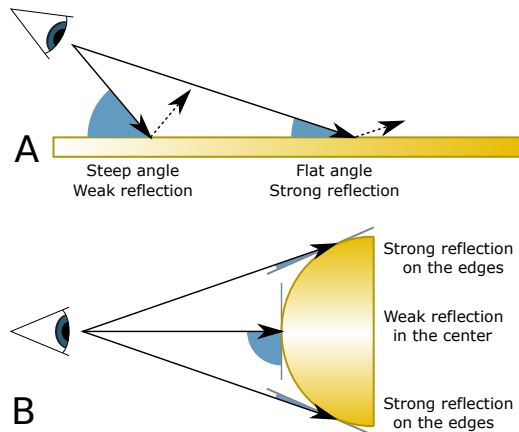


**Figure 4:** Principle of the Fresnel effect; the amount of reflection on a reflective surface depends on the viewing angle (A). When applied to spherical object; the edges exhibit strong reflections due to the shallow viewing angle (B).

A physically accurate calculation of this effect is quite complicated, especially when taking into consideration that due to chromatic dispersion, the strength of the Fresnel effect also depends on the light components' wavelengths. Instead, we use a simplified version of this effect to generate a mask for overlaying the PCD color gradient. Our Fresnel-Inspired PCD (FI-PCD) mask  $M_{PCD}$  is calculated similarly to ghosted views [GNKP10] using the following formula:

$$M_{PCD} = f_{scale} * (1 - |2 * \frac{\arccos(\vec{I} \cdot \vec{N})}{\pi} - 1|)^s$$

$\vec{I}$  and  $\vec{N}$  are the incident and normal vectors at the surface respectively. The scaling factor  $f_{scale}$  can be used to adjust the effect strength. Similarly, the variable  $s$  controls the steepness of the transition from surface to PCD scale. In our application, we have empirically chosen a scaling factor of 1 and a steepness of 2.

$M_{PCD}$  is dependent on the angle between the normal and incident vectors, reaching its maximal value when they are orthogonal to each other. On spherical or tubular models, the Fresnel effect strongly increases the reflectiveness around the edges of the model (Fig. 4B).

Our final FI-PCD visualization comprises two different images, both of them renderings of the vessel surface. The first one has the parameters mapped to its color (Fig. 5A), the second is colored entirely according to the PCD scale (Fig. 5B). For each pixel in the final image, the pixel's value in the mask  $M_{PCD}$  is extracted and used as weight for the linear interpolation between the two images (Fig. 5C). For example, black  $M_{PCD}$  pixels yield the color-coded parameter value and white  $M_{PCD}$  pixels yield the PCD-based color-coding.

The resulting FI-PCD visualization (Fig. 5D) allows mapping a scalar parameter to any color scale, while PCD depth cues are shown only on the edges of the model. They are still clearly visible to the user while interference with the object's surface color is reduced. Usually, the physician would rotate the vessel in a way that the interesting areas are facing the camera instead of being relegated to the edge of the model. In addition to providing depth cues by hue, displaying the PCD scale at the edges also increases the perceptibility of overlaps, which is another important depth cue.

### 3.3. Implementation

Generation and composition of both images is performed mostly in the fragment shader.

When rendering the surface, the attribute values for the surface are sent to the graphics card as vertex attributes. Additionally, the highest and lowest values of the attribute as well as the highest and lowest depth values from the previously rendered frame are stored in the fragment shader as uniform variables. Then, the attributes are interpolated between vertices, normalized to a  $[0, 1]$  range and transformed into a color value by the fragment shader. The transformation is performed linearly in RGB color space between white ( $\#ffffff$ ) and orange ( $\#ff7f00$ , pilot study) or green ( $\#00ff00$ , final study). Next, the resulting color value is discretized into five distinct shades and used as surface color.

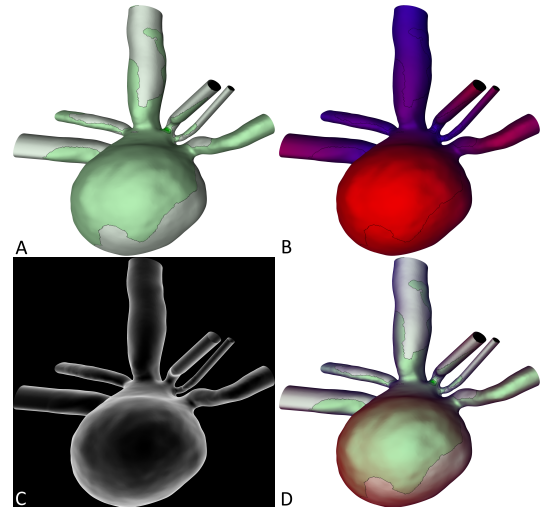


**Figure 5:** Composition of images to create the FI-PCD visualization: Surface color image (A), PCD image (B), Composition mask (C) and resulting FI-PCD image (D).

The boundaries between color shades are generated dynamically on a per-triangle base by analyzing the affinity of each vertex to a certain color class. For each triangle with different affinities at the edges, the fragment shader draws a black line separating these vertices. This approach allows for a very fast generation of dynamic outlines on the surface, without the need for any pre-processing or the creation of new geometry. Unfortunately, since the lines are always at the center between two vertices, they do not always line up exactly with the actual color transition. On a model with a decent triangle resolution, this effect is only noticeable when zooming in very closely to the surface.

The second image is generated by normalizing the current fragment's depth using the previously stored depth range and mapping the resulting value to the PCD color scale. Using the depth range from the previous frame allows us to draw the geometry using a single rendering pass, although it produces a barely noticeable flicker in the PCD color scale during fast animations. Afterwards, the  $M_{PCD}$  value is calculated and used to compute the composition of both images.

### 4. Evaluation

Our evaluation consists of two separate studies; a pilot study with participants from the general public, and a final study with experts in the fields of medical engineering and flow simulation. All participants were shown 3D visualizations of intra-cranial vessel surfaces models. These models had one of multiple available attributes mapped to their surface, such as pressure or wall shear stress. Participants were shown two points on these datasets and had to select either the one closest to them or the one with the highest parameter.

B. Behrendt & P. Berg & B. Preim & S. Saalfeld / Combining PCD and Parameter Mapping for Vascular Surface Models

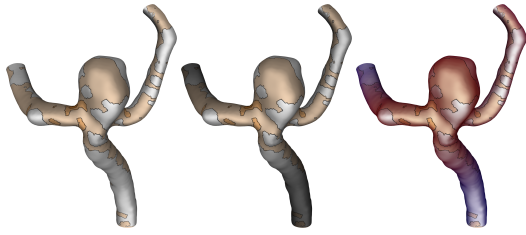


**Figure 6:** The different shadings used in the first study: No depth cues, trivial brightness cues and FI-PCD (f.l.t.r.)

The datasets were shown with three different shading styles. The first style was a normal, phong-shaded visualization without any distinct depth enhancement. The second used brightness as a depth cue. Distant triangles were reduced in brightness, with the highest possible reduction being 75%. This value was chosen empirically as a trade-off between having a strong effect on depth perception while still being able to discern the color of farther away parts of the model. The last style was our implementation of FI-PCD. All three visualization styles can be seen in Figure 6.

We expected the visualization without depth cues to perform worst in the depth judgment, but best in the parameter judgment task. As both brightness-based cues and FI-PCD would partially overlay the surface color scale, we expected them to perform equally well, but not as good as the visualization without depth cues. Since PCD has proven superior to brightness- or contrast-based cues by studies in the past (such as [KOCC14]), we expected FI-PCD to perform best in the depth judgment task.

The pilot study allowed us to identify several flaws in our technique. Before the final study, we corrected these problems by changing some aspects of both our visualization as well as the application. First, the color scale used to encode the surface attribute was changed from white-to-orange to white-to-green. The original orange scale was chosen due to aesthetic reasons. However, many participants in the pilot study noted that red areas from the FI-PCD shading interfered with orange areas from the surface attribute color scale. Since PCD only uses the red and blue color channel, green was chosen for the surface attribute to prevent color overlaps. A comparison between the two color scales in combination with FI-PCD can be seen in Figure 7.

We also added a permanent legend for the used color scales in the bottom left corner of the screen. This was done in response to some participants in the first study confusing the meaning of some of the colors during the course of the study. The legend always encoded the surface attribute color scale in combination with the current depth enhancement color scale. All three scales can be seen in Figure 8.

#### 4.1. Application

When started, the test application presents the user with a few instructional pages. All of them include a "Continue"-button that becomes enabled after five seconds and allows the participant to ad-

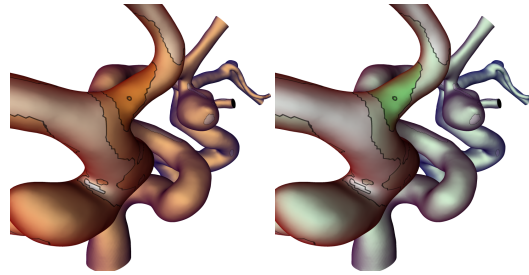


**Figure 7:** Different color scales used in the first (left) and second (right) study in combination with FI-PCD.

vance to the next screen. The first and second pages contain general information about the study as well as labeled example images for all types of visualizations used in this study, as seen in Figure 9. To prevent any bias, these images are always shown in a random order.

The actual study consists of two blocks, where the user has to select either the point closest to them, or the one with the highest scalar surface parameter. Therefore, the user has to identify the spatial relation or ranking of scalar values of two selected points on the surface (Fig. 10). Additionally, they always have the option to click a button labeled "Not sure" if they cannot decide for one of the points. During each task, the application measures the completion time, rotation time and whether the user clicked the correct point or hit the "Not sure"-button instead. For the rotation time, we counted the amounts of single frames that a rotation was performed in and converted them to a duration in seconds. Frames where the user kept the left mouse button pressed without moving the mouse (therefore not actually performing a rotation) were not included.

Each block is introduced by another instructional page, which is then followed by six dedicated tutorial datasets. They serve as a way to familiarize the user with the visualizations and tasks, therefore their measurements are excluded from the final statistic. Furthermore, a learning effect during the actual evaluation is prevented.

After completing the tutorial for each block, the user sees a message explaining that the training part is over and asking them if they have any questions before proceeding. This was done to ensure they were properly prepared and did not have to ask questions during the time-measured evaluation. They were encouraged to complete

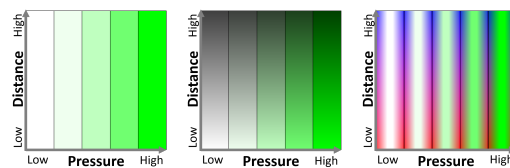


**Figure 8:** The color scale legends shown in the final study: No depth cues, trivial brightness cues and FI-PCD (f.l.t.r.)

B. Behrendt & P. Berg & B. Preim & S. Saalfeld / Combining PCD and Parameter Mapping for Vascular Surface Models

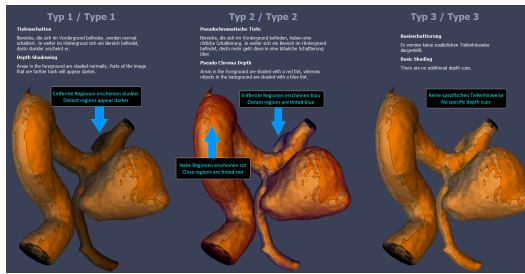


**Figure 9:** Instructional page detailing the different visualizations (ordered randomly). For the second study, the images were updated to reflect the changed surface color scale.



**Figure 11:** Experimental setup for the pilot study. The two disabled monitors in the corner were not part of the study.

each task as fast and accurately as possible due to the time measurement. "Guessing" the correct answer was discouraged in favor of using the "Not sure"-button.

The order of blocks was consistent for all participants, starting with the depth judgment tasks and then switching over to the parameter judgment task. Each task consisted of 30 images in total, six of them being the training images. All users were shown the same images, although they were ordered randomly. The application ensured that the same dataset did not appear twice in a row. The participants did not receive any immediate feedback about the correctness of their answers during the study, but statistics about their general performance were made available to them afterwards upon request.

#### 4.2. Questionnaire

After completing the assignments on the computer, all participants were asked to fill out a questionnaire. In addition to age, biological gender and known visual disorders, participants were asked if they have experience with analyzing medical data or modeling 3D

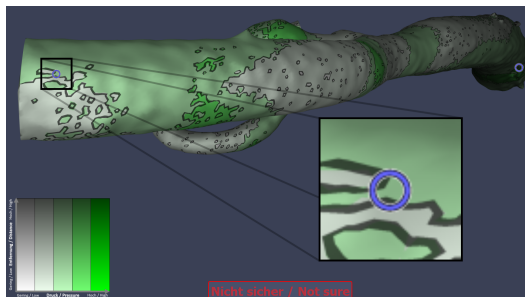


**Figure 10:** One of the datasets with two marked points shown to the participants as part of the depth judgment task. The image used brightness-based depth cues and the green color scale from the final study.

objects and whether they play 3D video games regularly. For visual disorders, we were mostly interested in those that impede the ability to perceive color or depth. Since there are many cases where people are unaware of their color perception impairment, we added a very abbreviated color blindness test using three Ishihara plates. Two of them had numbers encoded in them (42 and 6) while the last one did not. None of the participants that had not already denoted a form of color blindness in the questionnaire failed this test.

At the end, participants were asked to rank the three types of visualizations according to their usefulness for perceiving depth and the surface attribute as well as their general aesthetic. They were also given space for any additional remarks.

#### 5. Pilot Study

For the pilot study, we took advantage of the popular open house day at our university as a means of finding volunteers. Visitors of this event were asked to participate in our study. Both verbal explanations as well as written instructions and other materials were made available to the participants.

Half of the participants were randomly selected to be given limited control over the camera during the study, whereas they can rotate the dataset by ten degrees in any direction. These participants were shown an extra paragraph in one of the instructional pages of the application explaining that they had the ability to orbit the camera. If they did not rotate the camera at least once during the tutorial, they were reminded by a pop-up dialog.

##### 5.1. Participants

A total number of 104 people from the general public volunteered to participate in the pilot study. Ten of them were later rejected due to vision impairments (i.e. various forms of color blindness or problems with depth perception), failing to comprehend the assignment or not filling out the corresponding questionnaire. The age of the participants ranges from 11 to 73, with an average of 28.6 and a standard deviation of 14. Out of the 94 participants that were included in the evaluation, 40 were female (42.6%).

## 5.2. Setup

In order to allow for a high number of participants, we set up four PCs for simultaneous use (Fig. 11). They were positioned in a corner of the room to prevent distractions from the rest of the event. To ensure comparability of the results between the different stations, we used PCs with similar hardware specifications and identical screens. All stations ran the application at a resolution of  $1920 \times 1080$  with 60 frames per second.

The participants were given a short verbal introduction about the topic of vessel visualization in general and the study in particular. To keep any descriptions simple and explanations short, the different scalar attributes shown in the visualizations were always just referred to as "pressure" despite also including wall shear stress. After that, they were instructed to sit down at one of the stations and follow the on-screen instructions from the application.

## 5.3. Results

For each participant, we calculated four values from our measurement for each shading style. *Correctness* is the percentage of correct answers, e.g. how often participants selected the nearest point (during the depth judgment task) or the point with higher scalar value (during the parameter judgment task), respectively. *Certainty* denotes the percentage of answers where the user selected any of the points and not the "Not sure"-button. *Duration* is the average time in seconds the users took for each image. *Rotation* is the average time the user spend rotating the dataset. For this value, we only included users who actually rotated the dataset.

The ability of the participants to pick the point closest to them benefited from having any form of depth cues enabled (Fig. 12). Without them, they were only correct in 79% of the depth judgment tasks. Brightness-based depth cues increased their accuracy to 90%, whereas FI-PCD only increased it to 85%. This is surprising, as we were expecting the FI-PCD to provide much better depth cues than the brightness-based approach.

Although being reminded after each training session that they could rotate, only 35 of the 50 users with the ability to rotate actually made use of it. Three of them performed so little rotation that we assume that to be accidental. This was possibly a result of being overwhelmed due to unfamiliarity with 3D visualizations. Users that stated experience in 3D modeling or 3D video games rotated for an average of 0.3 seconds per dataset, whereas users with no experience only rotated for 0.19 seconds.

The values for certainty and rotation are extremely similar for each of the three shading styles. The users generally rarely used the "Not sure"-button in this study. The average duration was slightly higher for the visualization without depth cues (4.2 s) in comparison to brightness-based cues (3.8 s) and FI-PCD (4.0 s).

For the parameter judgment task, the visualization without cues reached the best average correctness (96%, Fig. 13). Users also performed fastest, with an average duration of 2.9 s per image. This result was to be expected, as there are no additional color or brightness gradients added to the surface color. The brightness-based depth cues performed better than FI-PCD in regards to correctness (92% compared to 80%) and duration (3.2 s compared to 3.5 s).

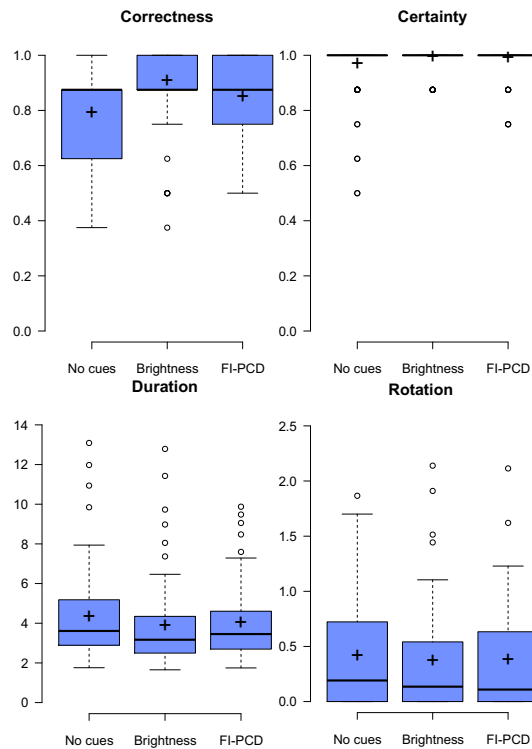


**Figure 12:** Box plots showing correctness (top left), certainty (top right), duration in seconds (bottom left) and rotation duration in seconds (bottom right) for the depth judgment task over all participants from the pilot study.

This most likely stems from our choice of color scale to encode the surface parameters in this study. Many participants remarked that the orange from the surface color scale was interfering with the red from the PCD scale, thus making it hard to distinguish them.

Interestingly, in order to interpret the colors of areas strongly affected by depth cues (i.e. those close to the edge of the vessel when using FI-PCD or those in the background when using brightness cues), users often resorted to "counting" color gradients. They would search for an area that was completely white and then count the boundaries they had to cross to reach the marked point. That way, they could tell which area represented a higher parameter value even without being able to distinguish the colors directly. Since this approach requires a visually uninterrupted path from a marked point to a white area, it was not possible in all cases.

Just as in the depth judgment task, the certainty for all shading styles is very similar. Rotation was used even more rarely in this task. Since the marked points were never obstructed by other geometry, there was little point in rotating the dataset to compare the surface coloring.

B. Behrendt & P. Berg & B. Preim & S. Saalfeld / Combining PCD and Parameter Mapping for Vascular Surface Models

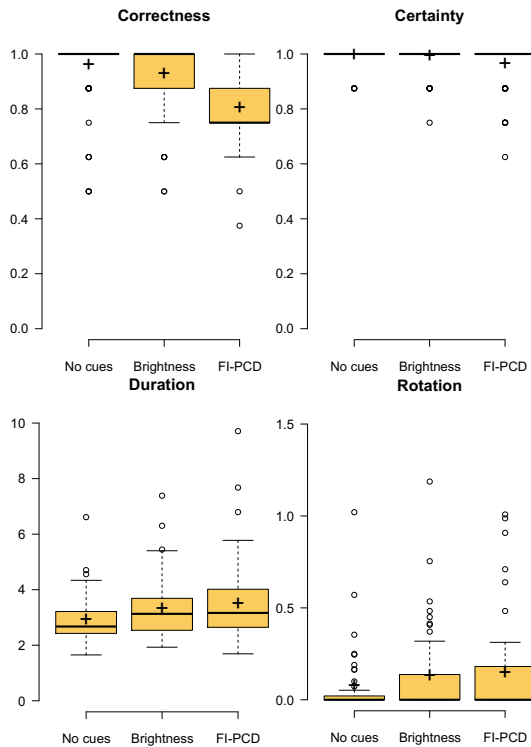


**Figure 13:** Box plots showing correctness (top left), certainty (top right), duration in seconds (bottom left) and rotation duration in seconds (bottom right) for the parameter judgment task over all participants from the pilot study.

We also analyzed the correctness in regards to whether the users made use of rotation during the tasks. The ability to rotate the view had very little effect on the results of the surface parameter task (Fig. 14, bottom). The correctness of the depth judgment task increased when rotation was used on the FI-PCD images as well as those without depth cues. Since parallax movement is another important depth cue, this improvement is not surprising.

**6. Final Study**

For the final study, we directly approached several experts in the fields of medical engineering and flow simulation. Due to the lower number of participants in this study, we decided against splitting them into two groups. Therefore, we allowed all of them to rotate the camera.

**6.1. Participants**

Eleven experts volunteered to take part in our final study. One person was excluded due to color blindness. The age of the included

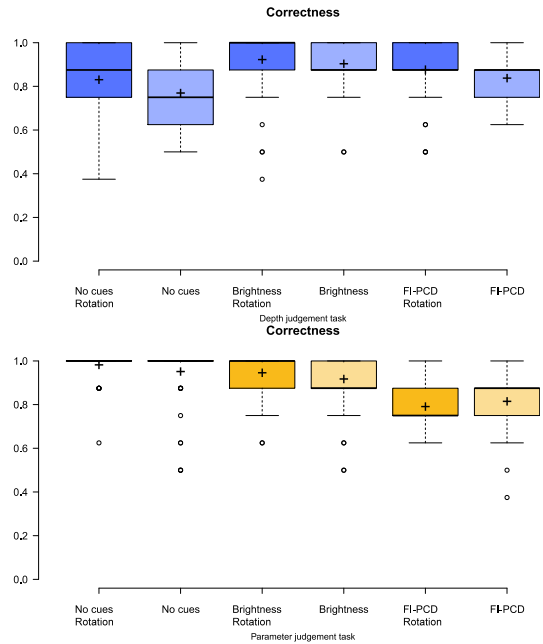


**Figure 14:** Influence of rotation on the ability to judge depth (top), and surface parameters (bottom)

participants ranged between 22 and 41 (average of 29.1), with two of them being female (20 %).

**6.2. Setup**

The second study was performed on a laptop, as it took place at our participant’s workplace. Despite having less powerful hardware than the PCs used in the first study, it was still able to run the application at 1920 × 1080 with 60 frames per second.

For this study, the introduction to vessel visualization was either omitted or kept very brief, since most participants were familiar with this field already. The instructions given by the application itself remained unchanged from the pilot study.

**6.3. Results**

In our second study, the FI-PCD method reached better results (Fig. 15). During the depth judgment task, users were able to pick the correct point in 94 % of the cases. With the brightness-based shading, they were able to choose correctly in 90 % of the cases. Without any depth cues, the participants only reached 85 % accuracy.

The same trend is visible in the certainty plots. Overall, the duration and rotation plots from the second study show the same trends as those in the first study. Interestingly, users took longer for their decision and also rotated the view more when viewing the datasets with FI-PCD compared to brightness-based depth cues. This may

*B. Behrendt & P. Berg & B. Preim & S. Saalfeld / Combining PCD and Parameter Mapping for Vascular Surface Models*

be due to the fact that the combination of PCD and surface color scale can no longer be pre-attentively perceived.

As expected, users were able to judge the parameters best when no depth cues were present, reaching a mean correctness of 98 %. Brightness-based depth cues produced an almost identical result with a mean correctness of 96 %. FI-PCD shading had the strongest negative effect on the participant’s ability to compare parameter values on the surface, although not as strong as in the first study. The mean correctness in this case was 90 %.

The average duration for each decision (from both tasks) was significantly higher in the second study (5.5 s) compared to the first (3.7 s). Similarly, the average rotation duration was also higher (0.3 s compared to 0.2 s). This may indicate that in the second study, participants put more effort into the evaluation.

**7. Discussion**

Our studies have shown that FI-PCD can increase the perception of depth while maintaining recognizability of surface scales on

the vessel surface. For the latter, a careful choice of color scale is required to avoid conflicts with the color gradients introduced by PCD. In our first study, we used an inappropriate color scale to encode surface parameters. This strongly reduced our method’s ability to convey both depth and surface parameters. We were able to remedy this problem in the second study by choosing a different scale that relies only on the green color channel, which goes unused by PCD. This resulted in a higher increase of depth perception than classic, brightness-based depth cues.

We decided to use a discretized color scale instead of a smooth one. This reduces ambiguity between the surface color and PCD scale while at the same time highlights areas with high or low values, which physicians are often interested in since their decisions are discrete as well. The highlighting was increased further by the introduction of outlines around the differently colored surface regions. This created a robust visualization that still allowed users to compare parameter values on the surface even when overlaid with another color or brightness gradient.

Both studies showed that overlaying the color channel with depth

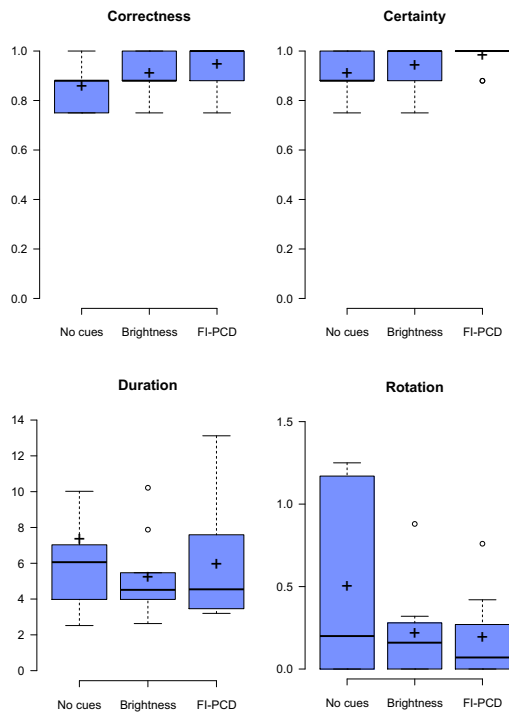


**Figure 15:** Box plots showing correctness (top left), certainty (top right), duration in seconds (bottom left) and rotation duration in seconds (bottom right) for the depth judgment task over all participants from the final study.

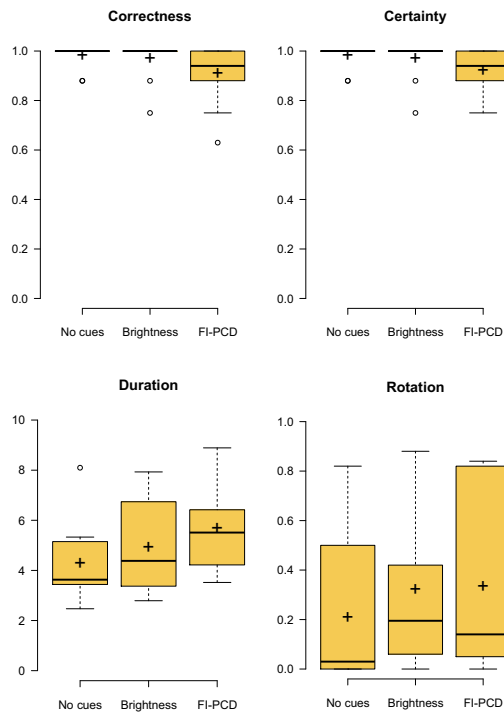


**Figure 16:** Box plots showing correctness (top left), certainty (top right), duration in seconds (bottom left) and rotation duration in seconds (bottom right) for the parameter judgment task over all participants from the final study.

cues reduces the recognizability of the surface color scale. This effect was strongest when using FI-PCD. A likely explanation is that FI-PCD affects the color of both close and distant regions, whereas brightness-based depth cues only affect distant regions. Therefore, FI-PCD should be kept as an optional addition to any visualization that can be disabled in case an in-depth comparison between the scalar values of different surface points is required.

## 8. Conclusion & Future Work

With FI-PCD, we have introduced a novel rendering technique that combines Pseudo Chromadepth with color-encoded surface attributes to visualize vascular anatomy in combination with scalar parameters. We have performed two studies to evaluate our technique. While we could show that FI-PCD can enhance the perception of depth, there are still issues that need to be improved on.

First, FI-PCD tends to distort the underlying color scale. This can be partly remedied by choosing a scale that does not interfere with the red and blue colors from PCD, such as our white-to-green scale. However, it would be interesting to see if this effect can be further reduced by using different values for the scaling factor and steepness in our FI-PCD formula. Reducing the scaling factor or increasing the steepness would make the PCD color scale less prominent in the visualization. Therefore, it may be possible to find a setting that results in a better trade-off between depth and surface color perception.

In many scenarios, the physician would not only be interested in a surface parameter, but also blood flow patterns. Simply displaying them inside of the vessel anatomy using established smart visibility techniques would likely produce unsatisfactory results. In addition to having to cut or fade away parts of the surface to reveal the underlying flow (thus making it harder to see the surface color), displaying path lines with their own color scale would also add another layer of complexity to the color channel. A seamless way of integrating flow visualization would therefore be a useful extension.

## Acknowledgments

We would like to warmly thank Prof. Douglas W. Cunningham and Maria Lutz for their guidance and helpful remarks concerning the study design. Thanks also go to Patrick Saalfeld for his help with the statistical evaluation of our study results.

The work of this paper is funded by the European Regional Development Fund under the operation number 'ZS /2016/04/78123' as part of the initiative "Sachsen-Anhalt WISSENSCHAFT Schwerpunkte".

## References

- [BC98] BAILEY M., CLARK D.: Using ChromaDepth to Obtain Inexpensive Single-image Stereovision for Scientific Visualization. *Journal of Graphics Tools* 3, 3 (1998), 1–9. 2
- [BCFW08] BARTZ D., CUNNINGHAM D. W., FISCHER J., WALLRAVEN C.: The Role of Perception for Computer Graphics. In *Eurographics (STARs)* (2008), pp. 59–80. 2
- [BGC11] BAER A., GASTEIGER R., CUNNINGHAM D., PREIM B.: Perceptual evaluation of ghosted view techniques for the exploration of vascular structures and embedded flow. In *Computer Graphics Forum* (2011), vol. 30, pp. 811–820. 2
- [BSB06] BONNEVILLE F., SOUROUR N., BIONDI A.: Intracranial aneurysms: An overview. *Neuroimaging clinics of North America* 16, 3 (2006), 371–82, vii. 1
- [GNKP10] GASTEIGER R., NEUGEBAUER M., KUBISCH C., PREIM B.: Adapted Surface Visualization of Cerebral Aneurysms with Embedded Blood Flow Information. In *VCBM* (2010), pp. 25–32. 2, 4
- [GSB\*16] GLASSER S., SAALFELD P., BERG P., MERTEN N., PREIM B.: How to Evaluate Medical Visualizations on the Example of 3D Aneurysm Surfaces. In *Eurographics Workshop on Visual Computing for Biology and Medicine* (2016). 2
- [GSBH13] GROSSET A., SCHOTT M., BONNEAU G.-P., HANSEN C. D.: Evaluation of Depth of Field for depth perception in DVR. In *2013 IEEE Pacific Visualization Symposium (PacificVis)* (2013), IEEE, pp. 81–88. 2
- [JQD\*08] JOSHI A., QIAN X., DIONE D. P., BULSARA K. R., BREUER C. K., SINUSAS A. J., PAPADEMETRIS X.: Effective visualization of complex vascular structures using a non-parametric vessel detection method. *IEEE transactions on visualization and computer graphics* 14, 6 (2008), 1603–1610. 2
- [KOCC14] KERSTEN-OERTEL M., CHEN S. J.-S., COLLINS D. L.: An evaluation of depth enhancing perceptual cues for vascular volume visualization in neurosurgery. *IEEE transactions on visualization and computer graphics* 20, 3 (2014), 391–403. 2, 5
- [LLPH15] LAWONN K., LUZ M., PREIM B., HANSEN C.: Illustrative Visualization of Vascular Models for Static 2D Representations. In *Medical Image Computing and Computer-Assisted Intervention – MICCAI 2015*. 2015, pp. 399–406. 2
- [MKH\*12] MORITA A., KIRINO T., HASHI K., AOKI N., FUKUHARA S., HASHIMOTO N., NAKAYAMA T., SAKAI M., TERAMOTO A., TOMINARI S., YOSHIMOTO T.: The natural course of unruptured cerebral aneurysms in a Japanese cohort. *The New England journal of medicine* 366, 26 (2012), 2474–2482. 1
- [PBC\*16] PREIM B., BAER A., CUNNINGHAM D., ISENBERG T., ROPINSKI T.: A survey of perceptually motivated 3d visualization of medical image data. In *Computer Graphics Forum* (2016), vol. 35, pp. 501–525. 1, 2
- [RE01] RHEINGANS P., EBERT D.: Volume illustration: Nonphotorealistic rendering of volume models. *IEEE transactions on visualization and computer graphics* 7, 3 (2001), 253–264. 2
- [RHD\*06] RITTER F., HANSEN C., DICKEN V., KONRAD O., PREIM B., PEITGEN H.-O.: Real-time illustration of vascular structures. *IEEE transactions on visualization and computer graphics* 12, 5 (2006), 877–884. 2
- [RS06] ROPINSKI T., STEINICKE F., HINRICHS K.: Visually Supporting Depth Perception in Angiography Imaging. In *Smart Graphics*, vol. 4073 of *Lecture Notes in Computer Science*. 2006, pp. 93–104. 2
- [Ste87] STEENBLIK R. A.: The Chromostereoscopic Process: A Novel Single Image Stereoscopic Process. McAllister D. F., Robbins W. E., (Eds.), *SPIE Proceedings*, pp. 27–34. 2
- [Wie03] WIEBERS D. O.: Unruptured intracranial aneurysms: Natural history, clinical outcome, and risks of surgical and endovascular treatment. *The Lancet* 362, 9378 (2003), 103–110. 1

# The FAUST Framework: Free-Form Annotations on Unfolding Vascular Structures for Treatment Planning

Patrick Saalfeld<sup>a</sup>, Sylvia Glaßer<sup>a</sup>, Oliver Beuing<sup>b</sup>, Bernhard Preim<sup>a</sup>

<sup>a</sup>Department of Simulation and Graphics, University of Magdeburg, Germany

<sup>b</sup>Department of Neuroradiology, University Hospital Magdeburg, Germany

---

## Abstract

For complex interventions, such as stenting of a cerebral aneurysm, treatment planning is mandatory. Sketching can support the physician as it involves an active involvement with complex spatial relations and bears a great potential to improve communication. These sketches are employed as direct annotation on 2D medical image data and print outs, respectively. Annotating 3D planning models is more difficult due to possible occlusions of the complex spatial anatomy of vascular structures. Furthermore, the annotations should adapt accordingly to view changes and deforming structures.

Therefore, we developed the FAUST framework, which allows creating 3D annotations by freely sketching in the 3D environment. Additionally to generic annotations, the physician is supported to create the most common treatment options with sketching single strokes only. We allow an interactive unfolding of vascular structures with adapting annotations to still convey their meta information. Our framework is realized on the zSpace, which combines a semi-immersive stereoscopic display and a stylus with ray-based interaction techniques.

We conducted a user study with computer scientists, carried out a demo session with a neuroradiologist and assessed the performance. The user study revealed a positive rating of the interaction techniques and a high sense of presence. The neuroradiologist stated that our framework can support treatment planning and leads to a better understanding of anatomical structures. Our performance evaluation showed that our sketching approach is usable in real-time with a large number of annotations. Furthermore, our approach can be adapted to a wider range of applications including medical documentation.

**Keywords:** 3D Sketching, Annotations, Semi-immersive Environments, Treatment Planning, Vascular Structures

---

## 1. Introduction

For clinical treatment planning, physicians need to obtain a spatial understanding of the patient's anatomy and pathologies [1]. Parameters such as shape, volume and spatial relationships of structures have to be considered [2]. Software assistants support the physician in medical practice to reliably and efficiently carry out special tasks [3]. Such medical issues comprise access planning, resection and implant planning. Here, the assisting software may provide the possibility to annotate pathologic variations and visualize treatment options [1, 4]. Such sketched annotations are beneficial to communicate and elaborate complex treatment strategies without the necessity to draw precisely and accurately [5]. However, annotations on 3D image data are usually drawn image-based [6], which causes problems when physicians change the view and annotations do not adapt accordingly. A common solution is recalculating the position in the image domain [7], which introduces difficulties during relocation of annotations reasoned by disturbing non-continuous motions [8]. Furthermore, a mental and algorithmic combination of the 3D model and the image domain comprising the annotations has to be carried out. In our FAUST frame-

work, we allow to create annotations directly in object space as 3D sketches. Hence, we bring together 3D sketching with computer-assisted surgery planning. We *pin* the annotations to the 3D model. Thus, our annotations still convey their meta information on dynamic medical data, such as time-varying or unfolding data. 3D sketches are usually used and appreciated in product design [9, 10, 11], which takes advantage of stylists' skills, acquired through training over time [9]. However, for physicians the annotation of medical structures in 3D with complex treatment options can be laborious and includes the risk of not achieving the desired result. Therefore, our FAUST framework assists the physician in different ways:

- the physician can create generic annotations as well as the most common treatment options by sketching and combining center lines only,
- an optional geometric constraint that allows for a direct projection of the sketch on the surface model,
- a semi-immersive system combining a stereoscopic display with head tracking to support depth perception, and
- the 3D sketching, realized with a six degrees of freedom (6DoF) stylus and ray-based interaction techniques.

---

Email address: saalfeld@isg.cs.uni-magdeburg.de (Bernhard Preim)

We decided to use the semi-immersive 3D User Interface (3DUI) *zSpace* instead of a fully immersive system, because it is less intruding to the typical workflow of a physician but still provides important depth cues such as motion and binocular parallax.

As an example of a spatially complex vascular structure, we chose the *Circle of Willis* (CoW), which comprises a circular combination of arteries supplying the brain and surrounding structures (see Figure 1). Beneath the clinical importance, the CoW is well suited for our approach for two reasons. First, it includes many different sub-structures, which results in a variety of access paths and treatment options. The possibility to freely annotate supports the visualization of different treatment plans. Second, the CoW is represented either in its real, self-occluding 3D anatomical state or as a simplified 2D illustration. To maintain a mental representation of both states including annotations, an interactive and seamless transition can support the physician.

The evaluation of our framework has three parts. First, we conduct a user study to reveal usability problems and to quantify the sense of *presence*. Presence is a measure to assess immersion, and thus, an indicator of how beneficial the semi-immersive system is. Second, we carry out an intensive demonstration session and unstructured interview with an experienced neuroradiologist. Third, we assess different performance aspects, i.e., the necessary calculation time to attach annotations to the CoW as well as the frame rate during interaction and unfolding. The average ratings of the interaction techniques, usability and presence yield positive ratings. The results of our interview indicate that our framework improves the spatial overview of vascular structures and supports the understanding of anatomical structures compared to angiographic 2D images. Regarding the performance evaluation, we achieve real-time frame rates for the attachment of annotations and during interaction with a high number of annotations.

Our paper is organized as follows: **Section 2** provides a short medical background. Here, the CoW is described in more detail and a medical application scenario is motivated based on an interview with a neuroradiologist. **Section 3** summarizes related work in the fields of annotations in combination with sketch-based interfaces, unfolding of medical data and animation of 3D structures. In **Section 4**, the preprocessing steps to convert the medical data in a planning model are described. Based on this model, the unfolding procedure is explained. **Section 5** presents our FAUST framework containing input and output devices as well as interaction techniques. **Section 6** summarizes the evaluation, **Section 7** discusses challenges to integrate the framework into clinical routine and **Section 8** concludes our paper.

## 2. Medical Background and Application Scenario

Diagnosis and treatment of cerebrovascular diseases is a frequent and challenging task in clinical practice. The treatment of cerebral vessels requires in-depth knowledge of patient-individual morphology. The central part of the cerebral vessel

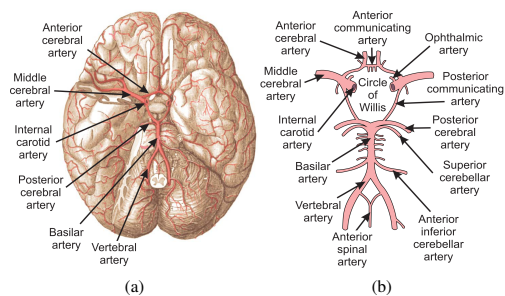


Figure 1: The blood supply of the brain is maintained by the anterior and the posterior cerebral circulation (a) and the CoW (b) as backup circulation (adapted from illustrations from Gray [12]).

system is the CoW (see Figure 1). It comprises a circular combination of arteries supplying the brain and surrounding structures. Its formation allows for bypassing the blood flow in case of a blocked artery. However, the anatomical manifestation of the arteries underlies strong, patient-specific variations with respect to shape and length [13]. Furthermore, there are several CoW configurations where some arteries are underdeveloped or completely missing. Therefore, the CoW is an excellent example for the challenging and complex 3D anatomy.

For an in-depth understanding of our application scenario, we interviewed a neuroradiologist (co-author of this paper) with more than 20 years of professional experience. We stated questions regarding endovascular treatment of cerebral aneurysms, i.e., saccular dilatations of cerebral arteries. Regarding the cause of aneurysms, some risk factors are identified. For example, in 10% of the cases, the afflicted patients have a genetic predisposition. Aneurysms bear an annual chance of 1% to actually rupture [14], resulting in death or permanent disability in more than 40% of the cases [15]. Overall, approximately 2% to 5% of the entire population is affected by cerebral aneurysms [14, 16]. Treatment is usually carried out via *surgical clipping* or *endovascular therapy*. The first one aims at a closure of the aneurysm neck with a clip. Endovascular therapy includes the deployment of stents and flow diverters, which redirect the cerebral blood flow yielding a decreased blood flow in the aneurysm. Another therapy is endovascular coiling, where small wires are placed inside the aneurysm to promote blood clotting and a possible occlusion of the aneurysm. Stenting and coiling are also used in combination. The choice of treatment is based on several criteria, e.g., location, shape and size of the aneurysm. Furthermore, treatment methods vary in aspects such as the used access path as well as different clip sizes, stent lengths and coil types. We account for the huge variety of different parameters and configurations by letting the physician sketch freely, and thus, allow him to take into account even special cases.

An example for such a special case are unruptured aneurysms with increased neck sizes. The large neck sizes are not suited for plain or balloon-assisted coiling. They frequently require stenting to protect the parent vessels permanently. Even

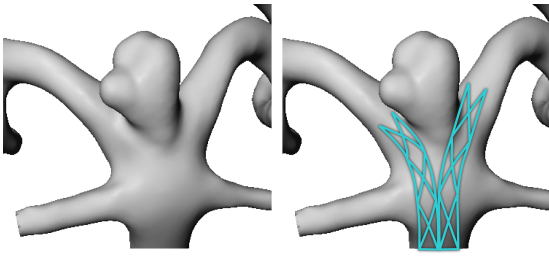


Figure 2: Illustration of Y-stenting, where two stents are inserted.

two stents may be necessary in aneurysms arising at a bifurcation. Here, Y-, X- or T-stenting procedures are performed (see Figure 2). For Y-shaped stents (also called *kissing stents*), two guide wires are carefully positioned such that the two stents can be released alternately. Therefore, the patient-individual anatomy must be analyzed, which often involves the acquisition of 3D digital subtraction images to overcome superimposition in the 2D angiography image data. Special care is required to prevent hampering of the blood supply by blocking branching arteries. Furthermore, both stents should end at the same position and should be adapted to the patient-individual vessel diameter. To further reduce the aneurysm’s inflow and to promote blood clotting and a possible closure, coils are deployed after the Y-stenting. The treatment planning involves a thorough evaluation of the patient-specific CoW’s spatial anatomy. More important, the aneurysm and the direct surroundings have to be analyzed.

We developed the FAUST framework to support the clinician with free-form sketching. With the possibility of 3D annotations, various options are considered, e.g., different stent configurations, coil lengths and access paths. The framework also favors the evaluation of patient-specific spatial anatomy and can reveal branching arteries.

### 3. Related Work

This section comprises related work of labels as a form of annotations in immersive environments as well as sketch-based interfaces. Additionally, we describe how curved structures from medical image data are unfolded. Lastly, animations are discussed for a seamless blending of structures from their original, curved shape to a flattened one.

Annotations in medicine are primarily used as textual labels to support education [17]. They are either visualized as internal labels on the structure’s surface or beneath them as external labels [18]. Recently, labeling approaches were used in immersive environments. Tatzgern et al. [19] use automatically placed labels in an augmented reality to annotate 3D structures with images and texts. Nowke et al. [20] use automatically placed labels in a CAVE (cave automatic virtual environment). In contrast, an *interactive positioning* of labels avoids the usage of a complex label layout algorithm, but introduces challenges regarding user interaction. An example of interactively placed annotations is the work from Assenmacher et al. [21]. They

present a framework for various types of annotations including different input and output metaphors. The comparison of Madsen et al. [8] shows that directly placing annotations in object space instead of image space leads to the best performance for label location tasks. Our goal is not only to locate existing annotations, but also to create them in object space.

Sketching is related to labels in terms of enriching medical data with meta information. For example, sketching is used as an intuitive interaction technique to annotate medical reports [6] or to segment structures in 2D image data [22]. In clinical practice, sketching is also an easy supplement for patient education or interchange with the medical staff. Another possibility is using *Sketch-based Interfaces for Modeling* (SBIM) [23] to directly create medical structures, e.g., branching vessels with integrated blood flow [24]. Fleisch et al. [9] describe a *3D sketching* environment and try to close the gap between 2D sketching and 3D modeling in an immersive environment for designers. They present techniques for creating and modifying 3D curves, such as stroke splitting and oversketching. Saalfeld et al. [25] use a semi-immersive environment to sketch different vascular structures for medical education. Wang et al. [26] and Jackson et al. [27] combine 2D sketching and an immersive environment. The former work allows freehand sketching for cartoonists on a virtual, user-definable 3D canvas, i.e., the user is restricted to a virtual plane. The latter work allows users to import existing 2D sketches and interactively *lift* 2D curves into space to create 3D structures. In our previous work, we presented the concept to sketch treatment methods directly on 3D structures [28]. Perkunder et al. [11] investigated differences of 2D and 3D sketching for modeling in a study. There, sketching in a 3D environment was perceived more stimulating and attractive than under 2D conditions.

Curved tubular structures, such as blood vessels, bronchi or the colon, are of high interest in medicine. For the assessment of these structures, tomographic image data is acquired. However, the necessary information rarely lies in a single image plane, which motivates the unfolding of these structures. An established technique for this limitation is *Curved Planar Reformation* (CPR) [29]. Here, the center line of the tubular structure is derived and flattened. The flattened structure is then mapped into a new, single image providing its longitudinal view. There exist several adaptations of the CPR which focus on specific structures. For example, Williams et al. [30] introduced an extension which is suitable for large, hollow structures such as the trachea or the colon. To investigate the whole tubular structure with these two methods, the visualization has to be rotated around the central axis. An approach to aggregate these rotated images in one image was suggested by Mistelbauer et al. [31]. All these techniques allow a depiction of the unfolded structures in an additional 2D view. However, the task to mentally transfer the distorted unfolded image to the 3D volume rendering view is left to the physician. Neugebauer et al. [32] solved this by embedding a 2D projection of a cerebral aneurysm surface as contextual information around the 3D visualization. Another approach is used by Vilanova et al. [33]. They integrate the unfolding directly into the 3D volume rendering by using the center line of a colon to flatten it for virtual endoscopy. Our so-

lution is based on this idea. However, instead of visualizing the unfolded structure only, we allow the physician to seamlessly blend between the original and unfolded 3D representation in an animated, interactive manner.

To visualize the seamless transition of the original to the unfolded representation, animations may be used. In general, there are two possibilities to represent the animation of 3D meshes: keyframe and skeletal animations [34]. In *keyframe animations*, several sequences of the same but deformed mesh are stored. For the animation, the sequences are played consecutively. This approach is memory-intensive since each mesh has to be loaded during animation. Furthermore, the final result depends on the amount of keyframes, which have to be hand-crafted in a time-consuming process. Therefore, we use skeletal animation, which strongly simplifies the animation procedure and is supported by a wide range of development frameworks. In *skeletal animation*, the original surface representation is provided with a skeleton represented by a set of interconnected bones. As a skeleton, the center line can be employed. Here, each line segment of the center line becomes a bone of the skeleton. In contrast to keyframe animation, the vertices of the surface are not animated directly. Instead, in a process called *skinning*, every vertex is assigned to one or multiple bones with a specific weight. The weight determines how strongly each bone influences a specific vertex. Now the bones are animated and the vertices are transformed accordingly. The results can lead to intersection and distortion artifacts. These are addressed with different approaches, e.g., representing the surface implicitly, calculate the deformations for the implicit representation and transfer the results back to the geometry [35]. The work of Chaudhry et al. [36] compares different techniques regarding efficiency and realism. In our work, we unfold from a folded state and, thus, no intersection artifacts occur.

#### 4. Material

This section describes the process to transform the 3D medical image data of the CoW into a surface model. Afterwards, the workflow to create the animated unfolding vessel is described. The whole process is illustrated in Figure 3.

##### 4.1. Reconstruction of the 3D Surface Mesh

We extract the CoW from a healthy patient’s MRI data set which was acquired for clinical education using the MAGNETOM Skyra 3T (Siemens Healthcare GmbH, Erlangen, Germany) combined with a 20-channel-head/neck coil with a voxel resolution of  $.26\text{ mm} \times .26\text{ mm} \times .5\text{ mm}$ . For the 3D surface mesh extraction, we follow the procedure describe by Glaßer et al. [37]. The mesh was extracted with MeVisLab, a rapid prototyping tool for medical image processing (Fraunhofer MEVIS, Bremen, Germany) by applying a threshold-based segmentation. Subsequently, we smoothed the extracted triangular surface mesh with Sculptris (Pixologic, Los Angeles, U.S.A.) and cutted off unnecessary outlets with Blender (Blender foundation, Amsterdam, the Netherlands). After that, we artificially

modeled an aneurysm and a stenosis based on real clinical patient data. The generated pathologies were approved by an interventional neuroradiologist.

##### 4.2. Unfolding of the Reconstructed Mesh

As discussed in Section 3, we use skeletal animation for the unfolding. Normally, the skeleton consists of a hierarchical set of connected bones. However, the reconstructed CoW is a closed surface with a genus of one, i.e., it has a hole, an automatic procedure to create a center line would result in a cyclic graph instead of a hierarchy. Therefore, we create the animation manually with 3ds Max (Autodesk, Inc., California, U.S.A.). We first create multiple skeletons and attach them to the reconstructed CoW (Fig. 3). After skinning, we manually unfold the skeletons with a combination of forward and inverse kinematics. This process allows us to pay particular attention to prevent strong deformations. Now, we define two keyframe states: one in the original folded state and the second in the unfolded state. We animate the unfolding by interpolating between these two keyframes (Fig. 4). In character animation, the limbs of the initial mesh are normally spread apart, which eases the rigging and skinning process and reduces deformations during animations. This is different for the CoW due to its initial folded state. Yet, the thereby introduced deformations are acceptable even for medical treatment planning. This is due to the fact that the unfolded structure primarily supports the physician to illustrate vessel transitions and spatial relationships, which are persistent even in the unfolded structure. For the original, folded structure, anatomical correctness is required, but this structure is not affected by the deformations.

#### 5. Annotation of Unfolding Vascular Structures

This section comprises details about the used hardware of our 3DUI. Next, the free-form annotations are described, including technical realization aspects, different types of annotations and their visualization. After that, the illustration possibilities of the CoW are explained and the used interaction techniques are described, including the animated unfolding. Our framework is developed with the game engine Unity (Unity Technologies, San Francisco, U.S.A.).

##### 5.1. Input and Output Device

We decided to use the semi-immersive zSpace (zSpace Inc., San Francisco, U.S.A.) system for our FAUST framework. It combines binocular and motion parallax in a fish tank environment, which are important depth cues to support the physician in estimating sizes and relationships of anatomical structures [38]. Fish tank environments are in particular suitable in scenarios where the user manipulates the virtual world from *outside in* and the size of the virtual object is smaller than the user’s body [39], which applies for the CoW. The zSpace’s stereoscopic display renders full HD with 120 Hz. The binocular parallax is achieved with circular polarized rendered images for passive glasses. The glasses are tracked through infrared (IR) markers with 6DoF and enable motion parallax. As input

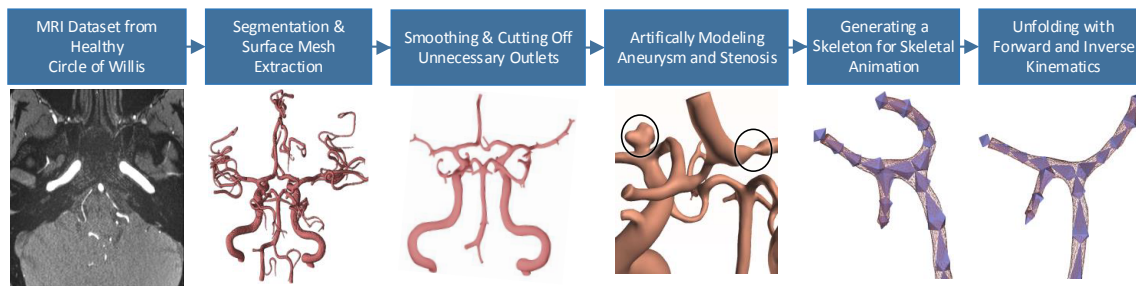


Figure 3: Workflow to create the unfolding Circle of Willis from Magnetic Resonance Images (MRI).

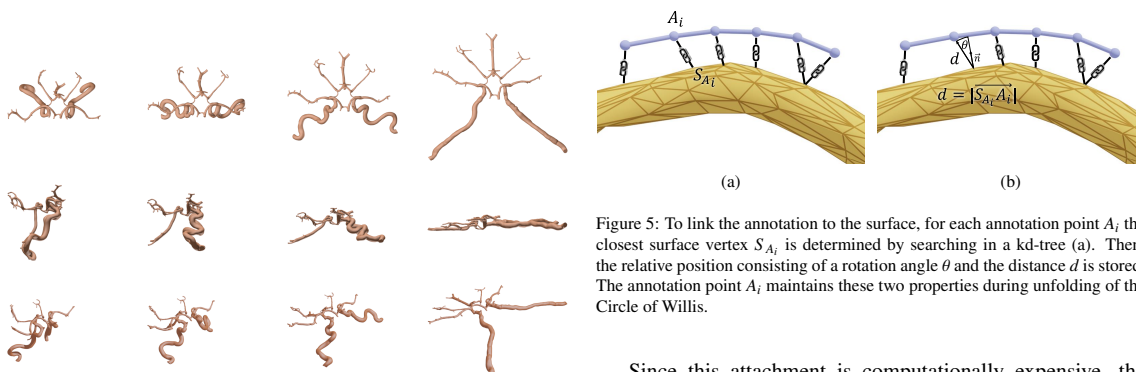


Figure 4: Overview of the animated unfolding from orthographic top (1st row), orthographic left (2nd row) and perspective 3D (3rd row).

device, a stylus connected to the zSpace is used which is tracked with IR LEDs and allows 6DoF interaction. The orientation of the stylus is virtually extended into the rendered scene and is represented as a visible ray to enable ray-based interaction.

### 5.2. Creating and Attaching Annotations

The free-form annotations are created with equidistantly resampled points from the stylus. These points are linked to the 3D surface. Thus, they adapt their position and shape during the unfolding of the CoW. To link the points of the annotation to the surface, for each annotation point  $A_i$  the closest surface vertex  $S_{A_i}$  is used. To find  $S_{A_i}$  in an efficient way, we store all vertices of the surface in a kd-tree. However, the interactive unfolding changes the position of the surface's vertices. Therefore, an adjustable amount of kd-trees in different unfolding states is generated and stored in a list. If the user starts annotating, the current unfolding state is compared with states in the list. The most similar state and, thus, kd-tree is selected. Now, a relative description between  $A_i$  and  $S_{A_i}$  is necessary. First, the distance  $d = |\overrightarrow{S_{A_i}A_i}|$  is calculated. Then, the angle between the normal  $\vec{n}$  from  $S_{A_i}$  and the vector  $\vec{v} = \overrightarrow{S_{A_i}A_i}$  is calculated as  $\theta = \angle(\vec{n}, \vec{v})$  and stored as a quaternion. During unfolding, we ensure that this relative description, i.e., the distance  $d$  and  $\theta$  are maintained. This process is illustrated in Figure 5.

Figure 5: To link the annotation to the surface, for each annotation point  $A_i$  the closest surface vertex  $S_{A_i}$  is determined by searching in a kd-tree (a). Then, the relative position consisting of a rotation angle  $\theta$  and the distance  $d$  is stored. The annotation point  $A_i$  maintains these two properties during unfolding of the Circle of Willis.

Since this attachment is computationally expensive, the number of annotation points is critical. However, a reduced amount of points leads to a visual unpleasing representation of annotations. In general, the amount of sample points could be reduced by discarding points which do not contribute to the general shape, e.g., with the Douglas-Peucker Algorithm [40]. However, such approaches are not appropriate for our scenario due to the animated unfolding inducing a non-rigid change of the annotation shape. Therefore, we equidistantly resample the points. This is realized by discarding all points which exhibit a distance to their neighbors that falls below a certain threshold  $t$ . If the user moves the stylus very fast, this threshold is exceeded. In this case, additional points are generated between the last and newest point. This fast and simple resampling method is only problematic if either the threshold  $t$  is too large and, thus, no detailed annotations can be sketched or if the sampling rate is too low during fast sketching. We empirically determined  $t$  by sketching coils, which are the thinnest structures and require the most details. Since our framework allows real-time sketching with this threshold, the first problem is addressed. To assess the sampling rate of the stylus in combination with sketching speed, we sketched several annotations in fast speed. Here, we measured a covered distance of approximately 19 cm/s. The stylus is tracked with 100 Hz, i.e., a sampling point is created around every 19 mm. This distance is sufficient for annotations with low curvature, e.g., stents and access paths. For annotations with higher curvature, the physician usually pays particular attention on details and, therefore, sketches with less lower speed.

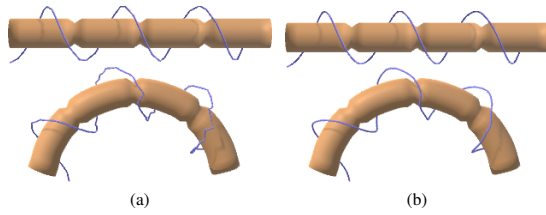


Figure 6: The illustration shows a bended tubular shape surrounded by a spiral free-form annotation. The distortion of the annotation during bending is shown for no smoothing (a) and 5-neighborhood Gaussian smoothing (b).

During the unfolding, undesired effects could hamper the visualization of the sketches, i.e., a sketched straight line in the unfolded state could result in a zig-zag line in the folded state. To weaken this effect, we smooth the visual representation of the annotation points with 5-neighborhood Gaussian smoothing (Fig. 6).

### 5.3. Types and Visualization of Annotations

The user can create three different types of annotations: generic annotations, stents and coils. This differentiation is chosen based on typical tasks in treatment planning. Stents and coils are the most common treatment options. For heterogeneous tasks, such as highlighting important regions and illustrating access paths, our generic annotations are a flexible tool to sketch different configurations. For all types, we procedurally generate a cylindrical surface mesh along the sketched line in real-time. This allows us to support depth perception by applying shading techniques to the 3D surface. Furthermore, the radius of the cylindrical surface can be adjusted. Thus, the user can sketch stents with varying diameters for different vessels or thin coils inside an aneurysm. To aid the user in the process of sketching, annotations can be constrained to lay on the planning model's surface. This helps to, e.g., illustrate an access path along a vessel. For the *generic annotations*, the user can choose between four different colors. All colors are rendered with an illustrative cel-shading [41] to support visual differentiation between the CoW and generic annotations. A silhouette further improves the contrast between the vessel structure and background. To annotate the vascular structure with *stents*, we applied a grid texture to the cylindrical surface. By using the alpha channel of the texture, the user is able to look through the struts, which results in a realistic stent illustration. Here,  $x$  and  $y$  texture coordinates are necessary. These are calculated during sketching by increasing the  $x$ -coordinate along the sketched path. The  $y$ -coordinate is mapped around the 360 degrees of the cylinder. For *coils*, a brushed metal texture is applied with the same approach. Additionally, metal shading properties are applied to the shader. All sketching types are shown in Figure 7.

### 5.4. Visualization of the Vascular Structures

The CoW is visualized with a physically-based rendering to obtain a realistic surface representation. This technique simulates the behavior of light more realistically. For example, the

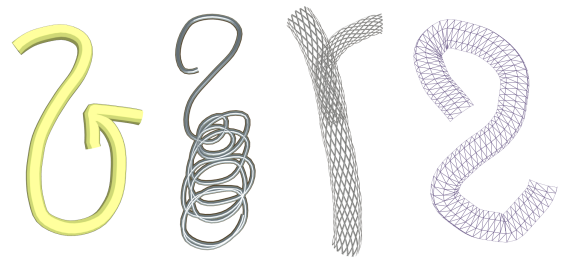


Figure 7: An overview of different annotation types from left to right: generic yellow annotation, coil, stent. The last image shows the wireframe of our procedurally generated cylinder.

idea of energy conservation is used, e.g., less light is reflected than received, specular light minimizes the diffuse amount of light and a Fresnel effect is added (the surface becomes more reflective at grazing angles) [42]. This representation is further improved with a texture. In contrast to the annotations, the texture coordinates cannot be calculated directly, since the vessel and its branches can be arbitrarily located. A time-consuming approach to set these coordinates is to create them in a 3D modeling application. We choose an automatic approach from procedural terrain modeling, i.e., tri-planar texture mapping [43]. Here, the normal of each vertex is mapped to a texture on the  $x$ -,  $y$ -, and  $z$ -plane. The resulting color is a weighted combination of the three texture colors. This weight depends on the amount the normal is facing in one of the directions. For example, if the normal is facing exactly to the  $z$ -direction, only the color of the  $x$ - $y$ -plane would be taken into account. The same technique is used for a normal map to give the impression of depth on the vascular surface. To allow the users to draw inside the CoW, we let them choose between two visualizations: a fully opaque one and a shading technique which reveals the inside of the vessel. In Figure 8, the two visualization techniques with and without texture and normal mapping are depicted.

### 5.5. Interaction Techniques

#### 5.5.1. Translation and Rotation

The interaction technique to translate and rotate objects commonly used (e.g., by all shipped zSpace demonstrations) is a direct ray-based one. There, the stylus is virtually extended into the scene. By pressing a stylus button, the object is pinned to the virtual ray. Now, every stylus movement results in a translation and rotation of the CoW. Although this interaction technique was understood immediately in our user tests, participants had problems to rotate the CoW accurately. Therefore, we decoupled translation and rotation by triggering each transformation with a different stylus button (Fig. 9). If the translation button is pressed, the position of the virtual ray tip  $T$  is used to calculate the stylus' movement delta  $\vec{m}$  with  $\vec{m} = \overrightarrow{T_{start}T_{end}}$ . The object is then translated by the amount of  $\vec{m}$ . For rotation, we used the Arcball 3D technique, since it was preferred when it was compared to direct interaction in a study conducted by Katzakis et al. [44]. Here, the structure is surrounded by an invisible sphere. The intersection point  $P_i$  of the ray and the

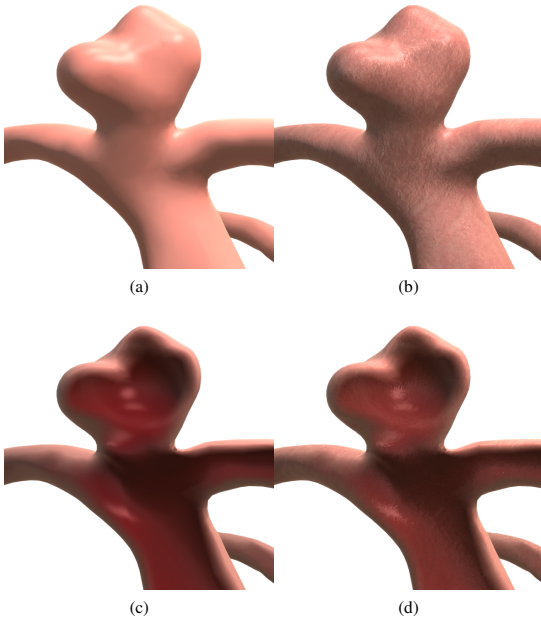


Figure 8: The physician can choose between an opaque (a, b) and semi-transparent (c, d) visualization of the vascular structure. To improve the visualization, we applied a texture and bump map to the surface via tri-planar texture mapping (b, d).

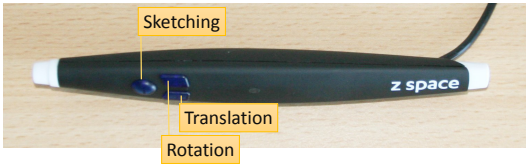


Figure 9: The zSpace's stylus with the assigned functions to the different buttons.

sphere surface is used to calculate the rotation delta  $\alpha$ . If the rotation button is pressed, the vector  $\vec{v}_1$  is determined with the sphere center  $S_c$  as  $\vec{v}_1 = \overrightarrow{S_c P_i}$ . During movement of the stylus, the new vector  $\vec{v}_2 = \overrightarrow{S_c P_{iNew}}$  is calculated. The rotation axis  $\vec{R}$  is extracted as  $\vec{v}_1 \times \vec{v}_2$  and the rotation angle  $\alpha$  is defined as  $\alpha = \angle \vec{v}_1 \vec{v}_2$ . The translation and rotation are illustrated in Figure 10.

To support the physician maintaining an overview of the CoW's orientation, a torso with synchronized orientation is visualized in the right bottom corner (see Figure 11). Additionally, the physician can reset the view by pressing a button that restores the initial frontal view.

### 5.5.2. Animated Unfolding

For the animation of the unfolding CoW, a slider widget is used (Fig. 11). The value of the slider is mapped to 0 and 1, representing the two keyframe states (0: original and folded,

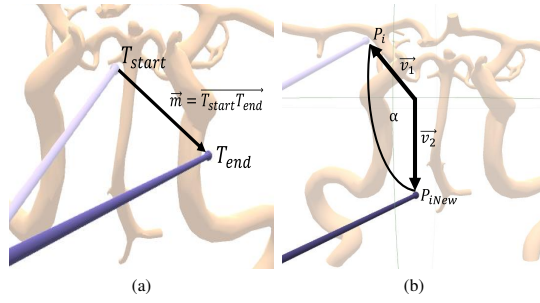


Figure 10: The translation is realized by moving the 3D object about the movement delta of the ray tip (a). For rotation, the Arcball 3D technique [44] is used, where the rotation is derived from the ray intersection with an invisible bounding sphere (b).

1: unfolded, recall Section 4.2) of the skeletal animation generated in 3ds Max. If the slider value is changed, the position and orientation of every skeleton's bone is interpolated to this value, resulting in a transforming CoW. The value is continuously approached over time to guarantee a smooth transition without abrupt changes of the unfolding state.



Figure 11: A screenshot of the FAUST framework. On the left, the physician can choose between different annotation and visualization types, constrain the sketches to the surface and reset the view. The interactive unfolding is realized with the slider widget at the bottom. The torso at the right bottom illustrates the current orientation of the Circle of Willis.

### 5.6. Using the FAUST Framework for a Y-Stenting Procedure

A possible sequence to plan the Y-stenting procedure with our framework is illustrated in Figure 12. The physician starts by investigating the vascular structures and highlighting pathologies with generic annotations (Fig. 12a). Then, the access paths have to be defined. Here, a completely unfolded CoW allows an easier 3D sketching. Additionally, the annotations are constrained to lie on the surface (Fig. 12b). Now, the Y-stent is placed to treat the aneurysm with a large neck size. Two stents have to be placed with different diameters (Fig. 12c). Finally, the physician reduces the aneurysm inflow by sketching thin coils inside the aneurysm (Fig. 12d).

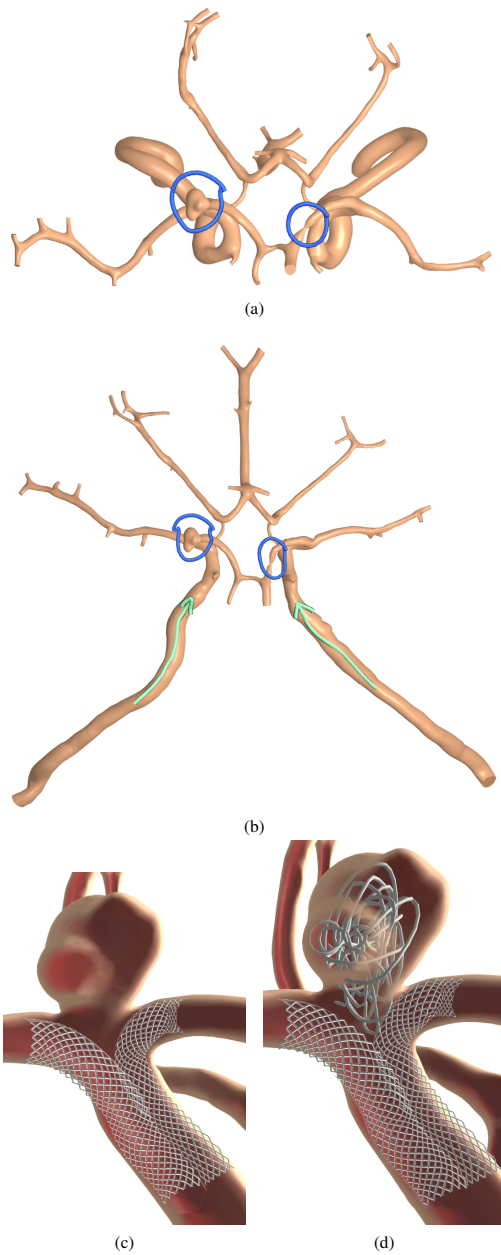


Figure 12: The images illustrate a possible treatment planning of the Y-stenting procedure. In (a) pathologies (an aneurysm and stenosis) of the Circle of Willis are highlighted with generic annotations. The unfolded CoW is depicted in (b). Two possible access paths are sketched on the vascular surface. In (c), the transparent visualization is used to allow the physician to sketch inside. A Y-stent is sketched in the splitting arteries under the aneurysm. The final step of treatment planning, i.e., placing the coil inside the aneurysm, is shown in (d).

## 6. Evaluation

Since our FAUST framework is designed for a specific medical application, the number of potential participants is limited. Additionally, the special hardware setup would not allow, e.g., a web-based study. Therefore, we decided to plan our user evaluation in two steps:

1. Computer scientists (no one is co-author of this paper) with advanced knowledge on vascular systems used our framework to sketch different annotations. Even if these users are no physicians, gaining information about usability and technical aspects of the framework is possible.
2. We performed a demo session and unstructured interview with a potential expert user (co-author of this paper), i.e., an experienced neuroradiologist. Here, the possible benefits achieved with our framework are evaluated.

Finally, we evaluate the performance by measuring the calculation time to attach annotations as well as the frame rate drop caused by adding annotations.



Figure 13: The setup for our user study: the 3DUI zSpace and our running FAUST framework.

### 6.1. User Study

All computer scientists that participated in our user study had basic medical background knowledge on the human vascular system, most common pathologies (aneurysms and stenoses) and treatment options (coiling, clipping and stenting). However, they were unfamiliar with the advanced Y-stenting procedure and the particularities of the CoW (recall Section 2). To account for this, we started our evaluation with an introduction to the vascular system of the CoW, highlighting the stenosis and aneurysm in our CoW surface, as well as describing the Y-stenting to treat the aneurysm. Then, we introduced each participant to the FAUST framework, including a training of interaction techniques to translate, rotate and unfold the CoW followed by an explanation of the 3D sketching. After the training session, we asked each participant to use our framework to plan different treatment options, i.e., sketch access paths and a

Table 1: Years of participants’ experience in domains related to our framework ( $\bar{x}$  – mean,  $s$  – standard deviation).

	<i>min</i>	<i>max</i>	$\bar{x}$	<i>s</i>
Exp. with Medical Applications	1	12	3.9	3.5
Exp. with Scientific Visualization	0	12	4	3.6
Exp. with 3DUIs	0	3	1.2	1

clipping, stenting and coiling procedure. Finally, the treatment planning for Y-stenting of the aneurysm of our CoW was performed.

During the training and treatment planning, the participants were asked to think aloud. After the demo session, a questionnaire was handed out which consisted of three parts:

1. a demographic part including questions regarding years of experience in the field of medical applications, scientific visualization and 3DUIs,
2. questions regarding the usability and user comfort of the unfolding and sketching, as well as
3. the presence questionnaire from Witmer and Singer [45] which quantifies aspects such as realism and the quality of the interface. This questionnaire allowed us to understand the benefit achieved through the zSpace. Some questions did not match our framework, e.g., questions regarding sound or haptic feedback. Hence, these were left out.

The questions of part (2) and (3) were stated with a 7-point Likert scale.

### 6.1.1. Results

Nine participants took part in our study (one female, eight males) with an age between 26 and 38 ( $\bar{x}$  (mean) = 28.8). The experience of our participants in different domains is represented in Table 1.

Although the participants had very little experience with 3DUIs ( $\bar{x}$  = 1.2 years) compared to medical applications ( $\bar{x}$  = 3.9 years), the rating of the interaction techniques was overall positive. This is in particular relevant since a similar experience ratio can be expected by physicians. The simplicity and plausibility of the unfolding were rated with *md* (median) = 3 (*min* = 2, *max* = 3). The question *how naturally the sketching is* was rated with a *md* = 2 (*min* = 0, *max* = 3). This result is promising, since 3D sketching bears the risk to be complicated due to the introduced third dimension. For the presence questionnaire, we combined the questions into the pre-defined categories: *Possibility to Act* (PA), *Realism* (R), *Possibility to Examine* (PE), *Quality of Interface* (QI) and *Self-evaluation of Performance* (SE). The results are summarized in Figure 14. All categories were positively rated, which supports our intention to use the zSpace to make the representation of the CoW more realistic and tangible. The lowest result was achieved in the category QI. The participants had difficulties to locate the stylus tip during the first annotations, which resulted in misplaced annotations. Their comments confirm that this is the reason why QI was rated lower than the other categories.

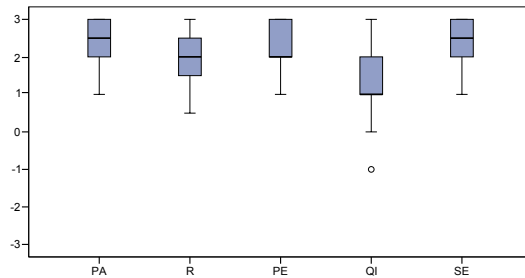


Figure 14: Boxplots summarize the results for different categories of the presence questionnaire [45]: Possibility to Act (PA), Realism (R), Possibility to Examine (PE), Quality of Interface (QI), Self-evaluation of Performance (SE). All categories were rated positively by the majority of our participants. For the categories PA, PE and SE, not all whiskers are visible, since the upper quartile is equal to the maximum. The circle in the category QI marks an outlier.

Five participants commented positively on the representation of the sketches. They stated that the shading supports shape perception and is visually pleasing. Further positive aspects mentioned by the participants are the realistic appearance of the CoW due to shading and fish tank VR as well as the intuitive control of the slider widget. The problems of the first misplaced annotations could be addressed by projecting a shadow of the stylus ray to a plane below the CoW.

## 6.2. Unstructured Interview

The unstructured interview was performed with the neuro-radiologist, who supported us in defining our application scenario (recall Section 2). The setup of the interview is similar to the user study, except that the medical introduction was left out.

### 6.2.1. Results

The physician highlighted the several benefits:

- The sketching works well to describe access paths. The unfolded view supports this even more, because lines to describe the path could be sketched more easily.
- The unfolded state gives a spatial overview of the vascular structure and transitions, which is more difficult in 2D displays.
- The framework supports getting a better understanding of anatomical structures, e.g., the size of the aneurysm neck or the location of small branching vessels. This helps during interventions where the angiographic 2D images lead to occlusion.
- For Y-stenting, it is necessary that both stents end at the same position. Here, the original folded structure could be used to mark this position. The following unfolding supports the estimation of the necessary length of the stents.

Additionally to that, the neuro-radiologist suggested additional features to improve our framework and pointed out drawbacks.

For example, a tool to allow the measurement of vessel diameters would be helpful. Furthermore, the combination of several sketches to realize complex spatial structures is difficult to achieve. He suggested a feature which allows to snap on old sketches or merge points which are close to each other.

### 6.3. Performance

For the performance evaluation we used the same desktop computer as in our user study. It is equipped with an Intel Core i7-2600K (3.7 GHz), 16 GB RAM and a Nvidia Quadro 4000. The most calculation-intensive steps in our framework are the attachment of annotations to the CoW and their non-rigid transformations during unfolding. Each annotation consists of a sequence of connected control points. The number of these points is essential for the performance. However, statements regarding their quantity without considering the resulting annotations would be meaningless. Therefore, we sketched several annotations and counted the control points. To create stents, generic annotations and coils, in average 30, 40 or 250 control points are necessary. Thus, for one annotation approximately  $(30 + 40 + 250)/3 = 107$  control points are used.

To quantify the performance, we logged the time that is necessary to attach 107 control points on our CoW mesh with 33653 vertices and 65514 triangles. This took on average 151 ms. Since the attachment is performed after the physician finishes sketching, this time is almost unnoticeable. Additionally, we analyzed the frame rate of our framework during interaction and unfolding. Initially, FAUST runs with 30 frames per second (FPS). We measured the frame rate after adding control points in steps of 500. The performance drop was around 1 FPS every 500 control points, i.e., at 2000 added control points, 25 FPS were achieved. With 4500 control points, the framework runs at 20 FPS. FAUST is impractical to use below 15 FPS, which happens if more than 7000 control points are used. Using the approximated control point number of an annotation, this means  $7000/107 = 65$  annotations could be added until the framework is unusable. Our tests and interview with the neuroradiologist show, that not even one third of 65 annotations is used, i.e., our framework runs at usable frame rates for treatment planning.

## 7. Integration into Clinical Practice

To introduce our framework into clinical practice, several aspects have to be considered. The most important ones are:

1. the acquisition costs,
2. available space,
3. familiarization to the 3D display, glasses and ray-based interaction techniques as well as
4. the time pressure in clinical routine.

We discussed these issues with our clinical partners. The acquisition costs of the zSpace are moderate compared to other hardware in interventional radiology. If available space is problematic, the zSpace display is usable as a normal 2D display and, thus, can replace the existing one used for treatment planning.

The polarized glasses are the most invasive component, since they darken the view of the physician. This would be problematic during interventions; for planning alone, it is acceptable. Regarding the familiarization aspect, innovations in interventional radiology are common. Therefore, neuroradiologists are used to invest learning time for new technology. The fundamental precondition for this is that the introduced technology is beneficial for the patient, e.g., regarding risk minimization during interventions. The same argument applies for the time pressure during clinical routine. If the framework supports patient safety, this is more important than short planning times. To assess these aspects, we have to evaluate this in further studies. Considering the general possibility to fit in additional planning, this is possible for either elected and critical cases. For elective cases, where sufficient planning time is available, the treatment usually starts with medication for several days before an intervention. In this period, our Faust framework can be used for treatment planning. Even for critical cases, where an aneurysm is ruptured, it is not unusual to observe the patient overnight and start with treatment the next day. Even in this period, the application of our framework is possible.

## 8. Conclusion

Complex structures, such as patient-individual vessel trees with pathologies, require an excellent knowledge of the spatial variations and the 3D extent. At the example of the CoW with two pathologies, we investigated the possibility to support physicians in treatment planning. Our FAUST framework allows to freely create 3D sketches and, thus, enables the physician to annotate structures with a wide variety of different treatment options. Through our interactive unfolding, the whole CoW can be investigated at once and occlusions can be resolved. Conventional imaging cannot depict the same information, e.g., digital angiography yields a projection image with superimpositions and tomographic image data is not sufficient for assessing bended vessel structures.

The evaluation with computer scientists and a neuroradiologist indicates the usability of our interaction techniques as well as the usefulness of our framework for treatment planning.

Our FAUST framework was evaluated with the application of cerebral aneurysms, but it can be adapted to a wide range of complex anatomical structures, including treatment of vascular diseases in general or an unfolding colon. Here, other dynamic data can be used, such as time varying data of a beating heart. For future work, we want to investigate the usage of our framework in the area of patient documentation. The possibility to preserve a wide variety of annotations together with a 3D representation of the structure could greatly improve documentation.

### Acknowledgment

This work was partially funded by the *German Federal Ministry for Economic Affairs and Energy* (grant number 'ZF4028201BZ5') and the *German Federal Ministry of Education and Research* within the research campus *STIMULATE* (grant number '13GW0095A').

## References

- [1] Preim B, Botha CP. *Visual Computing for Medicine: Theory, Algorithms, and Applications*. San Francisco, CA, USA: Morgan Kaufmann Publishers Inc.; 2013.
- [2] Rössling I, Cyrus C, Dornheim L, Boehm A, Preim B. Fast and Flexible Distance Measures for Treatment Planning. *International Journal of Computer Assisted Radiology and Surgery* 2010;5(6):633–46.
- [3] Klein J, Friman O, Hadwiger M, Preim B, Ritter F, Vilanova A, et al. Visual computing for medical diagnosis and treatment. *Computers & Graphics* 2009;33(4):554–65.
- [4] Krüger A, Kubisch C, Strauß G, Preim B. Sinus Endoscopy - Application of Advanced GPU Volume Rendering for Virtual Endoscopy. *IEEE Transactions on Visualization and Computer Graphics* 2008;14(6):1491–8.
- [5] Jorge J, Samavati F. *Sketch-based Interfaces and Modeling*. Springer London; 2011.
- [6] Reiner B, Siegel E. Radiology Reporting: Returning to Our Image-Centric Roots. *American Journal of Roentgenology* 2006;187:1151–5.
- [7] Hartmann K, Götzelmann T, Ali K, Strothotte T. Metrics for Functional and Aesthetic Label Layouts. In: *Proc. of Smart Graphics*. Springer-Verlag; 2005, p. 115–26.
- [8] Madsen JB, Tatzgern M, Madsen CB, Schmalstieg D, Kalkofen D. Temporal Coherence Strategies for Augmented Reality Labeling. *IEEE Trans Vis Comput Graph* 2016;22(4):1415–23.
- [9] Fleisch T, Brunetti G, Santos P, Stork A. Stroke-input methods for immersive styling environments. In: *Proc. of Shape Modeling and Applications*. 2004, p. 275–83.
- [10] Israel J, Wiese E, Mateescu M, Zöllner C, Stark R. Investigating three-dimensional sketching for early conceptual design results from expert discussions and user studies. *Computers & Graphics* 2009;33(4):462–73.
- [11] Perkunder H, Israel JH, Alexa M. Shape modeling with sketched feature lines in immersive 3d environments. In: *Proc. of Sketch-Based Interfaces and Modeling*. 2010, p. 127–34.
- [12] Gray H, Lewis WH. *Anatomy of the Human Body*. Philadelphia, Lea & Febiger; 1918.
- [13] Kayembe KN, Sasahara M, Hazama F. Cerebral Aneurysms and Variations in the Circle of Willis. *Stroke* 1984;15(5):846–50.
- [14] Ujiie H, Sato K, Onda H, Oikawa A, Kagawa M, Takakura K, et al. Clinical analysis of incidentally discovered unruptured aneurysms. *Stroke* 1993;24(12):1850–6.
- [15] Bederson JB, Connolly ES, Batjer HH, Dacey RG, Dion JE, Diringer MN, et al. Guidelines for the Management of Aneurysmal Subarachnoid Hemorrhage: A Statement for Healthcare Professionals From a Special Writing Group of the Stroke Council, American Heart Association. *Stroke* 2009;40(3):994–1025.
- [16] Vlak MH, Algra A, Brandenburg R, Rinkel GJ. Prevalence of unruptured intracranial aneurysms, with emphasis on sex, age, comorbidity, country, and time period: a systematic review and meta-analysis. *Lancet Neurol* 2011;10(7):626–36.
- [17] Oeltze-Jafra S, Preim B. Survey of Labeling Techniques in Medical Visualizations. In: *Proc. of Eurographics Workshop on Visual Computing for Biology and Medicine (EG VCBM)*. 2014, p. 199–208.
- [18] Götzelmann T, Ali K, Hartmann K, Strothotte T. Form follows function: Aesthetic interactive labels. In: *Proc. of Computational Aesthetics in Graphics, Visualization and Imaging*. 2005, p. 193–200.
- [19] Tatzgern M, Kalkofen D, Grasset R, Schmalstieg D. Hedgehog Labeling: View Management Techniques for External Labels in 3D Space. In: *IEEE Virtual Reality*. 2014, p. 27–32.
- [20] Nowke C, Schmidt M, van Albada SJ, Eppler JM, Bakker R, Diesmann M, et al. VisNEST - Interactive analysis of neural activity data. In: *IEEE Symposium on Biological Data Visualization*. 2013, p. 65–72.
- [21] Assenmacher I, Hentschel B, Ni C, Kühlen T, Bischof C. Interactive Data Annotation in Virtual Environments. In: *Proc. of Eurographics Conference on Virtual Environments*. 2006, p. 119–26.
- [22] Heckel F, Moltz JH, Tietjen C, Hahn HK. Sketch-Based Editing Tools for Tumor Segmentation in 3D Medical Images. *Computer Graphics Forum* 2013;32(8):144–57.
- [23] Olsen L, Samavati FF, Sousa MC, Jorge JA. Sketch-based modeling: A survey. *Computers & Graphics* 2009;33(1):85–103.
- [24] Saalfeld P, Baer A, Preim U, Preim B, Lawonn K. A Sketch-Based Interface for 2D Illustration of Vascular Structures, Diseases, and Treatment Options with Real-Time Blood Flow; vol. 598: chap. *Computer Vision, Imaging and Computer Graphics Theory and Applications: International Joint Conference, Revised Selected Papers*. Springer International Publishing; 2016, p. 19–40.
- [25] Saalfeld P, Stojnic A, Preim B, Oeltze-Jafra S. Semi-Immersive 3D Sketching of Vascular Structures for Medical Education. In: *Proc. of Eurographics Workshop on Visual Computing for Biology and Medicine (EG VCBM)*. 2016, p. 123–32.
- [26] Wang M, Fei G, Xin Z, Zheng Y, Li X. 3d freehand canvas. In: *Proc. of Technologies for E-Learning and Digital Entertainment*. 2008, p. 602–12.
- [27] Jackson B, Keefe DF. Lift-Off: Using Reference Imagery and Freehand Sketching to Create 3D Models in VR. *IEEE Trans Vis Comput Graph* 2016;22(4):1442–51.
- [28] Saalfeld P, Glaßer S, Beuing O, Grundmann M, Preim B. 3D Sketching on Interactively Unfolded Vascular Structures for Treatment Planning. In: *IEEE Symposium on 3D User Interfaces (3DUI)*. 2016, p. 267–8.
- [29] Kanitsar A, Fleischmann D, Wegenkittl R, Felkel P, Gröller ME. CPR: Curved Planar Reformation. In: *Proc. of IEEE Visualization*. 2002, p. 37–44.
- [30] Williams D, Grimm S, Coto E, Roudsari A, Hatzakis H. Volumetric curved planar reformation for virtual endoscopy. *IEEE Transactions on Visualization and Computer Graphics* 2008;14(1):109–19.
- [31] Mistelbauer G, Morar A, Varchola A, Scherthaner R, Baclija I, Köchl A, et al. Vessel Visualization Using Curvicircular Feature Aggregation. *Computer Graphics Forum* 2013;32(3):231–40.
- [32] Neugebauer M, Gasteiger R, Beuing O, Diehl V, Skalej M, Preim B. Map Displays for the Analysis of Scalar Data on Cerebral Aneurysm Surfaces. In: *Computer Graphics Forum (EuroVis)*; vol. 28 (3). 2009, p. 895–902.
- [33] Vilanova Bartoli A, Wegenkittl R, König A, Gröller E. Nonlinear virtual colon unfolding. In: *Proc. of IEEE Visualization*. 2001, p. 411–579.
- [34] Lobao AS, Evangelista BP, Grootjans R. *Beginning XNA 3.0 Game Programming: From Novice to Professional*. 1st ed.; Berkely, CA, USA: Apress; 2009.
- [35] Vaillant R, Barthe L, Guennebaud G, Cani MP, Rohmer D, Wyvill B, et al. Implicit Skinning: Real-time Skin Deformation with Contact Modeling. *ACM Trans Graph* 2013;32(4):125:1–125:12.
- [36] Chaudhry E, Bian S, Ugail H, Jin X, You L, Zhang JJ. Dynamic skin deformation using finite difference solutions for character animation. *Computers & Graphics* 2015;46:294–305.
- [37] Glaßer S, Hoffmann T, Voß S, Klink F, Preim B. Extraction of Patient-Specific 3D Cerebral Artery and Wall Thickness Models from 2D OCT and Structured-Light 3D Scanner Data. In: *Proc. of German Society of Computer- and Robot-Assisted Surgery (CURAC)*. 2016, p. 197–202.
- [38] Baer A, Hübler A, Saalfeld P, Cunningham D, Preim B. A Comparative User Study of a 2D and an Autostereoscopic 3D Display for a Tympanoplastic Surgery. In: *Proc. of Eurographics Workshop on Visual Computing for Biology and Medicine (EG VCBM)*. 2014, p. 181–90.
- [39] Demiralp C, Jackson CD, Karelitz DB, Zhang S, Laidlaw DH. CAVE and Fishtank Virtual-Reality Displays: A Qualitative and Quantitative Comparison. *IEEE Transactions on Visualization and Computer Graphics* 2006;12(3):323–30.
- [40] Douglas DH, Peucker TK. Algorithms for the Reduction of the Number of Points Required to Represent a Digitized Line or its Caricature. *Cartographica: The International Journal for Geographic Information and Geovisualization* 1973;10(2):112–22.
- [41] McGuire M, Fein A. Real-time Rendering of Cartoon Smoke and Clouds. In: *Proc. of International Symposium on Non-photorealistic Animation and Rendering*. 2006, p. 21–6.
- [42] Pharr M, Humphreys G. *Physically Based Rendering, Second Edition: From Theory To Implementation*. Morgan Kaufmann Publishers Inc.; 2010.
- [43] Nguyen H. *Gpu Gems 3*. Addison-Wesley Professional; 2007.
- [44] Katzakis N, Seki K, Kiyokawa K, Takemura H. Mesh-Grab and Arcball-3D: Ray-based 6-DOF Object Manipulation. In: *Proc. of Asia Pacific Conference on Computer Human Interaction*. 2013, p. 129–36.
- [45] Witmer BG, Singer MJ. Measuring Presence in Virtual Environments: A Presence Questionnaire. *Presence: Teleoperators and Virtual Environments* 1998;7:225–40.





# Guidelines for Quantitative Evaluation of Medical Visualizations on the Example of 3D Aneurysm Surface Comparisons

P. Saalfeld<sup>1</sup>, M. Luz<sup>1</sup>, P. Berg<sup>2</sup>, B. Preim<sup>1</sup> and S. Saalfeld<sup>1</sup>

<sup>1</sup>Department of Simulation and Graphics, Otto-von-Guericke University, Magdeburg, Germany  
patrick@isg.cs.uni-magdeburg.de, maria.luz@ovgu.de, bernhard@isg.cs.uni-magdeburg.de, sylvia.saalfeld@ovgu.de

<sup>2</sup>Department of Fluid Dynamics and Technical Flows, Otto-von-Guericke University, Magdeburg, Germany  
philipp.berg@ovgu.de

## Abstract

Medical visualizations are highly adapted to a specific medical application scenario. Therefore, many researchers conduct qualitative evaluations with a low number of physicians or medical experts to assess the benefits of their visualization technique. Although this type of research has advantages, it is difficult to reproduce and can be subjectively biased. This makes it problematic to quantify the benefits of a new visualization technique. Quantitative evaluation can objectify research and help bringing new visualization techniques into clinical practice. To support researchers, we present guidelines to quantitatively evaluate medical visualizations, considering specific characteristics and difficulties. We demonstrate the adaptation of these guidelines on the example of comparative aneurysm surface visualizations. We developed three visualization techniques to compare aneurysm volumes. The visualization techniques depict two similar, but not identical aneurysm surface meshes. In a user study with 34 participants and five aneurysm data sets, we assessed objective measures (accuracy and required time) and subjective ratings (suitability and likeability). The provided guidelines and presentation of different stages of the evaluation allow for an easy adaptation to other application areas of medical visualization.

**Keywords:** evaluation, medical visualization, aneurysm surface comparison

**ACM CCS:** I.3.3 [Computer Graphics]: Picture/Image Generation and Display Algorithms, G.3 Probability and Statistics Experimental Design J.2 Physical Sciences and Engineering Mathematics and Statistics

## 1. Introduction

Medical visualizations are developed to support the in-depth understanding of diagnostic processes, therapeutic decisions and to satisfy intra-operative information needs. Evaluation is mandatory to assess existing visualization techniques, develop new ones, answer research questions and generate and verify postulated hypotheses. Here, a wide variety of evaluation strategies exists. Since the visualization techniques are highly adapted to the specific medical application scenario, prior knowledge is often required, which narrows the range of eligible participants. As a result, many researchers conduct qualitative evaluations with a low number of medical experts to assess the benefits of their visualization technique. However, the acquired results are difficult to reproduce. Furthermore, the medical experts usually are cooperation partners and co-authors

of the presented work, where a subjective bias is hardly avoidable. Hence, quantitative evaluation can objectify research, provide additional information and determine whether a statistically significant difference is achieved.

In this paper, we present guidelines for the statistical evaluation of medical visualizations based on the example of comparative aneurysm surface views. We discuss possible study designs and list common measurable properties to assess users' objective and subjective performance. The subsequent analysis allows for determination of statistical significance.

Our medical application scenario covers intracranial aneurysms. The segmentation of such vessel pathologies is an important research area. To create reproducible results and to reduce the work load of clinicians, automatic segmentations of vascular structures

are desired. Due to patient-specific anatomies and pathologies, such automatic solutions remain challenging, and aiming for a general automatic segmentation framework is probably illusory [LABFL09]. Aneurysms bear the risk of rupture, which may cause severe consequences for the patients. For an improved intervention planning, patient-specific 3D surface models of the aneurysm and the surrounding vascular tree are extracted. They allow for the extraction of morphological parameters [LEBB09] or the simulation of the internal blood flow [BRB\*15]. The results are included into the minimally invasive surgical plan as well as the post-processing applications within the clinical environment.

Our application scenario does not focus on the segmentation technique, but rather on the comparative visualization of different segmentation results. During the segmentation process, the medical expert requires feedback on how parameters influence the segmentation results, since small parameter adjustments may induce enormous changes on the surface mesh. To guide the clinical expert through the process, we developed three different comparative visualization techniques to show surface mesh variations.

Our quantitative evaluation determines the most suitable visualization technique to assess changes in the aneurysm volumes. Here, we consider objective measures and subjective ratings. The visualization techniques are applied to five cerebral aneurysms, each approximated with three slightly different surface meshes.

This work is an extension of our previous work [GSB\*16]. We use the application scenario of cerebral aneurysms to provide three techniques for the visualization of two similar but not identical aneurysm surface meshes, which mutually penetrate and overlap. The additional contributions of this paper are:

- We present comprehensive guidelines to quantitatively evaluate medical visualizations, considering specific characteristics and difficulties. Here, we provide instructions for computer scientists and engineers to carry out statistical evaluation.
- These guidelines are represented as a decision tree, comprising the most common statistical tests. The tree can be used as guidance leading researchers from their research question to the choice of a matching statistical test for the desired quantitative evaluation.
- In addition to the identification of the best suited visualization technique regarding accuracy and required time, we also carry out a quantitative evaluation of user subjective ratings, yielding statistically significant results.
- Finally, we evaluate whether the participants' experience with medical visualizations has a significant influence on their accuracy and required time to decide which aneurysm possesses the larger volume.

## 2. Related Work

In recent years, findings from psychophysical studies were incorporated to enhance 2D and 3D visualizations [BCFW08] influencing also the evaluation process of visualizations. For the assessment of a visualization's suitability and performance, user studies offer a

scientifically sound method [KHI\*03]. Lam *et al.* [LBI\*12] introduced an in-depth discussion of seven evaluation scenarios for information visualization, which are subdivided in scenarios for understanding data analysis processes and in scenarios for visualization evaluation. Their approach focused on evaluation goals and questions that guide the users to select appropriate methods based on the provided context within the different scenarios. Our proposed pipeline can be categorized into the evaluation of user performance, evaluation of visualization type, as well as evaluation of visual data analysis and reasoning. We chose the quantitative statistical evaluation as a goal and provide detailed information as well as the required statistical tests to achieve it.

Isenberg *et al.* [IIC\*13] presented a systematic review of the evaluation practices in visualization. They employed several evaluation categories and concluded that the *Qualitative Result Inspection* was most often used by all reviewed papers. Further emphasis on the evaluation of algorithmic performance as well as an increasing trend in the evaluation for user experience and user performance were reported.

Examples for this quantitative trend in medical visualizations are user studies performed by Gasteiger *et al.* [GNKP10] and Baer *et al.* [BGCP11]. Gasteiger *et al.* evaluated an aneurysm visualization based on the participant's grade of satisfaction w.r.t. depth perception, spatial relationships, flow perception and surface shape. Subsequently, Baer *et al.* [BGCP11] compared this visualization technique against two others and were able to determine statistically significant differences for the visualizations. Borkin *et al.* [BGP\*11] determined which visualization technique of the endothelial shear stress of coronary arteries is best suited. The study provided by Díaz *et al.* [DRN\*15] comprises a test setup to evaluate different shading techniques for volume data sets. Their evaluation included a quantitative statistical analysis as well. The survey by Preim *et al.* [PBC\*16] presents perception-based evaluations of medical visualization techniques focusing on shape and depth cues. They proposed to design studies in such a way that a broad range of users can participate by creating tasks that are solvable with general visual perception abilities. It provides essential aspects of perceptual experiment methods as well as a discussion of the type and setting of an evaluation, stimuli, participants, tasks and major results for selected medical visualization techniques. In contrast, the presented approach focuses more on detailed information about the required tests for a quantitative statistical evaluation, but also provides general information about study design and experimental setup choices.

Visualizations of vessels are often depicted as 3D surfaces due to their complex and patient-individual shape [SOBP07, PO08]. Furthermore, overview visualizations are possible, e.g. the CoWRadar visualization for cerebral vessels [MMNG15]. Since we intend to employ aneurysm surface meshes for morphological analyses and subsequent Computational Fluid Dynamics (CFD) simulations, we focus on 3D surface visualization methods. The depiction of cerebral aneurysms mostly involves the visual representation of hemodynamic parameters, e.g. scalar parameters are displayed via colour-coded surface views [CSP10]. Gasteiger *et al.* [GNKP10] developed an illustrative visualization of aneurysms using a Fresnel shading to reveal the embedded blood flow. This work strongly motivated our visualization technique *Vis<sub>B</sub>*.

One of our visualizations is inspired by the image-based rendering of intersecting surfaces [BBF\*11]. This technique is based on the approach by Weigle and Taylor [WT05]. Next to the integration of additional local distance cues, they enabled interactive manipulation of the surfaces. Geurts *et al.* [GSK\*15] employed a visual comparison of medical segmentation results to allow for an evaluation of the segmentation quality. They provided additional information with landmark-based clustering to detect similar segmentation results. For the visualization itself, a colour-coding of the surface was employed. There also exist illustrative approaches, e.g. the visualization presented by Carnecky *et al.* [CFM\*13]. However, we aim at a fast comparison of cerebral aneurysm volumes. Therefore, we want to reduce the visual complexity and choose the concepts provided by Busking *et al.* [BBF\*11] as inspiration for one of our visualization techniques ( $Vis_C$ ).

Our visualization techniques show different segmentation results from the same patient, which can also be interpreted as uncertainty visualization. Grigoryan and Rheingans [GR04] presented point-based probabilistic surfaces, which visualize surface models of medical structures such as tumors. Hence, the surface points are displaced to reflect the uncertainty at that point. The method by Pöthkow and Hege [PH11] comprises a feature-based visualization for iso-surfaces with uncertainties. Their approach employs colour-coding, glyphs and direct volume rendering.

The presented approach only covers a specific part of a medical application scenario and explains which statistical test can be adapted to evaluate the medical visualization. In the longer term, medical visualization aims at the support of medical decision making. For example, Lang *et al.* [LRHea05] reported a change of operation planning due to the influence of computer-assisted risk analysis.

### 3. Comparative Visualization of Cerebral Aneurysms

This section presents the aneurysm image data, the segmentation process and the three visualization techniques  $Vis_A$ ,  $Vis_B$  and  $Vis_C$ .

#### 3.1. Cerebral aneurysm image data and image processing

Cerebral aneurysms are pathologic dilatations of the cerebral artery walls, which may rupture and cause a subarachnoid hemorrhage with severe consequences for the patient. Treatment is carried out via endovascular intervention or neurosurgical clipping. However, the treatment itself may cause complications such as hemorrhages. To avoid unnecessary treatment, rupture risk assessment is an active clinical research area.

In clinical practice, rupture risk factors mainly comprise the aneurysm's morphology and whether the aneurysm is asymptomatic or symptomatic [WvdSAR07]. Hence, the extraction of aneurysm surface meshes provides additional information such as the evaluation of the ostium area (i.e. the orifice between the aneurysm sac and the parent artery) [LEBB09]. Further research directions involve the simulation of the internal blood flow, since unstable and complex blood flow was correlated with increased rupture risk [CCA\*05].

Again, a patient-specific surface mesh is the prerequisite for volume grid extraction and a subsequent CFD simulation.

For the diagnosis of cerebral aneurysms, rotational angiography (RA) is considered as gold standard imaging method [GLR\*09] due to the high spatial resolution. Based on RA data, the 3D digital subtraction angiography (DSA) data sets are reconstructed. To obtain the slightly similar surface meshes, we exploit the reconstruction process of the RA data from the DSA suite (Siemens Artis zeego, Siemens Healthcare GmbH, Erlangen, Germany). Five patient-specific cerebral aneurysm data sets ( $P_1$ – $P_5$ ) were reconstructed using the Hounsfield Units (HU) setting and three different image characteristics: smooth, normal and sharp [BSV\*17]. The HU kernel is recommended for quantitative measurements. The sharp setting maximizes spatial resolution but yields increased noise levels, whereas the smooth setting reduces artifacts as well as the spatial resolution. A compromise between smooth and sharp is provided by the normal setting [syn16]. The five aneurysms stem from five female patients with mean age of 49 years (range 45–59 years). One cerebral aneurysm was located at the anterior communicating artery, one at the posterior communicating artery, two at the internal carotid artery and one at the bifurcation of the middle cerebral artery. Their size varied from 2.5 to 11.2 mm (mean size). All patients were treated with endovascular coiling.

Reconstructing the RA data,  $P_1$ – $P_5$  with the three different reconstruction modes yields three DSA data sets for each patient. Aneurysm segmentation was carried out via thresholding [GBNP15]. The segmentation and surface mesh generation was performed in MeVisLab 2.7 (MeVis Medical Solutions AG, Bremen, Germany). To provide a visual separation between parent vessel and aneurysm, we extracted an ostium for each patient using Blender 2.74 (Blender Foundation, Amsterdam, the Netherlands). The ostia were extruded to create ruff-like structures in order to support the participants and the evaluation of the aneurysm size. The extraction of surface meshes and ostia is described in more detail in [GSB\*16]. Figure 1 illustrates the aneurysm surface meshes for  $P_1$ – $P_5$  as well as surface meshes for a single patient based on the three reconstruction modes.

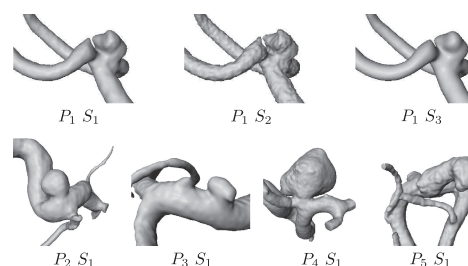


**Figure 1:** Depiction of aneurysm surface meshes. For patient  $P_1$ , the three resulting segmentations  $S_1$ ,  $S_2$  and  $S_3$  based on the three reconstruction modes (HU normal, HU sharp and HU smooth) are shown (top). Surface meshes of the remaining patients  $P_2$ – $P_5$  reconstructed with HU normal are visualized (bottom).

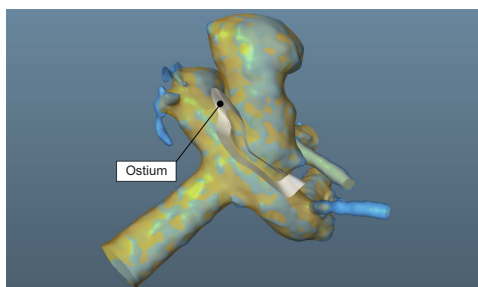


**Figure 2:** Depiction of the iso-surface view  $Vis_A$ . In case the surface mesh of  $A_{Ref}$  exceeds the surface mesh of  $A_{Comp}$ , the orange surface becomes visible. Otherwise, the cyan mesh is visible. The ruff-like structure provides information about the ostium.

### 3.2. Comparative visualization techniques

To evaluate differences of the aneurysm volume, we developed three visualization techniques: the iso-surface view  $Vis_A$ , the boundary-enhancing shading view  $Vis_B$  and the colour-coded map surface view  $Vis_C$ .  $Vis_A$  and  $Vis_B$  show two aneurysms, where the first one is referred to as  $A_{Ref}$ , i.e. the reference aneurysm, and the second one as  $A_{Comp}$ , i.e. the aneurysm for comparison. Note that the ordering of the aneurysms is important, and employing  $A_{Ref}$  first and  $A_{Comp}$  second yields a different visualization result than the usage of  $A_{Comp}$  first and  $A_{Ref}$  second. In the following, the visualization techniques will be described in more detail.

#### 3.2.1. The iso-surface view – $Vis_A$

The iso-surface view is a rather straightforward direct visualization of the two surface meshes of the aneurysms  $A_{Ref}$  and  $A_{Comp}$ . It is realized in MeVisLab using the Open Inventor Library. For  $A_{Ref}$  an orange  $[RGB = (1, 0.33, 0)]$ , and for  $A_{Comp}$  a cyan  $[RGB = (0.33, 0.66, 1)]$  transparent surface mesh is simultaneously visualized with opacity values of 0.5 (see Figure 2). The colour-coding uses complementary colours and accounts for red-green colour blindness. Beyond mesh extraction, no further preprocessing is required.

#### 3.2.2. The boundary-enhanced view – $Vis_B$

The second visualization technique  $Vis_B$  (see Figure 3) is based on the Fresnel shading approach, which was successfully employed for aneurysm visualization comprising an inner blood flow visualization [GNKP10] or the outer vessel wall revealing the colour-coded inner vessel wall [GLH\*14]. This technique is also referred to as ghosted view or x-ray shading. Although we do not include additional information yet, e.g. the inner blood flow, we do integrate this visualization technique in our user study since we are interested in a possible extension of the visualization with the above-mentioned information in the future.

The opacity  $o$  for each surface mesh is assigned in the fragment shader and depends on the normal  $\vec{n}$  and the viewing vector  $\vec{v}$ :

$$o = 1 - (\vec{n} \cdot \vec{v})^f,$$

where  $f$  serves as edge fall-off parameter. This parameter strongly influences the visualization of possible inner structures. We use an empirically determined value of  $f = 0.7$ . The same colours are used for  $Vis_A$  and  $Vis_B$ . The visualization technique is realized in MeVisLab using the Open Inventor vertex and fragment shader modules where the user can directly provide shader code as input.

#### 3.2.3. The map surface view – $Vis_C$

In contrast to  $Vis_A$  and  $Vis_B$ , the map surface view visually provides quantitative information for the distance between  $A_{Ref}$  and  $A_{Comp}$ . For the gathering of the distance information, the estimation of the nearest vertex pairs from  $A_{Ref}$  and  $A_{Comp}$  is carried out. We calculate the normals of the  $A_{Ref}$  surface mesh and approximate the distance based on the intersection with  $A_{Comp}$ . The normals of  $A_{Ref}$  point inwards. If  $A_{Comp}$  is larger than  $A_{Ref}$ , the intersection in negative normal direction is nearer to  $A_{Ref}$ 's vertex than the intersection in positive normal direction and the distance value is stored as negative value. For visual representation, we normalize the extracted distance values to the interval  $[0, 1]$  since we want to store them as texture coordinates. Therefore, we clamp the original distance values to the interval  $[-0.1, 0.1]$  mm (a well suited range for small structures such as cerebral aneurysms) and rescale them to  $[0, 1]$ . Thus, texture values of 0.5 are assigned to parts where the surface meshes of  $A_{Ref}$  and  $A_{Comp}$  have a distance of almost 0 mm. Finally, we employ the colour map depicted in Figure 4 as texture and obtain  $Vis_C$  by using the Open Inventor Vertex Attributes module provided in MeVisLab. The colour map is based on the chosen colours for  $Vis_A$  and  $Vis_B$ . It is designed such that areas where  $A_{Ref}$  is larger than  $A_{Comp}$  are mapped to dark orange, whereas the quantitative distance information is provided by the hue's saturation. Blue areas indicate a larger local extent of  $A_{Comp}$ .

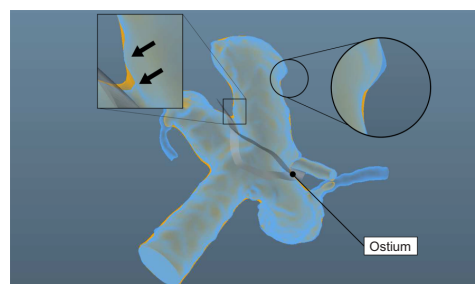


**Figure 3:** Depiction of  $Vis_B$ . The mesh extents become best visible at the boundary of the aneurysm (see circular inlay), which requires an interactive exploration of the 3D scene. The visualization shows a larger aneurysm neck of  $A_{Ref}$  (see rectangular inlay and arrows).

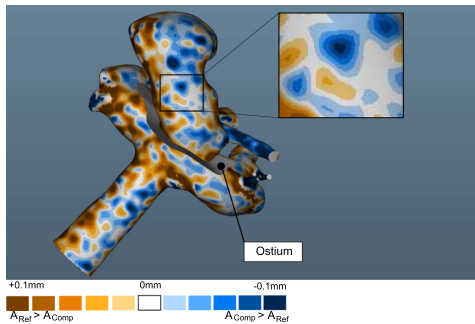


**Figure 4:** Depiction of visualization  $Vis_C$ . Similar to a relief map, colour-coding provides information whether  $A_{Ref}$  or  $A_{Comp}$  is larger. Hence, the colour saturation provides quantitative information.

#### 4. Guidelines for the Evaluation of Medical Visualization

Based on previous evaluation projects, discussions with statistical experts and the studies presented in Section 2, we derive guidelines for the evaluation of medical visualizations. These guidelines are summarized as a decision tree with several stages, see Figure 5, with focus on inferential statistics. These stages are described in more detail in the following.

The most general subdivision of methods is the distinction between quantitative and qualitative methods (Figure 5, Stage 1). While the former allows an analysis of *measurable properties*, the latter investigates *phenomena*. Important to note is that *user subjective ratings*, e.g. assessed with a Likert scale, are measurable properties as well. Quantitative evaluation methods can be applied to measurable properties to determine whether statistically significant findings can be extracted. On the other hand, qualitative evaluation is the right choice for explorative research questions to generate hypotheses as well as to provide basic information for a new application area. For example, if a new medical visualization should be developed, qualitative evaluation can be applied to determine the requirements for the novel visualization. Also, the decision making of a physician can be analysed to get a deeper understanding of the process from initial data inspection to the treatment decision. Here, the think-aloud method can be used to assess the influence of a new visualization technique on the interventional strategy. Our paper focuses on quantitative evaluation on the example of aneurysm surface visualization, i.e. a measurable comparison of different visualization techniques.

The next step for the conduction of the quantitative evaluation is to check whether all requirements are met for inferential analysis (Figure 5, Stage 2). Examples for requirements are a clear hypothesis and a sufficient sample size [Fie09]. If these requirements are not fulfilled, descriptive statistics can be performed, comprising an analysis of the distribution of the data and an evaluation of measures for central tendency and variance. Appropriate visualizations for this information should be provided via box plots, bar charts and histograms. Even for inferential statistics, these visualizations should be presented to support the interpretation of the data.

In the following, the evaluation strategies for inferential statistics are explained in more detail, including problems in the medical fields and suggestions. Due to the wide variety of statistical tests with diverse assumptions about the data distribution, the sample size and the number of compared conditions, we only point out common tests and when to apply them. For a more detailed overview including a justification, we direct the interested reader to the book of Andy Field [Fie09], which includes further references for each test.

##### 4.1. Parametric versus non-parametric tests

Parametric tests, such as a *t*-test, where differences between mean values are investigated, have more statistical power and, thus, a higher probability to reveal possible significances than non-parametric tests. However, they can only be applied if specific requirements are fulfilled, e.g. the sample size is sufficient and the data are scaled appropriately as well as normally distributed (Figure 5, Stage 3). In statistical practice, parametric tests are applied even if requirements are violated with the justification that these tests are robust against these violations [Fie09]. This makes it difficult for non-statistic professionals to decide when, e.g. a deviation from normal distribution is too strong and a sample size is too small, respectively. As a general suggestion, the *measure of central tendency* and the *scaling of the data* should be investigated. Different measures of central tendency comprise the mean, median and mode. A parametric test should only be considered if the *mean* is able to represent the central tendency. An example against this assumption is the usage of a forced-choice Likert scale (i.e. a neutral choice is missing) for data acquisition. Here, the mean value could lie between positive and negative ratings yielding the neutral choice that was prohibited in the initial setup. Thus, a misleading result would be reported. The median would be the appropriate measure of central tendency and a non-parametric test should be used. The scaling of the data can either be discrete (ordinal, nominal) or continuous (interval or ratio scale). For ordinal scaled data, such as ranked lists, the usage of a parametric test is debatable and, if in doubt, a non-parametric test is preferable. For continuous scaled data, a test of normal distribution accompanied by a visual inspection of the histogram should be performed [Fie09]. A possible test for this is the Shapiro–Wilk test, which examines whether the collected data came from a normally distributed population. Here, outliers should be considered as well. The additional visual inspection is necessary, since common small sample sizes in medical visualization rarely result in normally distributed data. Again, if the data significantly deviate from a normal distribution and the visual inspection is debatable, a non-parametric test is the preferable choice.

##### 4.2. Independent, dependent and confounding variables

The controlled variation on the independent variable (also called factor) leads to changes to the dependent variable. In medical visualization, a typical independent variable is the visualization technique, whereas the different techniques are the respective conditions (Figure 5, Stage 4). The number of conditions affects the option to realize a *post hoc* test (see Section 4.6). A possibility for the controlled variation is the usage of an established visualization technique and a new one. This variation influences the dependent

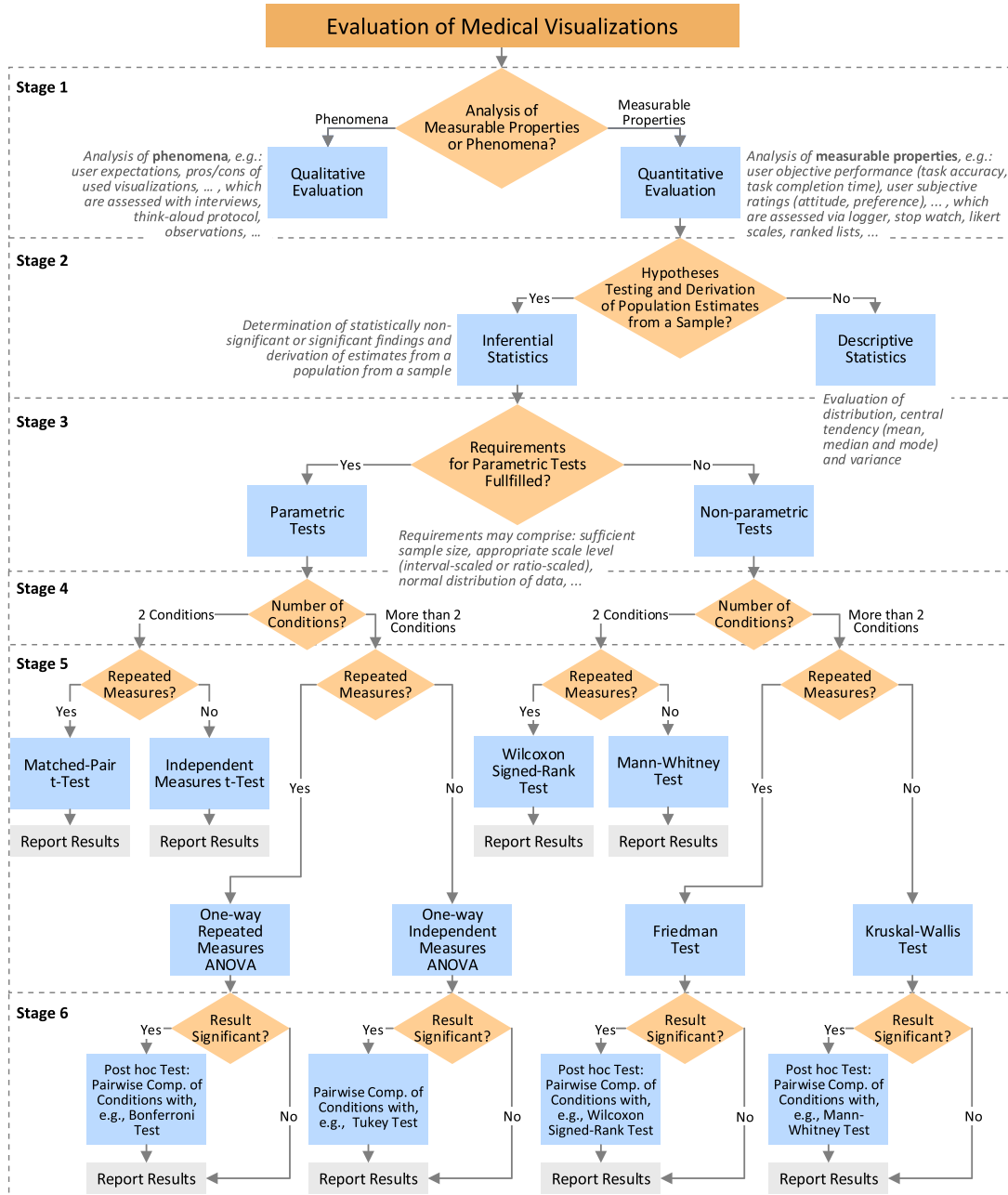


**Figure 5:** Guidelines represented as a decision tree with focus on quantitative evaluation (Stage 1). In Stage 2, the researcher decides if statistical significant findings are relevant or descriptive statistics are sufficient. The chosen statistical test depends on the collected data (Stage 3), the number of conditions (Stage 4) and the type of study (Stage 5). If more than two conditions were tested, post hoc tests are possible (Stage 6).

variable, which can be measured. Examples for dependent variables are objective measures, such as required time, or subjective ratings, such as preferability. The possibilities of an unwanted influence to the dependent variable are called confounding variables. General examples are participant's motivation and study duration, which influence the performance [CW11]. Important confounding variables in medical visualizations are differences in the perception of participants, e.g. colour blindness, or differences on the used output device, e.g. display brightness, size and contrast. Usually, different domain experts, i.e. highly specialized physicians, are asked to participate in the study. Their varying experience also influences the measurement. A general method to reduce the influence of confounding variables is to keep them as constant as possible. This is easier for some than for others. Display types, lighting situation and an overall equal setting can be held constant in usability labs. Differences in experience can be controlled by using questionnaires, which try to quantize the experience to a certain degree. Then, it is possible to restrict the study to participants with similar experience. Another problem arises if a new visualization technique is compared to an established one, which could lead to a novelty bias against the new visualization. Here, thorough training sessions can reduce the bias. Ideally, they are carried out until the learning curve reaches a plateau. In summary, the approach of keeping confounding variables constant does not eliminate them, but exposes every participant equally to them. Thus, variations in the results, e.g. regarding accuracy, are theoretically explained by the studied factors alone. However, by controlling every aspect of an experiment, the external validity is reduced, i.e. how good the results are transferable to clinical practice. Here, researchers have to find the right balance between control and realism or perform several studies with different degrees of external validity.

#### 4.3. Tasks and data sets

An evaluation task should represent main challenges of typical tasks as realistic as possible [CW11]. For medical visualizations, this assumption strongly limits the number of possible participants. A task imitating a real clinical scenario would require the know-how a physician gained during his education, training and experience. This aggravates in case of a special medical field, e.g. cerebral vessel pathologies. Here, an even smaller number of specialized surgeons and radiologists could participate. As a result, statistical analyses would lose power due to the small sample size. Therefore, the task is often approximated such that non-expert users can provide valuable test results. Typical examples for tasks related to medical visualizations are the estimation of size of pathologic structures for diagnosis or perceptually motivated tasks such as depth ordering of complex medical structures for intervention planning [PBC\*16]. However, this limits the relevance and possibility for generalization [Bae15].

In conclusion, multiple similar tasks should be implemented to strengthen the result's plausibility and to enhance the external validity and reliability. For example, different aneurysms can be shown to evaluate a single aneurysm visualization technique. Here, particular care should be taken to create tasks with similar difficulty. Otherwise, this can be the reason for a higher variance in the results. Also, the aggregation of this acquired data should be analysed either run- or participant-related, which is explained in Section 4.5.

#### 4.4. Experimental design

The type of experimental design can be divided into repeated measures design (within-subject), aiming at the variability of a particular value for the same individuals under different conditions, or the independent measures design (between-subject), aiming at differences between groups (Figure 5, Stage 5).

The choice of experimental design depends on the available participants and the evaluation goal. Independent measures studies avoid learning effects and the evaluation time is reduced for each participant compared to repeated measures design. However, groups of similar participants (w.r.t. age, experience, knowledge, etc.) have to be recruited. In the medical domain, these prerequisites are not easily met. Between-subject studies may suffer from interpersonal differences. Within-subject studies avoid these differences. Since they may suffer from learning or sequence effects, special care must be taken for the definition of tasks (e.g. the order of conditions across participants should be balanced) [CW11]. Although repeated measures designs are influenced by intra-personal differences (e.g. getting tired during the experiment), they may be superior to between-subject studies. When the same participants are involved and repeated measures are acquired, the overall variance is reduced and, thus, statistical significance can be reached more easily [Fie09].

In conclusion, repeated measures studies are recommended for the evaluation of medical visualizations due to the reduced variance and a lower number of required participants. However, certain evaluation goals such as the impact of surgical techniques on patients are not possible with repeated measures, since this surgery could only be carried out once for a single patient. An independent measures design should also be used if the risk of strong learning effects is too high. In medical visualization, this occurs if only a few data sets are available, which should be visualized with different techniques. Here, participants are able to recognize the data set and answer according to previous knowledge. Furthermore, an independent measures design is mandatory if the conditions are exclusive properties of the participants, e.g. physicians are either experts or novices. Differences regarding these groups can only be analysed if they are considered independently.

The chosen design ultimately influences the necessary statistical test that should be used to reveal differences between conditions. For example, acquired data that fulfill the requirements for a parametric test with more than two conditions and a within-subject design need to be analysed with a repeated measures ANOVA (an analysis of variance). An overview of the different test possibilities can be found in Figure 5.

#### 4.5. Data aggregation choices

The acquired data of the study can be related to *participants* and to *runs* of a study, respectively. Data sets should be related to participants if the impact of the studied factors (e.g. different visualizations) on participants is investigated. In contrast, if general features of a technical system are evaluated, the results are independent of the participants and, thus, the data sets should be related to single runs. Depending on this distinction, the data should be aggregated or not.

For example, a medical visualization technique should be evaluated. To improve the reliability of the measured results, five runs with different medical data sets are performed. After presenting all data sets, five results are obtained. A common mistake is to handle these five results independently. However, since this evaluation scenario is participant-related, the results must be aggregated to a single value for each participant. Inappropriate data aggregation might bias the results of statistical tests. If ignoring the aggregation of participant-related evaluations, the sample size is artificially enlarged. This leads to an underestimation of the true data variance. Both artificial enlargement of the sample size and the underestimation of variance reasoned by the lack of data aggregation make statistical testing considerably more liberal, i.e. statistically significant results are obtained although no true effects exist [LSM16].

#### 4.6. Using post hoc tests

Post hoc tests can be used optionally and are only possible if more than two conditions exist (Figure 5, Stage 6). More precisely, two conditions can be directly compared with each other (recall the tests contained in Figure 5, Stage 5). For more than two conditions, a first test reveals whether a statistically significant difference exists amongst them. Next, a pairwise comparison is carried out to compare the conditions against each other. For example, a repeated measures ANOVA for three conditions might reveal a significant difference between the conditions. If the researcher wants to identify which condition performed best or worst, the Bonferroni post hoc test is an appropriate method. This test compares pairwise mean values between each two groups with  $t$ -tests. A wide variety of post hoc tests exists [18 in SPSS 22.0 (IBM, New York, NY, USA)], making the right choice difficult. Figure 5 provides an overview of common statistical tests for this purpose. For more details, readers are referred to the book of Andy Field [Fie09].

### 5. Evaluation of 3D Aneurysm Surface Visualization

In the following, our exemplary quantitative user study is presented. We apply our guidelines described in the previous section.

#### 5.1. Participants

The participants were recruited from visitors of the *Long Night of Sciences* in Magdeburg, Germany. During this event, scientific institutes present their research to the general public. The majority of our participants were from the university's computer science and medical engineering departments. As a result, we were able to conduct a user study with 34 participants comprising five female and 29 male participants, with an age ranging from 16 to 66 years.

#### 5.2. Independent and dependent variables

For our application, the independent variable is the aneurysm surface visualization with the three conditions  $Vis_A$ ,  $Vis_B$  and  $Vis_C$  described in Section 3. The influence of experience with medical visualizations is used as a second independent variable. Here, we differentiate the medical visualization experience into the two conditions *MedVisExp* and *NoMedVisExp*. The two dependent variables comprising user

objective performance are *required task completion time* and *accuracy*. The required time is logged after each completion of a task. We instructed our participants to take the time they needed. Accuracy is defined as the number of correct answers, i.e. the number of right decisions whether aneurysm  $A_{Ref}$  or  $A_{Comp}$  is larger. As user subjective ratings, we used *suitability* and *preferability*. The ratings were assessed with a 5-point Likert scale ranging from -- (i.e. not suitable/preferable at all) to ++ (i.e. very suitable/preferable).

#### 5.3. Technical setup

The study was realized with MeVisLab. Thus, each participant was presented with a graphical user interface (GUI), which guided the participants through the study. The user interface was created with a TabView object using hidden tabs. Each time the participant answered a question, the next tab was shown. At first, the TabView comprises slides for medical background information. Since all visualization techniques were implemented in MeVisLab, they could be easily integrated in the TabView GUI as well. Selection of visualization techniques and data sets for the participants was automatically carried out via Python scripts. The logging of participant's inputs and time required for each task were stored as text files.

#### 5.4. Procedure and tasks

The GUI was presented to each participant, starting with a slide for the medical background information. Afterwards, examples of the three different visualizations  $Vis_A$ ,  $Vis_B$  and  $Vis_C$  were shown. Each of the visualizations as well as the interaction, e.g. zooming and rotating, were explained in detail by the supervisor. The participants were also encouraged to explore the scene and get familiar with the user interface for 3D exploration provided by MeVisLab. The test number  $t_i$  was assigned to the  $i$ th participant. Each participant had to solve 18 questions  $q_1$ – $q_{18}$ , i.e. six per visualization, and had to decide which aneurysm possesses the larger volume. Finally, the participants answered a questionnaire comprising demographics questions and user subjective ratings.

#### 5.5. Experimental design

For the comparison of the 3D visualizations, we use a repeated measures design. Here, each experiment is carried out such that all participants are confronted with each visualization technique six times. Thus, the amount of different visualization techniques shown is balanced. As a result, we repeat the question whether  $A_{Ref}$  is larger than  $A_{Comp}$  18 times, which enhances the external validity. To reduce the influence of training or sequence effects, we change the order of the shown visualization techniques as well as the employed patient and segmentation data with *a priori pseudo-randomization*. The pseudo-randomization is provided in detail in our previous work [GSB\*16]. In general, for the  $i$ th test  $t_i$  with questions  $q_1$ – $q_{18}$ , each visualization  $Vis_A$ ,  $Vis_B$  and  $Vis_C$  was shown six times in the pseudo-randomized order. The patient data  $P_1$ – $P_5$  as well as the order of segmentations were alternated. The pseudo-randomization ensures that each participant evaluates different data sets with varying segmentations, i.e. the participant does not see the same visualization technique with the same data sets for  $A_{Ref}$  and

$A_{Comp}$  twice. This also holds for the demonstration of visualizations during the introduction (recall Section 5.4), where the combinations of patient data and visualization techniques were not identical to the ones used in the test.

For the comparison regarding the medical experience, an independent measures design is used. This is necessary, since a participant cannot belong to both groups at the same time.

**6. Results**

Since our evaluation is participant-related, we aggregate the results of single participants (recall Section 4.5). The participants' answers form the set of observations for  $Vis_A$ ,  $Vis_B$  and  $Vis_C$ . We count for each participant how many times he or she correctly answered for each visualization yielding numbers from 0 to 6. We also collect the set of averaged required times  $t_A$ ,  $t_B$  and  $t_C$  that each participant needed for  $Vis_A$ ,  $Vis_B$  and  $Vis_C$ . For each investigated aspect, we formulate the null hypothesis ( $H_0$ ) and alternative hypothesis ( $H_1$ ) explicitly. In the following, we explain the evaluation process according to our guidelines presented in Figure 5. We carry out inferential statistics (Figure 5, Stage 2) for all dependent variables:

- Non-parametric versus parametric tests (Stage 3). We test if the samples fulfill the requirements for a parametric test (properly scaled and normally distributed).
- Analysis of number of conditions (Stage 4). Based on the number of conditions, an appropriate test is chosen.
- Experimental design (Stage 5). We carry out the statistical test depending on the experimental design over all conditions.
- Post hoc test (Stage 6). If the statistical test indicates significant differences amongst the conditions, we carry out a post hoc test. Each condition is compared pairwise to assess the highest and lowest performing condition.

All statistical tests were carried out with SPSS 22.0.

**6.1. Accuracy**

**6.1.1. Differences regarding visualization**

The first analysis determines whether there exists a significant difference between the three visualization techniques w.r.t. the amount of correct answers, which range from 0 to 6. Box plots for the accuracy for  $Vis_A$ ,  $Vis_B$  and  $Vis_C$  are provided in Figure 6 (left).

**Non-parametric versus parametric tests (Stage 3)** We employ the Shapiro–Wilk test separately for  $Vis_A$ ,  $Vis_B$  and  $Vis_C$  to determine whether the amount of right answers is normally distributed. The Shapiro–Wilk test yields the following significance levels:

- 0.003 for  $Vis_A$ ,
- 0.037 for  $Vis_B$  and
- 0.000 for  $Vis_C$ .

Since all visualizations differ significantly from a normal distribution ( $p < 0.05$ ), we use the non-parametric test for comparison.

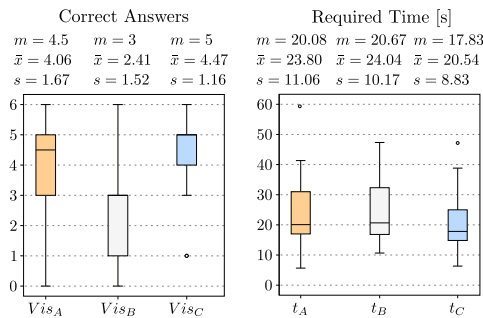


**Figure 6:** Box plots of the accuracy (left) and the required time (right) for  $Vis_A$ ,  $Vis_B$  and  $Vis_C$  including the median  $m$ , the mean  $\bar{x}$  and the standard deviation  $s$  are shown.

**Analysis of number of conditions (Stage 4)** The independent variable *visualization* has the three conditions  $Vis_A$ ,  $Vis_B$  and  $Vis_C$ . Therefore, tests for more than two conditions are considered.

**Experimental design (Stage 5)** According to our guidelines, we use the Friedman test, which compares the conditions based on ranks [non-parametric test, more than two conditions, repeated measures design (recall Figure 5)]. Here, we investigate if the visualization techniques lead to different results regarding accuracy. We define the hypotheses:

- $H_0$ : The participants achieve a similar accuracy with each visualization technique.
- $H_1$ : The participants achieve a different accuracy with the visualization techniques.

The Friedman test reveals that the accuracies significantly differ for the three visualizations ( $\chi^2(2) = 25.38$ ,  $p < 0.05$ ). Therefore, the hypothesis  $H_0$  must be rejected.

**Post hoc test (Stage 6)** Since the visualizations lead to significant differences regarding accuracy, we compare each technique pairwise to identify the most suited. We use the Wilcoxon signed-rank test for  $Vis_A$ ,  $Vis_B$  and  $Vis_C$ , which tests if their mean ranks differ. Because of the multiple tests, we use the Bonferroni correction method, i.e. adjusting the alpha by the number of comparisons (three comparisons yield one-third of  $0.05 = .0167$ ). The amount of correct answers is significantly higher for  $Vis_A$  ( $m = 4.5$ ) than for  $Vis_B$  ( $m = 3.0$ ) ( $Z = -3.76$ ,  $p < 0.0167$ ), where  $m$  denotes the median. Also, the amount of correct answers is significantly higher for  $Vis_C$  ( $m = 5.0$ ) than for  $Vis_B$  ( $m = 3.0$ ) ( $Z = -4.07$ ,  $p < 0.0167$ ). However, there is no significant difference between  $Vis_A$  ( $m = 4.5$ ) and  $Vis_C$  ( $m = 5.0$ ) ( $Z = 0.95$ ,  $p = 0.354$ ). Additionally considering the descriptive results,  $Vis_C$  ( $\bar{x} = 4.47$ ,  $s = 1.16$ ) performed better than  $Vis_A$  ( $\bar{x} = 4.06$ ,  $s = 1.67$ ).

Since  $Vis_B$  lead to the lowest results, we analysed how it compares with random guessing, where guessing would result in three correct answers. A Wilcoxon signed-rank test yields a significant difference ( $Z = -2.09$ ,  $p < 0.05$  with  $\bar{x}_{Vis_B} < \bar{x}_{guessing}$ ). Thus,  $Vis_B$

may systematically influence the participants to provide wrong answers.

### 6.1.2. Differences regarding medical experience

We want to investigate if there are significant differences regarding accuracy reasoned by experience with medical visualizations. The values of all three visualizations were averaged to a single value for each participant.

**Non-parametric versus parametric tests (Stage 3)** Every participant was assigned to one of the two experience groups. Only 10 of 34 participants had experience with medical visualization. Because of the small sample size in the experienced group, a non-parametric test is used.

**Analysis of number of conditions (Stage 4)** The independent variable *MedicalExperience* has the two conditions *MedVisExp* and *NoMedVisExp*. Therefore, tests for two conditions are considered.

**Experimental design (Stage 5)** Since each participant could be clearly matched to one of the experience groups, the measures were not repeated (between-subject). Thus, the Mann–Whitney test was used, which compares the sum of ranks of each group. We define the following hypotheses for experience with medical visualization:

$H_0$ : The experience with medical visualization has no impact on accuracy.

$H_1$ : The experience with medical visualization has an impact on accuracy.

The experience with medical visualization had no impact on accuracy ( $Z = -0.99$ ,  $p = 0.34$ , *MedVisExp*  $\bar{x} = 3.75$ ,  $s = 0.83$ ; *NoMedVisExp*  $\bar{x} = 3.40$ ,  $s = 1.03$ ). Thus, we cannot reject  $H_0$  and, thus, not accept the alternative hypothesis  $H_1$ . Since only two conditions were tested, no post hoc test and fifth stage is necessary.

## 6.2. Required time

### 6.2.1. Differences regarding visualization

We want to analyse whether there is a significant difference between the three visualization techniques w.r.t. the required time. Box plots for the required time for *Vis<sub>A</sub>*, *Vis<sub>B</sub>* and *Vis<sub>C</sub>* are provided in Figure 6 (right).

**Non-parametric versus parametric tests (Stage 3)** Similar to the previous analysis, we first determine whether there is a statistically significant difference between  $t_A$ ,  $t_B$  and  $t_C$ . We employ the Shapiro–Wilk test to determine whether the required times are normally distributed yielding the following significance levels:

- 0.029 for  $t_A$ ,
- 0.007 for  $t_B$  and
- 0.006 for  $t_C$ .

All three variables significantly deviate from a normal distribution ( $p < 0.05$ ). Therefore, we use a non-parametric test for comparison.

**Analysis of number of conditions (Stage 4)** Since the independent variable *visualization* has the three conditions *Vis<sub>A</sub>*, *Vis<sub>B</sub>* and *Vis<sub>C</sub>*, tests for more than two conditions are considered.

**Experimental design (Stage 5)** For the analysis of accuracy regarding the visualization techniques, we use the Friedman test. The corresponding hypotheses are:

$H_0$ : The visualization technique has no impact on the required time.

$H_1$ : The visualization technique has an impact on the required time.

As a result, the Friedman test reveals no significant difference ( $\chi^2(2) = 2.8$ ,  $p > 0.05$ ). Thus,  $H_0$  cannot be rejected. Since no statistically significant difference could be shown, we do not carry out a pairwise comparison of the required time. Comparing the descriptive data  $t_A$ ,  $t_B$  and  $t_C$ , the participants performed the tasks on average faster with *Vis<sub>C</sub>* ( $\bar{x} = 20.54$ ,  $s = 8.83$ ) compared to *Vis<sub>A</sub>* ( $\bar{x} = 23.80$ ,  $s = 11.06$ ) and *Vis<sub>B</sub>* ( $\bar{x} = 24.04$ ,  $s = 10.17$ ), respectively. Comparing the mean values of  $t_A$  and  $t_B$ , the participants required more time to fulfill the tasks with *Vis<sub>B</sub>*.

### 6.2.2. Differences regarding medical experience

Similar to the accuracy, we want to investigate if there are significant differences regarding the required time reasoned by medical visualization experience.

**Non-parametric versus parametric tests (Stage 3) and analysis of number of conditions (Stage 4)** Both stages are identical to the one used for the accuracy (Section 6.1.2). Therefore, a non-parametric test for two conditions is used.

**Experimental design (Stage 5)** We define the following hypotheses:

$H_0$ : The experience with medical visualization has no impact on the required time.

$H_1$ : The experience with medical visualization has an impact on the required time.

Participants with experience in medical visualization performed the task faster ( $\bar{x} = 20.67$  s,  $s = 7.23$ ) than participants without experience ( $\bar{x} = 27.90$  s,  $s = 8.02$ ). This was reflected in a significant result of the Mann–Whitney test ( $Z = -2.55$ ,  $p < 0.05$ ) and the alternative hypothesis  $H_1$  can be accepted. Since only two conditions were tested, no post hoc test is necessary.

## 6.3. Suitability and preferability

We want to investigate if there are significant differences in users' subjective ratings regarding our three visualization techniques. The collected data including the mode value, i.e. the answer (—, —, 0, +, ++) that was given most often for each question as well as the amount of participants that provide answer ++ and + are shown in Figure 7.

236

P. Saalfeld et al. / Guidelines for Evaluation of Medical Visualizations

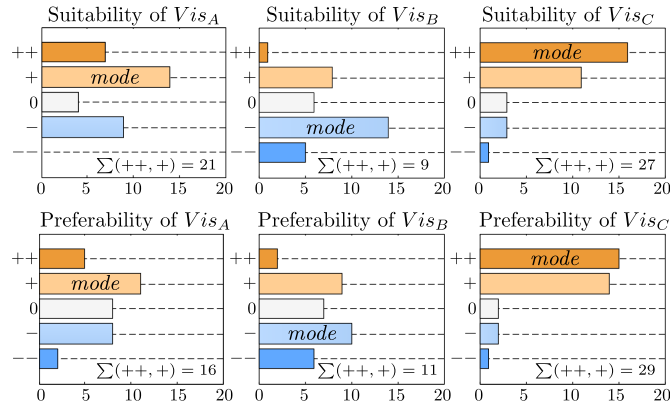


**Figure 7:** Evaluation results of the participants regarding suitability and preferability of  $Vis_A$ ,  $Vis_B$  and  $Vis_C$ . The mode value, i.e. the answer that was given most often for each question, is marked. Furthermore, the sum of answers ++ and + is provided.

**Non-parametric versus parametric tests (Stage 3)** Since the users' subjective ratings were taken with a Likert scale representing an ordinal scale, a non-parametric test is used.

**Analysis of number of conditions (Stage 4)** Since the independent variable *visualization* has the three conditions  $Vis_A$ ,  $Vis_B$  and  $Vis_C$ , tests for more than two conditions are considered.

**Experimental design (Stage 5)** Given three conditions and repeated measures, a Friedman test is used. We define the following hypotheses:

- $H_0$ : Participants perceive the visualizations equally suitable.
- $H_1$ : Participants perceive the visualizations differently suitable.
- $H_0$ : Participants like the visualizations to similar extent.
- $H_1$ : Participants like the visualizations to different extent.

Participants mostly rated  $Vis_C$  with ++ for suitability and preferability,  $Vis_A$  with + for suitability and preferability as well as  $Vis_B$  with - for suitability and preferability. The amount of participants rating  $Vis_C$  as suitable and very suitable (i.e. answers are + or ++) was highest with 27, followed by 21 for  $Vis_A$  and nine for  $Vis_B$ . Similarly, the amount of participants rating  $Vis_C$  as preferable and very preferable (i.e. answers are + or ++) was highest with 29, followed by 16 for  $Vis_A$  and 11 for  $Vis_B$ . These differences were reflected in a significant result for both suitability ( $\chi^2(2) = 21.76, p < 0.05$ ) and likeability ( $\chi^2(2) = 18.37, p < 0.05$ ). Thus, we accept both alternative hypotheses.

**Post hoc test (Stage 6)** Next, we compare the visualization techniques to identify the most suitable and the most preferable one. We apply the non-parametric Wilcoxon signed-rank test. Reasoned by multiple testing, we use the Bonferroni-adjusted alpha (one-third of  $0.05 = 0.0167$ ). Participants perceived  $Vis_C$  significantly more suitable than  $Vis_B$  ( $Z = -3.94, p < 0.0167$ ) and  $Vis_A$  significantly more suitable than  $Vis_B$  ( $Z = -2.68, p < 0.0167$ ).  $Vis_C$  and  $Vis_A$  do not differ in terms of suitability ( $Z = -1.86, p > 0.0167$ ). Al-

though participants consider  $Vis_C$  and  $Vis_A$  equally suitable for size comparison of aneurysms, they like  $Vis_C$  significantly more than  $Vis_A$  ( $Z = -2.80, p < 0.0167$ ). Moreover, participants liked  $Vis_C$  significantly more than  $Vis_B$  ( $Z = -3.66, p < 0.0167$ ). No differences in terms of likeability could be found between  $Vis_A$  and  $Vis_B$  ( $Z = -1.84, p > .0167$ ).

**7. Discussion**

The quantitative statistical analysis revealed significant differences of  $Vis_A$ ,  $Vis_B$  and  $Vis_C$  w.r.t. accuracy, suitability and likeability. The pairwise comparison identifies that  $Vis_B$  performed worst regarding accuracy and suitability. For the required time, no significant differences were revealed. An explanation for this is that the participants were instructed to take as long as they need to choose the larger aneurysm. Although  $Vis_A$  and  $Vis_C$  were better than  $Vis_B$  and achieved similarly good results regarding these aspects, the participants liked  $Vis_C$  significantly more. Considering the central tendency measures alone,  $Vis_C$  is superior concerning all aspects and is therefore the best visualization technique for comparing two aneurysm surfaces. A possible conclusion might be that a derived quantity, i.e. the distance, improves the identification of the larger aneurysm. Additionally,  $Vis_C$  is the only visualization combining both surfaces into one. This may reduce the mental workload and supports perception of differences at the cost of information loss. However, the results indicate that this loss is acceptable.

Our analysis regarding medical visualization experience showed interesting results. Although no statistically significant differences could be identified with or without experience regarding accuracy, participants with experience performed tasks significantly faster. This indicates that participants benefit from prior knowledge.

Remarkably,  $Vis_B$  achieved a lower success rate than guessing. We assume that the participants did not understand the design of  $Vis_B$ . They might wrongly interpret the ghosting view and did not focus on the border areas but instead on areas facing towards them.

These areas are pre-dominantly colour-coded in cyan, since the  $A_{Comp}$  aneurysm is always drawn after the orange  $A_{Ref}$  aneurysm. Hence,  $Vis_B$  is inappropriate for comparison of aneurysm surface volumes.

## 8. Conclusion

The ultimate goal of medical visualization is the application in clinical practice to support diagnosis, treatment planning and fulfill information needs. Beneath qualitative evaluation, which is primarily applied in visualization [IIC\*13], it is necessary to quantify the improvement of a new visualization technique with measurable and comparable properties, especially in accordance with the clinical approval procedure. In consequence, researchers should aim at quantitative evaluations whenever possible. In contrast, usually a small amount of physicians can participate in a study specialized in a sophisticated medical application. To overcome this limitation, the tasks of the user study should be simplified such that they are feasible for a broader range of participants and, thus, a quantitative evaluation. However, this happens at a loss of practical authenticity.

Our proposed guidelines allow for the comparative evaluation of three visualization techniques for the specific application of cerebral aneurysm volume assessment. For the evaluation of the aneurysm volume, the visualization should be reduced to basic information, i.e. no ghosted view techniques should be employed. Providing a colour-coded surface visualization with quantitative distance information, such as our new technique  $Vis_C$ , supports the users in detecting the largest volume. This was reflected by a statistically significantly higher accuracy and better subjective ratings.

For future work, different approaches can be pursued. The visualizations can be improved, for example by including depth cues such as ambient occlusion. Furthermore, a systematic analysis of the influence of the aneurysm volume difference could identify whether a visualization may be well-suited for the depiction of large volume differences, but rather improperly suited for small differences. Finally, we are interested in a more comprehensive analysis on the influence of medical experience. Thus, a more differentiated acquisition should allow for investigation of a possible dependency regarding accuracy and required time. In the bigger picture, a discussion of effect sizes for each result would provide the strength of a significant result and, thus, benefit the comparison of evaluation results across different user studies.

## Acknowledgement

We warmly thank Dr. Alexandra Baer for fruitful discussions and guidance for the evaluation. We thank Nico Merten for supporting us conducting the user study. We also thank the Institute for Neuroradiology, University of Magdeburg, for providing the medical image data. This work was partially funded by the Federal Ministry of Education and Research within the Forschungscampus STIMULATE (grant number '13GW0095A').

## References

- [Bae15] BAER A.: *Perception Guided Evaluation of 3D Medical Visualizations*. PhD thesis, University of Magdeburg, 2015.
- [BBF\*11] BUSKING S., BOTHA C., FERRARINI L., MILLES J., POST F. H.: Image-based rendering of intersecting surfaces for dynamic comparative visualization. *The Visual Computer* 27, 5 (2011), 347–363.
- [BCFW08] BARTZ D., CUNNINGHAM D., FISCHER J., WALLRAVEN C.: The role of perception for computer graphics. *Eurographics (STARs)* (2008), 59–80.
- [BGCP11] BAER A., GASTEIGER R., CUNNINGHAM D., PREIM B.: Perceptual evaluation of ghosted view techniques for the exploration of vascular structures and embedded flow. *Computer Graphics Forum* 30, 3 (2011), 811–820.
- [BGP\*11] BORKIN M., GAJOS K., PETERS A., MITSOURAS D., MELCHIONNA S., RYBICKI F., FELDMAN C., PFISTER H.: Evaluation of artery visualizations for heart disease diagnosis. *IEEE Transactions on Visualization and Computer Graphics* 17, 12 (2011), 2479–2488.
- [BRB\*15] BERG P., ROLOFF C., BEUING O., VOSS S., SUGIYAMA S., ARISTOKLEOUS N., et al.: The Computational Fluid Dynamics Rupture Challenge 2013 – Phase II: Variability of hemodynamic simulations in two intracranial aneurysms. *Journal of Biomechanical Engineering* 137, 12 (2015), 121008/1–13.
- [BSV\*17] BERG P., SAALFELD S., VOSS S., REDEL T., PREIM B., JANIGA G., BEUING O.: Does the DSA reconstruction kernel affect hemodynamic predictions in intracranial aneurysms? An analysis of geometry and blood flow variations. *Journal of NeuroInterventional Surgery* (2017), in print.
- [CCA\*05] CEBRAL J. R., CASTRO M. A., APPANABOYINA S., PUTMAN C. M., MILLAN D., FRANGI A. F.: Efficient pipeline for image-based patient-specific analysis of cerebral aneurysm hemodynamics: Technique and sensitivity. *IEEE Transactions on Medical Imaging* 24, 4 (2005), 457–467.
- [CFM\*13] CARNECKY R., FUCHS R., MEHL S., JANG Y., PEIKERT R.: Smart transparency for illustrative visualization of complex flow surfaces. *IEEE Transactions on Visualization and Computer Graphics* 19, 5 (2013), 838–851.
- [CSP10] CEBRAL J. R., SHERIDAN M., PUTMAN C. M.: Hemodynamics and bleb formation in intracranial aneurysms. *American Journal of Neuroradiology* 31, 2 (2010), 304–310.
- [CW11] CUNNINGHAM D., WALLRAVEN C.: *Experimental Design: From User Studies to Psychophysics*. A. K. Peters, Ltd., Natick, MA, 2011.
- [DRN\*15] DÍAZ J., ROPINSKI T., NAVAZO I., GOBBETTI E., VÁZQUEZ P.-P.: An experimental study on the effects of shading in 3d perception of volumetric models. *The Visual Computer* 33, 1 (2017), 47–61.
- [Fie09] FIELD A.: *Discovering Statistics using SPSS*. Thousand Oaks, California: Sage Publications, 2009.
- [GBNP15] GLASSER S., BERG P., NEUGEBAUER M., PREIM B.: Reconstruction of 3d surface meshes for blood flow

- simulations of intracranial aneurysms. In *Proceedings of Computer and Robotic Assisted Surgery* (Bremen, Germany, 2015), pp. 163–168.
- [GLH\*14] GLASSER S., LAWONN K., HOFFMANN T., SKALEJ M., PREIM B.: Combined visualization of wall thickness and wall shear stress for the evaluation of aneurysms. *IEEE Transactions on Visualization and Computer Graphics* 20, 12 (2014), 2506–2515.
- [GLR\*09] GEERS, A. J., LARRABIDE I., RADAELLI A., BOGUNOVIC H., VAN ANDEL H., MAJOIE C., FRANGI A. F.: Reproducibility of image-based computational hemodynamics in intracranial aneurysms: comparison of CTA and 3DRA. In *Proceedings of IEEE Symposium on Biomedical Imaging: From Nano to Macro* (Boston, USA, 2009), pp. 610–613.
- [GNKP10] GASTEIGER R., NEUGEBAUER M., KUBISCH C., PREIM B.: Visualization of cerebral aneurysms with embedded blood flow information. In *Proceedings of the Eurographics Workshop on Visual Computing for Biology and Medicine* (Leipzig, Germany, 2010), pp. 25–32.
- [GR04] GRIGORYAN G., RHEINGANS P.: Point-based probabilistic surfaces to show surface uncertainty. *IEEE Transactions on Visualization and Computer Graphics* 10, 5 (2004), 564–573.
- [GSB\*16] GLASSER S., SAALFELD P., BERG P., MERTEN N., PREIM B.: How to evaluate medical visualizations on the example of 3D aneurysm surfaces. In *Eurographics Workshop on Visual Computing for Biology and Medicine* (Bergen, Norway, 2016), pp. 153–162.
- [GSK\*15] GEURTS A., SAKAS G., KUIJPER A., BECKER M., VON LANSBERGER T.: Visual comparison of 3D medical image segmentation algorithms based on statistical shape models. In *Digital Human Modeling. Applications in Health, Safety, Ergonomics and Risk Management: Ergonomics and Health*, Vincent G. Duffy (Ed.), Cham: Springer (2015), pp. 336–344.
- [IIC\*13] ISENBERG T., ISENBERG P., CHEN J., SEDLMAIR M., MOLLER T.: A systematic review on the practice of evaluating visualization. *IEEE Transactions on Visualization and Computer Graphics* 19, 12 (2013), 2818–2827.
- [KHI\*03] KOSARA R., HEALEY C. G., INTERRANTE V., LAIDLAW D. H., WARE C.: User studies: why, how, and when? *IEEE Computer Graphics and Applications* 23, 4 (2003), 20–25.
- [LABFL09] LESAGE D., ANGELINI E. D., BLOCH I., FUNKA-LEA G.: A review of 3D vessel lumen segmentation techniques: Models, features and extraction schemes. *Medical Image Analysis* 13, 6 (2009), 819–845.
- [LBI\*12] LAM H., BERTINI E., ISENBERG P., PLAISANT C., CARPENDALE S.: Empirical studies in information visualization: Seven scenarios. *IEEE Transactions on Visualization and Computer Graphics* 18, 9 (2012), 1520–1536.
- [LEBB09] LALL R. R., EDDLEMAN C. S., BENDOK B. R., BATJER H. H.: Unruptured intracranial aneurysms and the assessment of rupture risk based on anatomical and morphological factors: Sifting through the sands of data. *Neurosurgical Focus* 26, 5 (2009), E2.
- [LRHea05] LANG H., RADTKE A., HINDENNACH M., SCHROEDER T., FRUHAUF, N. R., MALAGO M., BOURQUAIN H., PEITGEN H. O., OLDHAFER K. J., BROELSCH C. E.: Impact of virtual tumor resection and computer-assisted risk analysis on operation planning and intraoperative strategy in major hepatic resection. *Archives of Surgery* 140, 7 (2005), 629–638.
- [LSM16] LUZ M., STRAUSS G., MANZEY D.: Impact of image-guided surgery on surgeons' performance: A literature review. *International Journal of Human Factors and Ergonomics* 4, 3–4 (2016), 229–263.
- [MMNG15] MIAO H., MISTELBAUER G., NAŠEL C., GRÖLLER M. E.: CoWRadar: Visual quantification of the circle of willis in stroke patients. In *Proceedings of the Eurographics Workshop on Visual Computing for Biology and Medicine* (Chester, UK, 2015), pp. 1–10.
- [PBC\*16] PREIM B., BAER A., CUNNINGHAM D., ISENBERG T., ROPINSKI T.: A survey of perceptually motivated 3D visualization of medical image data. *Computer Graphics Forum* 35, 3 (2016), 501–525.
- [PH11] PÖTHKOW K., HEGE H.-C.: Positional uncertainty of isocontours: Condition analysis and probabilistic measures. *IEEE Transactions on Visualization and Computer Graphics* 17, 10 (2011), 1393–1406.
- [PO08] PREIM B., OELTZE S.: 3D visualization of vasculature: An overview. In *Visualization in Medicine and Life Sciences*, L. Linsen, H. Hagen and B. Hamann (Eds.), Berlin, Heidelberg: Springer (2008), pp. 39–59.
- [SOBP07] SCHUMANN C., OELTZE S., BADE R., PREIM B.: Model-free surface visualization of vascular trees. In *Proceedings of Eurographics Symposium on Visualization* (CA, USA, 2007), pp. 283–290.
- [syn16] syngo Application Software. Operator Manual, VD11. Siemens Healthcare GmbH, 2016.
- [WT05] WEIGLE C., TAYLOR R. M.: Visualizing intersecting surfaces with nested-surface techniques. In *Proceedings of IEEE Visualization* (Minneapolis, MN, USA, 2005), pp. 503–510.
- [WvdSAR07] WERMER M. J., VANDER SCHAAP I. C., ALGRA A., RINKE G. J.: Risk of rupture of unruptured intracranial aneurysms in relation to patient and aneurysm characteristics: an updated meta-analysis. *Stroke* 38, 4 (2007), 1404–1410.

### Supporting Information

Additional Supporting Information may be found in the online version of this article at the publisher's web site:

### Data S1

### Mini Abstract



# Explorative Blood Flow Visualization using Dynamic Line Filtering based on Surface Features

B. Behrendt<sup>1,2</sup> and P. Berg<sup>1,3</sup> and O. Beuing<sup>1,4</sup> and B. Preim<sup>1,2</sup> and S. Saalfeld<sup>1,2</sup>

<sup>1</sup>Research Campus STIMULATE

<sup>2</sup>Department of Simulation and Graphics, University of Magdeburg, Magdeburg, Germany

<sup>3</sup>Department of Fluid Dynamics and Technical Flows, University of Magdeburg, Magdeburg, Germany

<sup>4</sup>Institute of Neuroradiology, University Hospital Magdeburg, Magdeburg, Germany

---

## Abstract

*Rupture risk assessment is a key to devise patient-specific treatment plans of cerebral aneurysms. To understand and predict the development of aneurysms and other vascular diseases over time, both hemodynamic flow patterns and their effect on the vessel surface need to be analyzed. Flow structures close to the vessel wall often correlate directly with local changes in surface parameters, such as pressure or wall shear stress. Yet, in many existing applications, the analyses of flow and surface features are either somewhat detached from one another or only globally available. Especially for the identification of specific blood flow characteristics that cause local startling parameters on the vessel surface, like elevated pressure values, an interactive analysis tool is missing.*

*The explorative visualization of flow data is challenging due to the complexity of the underlying data. In order to find meaningful structures in the entirety of the flow, the data has to be filtered based on the respective explorative aim. In this paper, we present a combination of visualization, filtering and interaction techniques for explorative analysis of blood flow with a focus on the relation of local surface parameters and underlying flow structures. Coherent bundles of pathlines can be interactively selected based on their relation to features of the vessel wall and further refined based on their own hemodynamic features. This allows the user to interactively select and explore flow structures locally affecting a certain region on the vessel wall and therefore to understand the cause and effect relationship between these entities. Additionally, multiple selected flow structures can be compared with respect to their quantitative parameters, such as flow speed. We confirmed the usefulness of our approach by conducting an informal interview with two expert neuroradiologists and an expert in flow simulation. In addition, we recorded several insights the neuroradiologists were able to gain with the help of our tool.*

Categories and Subject Descriptors (according to ACM CCS): I.3.7 [Computer Graphics]: Three-Dimensional Graphics and Realism—Color, shading, shadowing, and texture I.4.8 [Computer Graphics]: Scene Analysis—Shading

---

## 1. Introduction

For the study of vascular diseases, such as aneurysms, both morphological features and hemodynamic parameters as well as their complex interaction need to be evaluated. More precisely, physicians are often interested in exploring blood flow patterns that cause specific hemodynamic features, such as changes in pressure or wall shear stress, on the vessel wall. Studies have shown that these hemodynamics correlate with the rupture of aneurysms and are therefore vital for risk assessment [CDM\*17, DCHS\*17]. Since both the rupture as well as the treatment procedure can lead to severe consequences for the patient, improved risk assessment helps to optimize patient-specific treatment plans.

A common and accepted visualization for cerebral blood flow is to display the vessel morphology as a 3D model and convey flow

patterns through either stream- or pathlines or map hemodynamic parameters directly onto the surface using a color scale. Pathlines are often filtered by their parameters, such as velocity magnitude or vorticity, to prevent occlusion. However, these filters require a general idea of which flow structures the user expects to find. For an explorative approach, where the physician wants to figure out what kind of flow causes a specific phenomenon on the vessel surface, their usefulness is limited.

In this paper, we present a set of techniques to interactively select and filter flow structures based on their effect on the vessel wall. Our approach combines the tasks of parameter visualization and pathline selection to create an intuitive and robust tool for explorative pathline filtering. By selecting regions on the vessel surface with hemodynamically interesting parameter values, such as local

extrema in pressure or wall shear stress, underlying flow structures are automatically highlighted. These highlights can then be further refined by applying filters based on parameters such as velocity, pressure or residence time.

Our work was designed in cooperation with an experienced neuroradiologist to identify complex interactions between hemodynamic parameters in general. The user's goal is to find flow structures correlating to medically interesting surface features. A general workflow would therefore involve finding those surface features, selecting a subset of them for further investigation and extracting flow structures related to the selected features. Based on this workflow, we identified the following key requirements for our application in cooperation with our clinical partners:

- Req. 1** It should support finding medically interesting surface regions through the visualization.
- Req. 2** The user should be able to easily select one or more surface regions and explore the associated local flow structures.
- Req. 3** To support exploration, the user should have control about what kinds of flow structures are extracted.
- Req. 4** The flow structures extracted from each selected feature should be visually distinguished.
- Req. 5** The user should be able to further explore the extracted flow structures based on their own features.

To evaluate our work, we specifically selected nine datasets, which yielded contradicting results using conventional analysis. The evaluation was carried out with two expert neuroradiologists and an expert of flow simulation. One of the neuroradiologists was involved in the design of our application, whereas the other is completely independent. In the evaluation section, we provide our exploration results for these datasets as well as an informal qualitative evaluation.

During the evaluation, we were able to show that our approach allowed for a systematic exploration and quantitative assessment of flow structures in aneurysms. Interesting structures such as vortices could be reliably detected and comprehensibly visualized, allowing the user to gain insights into the flow patterns both on a local and global scale.

## 2. Related Works

In this section, we discuss previous work on the visual exploration of medical flow with a focus on, but not restricted to, blood flow. Visual clutter is a main problem in 3D visualizations including stream- or pathlines. Interesting structures, such as vortices, are often hidden within other, more laminar flow. Therefore, a variety of methods have been developed to automatically or semi-automatically highlight important flow structures.

Van Pelt et al. introduced an implicit filtering technique by interactively selecting vessel cross sections as seeding planes [vBB\*10]. By positioning these planes the user can gain insights into global flow patterns, such as splitting flow. However, focusing on specific flow structures within these patterns beyond color-coding the flow velocity is not possible.

Gasteiger et al. presented a focus-and-context visualization technique that allows exploring blood flow directly beneath an interest-

ing area on the vessel surface [GNBP11]. By positioning an elliptical "lens" in screen-space, the user can clip away the vessel surface and reveal underlying flow. However, this is limited to the flow directly underneath the selected surface area. There is no way to trace the revealed pathlines to other interesting areas or even through the entire vessel. Additionally, since the lens is placed in screen-space, camera movement may result in an undesired change of the focal region.

Another approach of filtering lines based on screen-space was realized by Lee et al. [LMSC11]. They employed a filtering technique based on screen-space entropy and occlusion to determine whether a pathline should be shown. The calculated screen-space entropy can also be used to determine an optimal viewpoint. A drawback of this approach in an explorative scenario is its lack of real-time capabilities. Since the entropy is determined in screen-space, it has to be recalculated after each change of perspective.

Lawonn et al. used an automatic cut-away technique where the vessel surface is always removed when occluding any pathlines [LGV\*16]. This allows for a simultaneous visualization of blood flow and parameters on the vessel wall, such as thickness. Since the vessel is usually completely filled with pathlines, the lines have to be animated. While this reduces the amount of surface area that needs to be culled, it also prevents the entire flow course from being visible at one time.

Oeltze et al. used clustering to reduce visual clutter in simulated cerebral bloodflow data [OLK\*14]. Pathlines were clustered based on their geometry or attributes and visualized by a single representative for each resulting cluster. In a later publication, Oeltze et al. added dynamic seeding capabilities to better convey complex flow structures such as embedded vortices [OJJP16]. While both approaches highlight existing flow patterns in a dataset, the reduction of each of these patterns to a single line may fail to capture its full structure and shape as well as its relation to the vessel surface.

Instead of highlighting all flow structures present in a cerebral flow dataset, Gasteiger et al. presented a method to specifically extract and visualize the inflow jet and impingement zone in aneurysms [GLv\*12]. Van Pelt et al. extended this approach to allow for a comparative visualization of different stent configurations in the same aneurysm [vGL\*14]. The inflow jets of all configurations are displayed simultaneously using multiple colored arrows. Glyphs are employed for the visualization of the impingement zones from all configurations. Since the resulting visualization is tailored to a very specific application, it is not suitable for a more general, explorative approach.

Zachow et al. used information visualization techniques to explore nasal airflow data [ZMH\*09]. By linking a volume visualization with brush-based selection in parallel coordinates and scatterplots, the user is able to interactively highlight interesting parameter combinations, such as temperature or velocity. Our method allows for parameter selection based on scatterplots or parallel coordinates as well. However, the filtering capabilities of this approach are limited to parameters and cannot take the spatial position of certain flow phenomena into account.

Salzbrunn et al. introduced pathline predicates, a method of grouping vertices in a pathline based on their fulfillment of user-

defined criteria [SS06]. Multiple predicates can be combined using Boolean algebra to create more complex criteria. Born et al. adapted line predicates to support the exploration of cardiac blood flow by designing a set of pre-defined predicates [BPM\*13]. Users could adapt and combine these predicates to suit their specific needs for exploring cardiac flow data. In addition to predicates based on flow structures, such as vorticity or velocity, they also added a region-based predicate that would detect flow that passes by or originates in a certain anatomical area. However, these predicates were designed to work based on entire anatomical regions, such as a specific heart chamber. Therefore, the ability to assess local correlations between surface features and flow structures is restricted. A similar method for 4D PC-MRI data was presented by Broos et al. [BHK\*16]. They employed a user-defined transfer function to determine possible seed points for pathlines from a flow field. In conjunction with a mostly automatic surface visualization, this alleviates the need for a segmentation of the underlying data. Köhler et al. implemented line predicates to extract vortices from cardiac blood flow data [KGP\*13]. Although these vortices are reliably detected, this approach only allows for global filtering. Specifying a region of interest or focusing on only a single vortex that may correspond to a surface feature is not possible.

Meuschke et al. presented a combined visualization of hemodynamic flow and vessel surface information with a focus on near-wall flow [MVB\*17]. To prevent occlusion, the vessel surface is mapped onto a 2D plane and displayed alongside the 3D visualization. This approach focuses on correlating multiple surface parameters, such as wall shear stress and wall thickness. Although wall-near flow is visualized as context information, there is no way to extract flow bundles directly corresponding to interesting local surface features.

A surface-based filtering approach was realized by Neugebauer et al. [NLB\*13]. They employed an automatic detection of potentially interesting surface regions based on the surface geometry, although manual selection of a region is also possible. Instead of filtering existing pathlines according to their distance to the selected region of interest, they dynamically seed new lines close to the region. The generated lines are then classified based on a 2D representation. Further filtering of such a line bundle is not possible.

### 3. Medical Background

Cerebral aneurysms are pathologic dilations of brain-supplying arteries bearing the risk of rupture. Aneurysm rupture is mostly accompanied with subarachnoid hemorrhages that may cause fatal consequences for the patients. The treatment options comprise endovascular intervention and neurosurgical clipping. However, both endovascular and surgical therapy can cause severe complications. In the case of small aneurysms, the complication rate may even exceed the rupture rate [Wie03]. To minimize the risk for the otherwise healthy patients, careful pre-treatment assessment of the rupture risk is mandatory. In clinical practice, the most important rupture risk factors are the type of aneurysm (i.e., asymptomatic or symptomatic), age, sex, and aneurysm size and position [Wvd-SAR07]. Furthermore, morphological parameters, e.g., irregular shape, orientation and diameter [LEBB09] were correlated with rupture risk. However, the study of aneurysm-specific hemodynam-

ics with computational fluid dynamics (CFD) plays an increasing role [XTSM14].

Recent studies reported a correlation between certain hemodynamic information (e.g., concentrated inflow jets, small impingement regions and increased wall shear stress) and prior aneurysm rupture [CDM\*17, DCHS\*17]. However, the clinical application is limited by the lack of an exploration tool that allows a systematic analysis of the complex intra-aneurysmal flow or a detailed, objective and reproducible correlation of qualitative and quantitative parameters. To understand local blood flow phenomena and their impact on local characteristics like pressure or wall shear stress, an adapted exploration technique, as presented in this paper, is required.

### 4. Pre-Processing

In this section, we provide a brief overview about the data acquisition and computational fluid dynamics simulation. Afterwards, we will discuss what parameters are derived from the simulation data.

#### 4.1. Extraction of Simulated Blood Flow

The patient-specific datasets that are considered within this study were acquired using 3D digital subtraction angiography on an Artis Q angiography system (Siemens Healthcare GmbH, Forchheim, Germany). Segmentation was performed using a threshold-based segmentation with the open-source software MeVisLab 2.7 (MeVis Medical Solutions AG, Bremen, Germany). To account for multiple aneurysms, large vascular domains were considered. Hence, small artifacts such as melted vessels or holes, which occurred during the segmentation process, were manually removed on a sub-voxel level [GBNP15].

Before the hemodynamic simulations were carried out, each dataset was spatially discretized using tetrahedral as well as polyhedral elements. In order to account for the occurring velocity gradients, particularly close to the vessel wall, an appropriate grid size of  $\Delta x = 0.1 \text{ mm}$  was chosen [JBB\*13]. This resulted in a number of elements ranging from 5.3 to 8.9 million depending on the domain size.

The subsequent blood flow simulations were performed using the commercial fluid dynamics solver STAR-CCM+ 11 (Siemens Product Lifecycle Management Software Inc., Plano, TX, USA 75024). Here, the governing equations of mass and momentum conservation were solved. Regarding the boundary conditions, flow measurements of a healthy volunteer using 7T phase-contrast magnetic resonance imaging were applied at each inlet cross section [BSJ\*14]. A healthy volunteer provides highly resolved and representative intracranial flow rates, which are adapted depending on the size of the vessel and the locations of interest. Specifically, flow rates are scaled by the corresponding ratio of inflow areas. Acquiring patient-specific measurements is not clinical practice at the moment. Once these measurements are readily available in the future, they can be easily applied as inflow boundary conditions.

All vessel walls were assumed to be rigid, since information about wall thickness and wall properties cannot be extracted from clinical data. The assumption of rigid vessel walls in the context

extrema in pressure or wall shear stress, underlying flow structures are automatically highlighted. These highlights can then be further refined by applying filters based on parameters such as velocity, pressure or residence time.

Our work was designed in cooperation with an experienced neuroradiologist to identify complex interactions between hemodynamic parameters in general. The user's goal is to find flow structures correlating to medically interesting surface features. A general workflow would therefore involve finding those surface features, selecting a subset of them for further investigation and extracting flow structures related to the selected features. Based on this workflow, we identified the following key requirements for our application in cooperation with our clinical partners:

- Req. 1** It should support finding medically interesting surface regions through the visualization.
- Req. 2** The user should be able to easily select one or more surface regions and explore the associated local flow structures.
- Req. 3** To support exploration, the user should have control about what kinds of flow structures are extracted.
- Req. 4** The flow structures extracted from each selected feature should be visually distinguished.
- Req. 5** The user should be able to further explore the extracted flow structures based on their own features.

To evaluate our work, we specifically selected nine datasets, which yielded contradicting results using conventional analysis. The evaluation was carried out with two expert neuroradiologists and an expert of flow simulation. One of the neuroradiologists was involved in the design of our application, whereas the other is completely independent. In the evaluation section, we provide our exploration results for these datasets as well as an informal qualitative evaluation.

During the evaluation, we were able to show that our approach allowed for a systematic exploration and quantitative assessment of flow structures in aneurysms. Interesting structures such as vortices could be reliably detected and comprehensibly visualized, allowing the user to gain insights into the flow patterns both on a local and global scale.

## 2. Related Works

In this section, we discuss previous work on the visual exploration of medical flow with a focus on, but not restricted to, blood flow. Visual clutter is a main problem in 3D visualizations including stream- or pathlines. Interesting structures, such as vortices, are often hidden within other, more laminar flow. Therefore, a variety of methods have been developed to automatically or semi-automatically highlight important flow structures.

Van Pelt et al. introduced an implicit filtering technique by interactively selecting vessel cross sections as seeding planes [vBB\*10]. By positioning these planes the user can gain insights into global flow patterns, such as splitting flow. However, focusing on specific flow structures within these patterns beyond color-coding the flow velocity is not possible.

Gasteiger et al. presented a focus-and-context visualization technique that allows exploring blood flow directly beneath an interest-

ing area on the vessel surface [GNBP11]. By positioning an elliptical "lens" in screen-space, the user can clip away the vessel surface and reveal underlying flow. However, this is limited to the flow directly underneath the selected surface area. There is no way to trace the revealed pathlines to other interesting areas or even through the entire vessel. Additionally, since the lens is placed in screen-space, camera movement may result in an undesired change of the focal region.

Another approach of filtering lines based on screen-space was realized by Lee et al. [LMSC11]. They employed a filtering technique based on screen-space entropy and occlusion to determine whether a pathline should be shown. The calculated screen-space entropy can also be used to determine an optimal viewpoint. A drawback of this approach in an explorative scenario is its lack of real-time capabilities. Since the entropy is determined in screen-space, it has to be recalculated after each change of perspective.

Lawonn et al. used an automatic cut-away technique where the vessel surface is always removed when occluding any pathlines [LGV\*16]. This allows for a simultaneous visualization of blood flow and parameters on the vessel wall, such as thickness. Since the vessel is usually completely filled with pathlines, the lines have to be animated. While this reduces the amount of surface area that needs to be culled, it also prevents the entire flow course from being visible at one time.

Oeltze et al. used clustering to reduce visual clutter in simulated cerebral bloodflow data [OLK\*14]. Pathlines were clustered based on their geometry or attributes and visualized by a single representative for each resulting cluster. In a later publication, Oeltze et al. added dynamic seeding capabilities to better convey complex flow structures such as embedded vortices [OJJP16]. While both approaches highlight existing flow patterns in a dataset, the reduction of each of these patterns to a single line may fail to capture its full structure and shape as well as its relation to the vessel surface.

Instead of highlighting all flow structures present in a cerebral flow dataset, Gasteiger et al. presented a method to specifically extract and visualize the inflow jet and impingement zone in aneurysms [GLv\*12]. Van Pelt et al. extended this approach to allow for a comparative visualization of different stent configurations in the same aneurysm [vGL\*14]. The inflow jets of all configurations are displayed simultaneously using multiple colored arrows. Glyphs are employed for the visualization of the impingement zones from all configurations. Since the resulting visualization is tailored to a very specific application, it is not suitable for a more general, explorative approach.

Zachow et al. used information visualization techniques to explore nasal airflow data [ZMH\*09]. By linking a volume visualization with brush-based selection in parallel coordinates and scatterplots, the user is able to interactively highlight interesting parameter combinations, such as temperature or velocity. Our method allows for parameter selection based on scatterplots or parallel coordinates as well. However, the filtering capabilities of this approach are limited to parameters and cannot take the spatial position of certain flow phenomena into account.

Salzbrunn et al. introduced pathline predicates, a method of grouping vertices in a pathline based on their fulfillment of user-



acquisition and flow extraction, we will begin with the vessel visualization. Starting from there, the structure is as follows:

1. Visualization of the vessel surface with mapped surface parameters
2. Selection of one or more interesting surface regions
3. Extraction of pathlines related to the selected regions
4. Further filtering of extracted pathlines

For each of these steps, we will provide information about the user's interaction possibilities and explain our design decisions as well as the technical implementation.

### 5.1. Vessel Visualization

Initially, the user is presented with an empty visualization of the vessel surface. We employ Phong shading with a single headlight to convey the vessel shape. To prevent the surface from occluding the inner flow that the user will eventually add, it is always rendered semi-transparently. The amount of transparency can be configured, but defaults to an empirically determined value of 33%. While reducing the surface opacity does increase visibility of the inner flow, it also decreases the visibility of lighting effects and therefore reduces shape perception. We therefore decided to adopt a different strategy for applying lighting and transparency to the vessel surface that we call "glass lighting mode".

To emphasize the vessel boundaries even at higher transparency settings, we added a Fresnel effect to the lighting. Similar to [GNKP10], the lighting intensity is then multiplied with the vessel opacity for each vertex, although we consider both the Fresnel and the Phong lighting for this. Regions with strong lighting therefore appear more opaque, highlighting the vessel shape and creating an effect similar to looking through a glass bottle. The glass lighting mode is enabled by default, but can be disabled by the user in favor of using traditional Phong-shading with semi-transparent surfaces. A comparison between both modes can be seen in Figure 2.

To prevent visual clutter from overlapping parts of the vessel, the user can set the backfaces of the vessel to be always fully opaque, despite the previously mentioned transparency setting. This is disabled by default to prevent the user from missing details in the flow that otherwise may be hidden. Figure 2 shows an overview of the effect of this setting both in the traditional as well as the glass lighting mode.

To ensure correct image composition despite multiple, overlaying transparent fragments, we employ Order Independent Transparency (OIT) [Thi11]. Instead of rendering fragments directly into a framebuffer and resolving overlays using a depth test, we write their color and depth values into a shader storage buffer using a linked list structure. Fragments with an opacity of 1% or lower are discarded to reduce memory usage and GPU load during composition, as such fragments barely contribute to the visualization. The final image is composed by a separate fragment shader that is applied to a screen-filling quad, effectively being executed exactly once for each pixel on screen. Using the linked list from the previous rendering stage, the shader gains access to all fragments for the pixel and is therefore able to sort them according to depth and to perform appropriate alpha blending. This results in a correctly

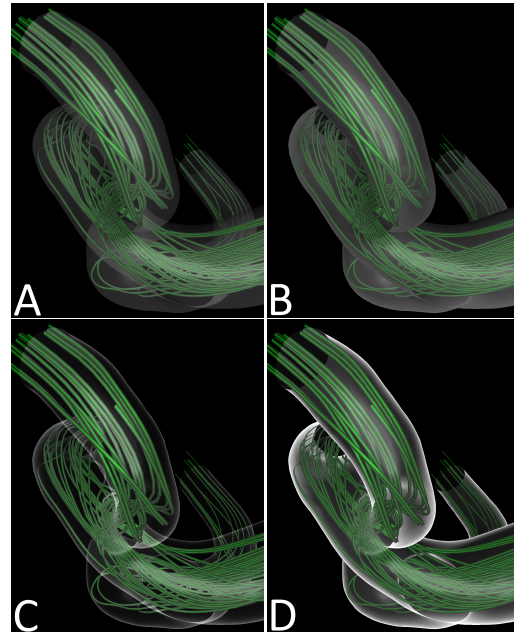


**Figure 2:** Different rendering modes for the vessel surface in the pathline viewer; Disabled (A,B) and enabled (C,D) glass lighting, disabled (A,C) and enabled opaque backfaces.



**Figure 3:** Comparison of parameter visualization using a smooth (left) and discrete color scale with five shades (right).

composed image generated entirely on the GPU without having to perform any pre-processing or ordering on the vertices prior to the rendering step.

### 5.2. Parameter Visualization

To add pathlines to the visualization, the user has to select at least one area on the vessel surface based on surface parameters. When the user is selecting these features on the vessel surface, naturally the surface is considered as the focus object. Therefore, it is now rendered fully opaque and allows mapping parameters using a color scale. The glass lighting mode is not available during this selection.

To map the surface parameters onto a color scale, they are uploaded to the GPU as vertex attributes. The fragment shader re-

B. Behrendt & P. Berg & O. Beuing & B. Preim & S. Saalfeld / Explorative Blood Flow Vis. using Dynamic Surface-based Filtering

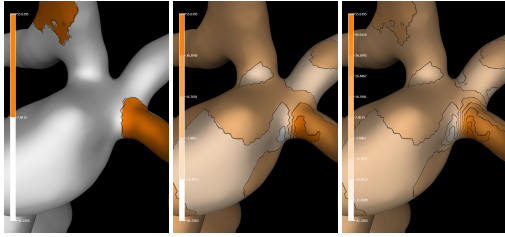


**Figure 4:** Wall shear stress visualized on the vessel surface using a color scale with 2 (left), 5 (middle) and 10 (right) discrete shades ranging from white to orange.

ceives the value range of the active parameter as a uniform variable and calculates the fragment color based on the currently selected color scale. In order to highlight interesting hotspots, which are characterized by local extrema of surface parameter values, we employ discretized color scales. This makes it easier for the user to detect and estimate the size and extent of a hotspot (Fig. 3), therefore fulfilling requirement 1.

The user can freely choose from a set of pre-defined color scales and configure the amount of discrete shades. Figure 4 shows a comparison of different settings for the amount of shades. A higher amount of shades adds more details to the image, but can also lead to a cluttered visualization. To further emphasize the transition between shades, the boundaries are highlighted using black outlines. Our clinical partners were interested in specific parameter ranges, i.e. areas with a normalized wall shear stress value below 20%. To identify these regions, more than five different shades were rarely necessary.

Since the color scale and range settings need to be changed in real-time, the color scale is applied entirely in the fragment shader. Parameter values are normalized to a [0-1] range and uploaded to the GPU as vertex attributes. Settings such as value ranges or the selected color scale are stored as uniform variables for the shader. Therefore, setting changes can be applied without the need to perform any changes to the stored parameter values.

To convey the meaning of the selected color scale, a color legend showing the parameter ranges for each shade is permanently visible on the left side of the image (Fig. 4). Any change to the color scale, the amount of shades or parameter range is reflected on the legend in real time. The selected color scale's domain is initially determined based on the active parameter's value range and can later be adjusted. This is useful in case the parameter value distribution in the dataset does not fully cover the natural range of that parameter or if the user is only interested in a specific sub-range. The adjustment can be performed manually by simply entering new minimum and maximum values, or semi-automatically by basing the scale only on the currently visible surface area instead of the entire parameter range.

Using the latter approach increases the detail dynamically when only a smaller part of the dataset is visible on screen (Fig. 5). To achieve this, the fragment shader responsible for rendering the sur-

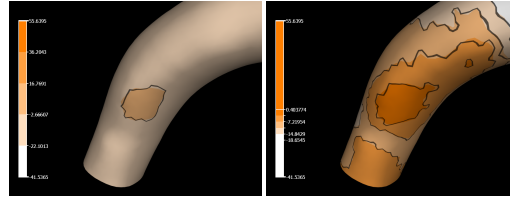


**Figure 5:** Comparison of a color scale mapped to the entire parameter range (left) against only mapping the currently visible range of parameter values (right).

face writes the parameter values it encounters into a buffer using atomic min/max operations. However, it may lead to overestimation of parameter differences, since smaller changes in the parameter value may lead to higher differences in the mapped color. To remedy this effect, the color legend will always show the entire parameter range, clearly indicating that the color scale currently only covers a part of the parameter range (Fig. 5). At any point, the user can fixate the current automatically determined range to prevent it from changing as a result of adjusting the camera.

### 5.3. Surface Patch Selection

When the user clicks on the vessel surface, we determine the vertex closest to the cursor position in screen-space. A simple way to select a feature on the surface would be to place a marker at the position of the closest vertex and then select all adjacent vertices in a specific distance. This type of selection is available in our toolkit but it is not the default setting. We decided against this approach as the primary method to select patches for several reasons. Using a distance threshold based on user input would add another step to the interaction, which we want to keep as simple as possible, according to requirement 2. It may also lead to confusion whether the distance threshold refers to the distance on the surface (resulting in a circular selection) or in 3D space (resulting in a spherical selection around the marker). Additionally, this type of interaction would limit the user to selecting circular or spherical sections of the surface.

Instead, we decided to allow selecting arbitrary regions on the surface. Unlike the approach by Neugebauer et al. [NLB\*13], we decided to base the region selection on hemodynamic instead of geometric features. We presume that a medically interesting region characterized by dissonant geometry would also be characterized by their hemodynamics. Therefore, we derive the selection shape directly from the surface parameter the user has enabled. We determine the color shade of the selected vertex and iteratively search for adjacent vertices with parameter values that would lead to the same color shade, effectively performing a flood fill on the surface (Fig. 6, top middle). Alternatively, the user can choose to also include "higher" or "lower" shades in the selection. This allows selecting arbitrarily shaped regions on the surface using a single click, whereas the parameter visualization itself works as a "selection preview".

We refer to these selections as "patches". It is possible to change

B. Behrendt & P. Berg & O. Beuing & B. Preim & S. Saalfeld / Explorative Blood Flow Vis. using Dynamic Surface-based Filtering

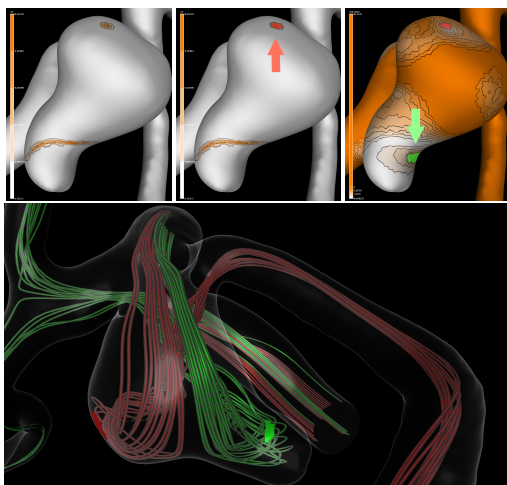


**Figure 6:** Workflow of selecting surface patches; surface visualization without any selection (top left), selection of one patch (red arrow), second selection using a different parameter (green arrow); pathlines passing each of the selected patches highlighted with matching colors (bottom).

the active surface parameter during the selection. Previously created patches will remain, whereas the placement of new patches will be based on the currently active parameter (Fig. 6, top right). We decided against using dynamic surface parameters, as they would likely make both the selection process and interpretation of the results more difficult.

By default, each singular selection creates a new patch. It is also possible to have multiple selections contribute to the same patch, even if the resulting surface is not coherent. If a selection based on surface parameters provides unsatisfactory results, the patch can manually be adjusted by drawing or erasing regions directly on the mesh. Visually, these patches are differentiated using pre-defined colors. Since the association of vertices to their respective patches is stored as flags in a 16 bit integral vertex attribute, it is possible for different patches to overlap. The total number of patches is therefore limited to 16. We assume this technical limitation to be unproblematic, as there would rarely be a situation where the user would need to create more than 16 different patches.

#### 5.4. Pathline Visualization

After the user completes the selection of interesting surface regions, they have the option to select a distance from which to extract pathlines representing the associated blood flow. Only pathlines that come closer to the selected vertices than the distance threshold at least once during their course are selected. The chosen distance can be changed at any time, causing the pathline extraction to be repeated. The extraction is done by building a KD tree from the surface patch vertices and calculating the shortest distance for each

pathline vertex from this patch. Only pathlines where at least one vertex is within the selected distance to the surface patch is included in the line bundle associated with that patch. We decided to use pre-integrated streamlines instead of dynamically seeding new lines close to the selected path due to the explorative nature of our application. Filtering existing pathlines only takes a few seconds, whereas creating new pathlines with dynamic seeding would take significantly longer.

If the user has selected multiple patches on the surface, the distance threshold can be configured individually for each patch. The resulting pathline bundles are colored according to the patches they belong to (Fig. 6, bottom), making them visually distinct (recall requirement 4). Pathlines belonging to different patches can be individually configured, such as by toggling their visibility or mapping parameters to their color, thickness or opacity. The patches themselves are visible on the vessel surface by default, but can also be individually hidden or rendered semi-transparently. This is useful for extensive patches that may otherwise create occlusions.

The pathlines are drawn as lines, then converted into view-aligned quads using the geometry shader. This allows the adjustment of the line on a per-vertex basis and also circumvents OpenGLs limitations on line width. Alongside each vertex, we store the integration time point as a vertex attribute. This allows animating the flow by mapping the temporal distance of the time point stored for each vertex with the current animation time point to opacity. The temporal range for which vertices are visible can be adjusted by the user.

#### 5.5. Pathline Filtering

To further refine the previously selected lines, pathline bundles can be filtered based on their parameters, such as pressure or velocity. This gives the user the ability to restrict the visualization of a previously extracted line bundle to a certain combination of features (requirements 3 and 5).

One way of filtering the bundles is to map their hemodynamic parameters to line thickness or opacity, effectively reducing visibility of lines with certain high or low parameter values. By mapping the residence time of a pathline in an aneurysm to opacity and thickness, for example, it is possible to highlight pathlines that stay inside the aneurysm for a larger amount of time (Fig. 7).

Instead of implicitly filtering pathlines using thickness or opacity, the user can explicitly select parameter ranges in a scatterplot or parallel coordinated view of the current pathline bundle. The scatterplot displays two parameters from the currently selected pathline bundle and allows the user to draw a selection rectangle. To allow filtering based on more than two parameters at the same time, we included a parallel coordinates diagram. The user can select which parameters are shown in this diagram and change their order. For each enabled parameter, they can interactively specify a range to filter pathline vertices.

Both the scatterplot and parallel coordinates diagram are synchronized. When the user performs a range selection on one parameter in a diagram, the selection is propagated to the other. In the parallel coordinates diagram, all lines belonging to a selected vertex are highlighted.

B. Behrendt & P. Berg & O. Beuing & B. Preim & S. Saalfeld / Explorative Blood Flow Vis. using Dynamic Surface-based Filtering

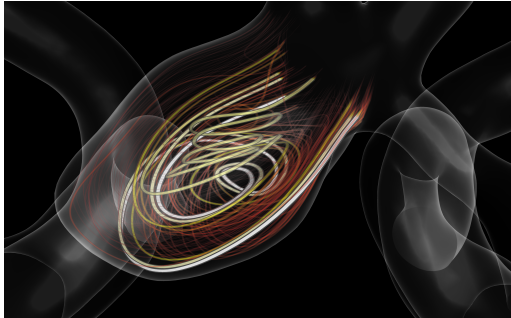


**Figure 7:** Visualization highlighting long-residing flow in an aneurysm by mapping residence time on line width, opacity and color (temperature scale) at the same time.

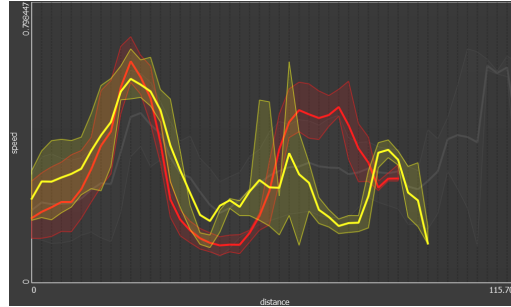


**Figure 9:** Line chart comparing two pathline bundles with the global set of pathlines with respect to their speed and flow distance.

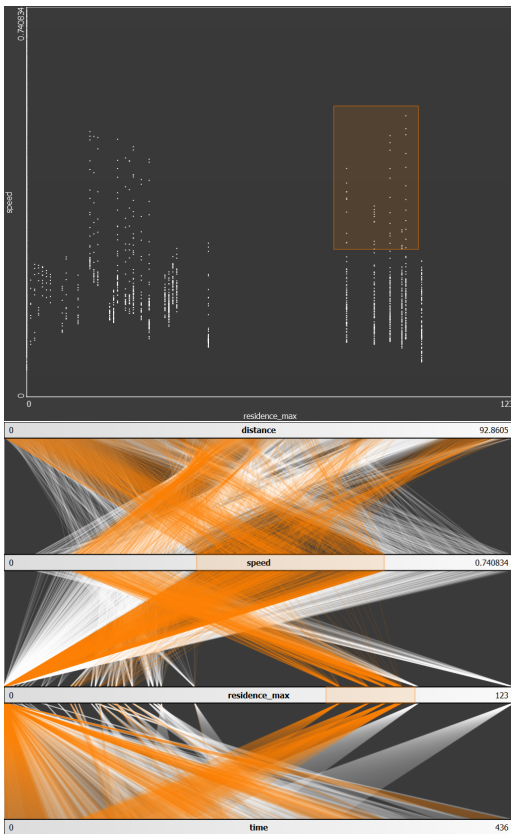


**Figure 8:** Scatterplot and parallel coordinates view showing three parameters of the same line bundle with synchronized selection.

To quantitatively compare two pathline bundles, they can both be plotted in a line chart (Fig. 9). Here, one parameter of each bundle (such as speed) is plotted either over time or flow distance with respect to their average, minimal and maximal value as well as their 25% quantile, median and 75% quantile. Each of these metrics can be individually toggled by the user. Figure 9 shows the area between the average speed as well as the 25% and 75% quantile of two line bundles (red and yellow) and the complete set of pre-integrated pathlines (grey) plotted over the flow distance. The graphs use the same color as the pathlines in the 3D visualization.

Once the user has performed a selection in any of the diagrams, the 3D view will be updated accordingly. There are several different ways in which highlighting or culling a certain parameter range can be performed (Fig. 10). The first method is vertex-based selection (Fig. 10, A and D). In this mode, only vertices matching the selected parameter ranges will be kept. While this approach represents the user's selection exactly, it tends to produce very short line segments in some areas (Figure 10, A). The line-based selection mode keeps an entire line if at least one vertex fits the parameter range (Fig. 10, B and E). This solves the problem of having very short line segments, but can lead to confusion as to which exact part of a pathline actually lies within the parameter range. The third mode is a combination of both previous modes. Like in the line-based mode, the entire line is kept. Additionally, vertices matching the parameter range are highlighted with white outlines (Fig. 10, C and F).

In addition to these three modes, the user can also choose how vertices or lines that do not match the parameter range are handled. They can either be removed from the visualization completely (Fig. 10, A-C) or be shown with strongly reduced opacity (Fig. 10, D-F). Completely removing them reduces visual clutter, but may also remove context information about the flow surrounding the selected areas. To convey these rather technical options to the user in an understandable way, they are presented in the user interface using expressive icons (Fig. 10, bottom).

B. Behrendt & P. Berg & O. Beuing & B. Preim & S. Saalfeld / Explorative Blood Flow Vis. using Dynamic Surface-based Filtering

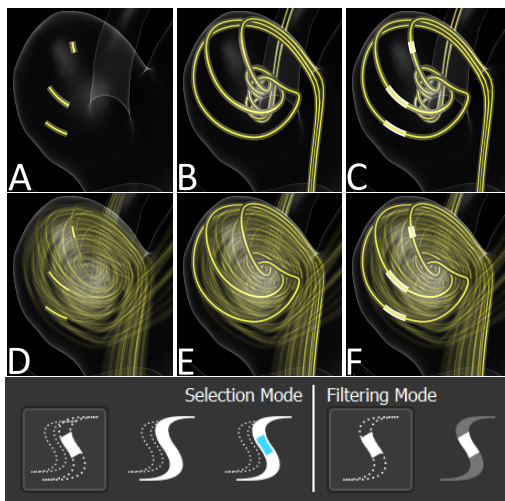


**Figure 10:** The six different combinations of filtering settings; vertex-based selection (A,D), line-based selection (B,E) and line-based selection with vertex highlights (C,F). Vertices / lines outside the selected parameter range are removed completely (A,B,C) or have their opacity reduced to 20% (D,E,F). Icons used to represent these options in the user interface (bottom).

### 5.6. Reverse Surface Selection

The usual workflow involves selecting an interesting surface region and then extracting pathlines that pass this section closely. In some situations, however, physicians would not only be interested in which flow structures cause a specific surface feature, but also what other surface features the selected flow structure may pass. Therefore, it is possible to select additional surface regions based on their distance to an already extracted pathline bundle (Fig. 11).

This is implemented similarly to the way the pathline bundles are selected, except now the pathline vertices are written to the KD tree and compared against the surface vertices. By default, the same distance threshold is used, although this can be adjusted. The user can then map any parameter to the generated surface to look for other interesting surface features (Fig. 11, right). Since we found the black outlines around the different shades of the color scale to be distracting in a view that also includes pathlines, we disabled them by default.

At any point during the described workflow, the user can go back to previous tasks without losing any information. For example, if the pathline filtering pointed the users to possibly interesting surface regions they have not yet selected, they can return to the surface patch selection mode and add additional patches.

## 6. Evaluation

To evaluate our methods, we asked two experienced neuroradiologists and an expert in flow simulation to apply it to nine aneurysms

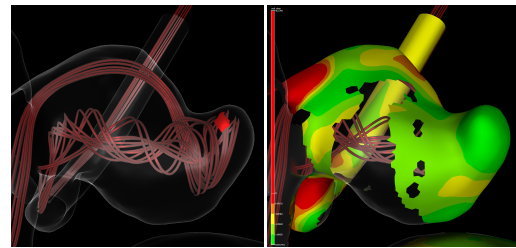


**Figure 11:** Original surface patch used to select a pathline bundle (left); additional surface regions extracted using the same bundle, with wall shear stress mapped to the color scale (right).

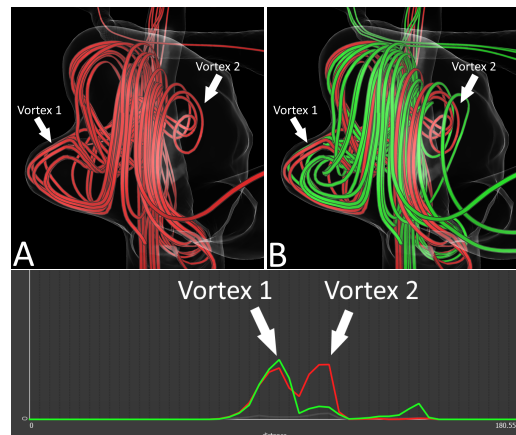


**Figure 12:** Using the line chart plotting average residence time over flow distance to differentiate multiple vortices from a complex flow structure; the line chart (bottom) clearly shows multiple structures being present in a flow bundle (A) and helps creating a selection that only contains one of the structures (B, green lines).

and recorded their findings. Two of these datasets were from a longitudinal study, acquired three years apart from each other. We also asked for general feedback in an informal interview afterwards.

The first neuroradiologist and the flow expert were able to use the tool themselves after a short introduction and demonstration on one dataset. The second neuroradiologist participated over the internet, using remote control. While she gave precise instructions on which patches to select, the actual interaction with the application was performed by us.

All three experts described our method as an advancement in the field of explorative flow visualization. They were able to quickly find interesting surface regions that almost always yielded interesting flow patterns such as vortices when selected. The color-coding proved especially useful for assessing which adjacent vessels a particular flow pattern drains into. According to the experts, a precise

*B. Behrendt & P. Berg & O. Beuing & B. Preim & S. Saalfeld / Explorative Blood Flow Vis. using Dynamic Surface-based Filtering*

selection of specific flow patterns based on their relation to surface features has previously not been possible. They highly appreciated the visualization of splitting flow. Overall, our combination of interaction, visualization and filtering techniques allows for systematic exploration and qualitative assessment of flow structures.

The first neuroradiologist was primarily interested in patches with either high or low normalized wall shear stress or high OSI. His main goal was to correlate vortex structures in the flow with specific hemodynamic parameters on the vessel wall. To facilitate comparability between datasets, the expert used similar or identical parameter ranges for the placement of surface patches and extraction of pathlines. In a few cases, the expert made use of the function to manually draw patches, for example when a patch would otherwise "bleed" into the parent vessel. The expert also used the line chart to determine if a pathline bundle contains more than one actual vortex structure. To correlate features from the line chart with the 3D visualization, the expert used vertex-based filtering (Fig. 10, A). He also used the line chart to determine if a pathline bundle contains more than one actual vortex structure by plotting the residence time over flow distance. Figure 12 shows an example of such a situation from the evaluation. The red line bundle contains two different vortices, which is not instantly obvious due to the complex nature of the flow in the 3D visualization, but clearly visible in the line chart. With this information, the expert was able to add another patch that captures a flow bundle only passing through one of these vortex structures (green line bundle).

Placing a single patch took the expert between 24 and 110 seconds, depending on the complexity of the vessel geometry and if he had to manually draw a patch. Since settings such as mapped surface parameter, number of color scale shades or custom parameter ranges were reset to a default value when switching between datasets, he wished for a way to change the default values or create custom presets to accelerate the process of placing patches.

Figure 13 shows two pathline bundles the first neuroradiologist selected in an aneurysm. The red bundle was selected based on a local pressure minimum, the green bundle based on a wall shear stress minimum. Both the red and green vortices only appear after the blood flow hits the vessel wall. The flow decelerates when entering the aneurysm and accelerates when leaving it (Fig. 13, right). Although the aneurysm is located at a bifurcation, the flow from both vortices drains exclusively into only one of the adjacent vessels.

The second and third dataset were acquired from the same patient at different points in time. The neuroradiologist was therefore interested in visualizing the development of the aneurysm and flow. Since our application did not directly support the comparison of datasets, he improvised by running two instances at the same time and manually adjusting the camera to show a similar angle (Fig. 14). Selecting a patch at a similar location in both datasets allowed for a qualitative comparison of the changes in flow patterns.

The second, independent neuroradiologist was primarily interested in visualizing splitting flow in aneurysms for the purpose of optimal flow diverter placement. She stated that highlighting the splitting flow structures can provide decision support for the placement of flow diverters. Usually, the physician wants to place a flow diverter to reduce pressure from the aneurysm without covering

neighboring vessels completely since this would stop blood supply via these vessels. According to the expert, experienced neuroradiologists are often able to infer this information from the wall geometry alone. However, visualizing the splitting flow could be a valuable help to less experienced neuroradiologists. Since the expert had limited interest in correlating flow structures with surface parameters, she mostly placed patches based on geometric features, such as blebs or the aneurysm dome. When filtering pathline bundles based on their hemodynamic parameters, this expert preferred line-based filtering with reduced opacity for filtered lines (Fig. 10, F) We did not record the time she took for patch selection since the interaction was not performed directly by the expert.

Our method proved to be stable in respect of the parameter chosen for the surface patch selection. Interesting flow structures often manifest in multiple surface parameter changes, either in different locations or different parameters. For example, the red line bundle in Figure 13 could have also been selected using the OSI parameter. In cases where a selection either did not yield an interesting flow structure or resulted in multiple structures at once, the resulting pathlines usually contained clues about more promising surface regions that could be selected instead. The ability to manually draw patches onto the surface without regard to the underlying parameters proved to be useful when the experts wanted to select a region based on vessel morphology that did not fully correlate to any surface parameter.

A point of criticism was that manually adjusting the surface color scales was often necessary. The color scale domain is initialized using the global parameter minimum and maximum, yet the physician is generally looking for local minima and maxima. These values may not always be visible initially due to the discrete nature of the color scale, therefore requiring manual adjustment. They requested various (possibly customizable) presets for these adjustments to be added to the application in order to save time when selecting surface patches with recurring parameter configurations.

All experts expressed their interest in being able to further quantify various aspects of our visualization. An example for that would be the ability to measure the size and extent of detected structures. More complex measures, such as the amount of flow that passes through a certain structure or directly underneath a surface patch, would be desirable as well. Adding quantitative measures for each line bundle would allow the physician to gain a deeper understanding of the flow patterns and also enable comparisons between the detected flow structures.

Another requested feature was the ability to place a plane into the parent vessel of an aneurysm and record the color and spatial positions of pathlines passing through it. This would generate a flow profile depicting which regions of the vessel cross section feed or drain into different flow structures. A potential use for this kind of information would be the optimization of stent placement.

## 7. Discussion

The feedback from all experts shows that our method can support the visual exploration of blood flow and its relation to surface features. According to their feedback, we were able to fulfill the requirements presented in Section 1. The use of a discrete color scale

B. Behrendt & P. Berg & O. Beuing & B. Preim & S. Saalfeld / Explorative Blood Flow Vis. using Dynamic Surface-based Filtering

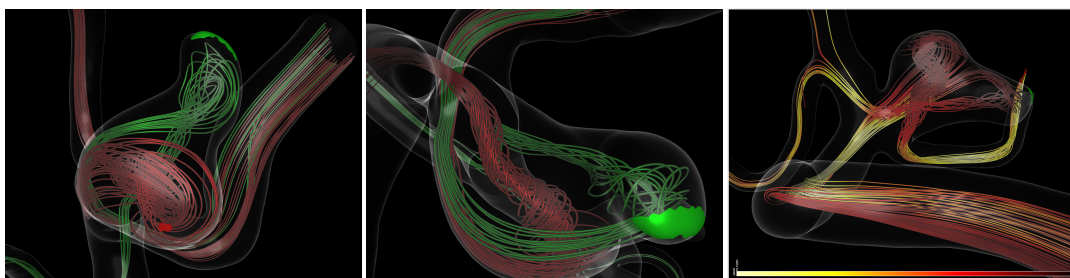


**Figure 13:** Flow selection performed by one of the neuroradiologists from three different perspectives; the right image has the flow velocity mapped onto the pathlines using a temperature color scale.

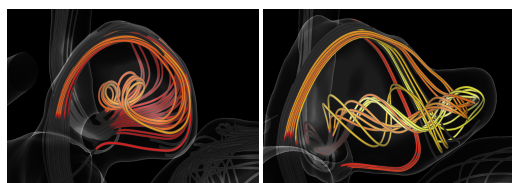


**Figure 14:** Comparison of the same aneurysm acquired in 2011 (left) and 2014 (right); the residence time is mapped onto a temperature color scale.

allows for a fast localization of extreme hemodynamic parameters. Unlike previous approaches such as [vBB\*10,ZMH\*09,GNBP11], the local flow structures associated to an interesting surface structure can be visualized with only a few mouse clicks. Further exploration of the resulting pathline bundles is possible by either mapping their parameters onto a color scale for filtering them in real-time using a parameter scatterplot, parallel coordinates view or line chart. Both the extraction of pathline bundles as well as the additional filtering can be performed in real-time. Color-coding the selected patches and associated pathlines allows for an easy visual assessment of the entire course of a bundle, similar to [vBB\*10].

At present, our application's ability to perform quantitative analysis in addition to qualitative assessments is limited. Users can easily find interesting flow structures and visually compare their quantitative parameters using the line chart. To remedy the lack of additional, in-depth analysis features, the quantitative data from any pathline bundle can be exported as a CSV file. This allows the user to employ an external application of their choice to perform further analysis.

## 8. Conclusion & Future Work

We have presented a set of intuitive techniques to allow for an interactive exploration of local blood flow based on surface features. Both clinical and the flow simulation expert appreciated the local selection techniques to analyze blood flow characteristics in combination with surface parameters. In fact, both of them stated that

they were missing this opportunity in their respective known tools. They also were interested in the visualization of the flow splitting and appreciated the presentation of the pathlines for the entire vessels. Furthermore, the sophisticated real-time filtering techniques including parameter-based filtering and usage of parallel coordinate views as well as the scatterplot could fulfill all of their requests regarding selection of specific blood flow characteristics.

Although tailored for the use on cerebral aneurysms, our methods can be easily adapted to other applications both in- and outside of the medical field. All that is required for our tool to work is a surface model and a set of arbitrarily generated pathlines. Having quantitative parameters mapped to them extends the filtering possibilities, but is not strictly required for our application to be used. Problems could arise when working with complex intertwining surface models, since occlusions might hinder the user's ability to select certain parts of the surface. Possible solutions in this scenario would be to use semi-transparent surfaces in combination with an automated selection algorithm, as presented by Mühler et al. [MTRP10].

For the scope of this paper, we limited our application to work with pre-integrated pathlines. This ensures that all interactions with our tool can be performed in real-time. For the future, we plan to add dynamic seeding capabilities to our application. If the users feel that a certain interesting area is under-detailed due to a lack of pathlines, they may dynamically add more detail by seeding additional pathlines.

At the moment, our tool is only focused on the exploration of a single dataset. There are, however, many scenarios in which physicians would like to compare different datasets. For example, a physician may want to see how a treatment procedure they have performed affected the blood flow in comparison to a dataset acquired before the procedure. To support these comparisons, further quantitative values in addition to the existing ones should be extracted, for example about the flow directly underneath a patch or the patch itself. Instead of simply showing multiple datasets side-by-side in isolated views, an integrated visualization would be desirable. This would require translating either the surface patches or the seed points for a selected pathline bundle to highlight how the flow has changed between datasets.

### Acknowledgments

We would like to give thanks to Prof. Christina Iosif for her participation in our evaluation and the very useful feedback she provided. Additional thanks go to Stefanie Glaßer and George Reeder for their help with the accompanying video to this paper.

The work of this paper is funded by the European Regional Development Fund under the operation number 'ZS /2016/04/78123' as part of the initiative "Sachsen-Anhalt WISSENSCHAFT Schwerepunkte" as well as the German Ministry of Education and Research (13GW0095A) within the STIMULATE research campus.

### References

- [BB17] BERG P., BEUING O.: Multiple intracranial aneurysms: A direct hemodynamic comparison between ruptured and unruptured vessel malformations. *International journal of computer assisted radiology and surgery* (2017). 4
- [BHK\*16] BROOS A. J. M., HOON, NIELS H. L. C. DE, KONING, PATRICK J. H. DE, GEEST, ROB J. VAN DER, VILANOVA A., JALBA A. C.: A Framework for Fast Initial Exploration of PC-MRI Cardiac Flow, 2016. 3
- [BPM\*13] BORN S., PFEIFLE M., MARKL M., GUTBERLET M., SCHEUERMANN G.: Visual analysis of cardiac 4D MRI blood flow using line predicates. *IEEE transactions on visualization and computer graphics* 19, 6 (2013), 900–912. 3
- [BSJ\*14] BERG P., STUCHT D., JANIGA G., BEUING O., SPECK O., THÉVENIN D.: Cerebral blood flow in a healthy Circle of Willis and two intracranial aneurysms: Computational fluid dynamics versus four-dimensional phase-contrast magnetic resonance imaging. *Journal of biomechanical engineering* 136, 4 (2014). 3
- [CDM\*17] CHUNG B. J., DODDASOMAYAJULA R., MUT F., DETMER F., PRITZ M. B., HAMZEI-SICHANI F., BRINIJKI W., KALLMES D., JIMENEZ C., PUTMAN C., CEBRAL J. R.: Angioarchitectures and Hemodynamic Characteristics of Posterior Communicating Artery Aneurysms and Their Association with Rupture Status. *American Journal of Neuroradiology* 38, 11 (2017), 2111–2118. 1, 3
- [DCHS\*17] DODDASOMAYAJULA R., CHUNG B., HAMZEI-SICHANI F., PUTMAN C. M., CEBRAL J. R.: Differences in Hemodynamics and Rupture Rate of Aneurysms at the Bifurcation of the Basilar and Internal Carotid Arteries. *American Journal of Neuroradiology* 38, 3 (2017), 570–576. 1, 3
- [GBNP15] GLASSER S., BERG P., NEUGEBAUER M., PREIM B.: Reconstruction of 3D Surface Meshes for Blood Flow Simulations of Intracranial Aneurysms. In *Proceedings of Computer- and Robot-Assisted Surgery (CURAC)* (2015), pp. 163–168. 3
- [GLV\*12] GASTEIGER R., LEHMANN D. J., VAN PELT R., JANIGA G., BEUING O., VILANOVA A., THEISEL H., PREIM B.: Automatic Detection and Visualization of Qualitative Hemodynamic Characteristics in Cerebral Aneurysms. *IEEE transactions on visualization and computer graphics* 18, 12 (2012), 2178–2187. 2
- [GNBP11] GASTEIGER R., NEUGEBAUER M., BEUING O., PREIM B.: The FLOWLENS: A focus-and-context visualization approach for exploration of blood flow in cerebral aneurysms. *IEEE transactions on visualization and computer graphics* 17, 12 (2011), 2183–2192. 2, 11
- [GNKP10] GASTEIGER R., NEUGEBAUER M., KUBISCH C., PREIM B.: Adapted Surface Visualization of Cerebral Aneurysms with Embedded Blood Flow Information. In *VCBM* (2010), pp. 25–32. 5
- [JBB\*13] JANIGA G., BERG P., BEUING O., NEUGEBAUER M., GASTEIGER R., PREIM B., ROSE G., SKALEJ M., THÉVENIN D.: Recommendations for accurate numerical blood flow simulations of stented intracranial aneurysms. *Biomedizinische Technik. Biomedical engineering* 58, 3 (2013), 303–314. 3
- [KGP\*13] KÖHLER B., GASTEIGER R., PREIM U., THEISEL H., GUTBERLET M., PREIM B.: Semi-automatic vortex extraction in 4D PC-MRI cardiac blood flow data using line predicates. *IEEE transactions on visualization and computer graphics* 19, 12 (2013), 2773–2782. 3
- [LEBB09] LALL R. R., EDDLEMAN C. S., BENDOK B. R., BATJER H. H.: Unruptured Intracranial Aneurysms and the Assessment of Rupture Risk based on Anatomical and Morphological Factors: Sifting Through the Sands of Data. *Neurosurgical focus* 26, 5 (2009), E2. 3
- [LGV\*16] LAWONN K., GLASSER S., VILANOVA A., PREIM B., ISENBERG T.: Occlusion-free Blood Flow Animation with Wall Thickness Visualization. *IEEE transactions on visualization and computer graphics* 22, 1 (2016), 728–737. 2
- [LMSC11] LEE T.-Y., MISHCHENKO O., SHEN H.-W., CRAWFIS R.: View point evaluation and streamline filtering for flow visualization. In *IEEE Pacific Visualization Symposium* (2011), pp. 83–90. 2
- [MTRP10] MÜHLER K., TIETJEN C., RITTER F., PREIM B.: The medical exploration toolkit: An efficient support for visual computing in surgical planning and training. *IEEE transactions on visualization and computer graphics* 16, 1 (2010), 133–146. 11
- [MVB\*17] MEUSCHKE M., VOSS S., BEUING O., PREIM B., LAWONN K.: Combined Visualization of Vessel Deformation and Hemodynamics in Cerebral Aneurysms. *IEEE transactions on visualization and computer graphics* 23, 1 (2017), 761–770. 3
- [NLB\*13] NEUGEBAUER M., LAWONN K., BEUING O., BERG P., JANIGA G., PREIM B.: AmniVis - A System for Qualitative Exploration of Near-Wall Hemodynamics in Cerebral Aneurysms. *Computer Graphics Forum* 32, 3pt3 (2013), 251–260. 3, 6
- [OJCP16] OELTZE-JAFRA S., CEBRAL J. R., JANIGA G., PREIM B.: Cluster Analysis of Vortical Flow in Simulations of Cerebral Aneurysm Hemodynamics. *IEEE transactions on visualization and computer graphics* 22, 1 (2016), 757–766. 2
- [OLK\*14] OELTZE S., LEHMANN D. J., KUHN A., JANIGA G., THEISEL H., PREIM B.: Blood Flow Clustering and Applications in Virtual Stenting of Intracranial Aneurysms. *IEEE transactions on visualization and computer graphics* 20, 5 (2014), 686–701. 2
- [SS06] SALZBRUNN T., SCHEUERMANN G.: Streamline predicates. *IEEE transactions on visualization and computer graphics* 12, 6 (2006), 1601–1612. 3
- [Thi11] THIBIEROZ N.: Order-independent transparency using per-pixel linked lists. *GPU Pro* 2 (2011), 409–431. 5
- [vBB\*10] VAN PELT R., BESCÓS J. O., BREEUWER M., CLOUGH R. E., GRÖLLER M. E., TER HAAR ROMENIJ B., VILANOVA A.: Exploration of 4D MRI Blood Flow using Stylistic Visualization. *IEEE transactions on visualization and computer graphics* 16, 6 (2010), 1339–1347. 2, 11
- [vGL\*14] VAN PELT R., GASTEIGER R., LAWONN K., MEUSCHKE M., PREIM B.: Comparative Blood Flow Visualization for Cerebral Aneurysm Treatment Assessment. *Computer Graphics Forum* 33, 3 (2014), 131–140. 2
- [Wie03] WIEBERS D. O.: Unruptured Intracranial Aneurysms: Natural History, Clinical Outcome, and Risks of Surgical and Endovascular Treatment. *The Lancet* 362, 9378 (2003), 103–110. 3
- [WvdSAR07] WERMER M. J., VAN DER SCHAAF I. C., ALGRA A., RINKEL G. J.: Risk of Rupture of Unruptured Intracranial Aneurysms in Relation to Patient and Aneurysm Characteristics. *Stroke* 38, 4 (2007), 1404–1410. 3
- [XTSM14] XIANG J., TUTINO V., SNYDER K., MENG H.: CFD: Computational Fluid Dynamics or Confounding Factor Dissemination? The Role of Hemodynamics in Intracranial Aneurysm Rupture Risk Assessment. *American Journal of Neuroradiology* 35, 10 (2014), 1849–1857. 3
- [ZMH\*09] ZACHOW S., MUIGG P., HILDEBRANDT T., DOLEISCH H., HEGE H.-C.: Visual exploration of nasal airflow. *IEEE transactions on visualization and computer graphics* 15, 6 (2009), 1407–1414. 2, 11



# Rupture Status Classification of Intracranial Aneurysms Using Morphological Parameters

Uli Niemann, Philipp Berg, Annika Niemann, Oliver Beuing, Bernhard Preim, Myra Spiliopoulou, Sylvia Saalfeld  
Otto-von-Guericke University Magdeburg, Germany  
Corresponding email: {uli.niemann, sylvia.saalfeld}@ovgu.de

**Abstract**—Intracranial aneurysms are pathologic dilations of the vessel wall, which bear the risk of rupture and of fatal consequences for the patient. Since treatment may be accompanied by severe complications as well, rupture risk assessment and thus rupture risk prediction plays an important role in clinical research. In this work, we investigate the potential of morphological features for rupture risk status classification in 100 intracranial aneurysms. We propose a pipeline for morphological feature extraction, rupture status classification with subsequent feature ranking and inspection. Our classification setup involves training separate models for each aneurysm type (sidewall or bifurcation) with multiple learning algorithms. We report on the classification performance of our pipeline and examine the predictive power of each morphological parameters towards rupture status classification. Further, we identify the most important features for the best models and study their marginal prediction.

**Keywords**—Medical Image Analysis; Intracranial Aneurysm; Morphological Parameters; Rupture Status Classification;

## I. INTRODUCTION

[1]. Numerous studies identified parameters such as aspect ratio, undulation index and nonsphericity index as statistically significant to the aneurysm rupture status [2], [3], [4]. However, although these studies allow for a retrospective analysis, the clinician needs further guidance in case an asymptomatic aneurysm was detected and the rupture risk should be determined. Therefore, we study to what extend the rupture status can be predicted with supervised classification models learned on morphological parameters that are available to the clinician. We extract common parameters that were found in other studies to correlate with rupture risk. We train separate classifiers for each aneurysm type (sidewall or bifurcation) using multiple learning algorithms. We juxtapose the impact of each feature towards the best models' predictions and study their marginal predictions.

## II. MATERIALS

Our pipeline is illustrated in Fig. 1. The preprocessing steps comprise the segmentation and neck curve extraction of the medical image data, which is explained in this section.

### A. Data Acquisition

The presented methods were developed for a database comprising 100 intracranial aneurysms from 74 patients (age: 33-85 years, 17 male and 57 female patients) at

the university hospital of Magdeburg, Germany. For each patient, 3D rotational angiography data was acquired as part of the necessary clinical work-up performed on an Artis Q (Siemens Healthineers, Forchheim, Germany). The dataset acquisition and the subsequent analysis steps are in accordance with the guidelines of the local ethics committee.

### B. Segmentation and Neck Curve Extraction

From digital subtraction data reconstructed from 3D rotational angiographies, the aneurysms and vessels are segmented with a threshold-based approach [5]. Afterwards, we extract the vessel's centerline with the vascular modeling toolkit (VMTK, vmtk.org) [6]. As prerequisite for feature extraction, the aneurysm has to be delineated from the parent vessel. For this purpose, we employ the automatic ostium detection of Saalfeld et al. [7].

## III. METHODS

With our pipeline, we extract morphological features and learn classification models that distinguish between unruptured and ruptured intracranial aneurysms.

### A. Extraction of Morphological Features

For each 3D surface mesh, we obtain the neck curve, the dome point  $D$  and the two base points  $B_1$  and  $B_2$  in our previous work [7]. Hence, the base points  $B_1$  and  $B_2$  are approximated as points on the centerline with largest distance where the rays from  $B_1$  and  $B_2$  to  $D$  are not intersecting the surface mesh. In Fig. 2, the extracted

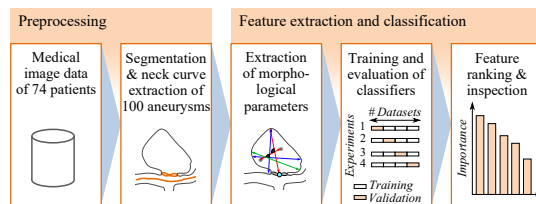


Figure 1. Pipeline of our presented approach: aneurysm segmentation from raw image data as well as subsequent automatized extraction of the centerline and the neck curve was carried out. Afterwards, the morphological parameters were extracted. Classifiers were trained and evaluated based on these parameters. Finally, feature ranking and inspection was conducted.

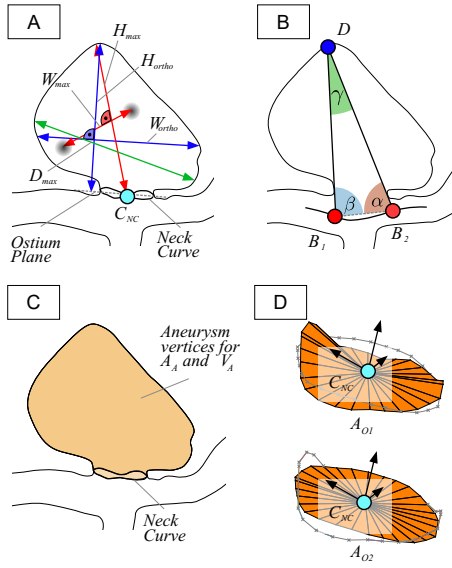


Figure 2. Illustration of the extracted morphological features  $H_{max}$ ,  $W_{max}$ ,  $H_{ortho}$ ,  $W_{ortho}$  and  $D_{max}$  (A). The angles  $\alpha$ ,  $\beta$  and  $\gamma$  are extracted based on  $B_1$ ,  $B_2$  and the dome point  $D$  (B). Separating the aneurysm from the parent vessel based on the neck curve yields  $A_A$  and  $V_A$  (C). The area of the ostium and the projected ostium, i.e.,  $A_{O1}$  and  $A_{O2}$ , are shown in (D), where  $C_{NC}$  denotes the center of the neck curve.

parameters are illustrated, where  $H_{max}$ ,  $W_{max}$ ,  $H_{ortho}$ ,  $W_{ortho}$  and  $D_{max}$  describe the aneurysm shape. The angles  $\alpha$  (with  $\alpha = \min(\angle DB_1B_2, \angle DB_2B_1)$ ),  $\beta$  (with  $\beta = \max(\angle DB_1B_2, \angle DB_2B_1)$ ) and  $\gamma$  are extracted based on  $B_1$ ,  $B_2$  and  $D$ , and  $\Delta_{\alpha\beta}$  denotes the absolute difference of  $\alpha$  and  $\beta$ .

Separating the aneurysm from the parent vessel based on the neck curve allows for extraction of the surface area  $A_A$  and the volume  $V_A$  of the aneurysm. We provide two measurements for the surface area of the ostium:  $A_{O1}$  and  $A_{O2}$  (recall Fig. 2-D). The parameter  $A_{O1}$  denotes the surface area of the ostium, i.e., the surface of the triangulated ostium area obtained by connecting the neck curve points with their mean  $C_{NC}$ . The parameter  $A_{O2}$  denotes the surface area of the neck curve when projected into a plane, see also [7] for more information. Hence,  $A_{O2}$  is extracted to obtain a comparable parameter to other studies that often employ a cutting plane to determine the ostium. Table I provides a brief description, summary statistics and a visualization of the distribution for each extracted parameter. Additionally, the statistical significance of multiple parameters w.r.t. rupture risk status, including  $D_{max}$ ,  $H_{max}$ ,  $AR_1$ ,  $AR_2$ ,  $\beta$  and  $\gamma$ , is shown in Table I.

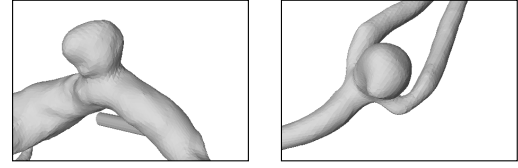


Figure 3. Illustration of a sidewall aneurysm at the side of the parent vessel wall (left) and a bifurcation aneurysm at a vessel bifurcation (right).

### B. Classification & Evaluation Setup

We model our classification problem with a two-class target feature (*unruptured* vs. *ruptured*), using the 100 samples described in subsection II-A and the 22 morphological parameters from Table I as input features. As motivated by the results reported in [8], we learn distinct models for the subset of sidewall aneurysms (SW; 9 ruptured out of 24) and for the subset of bifurcation aneurysms (BF; 29 ruptured out of 62). See Fig. 3 for an illustration of sidewall and bifurcation aneurysms. Further, we train our classifiers on a combined group (ALL; 43 ruptured out of 100), which includes 14 additional samples that could not be clearly identified as either sidewall or bifurcation aneurysms.

For classification, we employ 9 different algorithms: three decision tree variants (CART [9], C4.5 [10] and its successor C5.0), Naïve Bayes (NBAYES), a feed-forward neural network with a single hidden layer (NNET) [11], generalized partial least squares (GPLS) [12], random forest (RF) [13],  $k$ -nearest neighbor classifier (KNN) and gradient boosted trees (GBT) [14]. Some of the chosen classifiers may struggle because of the different scale of the variables or the dataset’s high dimensionality. Therefore, we optionally engage three preprocessing transformations to the dataset: the “range” transformation scales the data to be within  $[0,1]$ , the “z-score” transformation subtracts the mean and divides by the standard deviation, and the “pca” transformation performs “z-score” and a principal component analysis and retains only the first principal components where the cumulative percent of explained variance first exceeds 95%.

We evaluate our approach using 5 times repeated 10-fold cross-validation. In each run, we use a grid of tuning parameter values with 10 unique values per parameter to select the best parameter setting using accuracy (ratio of correctly labeled samples) as quality measure.

## IV. RESULTS

In this section, we report on our classification results and elaborate on the features with high impact on the model prediction.

### A. Rupture Status Classification

In Table II, we show the results of classification between *unruptured* aneurysms (negative class) and *ruptured* ones (positive class) on all samples (denoted as ALL), the subset

Table I  
 MORPHOLOGICAL FEATURES USED FOR CLASSIFICATION, WITH MEAN VALUES  $\bar{x}$  AND STANDARD DEVIATION  $s$ . BOXPLOTS SHOW THE FEATURE DISTRIBUTIONS FOR UNRUPTURED (U) AND RUPTURED (R) ANEURYSMS. P-VALUES WERE DERIVED FROM A STATISTICAL ANALYSIS USING THE NON-PARAMETRIC MANN-WHITNEY-U TEST; \*\* SIGNIFICANT CORRELATION (DOUBLE-SIDED) WITH  $p < 0.01$ ; \* SIGNIFICANT CORRELATION (DOUBLE SIDED) WITH  $p < 0.05$ .

Feature	Description	Status	$\bar{x} \pm s$	Distribution	p-value
$A_A$	Area of the aneurysm (without the ostium)	Unruptured	$79.40 \pm 86.77$		0.050
		Ruptured	$92.26 \pm 74.12$		
$V_A$	Volume of the aneurysm	Unruptured	$91.24 \pm 151.78$		0.092
		Ruptured	$91.72 \pm 114.92$		
$O_{A1}$	Area of the ostium (variant 1)	Unruptured	$11.34 \pm 7.90$		0.265
		Ruptured	$10.33 \pm 9.56$		
$O_{A2}$	Area of the ostium (variant 2)	Unruptured	$10.45 \pm 6.99$		0.262
		Ruptured	$9.41 \pm 8.29$		
$D_{max}$	Max. diameter of the aneurysm	Unruptured	$6.24 \pm 2.84$		<b>0.034*</b>
		Ruptured	$7.21 \pm 2.77$		
$H_{max}$	Max. height of the aneurysm	Unruptured	$4.74 \pm 2.54$		<b>0.012*</b>
		Ruptured	$5.88 \pm 2.59$		
$W_{max}$	Max. width of the aneurysm perpendicular to $H_{max}$	Unruptured	$5.08 \pm 2.66$		0.119
		Ruptured	$5.32 \pm 2.11$		
$H_{ortho}$	Height of the aneurysm approximated as length of the ray perpendicular to the ostium plane starting from $C_{NC}$	Unruptured	$4.26 \pm 2.41$		<b>0.030*</b>
		Ruptured	$5.17 \pm 2.41$		
$W_{ortho}$	Max. width parallel to the projected ostium plane	Unruptured	$5.59 \pm 2.67$		0.175
		Ruptured	$5.94 \pm 2.15$		
$N_{max}$	Max. NC diameter, i.e., the max. possible distance between two NC points	Unruptured	$4.02 \pm 1.49$		0.330
		Ruptured	$3.75 \pm 1.25$		
$N_{avg}$	Avg. NC diameter, i.e., the mean distance between $C_{NC}$ and the NC points	Unruptured	$3.51 \pm 1.20$		0.237
		Ruptured	$3.30 \pm 1.13$		
$AR_1$	Aspect ratio: $H_{ortho}/N_{max}$	Unruptured	$1.08 \pm 0.50$		<b>0.002**</b>
		Ruptured	$1.40 \pm 0.56$		
$AR_2$	Aspect ratio: $H_{ortho}/N_{avg}$	Unruptured	$1.23 \pm 0.56$		<b>0.003**</b>
		Ruptured	$1.60 \pm 0.65$		
$V_{CH}$	Volume of the convex hull of the aneurysm vertices	Unruptured	$100.36 \pm 160.37$		0.085
		Ruptured	$108.14 \pm 129.38$		
$A_{CH}$	Area of the convex hull of the aneurysm vertices	Unruptured	$92.23 \pm 93.64$		0.079
		Ruptured	$105.25 \pm 81.15$		
$EI$	Ellipticity index: $1 - (18\pi)^{\frac{1}{3}} V_{CH}^{\frac{2}{3}}/A_{CH}$	Unruptured	$0.27 \pm 0.02$		0.323
		Ruptured	$0.27 \pm 0.02$		
$NSI$	Non-sphericity index: $1 - (18\pi)^{\frac{1}{3}} V^{\frac{2}{3}}/A$	Unruptured	$0.17 \pm 0.25$		0.067
		Ruptured	$0.21 \pm 0.24$		
$UI$	Undulation index: $1 - \frac{V}{CH_V}$	Unruptured	$0.12 \pm 0.35$		0.686
		Ruptured	$0.10 \pm 0.39$		
$\alpha$	Min. of $\angle DB_1B_2$ and $\angle DB_2B_1$	Unruptured	$54.38 \pm 12.63$		0.287
		Ruptured	$56.90 \pm 11.57$		
$\beta$	Max. of $\angle DB_1B_2$ and $\angle DB_2B_1$	Unruptured	$80.70 \pm 17.07$		<b>&lt;0.001**</b>
		Ruptured	$92.13 \pm 17.29$		
$\gamma$	Angle at D, i.e. $\angle B_1DB_2$	Unruptured	$44.93 \pm 19.71$		<b>&lt;0.001**</b>
		Ruptured	$30.98 \pm 13.68$		
$\Delta_{\alpha\beta}$	Abs. difference between $\alpha$ and $\beta$	Unruptured	$26.32 \pm 22.66$		0.078
		Ruptured	$35.23 \pm 26.05$		

of sidewall aneurysms (SW) and the subset of bifurcation aneurysms (BF). In addition to accuracy, we depict two other quality measures: Cohen’s kappa and the area under the receiver operating characteristic (ROC) curve. Cohen’s kappa measures the model’s relative improvement in accuracy in comparison with the expected accuracy, i.e., the marginal probability of the majority class. A ROC curve is a graphical representation that juxtaposes sensitivity (true positive rate (TPR)) and false positive rate (FPR) for varying prediction thresholds of a binary classifier. The area under the ROC curve (AUC) takes values between 0 (0% TPR, 100% FPR) and 1 (100% TPR, 0% FPR), where a random classifier achieves an AUC of 0.5.

Table II  
CLASSIFICATION PERFORMANCE FOR EACH COMBINATION OF DATA SUBSET AND ALGORITHM. PREPR. = PREPROCESSING TRANSFORMATION; ACC. = ACCURACY; SW = SIDEWALL ANEURYSMS; BF = BIFURCATION ANEURYSMS.

Subset	Algorithm	Prepr.	Acc.	Kappa	AUC
ALL	GBT	-	0.69	0.28	0.70
	C5.0	-	0.66	0.21	0.69
	GPLS	-	0.66	0.21	0.69
	KNN	range	0.66	0.20	0.63
	CART	-	0.65	0.18	0.61
	NNET	range	0.62	0.13	0.64
	J48	-	0.62	0.13	0.64
	NBayes	-	0.61	0.10	0.58
	RF	-	0.60	0.07	0.62
	SW	GPLS	range	0.79	0.43
C5.0		-	0.78	0.40	0.84
KNN		pca	0.77	0.40	0.73
GBT		-	0.77	0.40	0.68
NNET		range	0.75	0.33	0.69
CART		-	0.75	0.33	0.63
RF		-	0.74	0.30	0.69
NBayes		-	0.72	0.26	0.68
J48		-	0.72	0.25	0.74
BF		GPLS	z-score	0.68	0.31
	KNN	pca	0.66	0.28	0.68
	NNET	z-score	0.63	0.20	0.65
	GBT	-	0.62	0.19	0.60
	NBayes	-	0.61	0.17	0.57
	CART	-	0.61	0.16	0.61
	J48	-	0.60	0.15	0.62
	RF	-	0.60	0.15	0.63
	C5.0	-	0.59	0.13	0.61

GBT performs best in accuracy on ALL with 69%, followed by C5.0, GPLS and KNN with each 66% (cf. Table II). All classification algorithms work better on the subset of SW aneurysms where GPLS with a range transformation yields best overall accuracy of 79% with an AUC of 0.73. For the BF subset, GPLS with a z-score transformation performs best with an accuracy of 68% and an AUC of 0.68. Overall, none of the classification algorithms outperforms all others on all three subsets.

We integrated the three best models per data subset in an

interactive web-application<sup>1</sup>, which lets the user study how a change in the choice of the values for a feature affects the model confidence. The user may select a sample from the training set, but she is also allowed to freely modify each feature value with the respective slider widget, whereupon the prediction confidence gets immediately updated. A horizontal bar chart visualizes the supporting or contradicting contribution of each input feature to the model’s prediction, based on the method of Ribeiro et al. [15].

B. Model Interpretation

For interpretation of our models, we analyze the best model of each subset. We identify the most important features, i.e., the features that have the highest impact on the model prediction (cf. Fig. 4). Feature importance

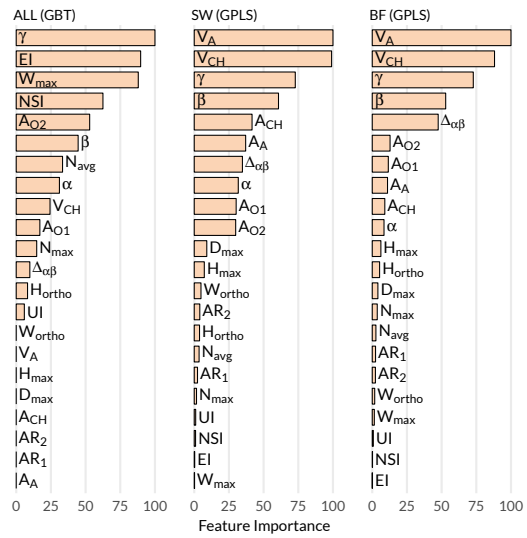


Figure 4. Feature importance for the best model of each data subset. Values are scaled up to 100 according to the highest feature importance.

scores are calculated as the sum of absolute differences between all pairs of consecutive points of the feature’s partial dependence plot. A partial dependence plot visualizes the relationship between a feature  $f$  and a model’s prediction while incorporating the average effect of the remaining features in the model. Thus, by providing an estimation of how the model’s prediction changes for each value of  $f$ , it is particularly useful for interpreting the models of complex non-parametric classification algorithms. We show the partial dependence plots of the five most important features of the best models per subset from Table II in Fig. 5.

Fig. 5 illustrates the high importance of the angle  $\gamma$  that characterizes rupture status classification, since this feature

<sup>1</sup>Available at <https://rbsenzaehler.shinyapps.io/RUSTiC/>.

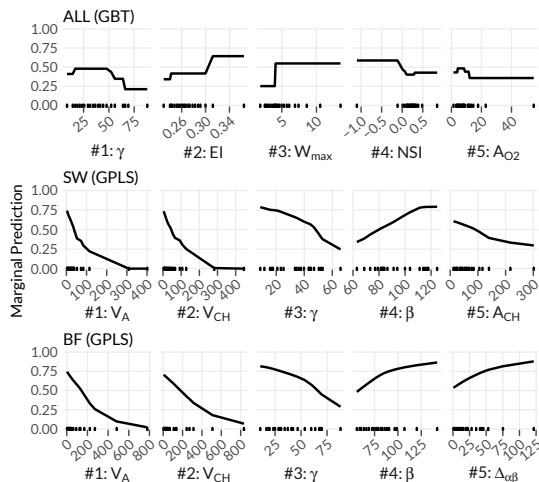


Figure 5. The partial dependence plots show the marginal prediction of the five most important variables for the best model of each data subset.

is ranked #1, #3 and #3 for each data subset’s best model. Although the curves show slight variations in their run, all three models have in common that the marginal probability of predicting the class *ruptured* decreases with increasing values of  $\gamma$ , which means that ruptured aneurysms tend to exhibit lower  $\gamma$  values (cf. Table I). Besides  $\gamma$ , other features, such as  $EI$  and  $W_{max}$  for ALL, and  $V_A$  and  $V_{CH}$  for SW and BF, exhibit a considerable relevance w.r.t. the model, as shown in Fig. 4 and 5.

## V. DISCUSSION

The partial dependence plots for the top-5 features found for the sidewall aneurysms (Fig. 5, middle subfigure) and for bifurcation aneurysms (Fig. 5, bottom subfigure) show that four out of the five features are the same and that the interdependencies between each of those input features and the target feature follow the same pattern. This is a different result in comparison with [8] who identified differences in the statistical significance of morphological parameters w.r.t. rupture status between sidewall and bifurcation aneurysms.

The importance scores in Fig. 4 indicate some higher-level interactions between the features. For example, although mean and standard deviation of the parameter  $EI$  are equal in unruptured and ruptured aneurysms (cf. Table I), it is ranked second most important (ALL). Apparently, the model uses  $EI$  in combination with one or more other features together to generate more robust predictions.

While the partial dependence plot clearly represents the influence of a single feature, interaction effects between two or more features are not represented. The decision tree variant C5.0 achieves 66% accuracy on all samples, just 3% less than the best model (cf. Table II). Being more

interpretable than GBT and GPLS and just slightly less accurate, we opt to study the model closer. In its best run, the algorithm generates multiple classification rules instead of a single tree. A representation of three of those class-characteristic rules is shown in Fig. 6. The left panel shows a rule with a high lift for unruptured samples that satisfy the condition  $AR_2 \leq 1.24 \wedge \gamma > 54.16$ . This partition (gray box) contains 20 unruptured and 2 ruptured samples. Thus, the lift is 1.6, i.e., in the partition described by the rule, the relative frequency of the class *unruptured* is 1.6 times higher in comparison with the relative frequency in the total training set. Two rules for the class *ruptured* are shown in the middle and right panel in Fig. 6 where the interaction effects between  $H_{ortho}$  and  $W_{ortho}$ , as well as between  $W_{max}$  and  $A_{O_2}$  are highlighted. Fig. 6 also indicates that none of the morphological features under study alone would reliably predict the rupture risk of the aneurysms. Indeed, building a classifier with only one input feature yields a model with 55% accuracy at best, which is outperformed by a classifier that predicts the majority class (57% accuracy).

While we consider our results to be promising, there are arguably some limitations and substantial room for improvement. First, the limited sample size, in particular for the subset of sidewall aneurysms, might increase the margin of error of the classification performance estimates. We are keen to evaluate the robustness of our models on a larger number of datasets. The second limitation concerns the quality of the class label due to this specific pathology. Samples that were labeled as unruptured could rupture at a later moment. A further limitation is the limited feature space: our classification models incorporate morphological characteristics only. However, other properties, such as hemodynamic features have been identified to be predictive [16], [17]. In future work, we would like to inspect samples with high classification error. Here, our goal is to derive descriptions of groups of aneurysms that are hard to classify, in order to better understand the reasons for misclassification. Further, we would like to study the potential of deep learning when applied on the segmented image data, e.g., using convolutional neural nets. More precisely, our interest is to quantify the positive or negative impact of a careful feature engineering step before rupture risk assessment in comparison with a model that is learned on raw image data.

## VI. CONCLUSION

In this paper, we studied the potential of morphological parameters of intracranial aneurysms for rupture status classification. We found that some of them are highly predictive towards the outcome, including the angle between the ostium’s base points  $\gamma$ . Although only trained on shape, size and angle features, the performance of our best models is promising. Thus, a natural extension of our work includes incorporating a broader range of feature types to improve accuracy.

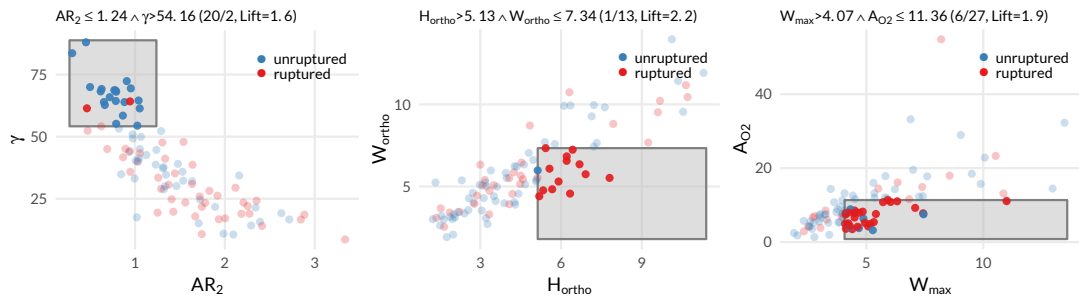


Figure 6. Three classification rules with high lift values extracted from  $C5.0$  for subset ALL. The title of a subfigure displays the rule's condition. The class counts and lift value of the partition are given in parenthesis. Samples that satisfy the rule condition are shown as opaque points within a gray box.

#### ACKNOWLEDGMENT

This work was partially funded by the German Federal Ministry of Education and Research within the Research Campus *STIMULATE* (grant number '13GW0095A').

#### REFERENCES

- [1] M. J. Wermer, I. C. van der Schaaf, A. Algra, and G. J. Rinkel, "Risk of rupture of unruptured intracranial aneurysms in relation to patient and aneurysm characteristics," *Stroke*, vol. 38, no. 4, pp. 1404–1410, 2007.
- [2] S. Dhar, M. Tremmel, J. Mocco, M. Kim, J. Yamamoto, A. H. Siddiqui, L. N. Hopkins, and H. Meng, "Morphology parameters for intracranial aneurysm rupture risk assessment," *Neurosurgery*, vol. 63, no. 2, pp. 185–197, 2008.
- [3] M. L. Raghavan, B. Ma, and R. E. Harbaugh, "Quantified aneurysm shape and rupture risk," *Journal of Neurosurgery*, vol. 102, no. 2, pp. 355–362, 2005.
- [4] J. Xiang, S. K. Natarajan, M. Tremmel, D. Ma, J. Mocco, L. N. Hopkins, A. H. Siddiqui, E. I. Levy, and H. Meng, "Hemodynamic–morphologic discriminants for intracranial aneurysm rupture," *Stroke*, vol. 42, no. 1, pp. 144–152, 2011.
- [5] S. Glaßer, P. Berg, M. Neugebauer, and B. Preim, "Reconstruction of 3D Surface Meshes for Blood Flow Simulations of Intracranial Aneurysms," in *Proc. of the Annual Meeting of the German Society of Computer- and Robot-Assisted Surgery*, 2015, pp. 163–168.
- [6] L. Antiga, M. Piccinelli, L. Botti, B. Ene-Iordache, A. Remuzzi, and D. A. Steinman, "An image-based modeling framework for patient-specific computational hemodynamics," *Medical & biological engineering & computing*, vol. 46, no. 11, p. 1097, 2008.
- [7] S. Saalfeld, P. Berg, A. Niemann, M. Luz, B. Preim, and O. Beuing, "Semi-automatic neck curve reconstruction for intracranial aneurysm rupture risk assessment based on morphological parameters," in *Proc. of Computer assisted radiology and surgery (CARS)*, 2018, to appear.
- [8] M. I. Baharoglu, A. Lauric, B.-L. Gao, and A. M. Malek, "Identification of a dichotomy in morphological predictors of rupture status between sidewall-and bifurcation-type intracranial aneurysms," *Journal of neurosurgery*, vol. 116, no. 4, pp. 871–881, 2012.
- [9] L. Breiman, J. Friedman, R. Olshen, and C. Stone, *Classification and Regression Trees*. Monterey, CA: Wadsworth and Brooks, 1984.
- [10] R. Quinlan, *C4.5: Programs for Machine Learning*. San Mateo, CA: Morgan Kaufmann Publishers, 1993.
- [11] W. N. Venables and B. D. Ripley, *Modern Applied Statistics with S*, 4th ed. Springer, 2002.
- [12] B. Ding and R. Gentleman, "Classification using generalized partial least squares," *Journal of Computational and Graphical Statistics*, vol. 14, no. 2, pp. 280–298, 2005.
- [13] L. Breiman, "Random forests," *Machine learning*, vol. 45, no. 1, pp. 5–32, 2001.
- [14] J. H. Friedman, "Greedy function approximation: a gradient boosting machine," *Annals of statistics*, pp. 1189–1232, 2001.
- [15] M. T. Ribeiro, S. Singh, and C. Guestrin, "Why should i trust you?: Explaining the predictions of any classifier," in *Proc. of ACM SIGKDD Knowledge Discovery and Data Mining*, 2016, pp. 1135–1144.
- [16] J. Cebal, F. Mut, J. Weir, and C. Putman, "Quantitative characterization of the hemodynamic environment in ruptured and unruptured brain aneurysms," *American Journal of Neuroradiology*, vol. 32, no. 1, pp. 145–151, 2011.
- [17] P. Berg and O. Beuing, "Multiple intracranial aneurysms: a direct hemodynamic comparison between ruptured and unruptured vessel malformations," *International journal of computer assisted radiology and surgery*, vol. 13, no. 1, pp. 83–93, 2018.



## Multiple Aneurysms AnaTomy CHallenge 2018 (MATCH)—phase II: rupture risk assessment

Philipp Berg<sup>1</sup> · Samuel Voß<sup>1</sup> · Gábor Janiga<sup>1</sup> · Sylvia Saalfeld<sup>1</sup> · Aslak W. Bergersen<sup>2</sup> · Kristian Valen-Sendstad<sup>2</sup> · Jan Bruening<sup>3</sup> · Leonid Goubergrits<sup>3</sup> · Andreas Spuler<sup>4</sup> · Tin Lok Chiu<sup>5</sup> · Anderson Chun On Tsang<sup>5</sup> · Gabriele Copelli<sup>6</sup> · Benjamin Csippa<sup>7</sup> · György Paál<sup>7</sup> · Gábor Závodszky<sup>7</sup> · Felicitas J. Detmer<sup>8</sup> · Bong J. Chung<sup>8</sup> · Juan R. Cebal<sup>8</sup> · Soichiro Fujimura<sup>9</sup> · Hiroyuki Takao<sup>9</sup> · Christof Karmonik<sup>10</sup> · Saba Elias<sup>10</sup> · Nicole M. Cancelliere<sup>11</sup> · Mehdi Najafi<sup>12</sup> · David A. Steinman<sup>12</sup> · Vitor M. Pereira<sup>11</sup> · Senol Piskin<sup>13</sup> · Ender A. Finol<sup>13</sup> · Mariya Pravdivtseva<sup>14</sup> · Prasanth Velvaluri<sup>15</sup> · Hamidreza Rajabzadeh-Oghaz<sup>16</sup> · Nikhil Paliwal<sup>16</sup> · Hui Meng<sup>16</sup> · Santhosh Seshadhri<sup>17</sup> · Sreenivas Venguru<sup>17</sup> · Masaaki Shojima<sup>18</sup> · Sergey Sindeev<sup>19</sup> · Sergey Frolov<sup>19</sup> · Yi Qian<sup>20</sup> · Yu-An Wu<sup>21</sup> · Kent D. Carlson<sup>21</sup> · David F. Kallmes<sup>21</sup> · Dan Dragomir-Daescu<sup>21</sup> · Oliver Beuing<sup>22</sup>

Received: 10 January 2019 / Accepted: 23 April 2019  
© CARS 2019

### Abstract

**Purpose** Assessing the rupture probability of intracranial aneurysms (IAs) remains challenging. Therefore, hemodynamic simulations are increasingly applied toward supporting physicians during treatment planning. However, due to several assumptions, the clinical acceptance of these methods remains limited.

**Methods** To provide an overview of state-of-the-art blood flow simulation capabilities, the Multiple Aneurysms AnaTomy CHallenge 2018 (MATCH) was conducted. Seventeen research groups from all over the world performed segmentations and hemodynamic simulations to identify the ruptured aneurysm in a patient harboring five IAs. Although simulation setups revealed good similarity, clear differences exist with respect to the analysis of aneurysm shape and blood flow results. Most groups (12/71%) included morphological and hemodynamic parameters in their analysis, with aspect ratio and wall shear stress as the most popular candidates, respectively.

**Results** The majority of groups (7/41%) selected the largest aneurysm as being the ruptured one. Four (24%) of the participating groups were able to correctly select the ruptured aneurysm, while three groups (18%) ranked the ruptured aneurysm as the second most probable. Successful selections were based on the integration of clinically relevant information such as the aneurysm site, as well as advanced rupture probability models considering multiple parameters. Additionally, flow characteristics such as the quantification of inflow jets and the identification of multiple vortices led to correct predictions.

**Conclusions** MATCH compares state-of-the-art image-based blood flow simulation approaches to assess the rupture risk of IAs. Furthermore, this challenge highlights the importance of multivariate analyses by combining clinically relevant metadata with advanced morphological and hemodynamic quantification.

**Keywords** Intracranial aneurysm · Rupture risk · Hemodynamic simulation · International challenge

✉ Philipp Berg  
berg@ovgu.de

<sup>1</sup> University of Magdeburg, Magdeburg, Germany

<sup>2</sup> Simula Research Laboratory, Lysaker, Norway

<sup>3</sup> Charité – Universitätsmedizin, Berlin, Germany

<sup>4</sup> Helios Hospital Berlin Buch, Berlin, Germany

<sup>5</sup> University of Hong Kong, Hong Kong, China

<sup>6</sup> University of Parma, Parma, Italy

<sup>7</sup> Budapest University of Technology and Economics, Budapest, Hungary

<sup>8</sup> George Mason University, Fairfax, VA, USA

<sup>9</sup> Tokyo University of Science, Tokyo, Japan

<sup>10</sup> Houston Methodist Research Institute, Houston, TX, USA

<sup>11</sup> Toronto Western Hospital, Toronto, ON, Canada

## Introduction

The assessment of intracranial aneurysm (IA) rupture probability or the differentiation between stable and unstable IAs still remains challenging. Hence, image-based hemodynamic simulations are increasingly used to account for patient-specific flow structures and detect potentially harmful conditions. However, the usefulness of computational fluid dynamics (CFD) in a clinical context remains uncertain.

After early single-case applications of numerical methods for IA flow description [1, 2], more advanced simulation studies containing larger case numbers were performed. Xiang et al. [3, 4] investigated 119 (and later 204) aneurysms using CFD and found that most ruptured IAs had complex flow, significantly lower wall shear stress (WSS), and larger oscillatory shear compared to the unruptured cohort. In contrast, Cebral et al. [5, 6] concluded (based on 210 cases) that rupture more likely occurs in IAs with significantly higher maximum WSS, concentrated inflow, and complex flow patterns. Recently, Detmer et al. [7] included 1631 aneurysms in their study and developed an aneurysm rupture probability model based on patient characteristics (age and gender), aneurysm location, morphology, and hemodynamics.

In addition to numerical investigations of blood flow, several verification and validation studies have been carried out to improve the acceptance of the underlying methods among physicians [8–12]. However, reliable acquisition of potentially relevant parameters can be difficult or be subject to a high variability, due to multiple interdisciplinary working steps. To address this observation and draw attention to required conditions for realistic hemodynamic simulations, Steinman et al. [13] organized a broad challenge (25 groups participating) that compared the fluid dynamics solver, discretization approaches, and solution strategies employed among participants. Good agreement with respect

to cycle-average velocity and peak systolic pressure calculation was obtained, but other clinically relevant parameters were not addressed. In a follow-up challenge (26 groups participating) organized by Janiga and Berg, participants were requested to predict aneurysm rupture and the corresponding rupture site using numerical methods [14, 15]. Over 80% of the groups chose the correct aneurysm, but the rupture site could not be found based on CFD. To address the overall variability of the important hemodynamic parameter WSS, Valen-Sendstad et al. [16] compared simulation results from 28 challenge contributions, providing only the source 3D images to each team. Based on the normalized WSS results of five middle cerebral artery aneurysms per group, they found that the inter-group variability was around 30%, with the highest differences with respect to maximum WSS and low shear area.

The present study focuses on the presentation of state-of-the-art segmentation and simulation approaches with respect to IA rupture risk assessment. In the frame of the Multiple Aneurysms AnaTomy CHallenge 2018 (MATCH), interested biomedical engineering groups were requested to segment and simulate a patient-specific dataset harboring five IAs. Furthermore, rupture probability suggestions were collected based on arbitrary criteria (e.g., any number of morphological and/or hemodynamic parameters). The results of the first phase (segmentation) are presented in Berg et al. [17], while this study focuses on the second phase (rupture risk assessment). Based on the presented findings, helpful recommendations regarding realistic and beneficial blood flow simulations are provided for future investigations.

## Materials and methods

### Case details and image acquisition

All five aneurysms that were the subject of MATCH were found in a single patient admitted to the hospital with acute subarachnoid hemorrhage due to rupture of one of the aneurysms. Two aneurysms were located at the right M1-segment, one at the left M1-segment, another one at the left MCA-bifurcation, and the fifth at the left posterior inferior cerebellar artery (PICA) (see Fig. 1). Four aneurysms were of similar size ranging between 4.4 mm and 5.6 mm. The two M1-aneurysms on the right were clipped, the others coiled.

The ruptured aneurysm was clearly identified by imaging. CT and subsequent MRI showed a subarachnoid hemorrhage mainly in the left premedullary cistern surrounding the PICA-aneurysm. In addition, both M1-aneurysms on the right were clipped, with no evidence of prior bleeding. This study was performed in accordance with the guidelines of the local ethics committee.

<sup>12</sup> University of Toronto, Toronto, ON, Canada

<sup>13</sup> The University of Texas at San Antonio, San Antonio, TX, USA

<sup>14</sup> University Medical Center Schleswig-Holstein, Kiel, Germany

<sup>15</sup> Christian-Albrechts-University, Kiel, Germany

<sup>16</sup> State University of New York, Buffalo, NY, USA

<sup>17</sup> Medtronic Engineering Innovation Centre, Hyderabad, India

<sup>18</sup> Saitama Medical University General Hospital, Saitama, Japan

<sup>19</sup> Tambov State Technical University, Tambov, Russia

<sup>20</sup> Macquarie University, Sydney, Australia

<sup>21</sup> Mayo Clinic, Rochester, MN, USA

<sup>22</sup> University Hospital Magdeburg, Magdeburg, Germany

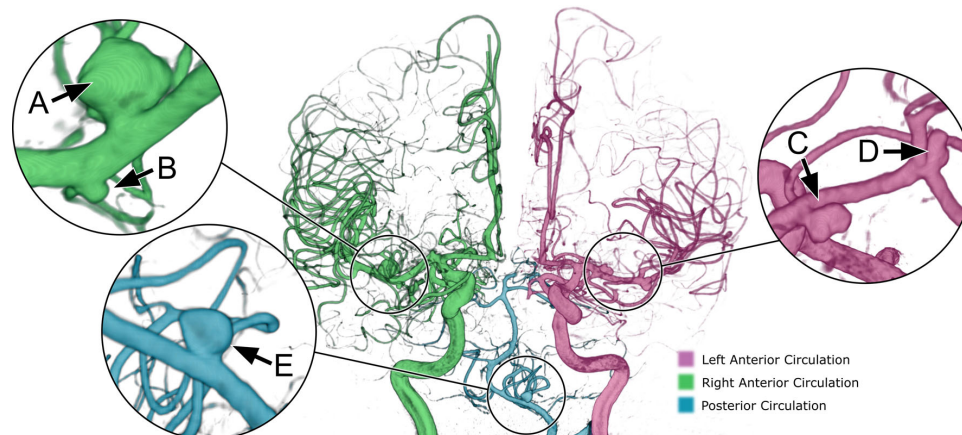


**Fig. 1** Illustration of the five IAs from the investigated aneurysm patient. Aneurysms A and B were located on the M1 segment of the right anterior circulation and C on the left M1 segment, respectively. Aneurysm D was found on the left middle cerebral artery bifurcation and aneurysm E

was located on the left posterior inferior cerebellar artery. The image data were acquired using 2D and 3D digital subtraction angiography, while only 3D rotational angiography data were provided to the MATCH participants

### Participating groups

MATCH was initially announced on November 03, 2017, and interested research groups were able to receive detailed information from the associated Web site (<https://www.ics2018.de>) and from newsletters of the 15th Interdisciplinary Cerebrovascular Symposium. Participants were asked to submit their simulation results until February 02, 2018, wherein the following items were requested:

- Participants were asked to perform hemodynamic simulations based on their own segmentations, and to identify which aneurysm ruptured using arbitrary criteria (e.g., hemodynamic parameters). In addition to the request to decide which aneurysm ruptured, participants were asked to provide a rupture probability ranking of the five IAs.
- Participants submitted an informal abstract (max. 1 page) containing author names, affiliations, and simulation details: (1) Mesh resolution, (2) solver, (3) time-step size (if unsteady), (4) type of in- and outflow boundary condition, (5) viscosity/density, and (6) reasons for choosing a particular aneurysm as being the ruptured one (aneurysm A-E) as well as ranking of rupture probability of each aneurysm. Further details were optional.

In total, 17 groups from 11 different countries followed the call and submitted an abstract. The groups had the following origins: Europe (Germany: 2; Hungary, Italy, Norway, Russia: 1); North America (USA: 5; CAN: 1); Asia (Japan: 2; India, Hong Kong: 1); Australia (1).

### Segmentations

3D rotational angiographies acquired on an Artis Q angiography system (Siemens Healthineers AG, Forchheim, Germany) were reconstructed on a Syngo X Workplace (Siemens Healthineers AG, Forchheim, Germany) using the kernel “HU auto” [18]. The details of the segmentation have already been described in Berg et al. [17].

### Hemodynamic simulations

Since each participant had the freedom to choose an arbitrary strategy regarding the hemodynamic simulations, the most important properties are described in the following. An overview regarding the simulation setups for MATCH is presented in Table 1 and Fig. 2.

### Spatial discretization

Although a variety of meshing strategies related to CFD exists, the use of unstructured grids with a combination of either tetrahedral (14 groups) or polyhedral (2 groups) cells with a few prism layers was most common. Only one group used an unstructured hexahedral mesh with five additional prism layers (Group 2). Regardless of the mesh type, an appropriate spatial resolution is essential to enable the generation of mesh-independent solutions. Here, reported cell sizes ranged between 0.1 and 0.3 mm, with a mean value and standard deviation of  $0.17 \pm 0.076$  mm. Thus, depending on the size of the considered vessel volume, the total number of cells per simulation was between 0.5 and 4.1 million.

**Table 1** Each group's technical details regarding the corresponding hemodynamic simulation and analysis as well as individual selections of the aneurysm with the highest rupture probability (correct choices are highlighted as bold)

Group	Inlet boundary condition	Blood treatment	Time dependency	Outlet boundary condition	Time step size	Parameters	No. param.	Aneurysm choice
<b>1</b>	<b>Womersley</b>	<b>Newtonian</b>	<b>Unsteady</b>	<b>Zero pressure</b>	<b>1E-02</b>	<b>Morph/hemo</b>	<b>16</b>	<b>E</b>
2	Plug	Non-Newt.	Unsteady	Zero pressure	1E-03	Morph/hemo	4	A
3	Plug	Newtonian	Steady	Zero pressure	–	Morph/hemo	2	C
4	Plug	Newtonian	Steady	Murray (d2)	–	Hemo	1	D
5	Womersley	Newtonian	Unsteady	0D model	1E-04	Morph/hemo	6	A
<b>6</b>	<b>2D PC-MRI</b>	<b>Non-Newt.</b>	<b>Unsteady</b>	<b>Constant pressure</b>	<b>1E-02</b>	<b>Morph/hemo</b>	<b>3</b>	<b>E</b>
7	Plug	Non-Newt.	Steady	Murray (d2)	–	Morph/hemo	4	A
<b>8</b>	<b>Womersley</b>	<b>Newtonian</b>	<b>Unsteady</b>	<b>Zero pressure</b>	<b>1E-03</b>	<b>Morph/hemo</b>	<b>4</b>	<b>E</b>
9	Womersley	Newtonian	Unsteady	0D model	1E-04	Morph/hemo	2	D
10	Plug	Newtonian	Unsteady	Zero pressure	5E-07	Hemo	2	D
11	Parabolic	Newtonian	Steady	Murray (d3)	–	Morph/hemo	2	A
12	Plug	Newtonian	Unsteady	Pressure waveform	5E-03	Hemo	3	C
13	Plug	Newtonian	Unsteady	Murray (d2)	1E-03	Morph/hemo	3	C
14	Plug	Newtonian	Unsteady	Zero pressure	5E-04	Morph/hemo	4	A
<b>15</b>	<b>Parabolic</b>	<b>Newtonian</b>	<b>Unsteady</b>	<b>Zero pressure</b>	<b>7E-03</b>	<b>Hemo</b>	<b>5</b>	<b>E</b>
16	Plug	Newtonian	Steady	Zero pressure	–	Hemo	5	C
17	Plug	Newtonian	Unsteady	Pressure waveform	1E-03	Morph/hemo	6	A

The following criteria are presented: (1) type of inlet boundary condition: constant (plug), parabolic, Womersley or phase-contrast magnetic resonance imaging (PC-MRI) profile, (2) blood treatment, assuming Newtonian or Non-Newtonian behavior, (3) time dependency: steady-state or time-varying simulations, (4) type of parameters for rupture risk assessment: morphologic and/or hemodynamic, (5) number of considered parameters, (6) selected aneurysm with the highest rupture probability

### Solver selection

To solve the equation for mass and momentum conservation, an appropriate and validated fluid dynamics solver is required. Here, most groups (11) decided to use a commercially available software package, which was either from ANSYS (Fluent or CFX, Canonsburg, Pennsylvania, USA) or from Siemens PLM (STAR CCM+, Plano, Texas, USA). Approximately one-third of the participants (five groups) applied open-source tools (e.g., OpenFOAM or Oasis). Only one group used an in-house fluid dynamics solver.

### Boundary conditions

Since only the image data were provided to the MATCH participants, patient-specific boundary conditions were not available. This represents a situation commonly encountered by research groups; as for the patient in this study with a subarachnoid hemorrhage, the acquisition of individual flow curves would mean an additional, unrequired intervention. Hence, participants were free to choose arbitrary boundary conditions.

Regarding the resolution of temporal effects, five groups (29%) performed steady-state simulations, while twelve groups (71%) considered unsteady flow with the simulation of two or more cardiac cycles. Interestingly, clear differences with respect to the time step size occurred, which ranged between 5E-7 s and 1E-2 s (mean 3E-3 ± 3.9E-3 s). Furthermore, variability regarding the type of inflow boundary condition was present. While 60% of the groups applied a constant plug profile for either velocity or flow rate, one quarter defined a *Womersley* equation profile, which describes the pulsatile character of the velocity profile. A parabolic flow was assumed by two groups and one group applied velocity profiles of the left internal carotid and vertebral artery from 2D phase-contrast MRI measurements of a healthy volunteer.

To characterize the entire computational system, outlet boundary conditions needed to be defined. Due to the lack of knowledge regarding pressure distributions in the distal vessels, eleven groups (65%) used either constant values or predefined pressure waves. The remaining six groups applied flow-splitting models, which were either based on in-house 0D models (two groups) [19], area-dependent weighting (two

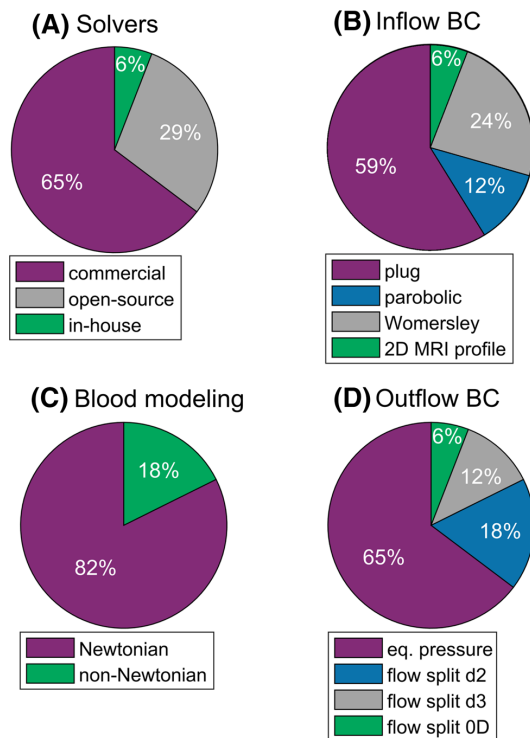


**Fig. 2** Distribution of methodological details regarding the variability of hemodynamic simulations: **a** type of the fluid flow solver, **b** type of inflow boundary condition (BC), **c** concept of blood treatment, **d** type of outflow boundary condition (d2 and d3 relate to the power coefficient of Murray's law, 0D indicated the application of a reduced splitting model)

groups), or the cube of the corresponding vessel diameter (two groups) [20].

Finally, all groups assumed rigid vessel wall conditions and no participant carried out fluid–structure interaction simulations to account for vessel movement or occurring wall stresses.

### Blood modeling

The treatment of blood with respect to its material properties was relatively consistent among the groups. Since blood is an incompressible fluid, the assumption of a constant density is well-accepted and values ranging between 1000 and 1100 kg/m<sup>3</sup> were applied (median = 1056 kg/m<sup>3</sup>).

Regarding the choice of viscosity, no clear consensus exists. While some studies claim that non-Newtonian effects influence the simulation results [21, 22], others have found no significant impact of available models on the flow fields [23, 24]. Nevertheless, researchers agree

that the choice of blood treatment has rather secondary effects compared to primary influences, e.g., geometry and inflow conditions. Within MATCH, 14 groups (82%) assumed a Newtonian fluid with a mean dynamic viscosity of  $3.65 \pm 0.21$  mPa s. The remaining three groups applied non-Newtonian models (either power law models or the *Carreau* model).

## Results

As a summary of the challenge, Table 1 contains the group-specific settings for their numerical investigation as well as their choice regarding the ruptured aneurysm.

### Rupture risk assessment

In the context of MATCH, the assessment of aneurysm rupture risk was mostly carried out using morphological in combination with hemodynamics parameters. For instance, only four groups considered patient information such as the aneurysm site. In this regard, it must be noted that only the DICOM dataset was provided to the participants to assess the ability of biomedical engineering related analysis. Hence, clinically relevant factors such as age, sex, smoking, hypertension were not disclosed.

Only three morphological parameters were chosen more than once (aspect ratio, size ratio and undulation index), while the following parameters were chosen only once: aneurysm neck area, aneurysm width, height-to-width ratio, bulge location, parent vessel diameter, volume-to-ostium ratio, non-sphericity index, aneurysm surface curvature, ratio between each aneurysm's volume, and volume of each aneurysm's least bounding sphere.

Besides the morphological analyses, participants applied hemodynamics parameters to assess the rupture probability of each aneurysm. By far the most often used parameter was WSS (in different variants), which was calculated by 13 groups. The second most applied variable was the oscillatory shear index (OSI, 9) followed by pressure (5), maximum velocity, velocity fluctuation, and relative residence time (each 2). The following parameters were used only once: inflow concentration index, energy loss, vorticity, helicity, low shear area, kinetic energy, and spectral power index.

Table 2 contains the rupture risk assessment strategies of all participants and reveals the basis for the individual decisions. Furthermore, it provides an overview of the usage of morphological and hemodynamic parameters by each group. One should notice that only five groups applied hemodynamic parameters exclusively to assess the rupture probability.

**Table 2** Overview of the participants rupture risk assessment strategies containing the number of considered morphologic as well as hemodynamic parameters (correct choices are highlighted as bold)

Group	Rupture risk assessment strategy	Parameters	
		Morph	Hemo
1	<b>Logistic regression models (based on CFD simulations of 1920 aneurysms) [7]</b>	9	7
2	Rupture resemblance score (based on CFD simulations of 542 aneurysms) [25]	2	2
3	Aneurysm size and energy loss [26]	1	1
4	WSS difference between the maximum and minimum flow condition	0	1
5	Combination of size, irregularity, low aspect ratio and low WSS, high OSI, high-frequency WSS instabilities [27]	3	3
6	<b>Location, diameter, WSS</b>	2	1
7	Location, size, ratio of volume and volume of least bounding sphere, streamlines, and WSS	3	1
8	<b>Internal scoring system based on dome/neck ratio, blebs, TAWSS, change in instantaneous WSS, OSI on daughter blebs</b>	2	3
9	Visual inspection of morphology (non-spherical shape) and flow instability (turbulent-like flow)	1	1
10	Pressure and WSS ratios	0	2
11	Size and low WSS	1	1
12	WSS, TAWSS, OSI	0	3
13	Rupture resemblance score (based on CFD simulations of 542 aneurysms) [25]	1	2
14	Aspect ratio, pressure difference, OSI, rupture risk parameter based on WSS and averaged velocity	1	4
15	<b>TAWSS, OSI, RRT, pressure distribution, stagnation points</b>	0	5
16	Relative changes of WSS, velocity, pressure, vorticity, helicity	0	5
17	Size, aspect ratio, WSS, OSI, RRT, ICI	2	4

With (TA)WSS (time-averaged) wall shear stress, OSI oscillatory shear index, RRT relative residence time, ICI inflow concentration index

**Selections by the challenge participants**

Participating groups selected the following aneurysms as being the ruptured one: Most groups (7/41%) selected aneurysm A as the most probable candidate, which is the largest one. It can be observed that five of these groups used low WSS in combination with increased OSI as indicators for aneurysm rupture.

Four groups (24%) correctly selected aneurysm E as being the ruptured one. While one group combined clinically relevant information (e.g., aneurysm site) with simulation results,

two groups applied rupture risk assessment models. These include multiple morphological as well as hemodynamic parameters that were associated with rupture in previous studies. Furthermore, it must be mentioned that one of the successful groups, focusing on hemodynamics exclusively, analyzed not only surface parameters, but also the flow behavior within the aneurysm (e.g., inflow jet, presence of multiple vortices).

Aneurysms C and D were selected by three groups each (18%). The selections by these groups were based on single hemodynamic parameters or visual inspection of morphology and flow instability. Finally, no group selected aneurysm B, which was the smallest one.

The rupture probability ranking revealed that aneurysm E was correctly selected by four groups (23.5%). Furthermore, the rupture probability of aneurysm E was ranked second by three groups (17.5%), third by four groups (23.5%), and fourth by two groups (12%). Finally, another four groups (23.5%) judged aneurysm E as being the least prone to rupture. Thus, a strong variability regarding the calculated rupture probability of the actual ruptured aneurysm exists. Table 3 contains the rupture risk probability rankings of all groups.

**Table 3** Rupture probability ranking provided by each MATCH participant based on the individual segmentations and hemodynamic simulations

Group	Rupture probability ranking				
	1st	2nd	3rd	4th	5th
1	<b>E</b>	D	A	C	B
2	A	C	D	<b>E</b>	B
3	C	D	<b>E</b>	B	A
4	D	<b>E</b>	A	B	C
5	A	<b>E</b>	C	D	B
6	<b>E</b>	A	C	D	B
7	A	<b>E</b>	C	D	B
8	<b>E</b>	C	D	A	B
9	D	C	A	<b>E</b>	B
10	D	A	<b>E</b>	C	B
11	A	C	<b>E</b>	D	B
12	C	B	D	A	<b>E</b>
13	C	A	D	B	<b>E</b>
14	A	C	D	B	<b>E</b>
15	<b>E</b>	D	C	A	B
16	C	A	B	D	<b>E</b>
17	A	C	<b>E</b>	D	B

The ruptured aneurysm (E) is highlighted in bold. Notice the strong variability with an exception for the smallest aneurysm B as being the least endangered

## Discussion

MATCH focused on the comparison of segmentation and simulation algorithms to assess the rupture risk probability of IAs. While it was demonstrated in the first phase that clear variations regarding the aneurysm surface representation exist [17], the second phase presents the real-world variability of rupture risk assessment.

### The role of hemodynamic simulations

It can be observed in the literature that an increasing number of blood flow simulations is being performed to improve the knowledge on patient-individual flow characteristics of IAs. While some studies focused on detailed hemodynamic descriptions for a limited number of cases [28, 29], others investigated blood flow variables in larger cohorts [4, 30, 31]. In this regard, significant differences between unruptured and ruptured IAs were identified. However, only snapshots of the disease state are considered and longitudinal studies are in a clear minority [32, 33].

In the frame of the second MATCH phase, it was observed that most groups applied not only hemodynamic, but also morphological parameters for their evaluation of the rupture probability (Table 2). This emphasizes the fact that at least with regard to the present knowledge, flow simulations cannot provide all necessary information to reliably assess IA rupture risk. Instead, a multivariate analysis by combining clinically relevant metadata with advanced morphological and hemodynamic quantification appears to be more promising.

Additionally, it is important to mention that certain minimum requirements with respect to the simulation setup are needed in the future to ensure plausible numerical results. These include appropriate segmentations, the generation of a sufficient volume mesh, the choice of justifiable boundary conditions, the selection of a verified fluid flow solver and a realistic modeling of blood. Apart from the first criterion, which has primary impact on the simulation results, no strong variations were present among the participating groups. However, clear differences regarding the subsequent data evaluation occurred as described in the following section.

### Rupture risk assessment

In contrast to earlier aneurysm challenges, which predefined the simulation domains or boundary conditions [13, 15], MATCH was designed to give all participants the chance to completely apply their own strategies. A realistic scenario was created, in which researchers were confronted with clinical image data and aneurysm risk quantification is requested by the attending physicians. In this regard, it was

noted that groups created individualized workflows to obtain segmentation and simulation results. Furthermore, the subsequent analyses revealed clear differences with respect to extent. While some groups only applied one or two parameters, other included up to sixteen in well-trained models. Specifically, several groups used low WSS in combination with high OSI to identify the ruptured aneurysm (e.g., all successful groups). However, aneurysm rupture does not necessarily take place in regions of lowest WSS and highest OSI, respectively [14]. Additionally, the sophisticated, model-based selections were related to strong clinical, as well as bioengineering experience. These models include either multiple morphological and hemodynamic parameters as well as the aneurysm's location [7], or advanced scoring systems with a particular focus on blebs and flow features.

Future studies require a systematic uncertainty quantification to assess the robustness of the applied models. In this regard, initial investigations in the context of MATCH are carried out [34] and existing examples from cardiovascular research could be transferred to cerebrovascular questions [35–37].

## Recommendations

The investigation of five IAs in a single patient certainly does not enable the derivation of generalizable rules regarding the future assessment of aneurysm rupture probabilities. However, certain recommendations can be formulated, which arise from observations during this international challenge:

1. MATCH emphasizes the importance of appropriate segmentation and should motivate groups to put highest efforts in this presimulation step. It was shown that one group, which reconstructed the neck of the ruptured aneurysm with the highest accuracy in MATCH Phase I [17], was also among the successful groups in Phase II. Further, the other three successful groups submitted no outlying segmentation results.
2. To obtain plausible blood flow results, a minimum spatial resolution of the discretized domain is needed to avoid influences due to mesh-dependence (e.g., most groups applied a base size of approximately 0.1 mm).
3. Since none of the groups that assumed steady-state flow conditions chose the correct aneurysm, time-dependent blood flow simulation should be carried out. This enables the prediction of complex transient flow phenomena, which were associated with rupture [38–40]. Further, as computational resources continue to improve, simulation times should not be a problem in the future. Nevertheless, as presented in Table 1, the type of inflow condition as well as the choice of blood description appear to be rather of secondary importance [16].

4. Regarding the outlet boundary condition, it is well known that with an increasing number of outflow cross sections, the influence on the flow fields rises. Thus, although the majority of groups used constant pressure conditions, it should be avoided by applying advanced flow-splitting methods. Furthermore, additional quantification studies are required in order to be able to simulate larger domains of the cerebral vasculature.
5. To identify relevant rupture risk assessment parameters in the future, they must be consistently compared in future studies. Within the challenge, neither single nor few morphological and hemodynamic parameters alone were sufficient for a robust and reliable rupture risk evaluation of IAs. Instead, the application of advanced and validated prediction models was successful, which include a variety of independent factors [7]. These consist of clinically important information from the patient as well as individual shape and flow parameters.

### Limitations

It must be noted that certain limitations exist regarding this challenge. First, only one patient was included in this study, although harboring five aneurysms. Thus, no generalizable conclusions are possible, and investigations with an increased number of cases are desirable. However, the inclusion of more cases would likely have led to a decreased number of participants and therefore to a limited comparability among real-world approaches.

Second, since no patient-specific wall information was provided in the frame of the study, all hemodynamic simulations were carried out based on the assumption of rigid vessels. Hence, the role of aneurysm vessel walls regarding aneurysm rupture remains unclear. Nevertheless, if reliable and accurate wall information is available, it is recommended to include it in future studies [41, 42].

Third, due to a lack of measured data, no patient-specific boundary conditions were provided. This, however, is a common situation in clinical practice. Especially in patients with SAH, flow measurements would mean an additional examination, which is inappropriate in emergency situations. In addition, such a measurement would not necessarily reflect the hemodynamic situation that was present during the rupture. In patients with innocent aneurysms, patient-specific flow conditions can be determined more easily, but even then, it would only be a snapshot in a physical state of rest that cannot reflect the fluctuations caused by different daily activities.

Fourth, the experience of each participant was not queried, as was done in previous challenges [16]. On the one hand, it certainly would have been interesting to correlate experience with rupture risk assessment outcome. However, “experi-

ence” is difficult to measure since neither the (active or passive) duration nor the number of simulated cases is an objective metric. Furthermore, multiple disciplines come into play (e.g., biomedical engineers, physicians, computer scientists), with personnel who possess different backgrounds and skills. Also, verified and validated techniques should be successful even with minor experience. Therefore, the challenge organizers decided against the inclusion of experience into the study.

Finally, it should be stated that MATCH was not designed to determine whether or not CFD is able to predict aneurysm rupture in general. It should rather be seen as an instrument that reveals potentials but also limitations of existing methods that include hemodynamics, but also emphasizes where further improvements are required toward clinical support. Hence, from the perspective of the challenge organizers, the aim of the study was not to end up with as many successful predictions as possible. Rather, the real value becomes visible in the separation between successful and unsuccessful choices and the associated methodologies. Therefore, MATCH should encourage groups with correct predictions to further improve their models and communicate them accordingly. Additionally, groups with incorrect aneurysm selection can re-evaluate their workflows for image-based blood flow simulations and integrate more advanced techniques to improve their methods.

### Conclusions

To demonstrate and compare existing blood flow simulation techniques for the rupture risk assessment of IAs, an international challenge was announced. Participants were given 3D imaging data containing five intracranial aneurysms from one patient and were asked to assess which aneurysm ruptured. Overall, 17 groups from 11 countries participated, and 4 groups correctly identified the ruptured aneurysm. Although this is only a 24% group success rate, successful selections were based on clinical data as well as advanced probability models. Thus, the challenge highlights the importance of multivariate analyses that combine clinically relevant metadata with advanced morphological and hemodynamic quantification. Furthermore, it is essential to work together to drive consensus on approach and best practices for hemodynamics simulations.

**Acknowledgements** This study was funded by the Federal Ministry of Education and Research in Germany within the Forschungscampus *STIMULATE* (Grant Number 13GW0095A) and the German Research Foundation (Grant Number 399581926). The authors highly acknowledge participants of MATCH Phase I, who contributed their segmentation results.

## Compliance with ethical standards

**Conflict of interest** The authors declare they have no conflict of interest.

**Ethical approval** All procedures performed in studies involving human participants were in accordance with the ethical standards of the institutional and/or national research committee and with the 1964 Helsinki Declaration and its later amendments or comparable ethical standards.

**Informed consent** Informed consent was obtained from all individual participants included in the study.

## References

- Steinman DA, Milner JS, Norley CJ, Lownie SP, Holdsworth DW (2003) Image-based computational simulation of flow dynamics in a giant intracranial aneurysm. *AJNR Am J Neuroradiol* 24(4):559–566
- Kobayashi N, Miyachi S, Okamoto T, Hattori K, Kojima T, Nakai K, Qian S, Takeda H, Yoshida J (2004) Computer simulation of flow dynamics in an intracranial aneurysm. Effects of vessel wall pulsation on a case of ophthalmic aneurysm. *Interv Neuroradiol: J Peritherapeutic Neuroradiol Surg Proced Relat Neurosci* 10(Suppl 1):155–160. <https://doi.org/10.1177/15910199040100s127>
- Xiang J, Natarajan SK, Tremmel M, Ma D, Mocco J, Hopkins LN, Siddiqui AH, Levy EI, Meng H (2011) Hemodynamic-morphologic discriminants for intracranial aneurysm rupture. *Stroke* 42(1):144–152. <https://doi.org/10.1161/STROKEAHA.110.592923>
- Xiang J, Yu J, Snyder KV, Levy EI, Siddiqui AH, Meng H (2016) Hemodynamic-morphologic discriminant models for intracranial aneurysm rupture remain stable with increasing sample size. *J Neurointerv Surg* 8(1):104–110. <https://doi.org/10.1136/neurintsurg-2014-011477>
- Cebral JR, Mut F, Weir J, Putman C (2011) Quantitative characterization of the hemodynamic environment in ruptured and unruptured brain aneurysms. *AJNR Am J Neuroradiol* 32(1):145–151. <https://doi.org/10.3174/ajnr.A2419>
- Cebral JR, Mut F, Weir J, Putman CM (2011) Association of hemodynamic characteristics and cerebral aneurysm rupture. *AJNR Am J Neuroradiol* 32(2):264–270. <https://doi.org/10.3174/ajnr.A2274>
- Detmer FJ, Chung BJ, Mut F, Slawski M, Hamzei-Sichani F, Putman C, Jiménez C, Cebral JR (2018) Development and internal validation of an aneurysm rupture probability model based on patient characteristics and aneurysm location, morphology, and hemodynamics. *Int J Comput Assist Radiol Surg* 13(11):1767–1779. <https://doi.org/10.1007/s11548-018-1837-0>
- Berg P, Stucht D, Janiga G, Beuing O, Speck O, Thévenin D (2014) Cerebral blood flow in a healthy Circle of Willis and two intracranial aneurysms: computational fluid dynamics versus four-dimensional phase-contrast magnetic resonance imaging. *J Biomech Eng*. <https://doi.org/10.1115/1.4026108>
- Roloff C, Stucht D, Beuing O, Berg P (2019) Comparison of intracranial aneurysm flow quantification techniques: standard PIV vs stereoscopic PIV vs tomographic PIV vs phase-contrast MRI vs CFD. *J Neurointerv Surg* 11(3):275–282. <https://doi.org/10.1136/neurintsurg-2018-013921>
- Raschi M, Mut F, Byrne G, Putman CM, Tateshima S, Viñuela F, Tanoue T, Tanishita K, Cebral JR (2012) CFD and PIV analysis of hemodynamics in a growing intracranial aneurysm. *Int J Numer Methods Biomed Eng* 28(2):214–228. <https://doi.org/10.1002/cnm.1459>
- Paliwal N, Damiano RJ, Varble NA, Tutino VM, Dou Z, Siddiqui AH, Meng H (2017) Methodology for computational fluid dynamic validation for medical use: application to intracranial aneurysm. *J Biomech Eng*. <https://doi.org/10.1115/1.4037792>
- Bouillot P, Brina O, Ouared R, Lovblad K-O, Farhat M, Pereira VM (2014) Particle imaging velocimetry evaluation of intracranial stents in sidewall aneurysm: hemodynamic transition related to the stent design. *PLoS ONE* 9(12):e113762. <https://doi.org/10.1371/journal.pone.0113762>
- Steinman DA, Hoi Y, Fahy P, Morris L, Walsh MT, Aristokleous N, Anayiotos AS, Papaharilaou Y, Arzani A, Shadden SC, Berg P, Janiga G, Bols J, Segers P, Bressloff NW, Cibis M, Gijzen FH, Cito S, Pallarès J, Browne LD, Costelloe JA, Lynch AG, Degroote J, Vierendeels J, Fu W, Qiao A, Hodis S, Kallmes DF, Kalsi H, Long Q, Kheifets VO, Finol EA, Kono K, Malek AM, Lauric A, Menon PG, Pekkan K, Esmaily Moghadam M, Marsden AL, Oshima M, Katagiri K, Peiffer V, Mohamied Y, Sherwin SJ, Schaller J, Goubergrits L, Usera G, Mendina M, Valen-Sendstad K, Habets DF, Xiang J, Meng H, Yu Y, Karniadakis GE, Shaffer N, Loth F (2013) Variability of computational fluid dynamics solutions for pressure and flow in a giant aneurysm: the ASME 2012 summer bioengineering conference CFD challenge. *J Biomech Eng* 135(2):21016. <https://doi.org/10.1115/1.4023382>
- Janiga G, Berg P, Sugiyama S, Kono K, Steinman DA (2015) The computational fluid dynamics rupture challenge 2013—phase I: prediction of rupture status in intracranial aneurysms. *AJNR Am J Neuroradiol* 36(3):530–536. <https://doi.org/10.3174/ajnr.A4157>
- Berg P, Roloff C, Beuing O, Voss S, Sugiyama S-I, Aristokleous N, Anayiotos AS, Ashton N, Revell A, Bressloff NW, Brown AG, Chung BJ, Cebral JR, Copelli G, Fu W, Qiao A, Geers AJ, Hodis S, Dragomir-Daescu D, Nordahl E, Bora Suzen Y, Owais Khan M, Valen-Sendstad K, Kono K, Menon PG, Albal PG, Mierka O, Münster R, Morales HG, Bonnefous O, Osman J, Goubergrits L, Pallares J, Cito S, Passalacqua A, Piskin S, Pekkan K, Ramalho S, Marques N, Sanchi S, Schumacher KR, Sturgeon J, Švihlová H, Hron J, Usera G, Mendina M, Xiang J, Meng H, Steinman DA, Janiga G (2015) The computational fluid dynamics rupture challenge 2013—phase II: variability of hemodynamic simulations in two intracranial aneurysms. *J Biomech Eng* 137(12):121008. <https://doi.org/10.1115/1.4031794>
- Valen-Sendstad K, Bergersen AW, Shimogonya Y, Goubergrits L, Bruening J, Pallares J, Cito S, Piskin S, Pekkan K, Geers AJ, Larrabide I, Rapaka S, Mihalef V, Fu W, Qiao A, Jain K, Roller S, Mardal K-A, Kamakoti R, Spirka T, Ashton N, Revell A, Aristokleous N, Houston JG, Tsuji M, Ishida F, Menon PG, Browne LD, Broderick S, Shojima M, Koizumi S, Barbour M, Aliseda A, Morales HG, Lefèvre T, Hodis S, Al-Smadi YM, Tran JS, Marsden AL, Vaipummadhom S, Einstein GA, Brown AG, Debus K, Niizuma K, Rashad S, Sugiyama S-I, Owais Khan M, Updegrove AR, Shadden SC, Cornelissen BMW, Majoie CBLM, Berg P, Saalfeld S, Kono K, Steinman DA (2018) Real-world variability in the prediction of intracranial aneurysm wall shear stress. The 2015 international aneurysm CFD challenge. *Cardiovasc Eng Tech* 9(4):544–564. <https://doi.org/10.1007/s13239-018-00374-2>
- Berg P, Voß S, Saalfeld S, Janiga G, Bergersen AW, Valen-Sendstad K, Bruening J, Goubergrits L, Spuler A, Cancelliere NM, Steinman DA, Pereira VM, Chiu TL, Tsang ACO, Chung BJ, Cebral JR, Cito S, Pallarès J, Copelli G, Csippa B, Paál G, Fujimura S, Takao H, Hodis S, Hille G, Karmonik C, Elias S, Kellermann K, Khan MO, Marsden AL, Morales HG, Piskin S, Finol EA, Pravdivtseva M, Rajabzadeh-Oghaz H, Paliwal N, Meng H, Seshadhri S, Howard M, Shojima M, Sugiyama S-I, Niizuma K, Sindeev S, Frolov S, Wagner T, Brawanski A, Qian Y, Wu Y-A, Carlson KD, Dragomir-Daescu D, Beuing O (2018) Multiple Aneurysms AnaTomy CHallenge 2018 (MATCH): phase I: segmentation. *Car-*

- diovas Eng Technol 9(4):565–581. <https://doi.org/10.1007/s13239-018-00376-0>
18. Berg P, Saalfeld S, Voß S, Redel T, Preim B, Janiga G, Beuing O (2018) Does the DSA reconstruction kernel affect hemodynamic predictions in intracranial aneurysms? An analysis of geometry and blood flow variations. *J Neurointerv Surg* 10(3):290–296. <https://doi.org/10.1136/neurintsurg-2017-012996>
  19. Chnafa C, Brina O, Pereira VM, Steinman DA (2018) Better than nothing: a rational approach for minimizing the impact of outflow strategy on cerebrovascular simulations. *AJNR Am J Neuroradiol* 39(2):337–343. <https://doi.org/10.3174/ajnr.A5484>
  20. Murray CD (1926) The physiological principle of minimum work: I. The vascular system and the cost of blood volume. In: *Proceedings of the national academy of sciences of the United States of America* 12(3):207–214
  21. Carty G, Chatpun S, Espino DM (2016) Modeling blood flow through intracranial aneurysms. a comparison of newtonian and non-newtonian viscosity. *J Med Biol Eng* 36(3):396–409. <https://doi.org/10.1007/s40846-016-0142-z>
  22. Frolov S, Sindeev S, Liepsch D, Balasso A, Arnold P, Kirschke JS, Prothmann S, Potlov AY (2018) Newtonian and non-Newtonian blood flow at a 90°-bifurcation of the cerebral artery. A comparative study of fluid viscosity models. *J Mech Med Biol* 18(05):1850043. <https://doi.org/10.1142/s0219519418500434>
  23. Fisher C, Rossmann JS (2009) Effect of non-newtonian behavior on hemodynamics of cerebral aneurysms. *J Biomech Eng* 131(9):91004. <https://doi.org/10.1115/1.3148470>
  24. Morales HG, Larrabide I, Geers AJ, Aguilar ML, Frangi AF (2013) Newtonian and non-Newtonian blood flow in coiled cerebral aneurysms. *J Biomech* 46(13):2158–2164. <https://doi.org/10.1016/j.jbiomech.2013.06.034>
  25. Xiang J, Yu J, Choi H, Dolan Fox JM, Snyder KV, Levy EI, Siddiqui AH, Meng H (2015) Rupture Resemblance Score (RRS): toward risk stratification of unruptured intracranial aneurysms using hemodynamic-morphological discriminants. *J Neurointerv Surg* 7(7):490–495. <https://doi.org/10.1136/neurintsurg-2014-011218>
  26. Qian Y, Takao H, Umezumi M, Murayama Y (2011) Risk analysis of unruptured aneurysms using computational fluid dynamics technology: preliminary results. *AJNR Am J Neuroradiol* 32(10):1948–1955. <https://doi.org/10.3174/ajnr.A2655>
  27. Khan MO, Chnafa C, Gallo D, Molinari F, Morbiducci U, Steinman DA, Valen-Sendstad K (2017) On the quantification and visualization of transient periodic instabilities in pulsatile flows. *J Biomech* 52:179–182. <https://doi.org/10.1016/j.jbiomech.2016.12.037>
  28. Valen-Sendstad K, Piccinelli M, Steinman DA (2014) High-resolution computational fluid dynamics detects flow instabilities in the carotid siphon: implications for aneurysm initiation and rupture? *J Biomech* 47(12):3210–3216. <https://doi.org/10.1016/j.jbiomech.2014.04.018>
  29. Valen-Sendstad K, Steinman DA (2014) Mind the gap: impact of computational fluid dynamics solution strategy on prediction of intracranial aneurysm hemodynamics and rupture status indicators. *AJNR Am J Neuroradiol* 35(3):536–543. <https://doi.org/10.3174/ajnr.A3793>
  30. Chung BJ, Doddasomayajula R, Mut F, Detmer F, Pritz MB, Hamzei-Sichani F, Brinjikji W, Kallmes DF, Jimenez CM, Putman CM, Cebal JR (2017) Angioarchitectures and Hemodynamic Characteristics of Posterior Communicating Artery Aneurysms and Their Association with Rupture Status. *AJNR Am J Neuroradiol* 38(11):2111–2118. <https://doi.org/10.3174/ajnr.A5358>
  31. Detmer FJ, Chung BJ, Mut F, Pritz M, Slawski M, Hamzei-Sichani F, Kallmes D, Putman C, Jimenez C, Cebal JR (2018) Development of a statistical model for discrimination of rupture status in posterior communicating artery aneurysms. *Acta Neurochir* 160(8):1643–1652. <https://doi.org/10.1007/s00701-018-3595-8>
  32. Boussel L, Rayz V, McCulloch C, Martin A, Acevedo-Bolton G, Lawton M, Higashida R, Smith WS, Young WL, Saloner D (2008) Aneurysm growth occurs at region of low wall shear stress: patient-specific correlation of hemodynamics and growth in a longitudinal study. *Stroke* 39(11):2997–3002. <https://doi.org/10.1161/STROKEAHA.108.521617>
  33. Soize S, Gawlitza M, Raoult H, Pierot L (2016) Imaging follow-up of intracranial aneurysms treated by endovascular means: Why, When, and How? *Stroke* 47(5):1407–1412. <https://doi.org/10.1161/STROKEAHA.115.011414>
  34. Goubergrits L, Hellmeier F, Bruening J, Spuler A, Hege HC, Voß S, Janiga G, Saalfeld S, Beuing O, Berg P (2019) Multiple Aneurysms AnaTomy CHallenge 2018 (MATCH)—Uncertainty quantification of geometric rupture risk parameters. *BioMed Eng OnLine* 18(1):35. <https://doi.org/10.1186/s12938-019-0657-y>
  35. Mirams GR, Pathmanathan P, Gray RA, Challenor P, Clayton RH (2016) Uncertainty and variability in computational and mathematical models of cardiac physiology. *J Physiol* 594(23):6833–6847. <https://doi.org/10.1113/JP271671>
  36. Sankaran S, Kim HJ, Choi G, Taylor CA (2016) Uncertainty quantification in coronary blood flow simulations: impact of geometry, boundary conditions and blood viscosity. *J Biomech* 49(12):2540–2547. <https://doi.org/10.1016/j.jbiomech.2016.01.002>
  37. Schiavazzi DE, Arbia G, Baker C, Hlavacek AM, Hsia TY, Marsden AL, Vignon-Clementel IE (2016) Uncertainty quantification in virtual surgery hemodynamics predictions for single ventricle palliation. *Int J Numer Methods Biomed Eng* 32(3):e02737. <https://doi.org/10.1002/cnm.2737>
  38. Doddasomayajula R, Chung B, Hamzei-Sichani F, Putman CM, Cebal JR (2017) Differences in hemodynamics and rupture rate of aneurysms at the bifurcation of the basilar and internal carotid arteries. *AJNR Am J Neuroradiol* 38(3):570–576. <https://doi.org/10.3174/ajnr.A5088>
  39. Sano T, Ishida F, Tsuji M, Furukawa K, Shimosaka S, Suzuki H (2017) Hemodynamic differences between ruptured and unruptured cerebral aneurysms simultaneously existing in the same location: 2 case reports and proposal of a novel parameter oscillatory velocity index. *World Neurosurg* 98:868.e5–868.e10. <https://doi.org/10.1016/j.wneu.2016.12.047>
  40. Berg P, Beuing O (2018) Multiple intracranial aneurysms: a direct hemodynamic comparison between ruptured and unruptured vessel malformations. *Int J Comput Assist Radiol Surg* 13(1):83–93. <https://doi.org/10.1007/s11548-017-1643-0>
  41. Voß S, Glaßer S, Hoffmann T, Beuing O, Weigand S, Jachau K, Preim B, Thévenin D, Janiga G, Berg P (2016) Fluid-structure simulations of a ruptured intracranial aneurysm: constant versus patient-specific wall thickness. *Comput Math Methods Med* 2016:9854539. <https://doi.org/10.1155/2016/9854539>
  42. Cebal J, Ollikainen E, Chung BJ, Mut F, Sippola V, Jahromi BR, Tulamo R, Hernesniemi J, Niemelä M, Robertson A, Frösen J (2017) Flow conditions in the intracranial aneurysm lumen are associated with inflammation and degenerative changes of the aneurysm wall. *AJNR Am J Neuroradiol* 38(1):119–126. <https://doi.org/10.3174/ajnr.A4951>

**Publisher's Note** Springer Nature remains neutral with regard to jurisdictional claims in published maps and institutional affiliations.



---

## APPENDIX

---

In the following, the papers of this cumulative habilitation thesis are listed in the same order as they were included in the Parts **I**, **II** and **III**. My individual contribution to each paper is listed in Sec. **A.1**. Further research papers that originated during my post-doc time focusing on minimal-invasive therapies apart from intracranial aneurysm treatment, and which are not included in this cumulative thesis, are provided in Sec. **A.2**.

### A.1 CONTRIBUTION

Hoffmann et al. (2016): Hoffmann, T., Glaßer, S., Boese, A., Eppler, E., Kalinski, T., Beuing, O., & Skalej, M. (2016). Experimental investigation of intravascular OCT for imaging of intracranial aneurysms. *International Journal of Computer-Assisted Radiology and Surgery (IJCARS)*, 11(2), 231–41

*Contribution: Idea & Conceptualization (33%), Implementation (25%), Evaluation/Interview creation and conduction (33%); Writing: Introduction/Conclusion (25%), Concept Presentation (25%), Evaluation (25%) Related Work (15%); Reviewing and Supervision.*

Glaßer et al. (2017): Glaßer, S., Hoffmann, T., Boese, A., Voß, S., Kalinski, T., Skalej, M., & Preim, B. (2017). Virtual inflation of the cerebral artery wall for the integrated exploration of oct and histology data. *Computer Graphics Forum*, 36(8), 57–68

*Contribution: Idea & Conceptualization (90%), Implementation (100%), Evaluation/Interview creation and conduction (75%); Writing: Introduction/Conclusion (90%), Concept Presentation (90%), Evaluation (50%) Related Work (90%); Coordination of the Project.*

Voß et al. (2016): Voß, S., Glaßer, S., Hoffmann, T., Beuing, O., Weigand, S., Jachau, K., Preim, B., Thévenin, D., Janiga, G., & Berg, P. (2016). Fluid-Structure Simulations of a Ruptured Intracranial Aneurysm - Constant versus Patient-Specific Wall Thickness. *Computational and Mathematical Methods in Medicine*, 9854539

*Contribution: Idea & Conceptualization (15%), Implementation (20%), Evaluation/Interview creation and conduction (25%); Writing: Introduction/Conclusion (20%), Concept Presentation (25%), Evaluation (10%) Related Work (10%); Reviewing and Supervision.*

Glaßer et al. (2016a): Glaßer, S., Berg, P., Voß, S., Serowy, S., Janiga, G., Preim, B., & Beuing, O. (2016a). From imaging to hemodynamics ? How reconstruction kernels influence the blood flow predictions in intracranial aneurysms. *Current Directions in Biomedical Engineering*, 2(1), 679–683

*Contribution: Idea & Conceptualization (33%), Implementation (50%), Evaluation/Interview creation and conduction (50%); Writing: Introduction/Conclusion (66%), Concept Presentation (66%), Evaluation (66%), Related Work (66%); Coordination of the Project.*

Saalfeld et al. (2018b): Saalfeld, S., Berg, P., Niemann, A., Luz, M., Preim, B., & Beuing, O. (2018b). Semiautomatic neck curve reconstruction for intracranial aneurysm rupture risk assessment based on morphological parameters. *International Journal of Computer Assisted Radiology and Surgery (IJCARS)*, 13(11), 1781–1793

*Contribution: Idea & Conceptualization (75%), Implementation (75%), Evaluation/Interview creation and conduction (100%); Writing: Introduction/Conclusion (90%), Concept Presentation (90%), Evaluation (100%) Related Work (90%); Coordination of the Project.*

Saalfeld et al. (2019): Saalfeld, S., Voss, S., Preim, B., Beuing, O., & Berg, P. (2019). Flow-splitting-based computation of outlet boundary conditions for improved cerebrovascular simulation in multiple intracranial aneurysms. *International Journal of Computer Assisted Radiology and Surgery (IJCARS)*. doi:<https://doi.org/10.1007/s11548-019-02036-7>

*Contribution: Idea & Conceptualization (33%), Implementation (80%), Evaluation/Interview creation and conduction (66%); Writing: Introduction/Conclusion (70%), Concept Presentation (100%), Evaluation (33%) Related Work (90%); Coordination of the Project.*

Behrendt et al. (2017): Behrendt, B., Berg, P., Preim, B., & Saalfeld, S. (2017). Combining pseudo chroma depth enhancement and parameter mapping for vascular surface models. In *Proc. of Eurographics Workshop on Visual Computing for Biology and Medicine (VCBM)* (pp. 159–168)

*Contribution: Idea & Conceptualization (15%), Implementation (10%), Evaluation/Interview creation and conduction (20%); Writing: Introduction/Conclusion (15%), Concept Presentation (15%), Evaluation (15%) Related Work (15%); Reviewing and Supervision.*

Saalfeld et al. (2017a): Saalfeld, P., Glaßer, S., Beuing, O., & Preim, B. (2017a). The FAUST framework: Free-form annotations on unfolding vascular structures for treatment planning. *Computers & Graphics*, 65, 12–21

*Contribution: Idea & Conceptualization (25%), Implementation (25%), Evaluation/Interview creation and conduction (33%); Writing: Introduction/Conclusion (25%), Concept Presentation (20%), Evaluation (10%), Related Work (25%); Reviewing and Supervision.*

Saalfeld et al. (2018a): Saalfeld, P., Luz, M., Berg, P., Preim, B., & Saalfeld, S. (2018a). Guidelines for quantitative evaluation of medical visualizations on the example of 3d aneurysm surface comparisons. *Computer Graphics Forum*, 37(1), 226–238

*Contribution: Idea & Conceptualization (60%), Implementation (33%), Evaluation/Interview creation and conduction (15%); Writing: Introduction/Conclusion (15%), Concept Presentation (15%), Evaluation (15%) Related Work (33%); Reviewing and Supervision.*

Behrendt et al. (2018): Behrendt, B., Berg, P., Beuing, O., Preim, B., & Saalfeld, S. (2018). Explorative blood flow visualization using dynamic line filtering based on surface features. *Computer Graphics Forum*, 37(3), 183–194

*Contribution: Idea & Conceptualization (20%), Implementation (10%), Evaluation/Interview creation and conduction (20%); Writing: Introduction/Conclusion (15%), Concept Presentation (15%), Evaluation (25%), Related Work (10%); Reviewing and Supervision.*

Niemann et al. (2018): Niemann, U., Berg, P., Niemann, A., Beuing, O., Preim, B., Spiliopoulou, M., & Saalfeld, S. (2018). Rupture status classification of intracranial aneurysms using morphological parameters. In *Proc. of IEEE Int. Symposium on Computer-Based Medical Systems (CBMS)* (pp. 48–53)

*Contribution: Idea & Conceptualization (50%), Implementation (33%), Evaluation/Interview creation and conduction (15%); Writing: Introduction/Conclusion (15%), Concept Presentation (15%), Evaluation (15%) Related Work (15%); Reviewing and Supervision.*

Berg et al. (2019c): Berg, P., Voß, S., Janiga, G., Saalfeld, S., Bergersen, A. W., Valen-Sendstad, K., Bruening, J., Goubergrits, L., Spuler, A., Chiu, T. L., Tsang, A. C. O., Copelli, G., Csippa, B., Paál, G., Závodszy, G., Detmer, F. J., Chung, B. J., Cebal, J. R., Karmonik, C., Elias, S., Cancelliere, N. M., Najafi, M., Steinman, D. A., Pereira, V. M., Piskin, S., Finol, E. A., Pravdivtseva, M., Velvaluri, P., Rajabzadeh-Oghaz, H., Paliwal, N., Meng, H., Seshadhri, S., Shojima, M., Sindeev, S., Frolov, S., Qian, Y., Wu, Y.-A., Carlson, K. D., Kallmes, D. F., Dragomir-Daescu, D., & Beuing, O. (2019c). Multiple aneurysms anatomy challenge 2018 (MATCH): Phase II: Rupture risk assessment. *International Journal*

of *Computer Assisted Radiology and Surgery (IJCARS)*. doi:[10.1007/s11548-019-01986-2](https://doi.org/10.1007/s11548-019-01986-2) Contribution: Idea & Conceptualization (15%), Implementation (15%), Evaluation/Interview creation and conduction (33%); Writing: Introduction/Conclusion (10%), Concept Presentation (10%), Evaluation (10%), Related Work (10%); Reviewing and Supervision.

## A.2 LIST OF FURTHER RESEARCH PAPERS

In Table [A.1](#), a list of research papers is provided that have been created during my postdoctoral phase where I contributed but that do not focus on computer support of intracranial aneurysms or cerebrovascular diseases. These papers cover various aspects concerning minimal invasive image-guided therapies as part of my research projects within the Forschungscampus *STIMULATE*.

Table A.1: Additional papers, where I contributed, focussing on minimal-invasive therapies. These papers are not part of the cumulative part of this thesis and are not related to IAs.

Citation	Publication
Hille et al., 2015	Hille, G., Glaßer, S., Riabikin, O., & Tönnies, K. (2015). Regionenbasierte rigide Bildregistrierung von präoperativen MR- und intraoperativen Dyna-CT-Bildern zur Interventionsunterstützung bei Wirbelkörpermetastasen. In <i>Proc. of Bildverarbeitung für die Medizin (BVM)</i> (pp. 175–180)
Klemm et al., 2015	Klemm, P., Glaßer, S., Lawonn, K., Rak, M., Völzke, H., Hegenscheid, K., & Preim, B. (2015). Interactive visual analysis of lumbar back pain. In <i>Proc. of Conf. on Information Visualization Theory and Applications (IVAPP)</i> (pp. 85–92)
Hille et al., 2016	Hille, G., Glaßer, S., & Tönnies, K. (2016). Hybrid level-sets for vertebral body segmentation in clinical spine MRI. <i>Procedia Computer Science</i> , 90, 22–27
Klemm et al., 2016	Klemm, P., Lawonn, K., Glaßer, S., Niemann, U., Hegenscheid, K., Völzke, H., & Preim, B. (2016). 3D regression heat map analysis of population study data. <i>IEEE Transactions on Visualization and Computer Graphics (TVCG)</i> , 22(1), 81–90
Merten et al., 2016	Merten, N., Glaßer, S., Lassen-Schmidt, B., Großer, O. S., Ricke, J., Amthauer, H., & Preim, B. (2016). Illustrative PET/ct visualisation of SIRT-treated lung metastases. In <i>Proc. of Eurographics Workshop on Visual Computing for Biology and Medicine (VCBM)</i> (pp. 99–104)
Pliske et al., 2016	Pliske, G., Voigt-Zimmermann, S., Glaßer, S., & Arens, C. (2016). Objective quantification of the vocal fold vascular pattern: Comparison of narrow band imaging and white light endoscopy. <i>European Archives of Oto-Rhino-Laryngology</i> , 273(9), 2599–2605
Hille et al., 2017	Hille, G., Merten, N., Serowy, S., Glaßer, S., Tönnies, K., & Preim, B. (2017). Assessing the benefits of interactive patient-specific visualisations for patient information. In <i>Proc. of Bildverarbeitung für die Medizin (BVM)</i> (pp. 224–229)
Merten et al., 2017	Merten, N., Saalfeld, S., Hanses, M., Becker, M., Adler, S., & Preim, B. (2017). A software prototype for treatment planning and intervention support of robot-assisted radiofrequency ablations of vertebral metastases. In <i>Proc. of Computer-Supported and Robot-Assisted Surgery (CURAC)</i> (pp. 89–94)
Nie et al., 2017	Nie, K., Glaßer, S., Niemann, U., Mistelbauer, G., & Preim, B. (2017). Classification of DCE-mri data for breast cancer diagnosis combining contrast agent dynamics and texture features. In <i>Proc. of Bildverarbeitung für die Medizin (BVM)</i>
Hille et al., 2018a	Hille, G., Saalfeld, S., Serowy, S., & Tönnies, K. (2018a). Multi-segmental spine image registration supporting image-guided interventions of spinal metastases. <i>Computers in Biology and Medicine</i> , 102, 16–20
Hille et al., 2018b	Hille, G., Saalfeld, S., Serowy, S., & Tönnies, K. (2018b). Vertebral body segmentation in wide range clinical routine spine MRI data. <i>Computer Methods and Programs in Biomedicine</i> , 155, 93–99
Hille et al., 2018c	Hille, G., Saalfeld, S., & Tönnies, K. (2018c). Computer-aided detection of the most suitable MRI sequences for subsequent spinal metastasis delineation. In <i>Proc. of Bildverarbeitung für die Medizin (BVM)</i> (pp. 93–99)
Merten et al., 2018	Merten, N., Adler, S., Hanses, M., Saalfeld, S., Becker, M., & Preim, B. (2018). Two-step trajectory visualization for robot-assisted spine radiofrequency ablations. In <i>Proc. of Bildverarbeitung für die Medizin (BVM)</i> (pp. 55–60)
Hille et al., 2019	Hille, G., Dünwald, M., Becker, M., Steffen, J., Saalfeld, S., & Tönnies, K. (2019). Segmentation of vertebral metastases in MRI using an U-Net like convolutional neural network. In <i>Proc. of Bildverarbeitung für die Medizin (BVM)</i> (pp. 31–36)
Merten et al., 2019a	Merten, N., Adler, S., Hille, G., Hanses, M., Becker, M., Saalfeld, S., & Preim, B. (2019a). A two-step risk assessment method for radiofrequency ablations of spine metastases. <i>Computers in Biology and Medicine</i> , 108, 174–181
Merten et al., 2019b	Merten, N., Genseke, P., Preim, B., Kreissl, M. C., & Saalfeld, S. (2019b). Towards automated reporting and visualization of lymph node metastases of lung cancer. In <i>Proc. of Bildverarbeitung für die Medizin (BVM)</i> (pp. 185–190)



---

## BIBLIOGRAPHY

---

- Abdurahman, S., Frysch, R., Bismark, R., Melnik, S., Beuing, O., & Rose, G. (2018). Beam hardening correction using cone beam consistency conditions. *IEEE Transactions on Medical Imaging*, *37*(10), 2266–2277.
- Alliez, P., Ucelli, G., Gotsman, C., & Attene, M. (2008). Recent advances in remeshing of surfaces. In *Shape Analysis and Structuring* (pp. 53–82). Springer.
- Alshekhlee, A., Mehta, S., Edgell, R. C., Vora, N., Feen, E., Mohammadi, A., Kale, S. P., & Cruz-Flores, S. (2010). Hospital mortality and complications of electively clipped or coiled unruptured intracranial aneurysm. *Stroke*, *41*(7), 1471–1476.
- ANKYRAS Product Website by GalgoMedical. (2019). <https://www.ankyras.com/en/index.html>. [Online; accessed 05-March-2019].
- Antiga, L., Piccinelli, M., Botti, L., Ene-Iordache, B., Remuzzi, A., & Steinman, D. A. (2008). An image-based modeling framework for patient-specific computational hemodynamics. *Medical & Biological Engineering & Computing*, *46*(11), 1097.
- Backes, D., Vergouwen, M. D., Velthuis, B. K., van der Schaaf, I. C., Bor, A. S. E., Algra, A., & Rinkel, G. J. (2014). Difference in aneurysm characteristics between ruptured and unruptured aneurysms in patients with multiple intracranial aneurysms. *Stroke*, *45*(5), 1299–1303.
- Bade, R., Schumann, C., Seshadhri, S., Janiga, G., Bölke, T., Krischek, Ö., Skalej, M., Rose, G., Thevenin, D., & Preim, B. (2007). High-quality Surface Generation for Flow Simulation in Cerebral Aneurysms. In *Proc. of Computer and Robotic Assisted Surgery (CURAC)* (pp. 125–128).
- Baer, A., Gasteiger, R., Cunningham, D., & Preim, B. (2011). Perceptual evaluation of ghosted view techniques for the exploration of vascular structures and embedded flow. *Computer Graphics Forum*, *30*(3), 811–820.
- Balzani, D., Böse, D., Brands, D., Erbel, R., Klawonn, A., Rheinbach, O., & Schröder, J. (2012). Parallel simulation of patient-specific atherosclerotic arteries for the enhancement of intravascular ultrasound diagnostics. *Engineering Computations*, *29*(8), 888–906.
- Behrendt, B., Berg, P., Beuing, O., Preim, B., & Saalfeld, S. (2018). Explorative blood flow visualization using dynamic line filtering based on surface features. *Computer Graphics Forum*, *37*(3), 183–194.
- Behrendt, B., Berg, P., Preim, B., & Saalfeld, S. (2017). Combining pseudo chroma depth enhancement and parameter mapping for vascular surface models. In *Proc. of Eurographics Workshop on Visual Computing for Biology and Medicine (VCBM)* (pp. 159–168).

- Berg, P., Saalfeld, S., Voß, S., Beuing, O., & Janiga, G. (2019a). A review on the reliability of hemodynamic modeling in intracranial aneurysms: Why computational fluid dynamics alone cannot solve the equation. *Neurosurgical focus*, 47(1), E15.
- Berg, P., Voß, S., Saalfeld, S., Janiga, G., Bergersen, A., Valen-Sendstad, K., Bruening, J., Goubergrits, L., Spuler, A., Cancelliere, N. M., Steinman, D. A., Pereira, V. M., Chiu, T. L., Tsang, A. C., Chung, B. J., Cebral, J. R., Cito, S., Pallarès, J., Copelli, G., Csippa, B., Paál, G., Fujimura, S., Takao, H., Hodis, S., Hille, G., Karmonik, C., Elias, S., Kellermann, K., Khan, M. O., Marsden, A. L., Morales, H. G., S., P., Finol, E. A., Pravdivtseva, M., Rajabzadeh-Oghaz, H., N., P., Meng, H., Seshadhri, S., Howard, M., Shojima, M., Sugiyama, S., Niizuma, K., Sindeev, S., Frolov, S., Wagner, T., Brawanski, A., Qian, Y., Wu, Y., Carlson, K., Daescu, D., D., & Beuing, O. (2018a). Multiple Aneurysms AnaTomy CHallenge 2018 (MATCH): Phase I: Segmentation. *Cardiovascular Engineering and Technology*, 9(4), 565–581.
- Berg, P. (2015). *CFD-basierte hämodynamische Untersuchung patientenspezifischer intrakranieller Aneurysmen* (Doctoral dissertation, Otto-von-Guericke University Magdeburg).
- Berg, P., Radtke, L., Voß, S., Serowy, S., Janiga, G., Preim, B., Beuing, O., & Saalfeld, S. (2018b). 3DRA reconstruction of intracranial aneurysms – How does voxel size influences morphologic and hemodynamic parameters. In *Proc. of IEEE Engineering in Medicine and Biology Society (EMBC)* (pp. 1327–1330).
- Berg, P., Saalfeld, S., Behrendt, B., Voß, S., Hille, G., & Larsen, N. (2019b). Local flow analysis in unruptured middle cerebral artery aneurysms with vessel wall enhancement. In *Proc. of Conf. on Computational and Mathematical Biomedical Engineering* (pp. 558–561).
- Berg, P., Saalfeld, S., Janiga, G., Brina, O., Cancelliere, N. M., Machi, P., & Pereira, V. M. (2018c). Virtual stenting of intracranial aneurysms: A pilot study for the prediction of treatment success based on hemodynamic simulations. *The International Journal of Artificial Organs*, 41(11), 698–705.
- Berg, P., Saalfeld, S., Voß, S., Redel, T., Preim, B., Janiga, G., & Beuing, O. (2018d). Does the DSA reconstruction kernel affect hemodynamic predictions intracranial aneurysms? An analysis of geometry and blood flow variations. *Journal of Neurointerventional Surgery*, 10(3), 290–296.
- Berg, P., Stucht, D., Janiga, G., Beuing, O., Speck, O., & Thévenin, D. (2014). Cerebral blood flow in a healthy Circle of Willis and two intracranial aneurysms: Computational fluid dynamics versus four-dimensional phase-contrast magnetic resonance imaging. *Journal of Biomechanical Engineering*, 136(4), 041003.

- Berg, P., Voß, S., Becker, M., Serowy, S., Redel, T., Janiga, G., Skalej, M., & Beuing, O. (2016). Bringing hemodynamic simulations closer to the clinics: A cfd prototype study for intracranial aneurysms. In *Proc. of IEEE Engineering in Medicine and Biology Society (EMBC)* (pp. 3302–3305).
- Berg, P., Voß, S., Janiga, G., Saalfeld, S., Bergersen, A. W., Valen-Sendstad, K., Bruening, J., Goubergrits, L., Spuler, A., Chiu, T. L., Tsang, A. C. O., Copelli, G., Csippa, B., Paál, G., Závodszy, G., Detmer, F. J., Chung, B. J., Cebral, J. R., Karmonik, C., Elias, S., Cancelliere, N. M., Najafi, M., Steinman, D. A., Pereira, V. M., Piskin, S., Finol, E. A., Pravdivtseva, M., Velvaluri, P., Rajabzadeh-Oghaz, H., Paliwal, N., Meng, H., Seshadhri, S., Shojima, M., Sindeev, S., Frolov, S., Qian, Y., Wu, Y.-A., Carlson, K. D., Kallmes, D. F., Dragomir-Daescu, D., & Beuing, O. (2019c). Multiple aneurysms anatomy challenge 2018 (MATCH): Phase II: Rupture risk assessment. *International Journal of Computer Assisted Radiology and Surgery (IJCARs)*. doi:[10.1007/s11548-019-01986-2](https://doi.org/10.1007/s11548-019-01986-2)
- Bernardo, A. (2017). Virtual reality and simulation in neurosurgical training. *World Neurosurgery*, *106*, 1015–1029.
- Besl, P. J., & McKay, N. D. (1992). Method for registration of 3-D shapes. In *Proc. of spie 1611, sensor fusion iv: Control paradigms and data structures*. doi:[10.1117/12.57955](https://doi.org/10.1117/12.57955)
- Bijlenga, P., Gondar, R., Schilling, S., Morel, S., Hirsch, S., Cuony, J., Corniola, M.-V., Perren, F., Rüfenacht, D., & Schaller, K. (2017). PHASES Score for the Management of Intracranial Aneurysm. *Stroke*, *48*(8), 2105–2112.
- Bilic, P., Christ, P. F., Vorontsov, E., Chlebus, G., Chen, H., Dou, Q., Fu, C.-W., Han, X., Heng, P.-A., Hesser, J., et al. (2019). The liver tumor segmentation benchmark (LiTS). *arXiv preprint arXiv:1901.04056*.
- Bohnstedt, B. N., Nguyen, H. S., Kulwin, C. G., Shoja, M. M., Helbig, G. M., Leipzig, T. J., Payner, T. D., & Cohen-Gadol, A. A. (2013). Outcomes for clip ligation and hematoma evacuation associated with 102 patients with ruptured middle cerebral artery aneurysms. *World Neurosurgery*, *80*(3-4), 335–341.
- Born, S., Pfeifle, M., Markl, M., Gutberlet, M., & Scheuermann, G. (2013). Visual analysis of cardiac 4D MRI blood flow using line predicates. *IEEE Transactions on Visualization and Computer Graphics*, *19*(6), 900–12.
- Bouillot, P., Brina, O., Ouared, R., Lovblad, K., Pereira, V. M., & Farhat, M. (2014). Multi-time-lag PIV analysis of steady and pulsatile flows in a side-wall aneurysm. *Experiments in Fluids*, *55*(6), 1746.
- Bouillot, P., Brina, O., Ouared, R., Lovblad, K.-O., Farhat, M., & Pereira, V. M. (2015). Hemodynamic transition driven by stent porosity in side-wall aneurysms. *Journal of Biomechanics*, *48*(7), 1300–1309.
- Brinjikji, W., Chung, B. J., Jimenez, C., Putman, C., Kallmes, D. F., & Cebral, J. R. (2017). Hemodynamic differences between unstable and stable unrup-

- tured aneurysms independent of size and location: A pilot study. *Journal of Neurointerventional Surgery*, 9(4), 376–380.
- Brisman, J. L., Song, J. K., & Newell, D. W. (2006). Cerebral aneurysms. *New England Journal of Medicine*, 355(9), 928–39.
- Broos, A. J., de Hoon, N. H., de Koning, P. J., Geest, R. J., Vilanova, A., & Jalba, A. C. (2016). A framework for fast initial exploration of PC-MRI cardiac flow. In *Proc. of Eurographics Workshop on Visual Computing for Biology and Medicine (VCBM)* (pp. 69–78).
- Bruneau, M., Amin-Hanjani, S., Koroknay-Pal, P., Bijlenga, P., Jahromi, B. R., Lehto, H., Kivisaari, R., Schaller, K., Charbel, F., Khan, S., et al. (2015). Surgical clipping of very small unruptured intracranial aneurysms: A multicenter international study. *Neurosurgery*, 78(1), 47–52.
- Byrne, G., Mut, F., & Cebal, J. (2014). Quantifying the large-scale hemodynamics of intracranial aneurysms. *American Journal of Neuroradiology*, 35(2), 333–338.
- Cebal, J. R., Mut, F., Weir, J., & Putman, C. (2011a). Quantitative characterization of the hemodynamic environment in ruptured and unruptured brain aneurysms. *American Journal of Neuroradiology*, 32(1), 145–151.
- Cebal, J., Detmer, F., Chung, B., Choque-Velasquez, J., Rezai, B., Lehto, H., Tulamo, R., Hernesniemi, J., Niemela, M., Yu, A., Williamson, R., Aziz, K., Sakur, S., Amin-Hanjani, S., Charbel, F., Tobe, Y., Robertson, A., & Frösen, J. (2019). Local hemodynamic conditions associated with focal changes in the intracranial aneurysm wall. *American Journal of Neuroradiology*, 40(3), 510–516.
- Cebal, J., Mut, F., Raschi, M., Scrivano, E., Ceratto, R., Lylyk, P., & Putman, C. (2011b). Aneurysm rupture following treatment with flow-diverting stents: Computational hemodynamics analysis of treatment. *American Journal of Neuroradiology*, 32(1), 27–33.
- Cebal, J. R., & Raschi, M. (2012). Suggested connections between risk factors of intracranial aneurysms: A review. *Annals of Biomedical Engineering*, 41(7), 1366–1383.
- Cebal, J. R., Vazquez, M., Sforza, D. M., Houzeaux, G., Tateshima, S., Scrivano, E., Bleise, C., Lylyk, P., & Putman, C. M. (2015). Analysis of hemodynamics and wall mechanics at sites of cerebral aneurysm rupture. *Journal of Neurointerventional Surgery*, 7(7), 530–536.
- Chen, C.-J., Kumar, J. S., Chen, S. H., Ding, D., Buell, T. J., Sur, S., Ironside, N., Luther, E., III, M. R., Park, M. S., Kalani, M. Y., Liu, K. C., & Starke, R. M. (2018). Optical coherence tomography. Future applications in cerebrovascular imaging. *Stroke*, 49(4), 1044–1050.
- Chen, Y., & Medioni, G. (1992). Object modelling by registration of multiple range images. *Image and Vision Computing*, 10(3), 145–155.
- Chnafa, C., Brina, O., Pereira, V., & Steinman, D. (2018). Better than nothing: A rational approach for minimizing the impact of outflow strategy on

- cerebrovascular simulations. *American Journal of Neuroradiology*, *39*(2), 337–343.
- Chnafa, C., Valen-Sendstad, K., Brina, O., Pereira, V., & Steinman, D. (2017). Improved reduced-order modelling of cerebrovascular flow distribution by accounting for arterial bifurcation pressure drops. *Journal of Biomechanics*, *51*, 83–88.
- Chung, B. J., Doddasomayajula, R., Mut, F., Detmer, F., Pritz, M. B., Hamzei-Sichani, F., Brinjikji, W., Kallmes, D. F., Jimenez, C. M., Putman, C. M., & Cebal, J. R. (2017). Angioarchitectures and hemodynamic characteristics of posterior communicating artery aneurysms and their association with rupture status. *American Journal of Neuroradiology*, *38*(11), 2111–2118.
- Cito, S., Geers, A. J., Arroyo, M. P., Palero, V. R., Pallarés, J., Vernet, A., Blasco, J., San Román, L., Fu, W., Qiao, A., Janiga, G., Miura, Y., Ohta, M., Mendina, M., Usera, G., & Frangi, A. F. (2015). Accuracy and reproducibility of patient-specific hemodynamic models of stented intracranial aneurysms: Report on the virtual intracranial stenting challenge 2011. *Annals of Biomedical Engineering*, *43*(1), 154–167.
- de Havenon, A., Chung, L., Park, M., & Mossa-Basha, M. (2016). Intracranial vessel wall MRI: A review of current indications and future applications. *Neurovascular Imaging*, *2*(1), 10.
- Detmer, F. J., Chung, B. J., Mut, F., Slawski, M., Hamzei-Sichani, F., Putman, C., Jiménez, C., & Cebal, J. R. (2018). Development and internal validation of an aneurysm rupture probability model based on patient characteristics and aneurysm location, morphology, and hemodynamics. *International Journal of Computer Assisted Radiology and Surgery (IJCARS)*, *13*(11), 1767–1779.
- Dhar, S., Tremmel, M., Mocco, J., Kim, M., Yamamoto, J., Siddiqui, A. H., Hopkins, L. N., & Meng, H. (2008). Morphology parameters for intracranial aneurysm rupture risk assessment. *Neurosurgery*, *63*(2), 185–197.
- Doddasomayajula, R., Chung, B., Hamzei-Sichani, F., Putman, C., & Cebal, J. (2017). Differences in hemodynamics and rupture rate of aneurysms at the bifurcation of the basilar and internal carotid arteries. *American Journal of Neuroradiology*, *38*(3), 570–576.
- Etminan, N. e. a. (2015). The unruptured intracranial aneurysm treatment score: A multidisciplinary consensus. *Neurology*, *85*(10), 881–889.
- Etminan, N., Brown, R. D., Beseoglu, K., Juvela, S., Raymond, J., Morita, A., Torner, J. C., Derdeyn, C. P., Raabe, A., Mocco, J., et al. (2015). The unruptured intracranial aneurysm treatment score: A multidisciplinary consensus. *Neurology*, *85*(10), 881–889.
- Etminan, N., & Rinkel, G. J. (2016). Unruptured intracranial aneurysms: Development, rupture and preventive management. *Nature Reviews Neurology*, *12*(12), 699.

- Fiorella, D., Albuquerque, F. C., Deshmukh, V. R., & McDougall, C. G. (2005). Usefulness of the neuroform stent for the treatment of cerebral aneurysms: Results at initial (3–6-mo) follow-up. *Neurosurgery*, *56*(6), 1191–1202.
- Fiorella, D., Woo, H. H., Albuquerque, F. C., & Nelson, P. K. (2008). Definitive reconstruction of circumferential, fusiform intracranial aneurysms with the pipeline embolization device. *Neurosurgery*, *62*(5), 1115–1121.
- Frösen, J., Piippo, A., Paetau, A., Kangasniemi, M., Niemelä, M., Hernesniemi, J., & Jääskeläinen, J. (2004). Remodeling of saccular cerebral artery aneurysm wall is associated with rupture: Histological analysis of 24 unruptured and 42 ruptured cases. *Stroke*, *35*(10), 2287–2293.
- Frösen, J., Tulamo, R., Paetau, A., Laaksamo, E., Korja, M., Laakso, A., Niemelä, M., & Hernesniemi, J. (2012). Saccular intracranial aneurysm: Pathology and mechanisms. *Acta Neuropathologica*, *123*(6), 773–786.
- Frysch, R., & Rose, G. (2015). Rigid motion compensation in interventional C-arm CT using consistency measure on projection data. In *Medical Image Computing and Computer-Assisted Intervention (MICCAI)* (pp. 298–306).
- Gasteiger, R. (2014). *Visual exploration of cardiovascular hemodynamics* (Doctoral dissertation, Otto-von-Guericke University Magdeburg).
- Gasteiger, R., Lehmann, D. J., van Pelt, R., Janiga, G., Beuing, O., Vilanova, A., Theisel, H., & Preim, B. (2012). Automatic Detection and Visualization of Qualitative Hemodynamic Characteristics in Cerebral Aneurysms. *IEEE Transactions on Visualization and Computer Graphics*, *18*(12), 2178–2187.
- Gasteiger, R., Neugebauer, M., Beuing, O., & Preim, B. (2011). The FLOWLENS: A focus-and-context visualization approach for exploration of blood flow in cerebral aneurysms. *IEEE Transactions on Visualization and Computer Graphics*, *17*(12), 2183–2192.
- Gasteiger, R., Neugebauer, M., Kubisch, C., & Preim, B. (2010). Adapted surface visualization of cerebral aneurysms with embedded blood flow information. In *Proc. of Eurographics Workshop on Visual Computing for Biology and Medicine (VCBM)* (pp. 25–32).
- Geers, A. J., Larrabide, I., Radaelli, A., Bogunovic, H., Van Andel, H. G., Majoie, C., & Frangi, A. F. (2009). Reproducibility of image-based computational hemodynamics in intracranial aneurysms: Comparison of cta and 3dra. In *2009 ieee international symposium on biomedical imaging: From nano to macro* (pp. 610–613). IEEE.
- Glaßer, S., Berg, P., Neugebauer, M., & Preim, B. (2015a). Reconstruction of 3d surface meshes for blood flow simulations of intracranial aneurysms. In *Proc. of Computer-Supported and Robot-Assisted Surgery (CURAC)* (pp. 163–168).
- Glaßer, S., Berg, P., Voß, S., Serowy, S., Janiga, G., Preim, B., & Beuing, O. (2016a). From imaging to hemodynamics ? How reconstruction kernels influence the blood flow predictions in intracranial aneurysms. *Current Directions in Biomedical Engineering*, *2*(1), 679–683.

- Glaßer, S., Hirsch, J., Berg, P., Saalfeld, P., Beuing, O., Janiga, G., & Preim, B. (2016b). Evaluation of time-dependent wall shear stress visualizations for cerebral aneurysms. In *Proc. of Bildverarbeitung für die Medizin (BVM)* (pp. 236–241).
- Glaßer, S., Hoffmann, T., Boese, A., Voß, S., Kalinski, T., Skalej, M., & Preim, B. (2015b). Histology-based evaluation of optical coherence tomographic characteristics of the cerebral artery wall via virtual inflating. In *Proc. of Eurographics Workshop on Visual Computing for Biology and Medicine (VCBM)* (pp. 149–158).
- Glaßer, S., Hoffmann, T., Boese, A., Voß, S., Kalinski, T., Skalej, M., & Preim, B. (2017). Virtual inflation of the cerebral artery wall for the integrated exploration of oct and histology data. *Computer Graphics Forum*, *36*(8), 57–68.
- Glaßer, S., Hoffmann, T., Voß, S., Klink, F., & Preim, B. (2016c). Extraction of patient-specific 3D cerebral artery and wall thickness models from 2d OCT and structured-light 3D scanner data. In *Proc. of Computer-Supported and Robot-Assisted Surgery (CURAC)* (pp. 197–202).
- Glaßer, S., Lawonn, K., Hoffmann, T., Skalej, M., & Preim, B. (2014). Combined visualization of wall thickness and wall shear stress for the evaluation of aneurysms. *IEEE Transactions on Visualization and Computer Graphics (TVCG)*, *20*(12), 2506–2515.
- Glaßer, S., Saalfeld, P., Berg, P., Merten, N., & Preim, B. (2016d). How to Evaluate Medical Visualizations on the Example of 3D Aneurysm Surfaces. In *Proc. of Eurographics Workshop on Visual Computing for Biology and Medicine (VCBM)* (pp. 153–162).
- Gotsman, C., Gumhold, S., & Kobbelt, L. (2002). Simplification and compression of 3d meshes. In A. Iske, E. Quak, & M. S. Floater (Eds.), *Tutorials on multiresolution in geometric modelling: Summer school lecture notes* (pp. 319–361). Springer Berlin Heidelberg.
- Gounis, M. J., Ughi, G. J., Marosfoi, M., Lopes, D. K., Fiorella, D., Bezerra, H. G., Liang, C. W., & Puri, A. S. (2019). Intravascular optical coherence tomography for neurointerventional surgery. *Stroke*, *50*(1), 218–223.
- Gray, H. (2000). *Anatomy of the Human Body*. Philadelphia: Lea & Febiger, 1918. Bartleby.com.
- Greving, J. P., Wermer, M. J., Brown Jr, R. D., Morita, A., Juvela, S., Yonekura, M., Ishibashi, T., Torner, J. C., Nakayama, T., Rinkel, G. J., et al. (2014). Development of the phases score for prediction of risk of rupture of intracranial aneurysms: A pooled analysis of six prospective cohort studies. *The Lancet Neurology*, *13*(1), 59–66.
- Guglielmi, G., Viñuela, F., Dion, J., & Duckwiler, G. (1991a). Electrothrombosis of saccular aneurysms via endovascular approach. *Journal of Neurosurgery*, *75*(1), 8–14.

- Guglielmi, G., Viñuela, F., Sepetka, I., & Macellari, V. (1991b). Electrothrombosis of saccular aneurysms via endovascular approach. *Journal of Neurosurgery*, *75*(1), 1–7.
- Hentschke, C. (2013). *Computer-aided detection of cerebral aneurysms in angiographics* (Doctoral dissertation, Otto-von-Guericke University Magdeburg).
- Higashida, R. T. (2000). Evolution of a new multidisciplinary subspecialty: Interventional neuroradiology/neuroendovascular surgery. *American Journal of Neuroradiology*, *21*(6), 1151–1152.
- Hilditch, C. A., Brinjikji, W., Tsang, A. C., Nicholson, P., Kostynskyy, A., Tymianski, M., Krings, T., Radovanovic, I., & Pereira, V. M. (2018). Application of PHASES and ELAPSS scores to ruptured cerebral aneurysms: How many would have been conservatively managed? *Journal of Neurosurgical Sciences*. doi:[10.23736/s0390-5616.18.04498-3](https://doi.org/10.23736/s0390-5616.18.04498-3)
- Hille, G., Glaßer, S., Riabikin, O., & Tönnies, K. (2015). Regionenbasierte rigide Bildregistrierung von präoperativen MR- und intraoperativen Dyna-CT-Bildern zur Interventionsunterstützung bei Wirbelkörpermetastasen. In *Proc. of Bildverarbeitung für die Medizin (BVM)* (pp. 175–180).
- Hille, G., Glaßer, S., & Tönnies, K. (2016). Hybrid level-sets for vertebral body segmentation in clinical spine MRI. *Procedia Computer Science*, *90*, 22–27.
- Hille, G., Dünnwald, M., Becker, M., Steffen, J., Saalfeld, S., & Tönnies, K. (2019). Segmentation of vertebral metastases in MRI using an U-Net like convolutional neural network. In *Proc. of Bildverarbeitung für die Medizin (BVM)* (pp. 31–36).
- Hille, G., Merten, N., Serowy, S., Glaßer, S., Tönnies, K., & Preim, B. (2017). Assessing the benefits of interactive patient-specific visualisations for patient information. In *Proc. of Bildverarbeitung für die Medizin (BVM)* (pp. 224–229).
- Hille, G., Saalfeld, S., Serowy, S., & Tönnies, K. (2018a). Multi-segmental spine image registration supporting image-guided interventions of spinal metastases. *Computers in Biology and Medicine*, *102*, 16–20.
- Hille, G., Saalfeld, S., Serowy, S., & Tönnies, K. (2018b). Vertebral body segmentation in wide range clinical routine spine MRI data. *Computer Methods and Programs in Biomedicine*, *155*, 93–99.
- Hille, G., Saalfeld, S., & Tönnies, K. (2018c). Computer-aided detection of the most suitable MRI sequences for subsequent spinal metastasis delineation. In *Proc. of Bildverarbeitung für die Medizin (BVM)* (pp. 93–99).
- Hoffmann, T., Boese, A., Glaßer, S., Beuing, O., & Skalej, M. (2015). Intravascular optical coherence tomography (OCT) as an additional tool for the assessment of stent structures. *Current Directions in Biomedical Engineering*, *1*(1), 257–260.
- Hoffmann, T., Glaßer, S., Boese, A., Eppler, E., Kalinski, T., Beuing, O., & Skalej, M. (2016). Experimental investigation of intravascular OCT for

- imaging of intracranial aneurysms. *International Journal of Computer-Assisted Radiology and Surgery (IJCARS)*, 11(2), 231–41.
- Hoffmann, T., Glaßer, S., Klink, F., Boese, A., & Skalej, M. (2014). Development of vessel phantoms using intravascular ultrasound (IVUS) datasets. In *Proc. of Current Directions in Biomedical Engineering* (Vol. 59, p. 893).
- Hugo Junkers Competition. (2019). <https://www.hugo-junkers-preis.de/>. [Online; accessed 05-July-2019].
- Ingall, T., Asplund, K., Mähönen, M., & Bonita, R. (2000). A multinational comparison of subarachnoid hemorrhage epidemiology in the WHO MONICA stroke study. *Stroke*, 31(5), 1054–1061.
- Isenberg, T., Isenberg, P., Chen, J., Sedlmair, M., & Moller, T. (2013). A systematic review on the practice of evaluating visualization. *IEEE Transactions on Visualization and Computer Graphics*, 19(12), 2818–2827.
- Iserhardt-Bauer, S., Hastreiter, P., Tomandl, B., Köstner, N., Schempershofe, M., Nissen, U., & Ertl, T. (2002). Standardized analysis of intracranial aneurysms using digital video sequences. In *Proc. of Medical Image Computing and Computer-Assisted Intervention (MICCAI)* (pp. 411–418).
- Janiga, G., Daróczy, L., Berg, P., Thévenin, D., Skalej, M., & Beuing, O. (2015). An automatic CFD-based flow diverter optimization principle for patient-specific intracranial aneurysms. *Journal of Biomechanics*, 48(14), 3846–3852.
- Jerman, T., Pernuš, F., Likar, B., & Špiclin, Ž. (2015). Computer-aided detection and quantification of intracranial aneurysms. In *Proc. of Medical Image Computing and Computer-Assisted Intervention (MICCAI)* (pp. 3–10).
- Jou, L.-D., Lee, D., Morsi, H., & Mawad, M. (2008). Wall shear stress on ruptured and unruptured intracranial aneurysms at the internal carotid artery. *American Journal of Neuroradiology*, 29(9), 1761–1767.
- Juvela, S. (2011). Prevalence of aneurysms and risk factors for intracranial aneurysms. *The Lancet Neurology*, 10(7), 595–597.
- Kadasi, L. M., Dent, W., & Malek, A. M. (2013). Cerebral aneurysm wall thickness analysis using intraoperative microscopy: Effect of size and gender on thin translucent regions. *Journal of Neurointerventional Surgery*, 5(3), 201–206.
- Katouzian, A., Karamalis, A., Lisauskas, J., & et al. (2012a). IVUS-histology image registration. In *Proc. of Biomedical Image Registration* (pp. 141–149).
- Katouzian, A., Karamalis, A., Sheet, D., & et al. (2012b). Iterative self-organizing atherosclerotic tissue labeling in intravascular ultrasound images and comparison with virtual histology. *IEEE Transactions on Biomedical Engineering*, 59(11), 3039–3049.
- Kayembe, K., Sasahara, M., & Hazama, F. (1984). Cerebral aneurysms and variations in the Circle of Willis. *Stroke*, 15(5), 846–850.

- Klemm, P., Glaßer, S., Lawonn, K., Rak, M., Völzke, H., Hegenscheid, K., & Preim, B. (2015). Interactive visual analysis of lumbar back pain. In *Proc. of Conf. on Information Visualization Theory and Applications (IVAPP)* (pp. 85–92).
- Klemm, P., Lawonn, K., Glaßer, S., Niemann, U., Hegenscheid, K., Völzke, H., & Preim, B. (2016). 3D regression heat map analysis of population study data. *IEEE Transactions on Visualization and Computer Graphics (TVCG)*, *22*(1), 81–90.
- Köhler, B., Gasteiger, R., Preim, U., Theisel, H., Gutberlet, M., & Preim, B. (2013). Semi-automatic vortex extraction in 4D PC-MRI cardiac blood flow data using line predicates. *IEEE Transactions on Visualizations and Computer Graphics*, *19*(12), 2773–82.
- Köhler, B., Born, S., Pelt, R. F. P. V., Hennemuth, A., Preim, U., & Preim, B. (2017). A survey of cardiac 4D PC-MRI data processing. *Computer Graphics Forum*, *36*(6), 5–35.
- Konakondla, S., Fong, R., & Schirmer, C. M. (2017). Simulation training in neurosurgery: Advances in education and practice. *Advances in Medical Education and Practice*, *8*, 465.
- Kouskouras, C., Charitanti, A., Giavroglou, C., Foroglou, N., Selviaridis, P., Kontopoulos, V., & Dimitriadis, A. S. (2004). Intracranial aneurysms: evaluation using CTA and MRA. Correlation with DSA and intraoperative findings. *Neuroradiology*, *46*(10), 842–50.
- Larsen, N., von der Brellie, C., Trick, D., Riedel, C., Lindner, T., Madjidyar, J., Jansen, O., Synowitz, M., & Flüh, C. (2018). Vessel wall enhancement in unruptured intracranial aneurysms: An indicator for higher risk of rupture? High-resolution MR Imaging and correlated histologic findings. *American Journal of Neuroradiology*, *39*(9), 1617.
- Lauric, A., Baharoglu, M. I., & Malek, A. M. (2012). Ruptured status discrimination performance of aspect ratio, height/width, and bottleneck factor is highly dependent on aneurysm sizing methodology. *Neurosurgery*, *71*(1), 38–46.
- Lawonn, K., Glaßer, S., Vilanova, A., Preim, B., & Isenberg, T. (2016). Occlusion-free blood flow animation with wall thickness visualization. *IEEE Transactions on Visualization and Computer Graphics (TVCG)*, *22*(1), 728–737.
- Lawonn, K. (2017). *Visual enhancement of focus structures in selected applications* (Doctoral dissertation, Otto-von-Guericke University Magdeburg).
- Lawonn, K., Luz, M., Preim, B., & Hansen, C. (2015). Illustrative visualization of vascular models for static 2d representations. In *Proc. of Medical Image Computing and Computer-Assisted Intervention (MICCAI)* (pp. 399–406).
- Lee, C. S., Park, J. U., Kang, J. G., & Lim, Y. C. (2012). The clinical characteristics and treatment outcomes of patients with ruptured middle cerebral artery aneurysms associated with intracerebral hematoma. *Journal of Cerebrovascular and Endovascular Neurosurgery*, *14*(3), 181–185.

- Lee, T.-Y., Mishchenko, O., Shen, H.-W., & Crawfis, R. (2011). View point evaluation and streamline filtering for flow visualization. In *Proc. of IEEE Pacific Visualization Symposium* (pp. 83–90).
- Lesage, D., Angelini, E. D., Bloch, I., & Funke-Lea, G. (2009). A review of 3D vessel lumen segmentation techniques: models, features and extraction schemes. *Medical Image Analysis, 13*(6), 819–845.
- Liang, F., Liu, X., Yamaguchi, R., & Liu, H. (2016). Sensitivity of flow patterns in aneurysms on the anterior communicating artery to anatomic variations of the cerebral arterial network. *Journal of Biomechanics, 49*(15), 3731–3740.
- Liang, L., Steinman, D. A., Brina, O., Chnafa, C., Cancelliere, N. M., & Pereira, V. M. (2019). Towards the clinical utility of CFD for assessment of intracranial aneurysm rupture – A systematic review and novel parameter-ranking tool. *Journal of Neurointerventional Surgery, 11*(2), 153–158.
- Lopes, D. K., & Johnson, A. K. (2012). Evaluation of cerebral artery perforators and the pipeline embolization device using optical coherence tomography. *Journal of Neurointerventional Surgery, 4*(4), 291–294.
- Lorensen, W. E., & Cline, H. E. (1987). Marching cubes: A high resolution 3d surface construction algorithm. In *Computer Graphics (Proceedings of SIGGRAPH 87)* (Vol. 21, pp. 163–169).
- Luessenhop, A. J., & Spence, W. T. (1960). Artificial embolization of cerebral arteries: Report of use in a case of arteriovenous malformation. *Journal of the American Medical Association, 172*(11), 1153–1155.
- Lv, N., Wang, C., Karmonik, C., Fang, Y., Xu, J., Yu, Y., Cao, W., Liu, J., & Huang, Q. (2016). Morphological and hemodynamic discriminators for rupture status in posterior communicating artery aneurysms. *PloS one, 11*(2), e0149906.
- Ma, D., Xiang, J., Choi, H., Dumont, T., Natarajan, S., Siddiqui, A., & Meng, H. (2014). Enhanced aneurysmal flow diversion using a dynamic push-pull technique: An experimental and modeling study. *American Journal of Neuroradiology, 35*(9), 1779–1785.
- Majidi, S., Sein, J., Watanabe, M., Hassan, A., Van de Moortele, P.-F., Suri, M., Clark, H., & Qureshi, A. (2013). Intracranial-derived atherosclerosis assessment: An in vitro comparison between virtual histology by intravascular ultrasonography, 7T MRI, and histopathologic findings. *American Journal of Neuroradiology, 34*(12), 2259–2264.
- Manthey, S., Hoffmann, T., Cattaneo, G., Beuing, O., Preim, B., & Saalfeld, S. (2017). Virtual enhancement of marker X-ray visibility for cerebral stents and flow diverters. In *Proc. of Computer-Supported and Robot-Assisted Surgery (CURAC)* (pp. 270–275).
- Mascitelli, J. R., Lawton, M. T., Hendricks, B. K., Nakaji, P., Zabramski, J. M., & Spetzler, R. F. (2018). Analysis of wide-neck aneurysms in the Barrow Ruptured Aneurysm Trial. *Neurosurgery*. doi:[10.1093/neuros/nyy439](https://doi.org/10.1093/neuros/nyy439)

- Mathews, M. S., Su, J., Heidari, E., & et al. (2011). Neuroendovascular Optical Coherence Tomography Imaging and Histological Analysis. *Neurosurgery*, *69*(2), 430–439.
- Matouk, C. C., Mandell, D. M., Günel, M., Bulsara, K. R., Malhotra, A., Hebert, R., Johnson, M. H., Mikulis, D. J., & Minja, F. J. (2012). Vessel wall magnetic resonance imaging identifies the site of rupture in patients with multiple intracranial aneurysms: Proof of principle. *Neurosurgery*, *72*(3), 492–496.
- Meng, Y., Gong, H., & Yang, X. (2013). Online geometric calibration of cone-beam computed tomography for arbitrary imaging objects. *IEEE Transactions on Medical Imaging*, *32*(2), 278–288.
- Menze, B. H., Jakab, A., Bauer, S., Kalpathy-Cramer, J., Farahani, K., Kirby, J., Burren, Y., Porz, N., Slotboom, J., Wiest, R., et al. (2015). The multimodal brain tumor image segmentation benchmark (brats). *IEEE Transactions on Medical Imaging*, *34*(10), 1993–2024.
- Merten, N., Glaßer, S., Lassen-Schmidt, B., Großer, O. S., Ricke, J., Amthauer, H., & Preim, B. (2016). Illustrative PET/ct visualisation of SIRT-treated lung metastases. In *Proc. of Eurographics Workshop on Visual Computing for Biology and Medicine (VCBM)* (pp. 99–104).
- Merten, N., Adler, S., Hanses, M., Saalfeld, S., Becker, M., & Preim, B. (2018). Two-step trajectory visualization for robot-assisted spine radiofrequency ablations. In *Proc. of Bildverarbeitung für die Medizin (BVM)* (pp. 55–60).
- Merten, N., Adler, S., Hille, G., Hanses, M., Becker, M., Saalfeld, S., & Preim, B. (2019a). A two-step risk assessment method for radiofrequency ablations of spine metastases. *Computers in Biology and Medicine*, *108*, 174–181.
- Merten, N., Genseke, P., Preim, B., Kreissl, M. C., & Saalfeld, S. (2019b). Towards automated reporting and visualization of lymph node metastases of lung cancer. In *Proc. of Bildverarbeitung für die Medizin (BVM)* (pp. 185–190).
- Merten, N., Saalfeld, S., Hanses, M., Becker, M., Adler, S., & Preim, B. (2017). A software prototype for treatment planning and intervention support of robot-assisted radiofrequency ablations of vertebral metastases. In *Proc. of Computer-Supported and Robot-Assisted Surgery (CURAC)* (pp. 89–94).
- Meuschke, M., Voß, S., Beuing, O., Preim, B., & Lawonn, K. (2017). Combined visualization of vessel deformation and hemodynamics in cerebral aneurysms. *IEEE Transactions on Visualization and Computer Graphics*, *23*(1), 761–770.
- Meuschke, M. (2019). *Visualization, classification, and interaction for risk analysis and treatment planning of cerebral aneurysms* (Doctoral dissertation, Otto-von-Guericke University Magdeburg).
- Meuschke, M., Günther, T., Wickenhöfer, R., Gross, M., Preim, B., & Lawonn, K. (2018). Management of Cerebral Aneurysm Descriptors based on an

- Automatic Ostium Extraction. *IEEE Computer Graphics and Applications*, 38(3), 58–72.
- Mittenentzwei, S. (2019). *Detektion und Visualisierung von geometrischen und hämodynamischen Eigenschaften intrakranieller Aneurysmen im Rahmen einer Langzeitstudie* (B.S. Thesis, Otto-von-Guericke University of Magdeburg).
- Miura, Y., Ishida, F., Umeda, Y., Tanemura, H., Suzuki, H., Matsushima, S., Shimosaka, S., & Taki, W. (2013). Low wall shear stress is independently associated with the rupture status of middle cerebral artery aneurysms. *Stroke*, 44(2), 519–521.
- Moench, T., Neugebauer, M., & Preim, B. (2011). Optimization of vascular surface models for computational fluid dynamics and rapid prototyping. In *Proc. of Int. Workshop on Digital Engineering* (pp. 16–23).
- Molyneux, A., Kerr, R., International Subarachnoid Aneurysm Trial (ISAT) Collaborative Group, et al. (2002). International Subarachnoid Aneurysm Trial (ISAT) of neurosurgical clipping versus endovascular coiling in 2143 patients with ruptured intracranial aneurysms: a randomized trial. *Journal of Stroke and Cerebrovascular Diseases*, 11(6), 304–314.
- Murray, C. D. (1926). The physiological principle of minimum work: I. the vascular system and the cost of blood volume. *Proceedings of the National Academy of Sciences of the United States of America*, 12(3), 207.
- Naggara, O. N., White, P. M., Guilbert, F., Roy, D., Weill, A., & Raymond, J. (2010). Endovascular treatment of intracranial unruptured aneurysms: Systematic review and meta-analysis of the literature on safety and efficacy. *Radiology*, 256(3), 887–897.
- Neugebauer, M. (2014). *Computergestützte Exploration von Blutfluss in zerebralen Aneurysmen – geometrische Verarbeitung und interaktive Visualisierung* (Doctoral dissertation, Otto-von-Guericke University Magdeburg).
- Neugebauer, M., Diehl, V., Skalej, M., & Preim, B. (2010). Geometric reconstruction of the ostium of cerebral aneurysms. In *Proc. of Vision, Modeling, Visualization (VMV)* (pp. 307–314).
- Neugebauer, M., Lawonn, K., Beuing, O., Berg, P., Janiga, G., & Preim, B. (2013). AmniVis - A system for qualitative exploration of near-wall hemodynamics in cerebral aneurysms. *Computer Graphics Forum*, 32(3), 251–260.
- Neyazi, B., Saalfeld, P., Berg, P., Skalej, M., Preim, B., & Saalfeld, S. (2019). Vr craniotomy for optimal intracranial aneurysm surgery planning. In *Proc. of Computer and Robotic Assisted Surgery (CURAC)* (accepted for publication).
- Nie, K., Glaßer, S., Niemann, U., Mistelbauer, G., & Preim, B. (2017). Classification of DCE-mri data for breast cancer diagnosis combining contrast

- agent dynamics and texture features. In *Proc. of Bildverarbeitung für die Medizin (BVM)*.
- Niemann, U., Berg, P., Niemann, A., Beuing, O., Preim, B., Spiliopoulou, M., & Saalfeld, S. (2018). Rupture status classification of intracranial aneurysms using morphological parameters. In *Proc. of IEEE Int. Symposium on Computer-Based Medical Systems (CBMS)* (pp. 48–53).
- Oeltze-Jafra, S., Meuschke, M., Neugebauer, M., Saalfeld, S., Lawonn, K., Janiga, G., Hege, H.-C., Zachow, S., & Preim, B. (2019). Generation and visual exploration of medical flow data. *Computer Graphics Forum*, *38*(1), 87–125.
- Oeltze-Jafra, S. (2017). *Visual analytics of medical and biological data* (Doctoral dissertation, Otto-von-Guericke University Magdeburg).
- Oeltze-Jafra, S., Cebral, J. R., Janiga, G., & Preim, B. (2016). Cluster analysis of vortical flow in simulations of cerebral aneurysm hemodynamics. *IEEE Transaction on Visualizations and Computer Graphics*, *22*(1), 757–66.
- Oeltze, S., Lehmann, D. J., Kuhn, A., Janiga, G., Theisel, H., & Preim, B. (2014). Blood flow clustering and applications in virtual stenting of intracranial aneurysms. *IEEE Transaction on Visualizations and Computer Graphics*, *20*(5), 686–701.
- Ong, C. S., Deib, G., Yesantharao, P., Qiao, Y., Pakpoor, J., Hibino, N., Hui, F., & Garcia, J. R. (2018). Virtual reality in neurointervention. *Journal of Vascular and Interventional Neurology*, *10*(1), 17.
- Osborn, E. A., & Jaffer, F. A. (2013). Imaging atherosclerosis and risk of plaque rupture. *Current Atherosclerosis Reports*, *15*, 359.
- Patel, I. J., Bezerra, H. G., Costa, M. A., Fujino, Y., & Hsu, D. (2013). Novel use of optical coherence tomography. *Journal of Neurointerventional Surgery*, *5*, e41. doi:[doi:10.1136/neurintsurg-2012-010391](https://doi.org/10.1136/neurintsurg-2012-010391)
- Pliske, G., Voigt-Zimmermann, S., Glaßer, S., & Arens, C. (2016). Objective quantification of the vocal fold vascular pattern: Comparison of narrow band imaging and white light endoscopy. *European Archives of Oto-Rhino-Laryngology*, *273*(9), 2599–2605.
- Potter, K., Rosen, P., & Johnson, C. R. (2012). From quantification to visualization: A taxonomy of uncertainty visualization approaches. In *Proc. of Conf. on Uncertainty Quantification in Scientific Computing* (Vol. 377, pp. 226–249).
- Preim, B., Baer, A., Cunningham, D., Isenberg, T., & Ropinski, T. (2016). A survey of perceptually motivated 3D visualization of medical image data. *Computer Graphics Forum*, *35*(3), 501–525.
- Preim, B., Ropinski, T., & Isenberg, P. (2018). A critical analysis of the evaluation practice in medical visualization. In *Proc. of Eurographics Workshop on Visual Computing for Biology and Medicine (VCBM)*. doi:[10.2312/vcbm.20181228](https://doi.org/10.2312/vcbm.20181228)

- Preim, B., & Saalfeld, P. (2018). A Survey of Virtual Human Anatomy Education Systems. *Computers & Graphics*, *71*, 132–153.
- Qureshi, A. I., Vazquez, G., Tariq, N., Suri, M. F. K., Lakshminarayan, K., & Lanzino, G. (2011). Impact of international subarachnoid aneurysm trial results on treatment of ruptured intracranial aneurysms in the united states. *Journal of Neurosurgery*, *114*(3), 834–841.
- Radaelli, A., Augsburger, L., Cebral, J., Ohta, M., Rüfenacht, D., Balossino, R., Benndorf, G., Hose, D., Marzo, A., Metcalfe, R., et al. (2008). Reproducibility of haemodynamical simulations in a subject-specific stented aneurysm model - a report on the virtual intracranial stenting challenge 2007. *Journal of Biomechanics*, *41*(10), 2069–2081.
- Raghavan, M. L., Ma, B., & Harbaugh, R. E. (2005). Quantified aneurysm shape and rupture risk. *Journal of Neurosurgery*, *102*(2), 355–362.
- Rinaldo, L., McCutcheon, B. A., Murphy, M. E., Shepherd, D. L., Maloney, P. R., Kerezoudis, P., Bydon, M., & Lanzino, G. (2017). Quantitative analysis of the effect of institutional case volume on complications after surgical clipping of unruptured aneurysms. *Journal of Neurosurgery*, *127*(6), 1297–1306.
- Ritter, F., Hansen, C., Dicken, V., Konrad, O., Preim, B., & Peitgen, H.-O. (2006). Real-time illustration of vascular structures. *IEEE Transactions on Visualization and Computer Graphics*, *12*(5), 877–884.
- Roloff, C., Stucht, D., Beuing, O., & Berg, P. (2019). Comparison of intracranial aneurysm flow quantification techniques: standard PIV vs stereoscopic PIV vs tomographic PIV vs phase-contrast MRI vs CFD. *Journal of Neurointerventional Surgery*, *11*(3), 275–282.
- Romijn, M., van Andel, H. G., van Walderveen, M., Sprengers, M., van Rijn, J., van Rooij, W., Venema, H., Grimbergen, C., et al. (2008). Diagnostic Accuracy of CT Angiography with Matched Mask Bone Elimination for Detection of Intracranial Aneurysms: Comparison with Digital Subtraction Angiography and 3D Rotational Angiography. *American Journal of Neuroradiology*, *29*(1), 134–9.
- Ropinski, T., Steinicke, F., & Hinrichs, K. (2006). Visually supporting depth perception in angiography imaging. In *Smart graphics vol. 4073 of lecture notes in computer science* (pp. 93–104).
- Saalfeld, P., Glaßer, S., Beuing, O., Grundmann, M., & Preim, B. (2016). 3D sketching on interactively unfolded vascular structures for treatment planning. In *IEEE Symposium on 3D User Interfaces (3DUI)* (pp. 267–268).
- Saalfeld, P., Glaßer, S., & Preim, B. (2015). 3d user interfaces for interactive annotation of vascular structures. In *Proc. of Mensch und Computer* (pp. 255–258).
- Saalfeld, P., Luz, M., Berg, P., Preim, B., & Saalfeld, S. (2018a). Guidelines for quantitative evaluation of medical visualizations on the example of

- 3d aneurysm surface comparisons. *Computer Graphics Forum*, 37(1), 226–238.
- Saalfeld, P., Glaßer, S., Beuing, O., & Preim, B. (2017a). The FAUST framework: Free-form annotations on unfolding vascular structures for treatment planning. *Computers & Graphics*, 65, 12–21.
- Saalfeld, P., Oeltze-Jafra, S., Saalfeld, S., Preim, U., Beuing, O., & Preim, B. (2017b). *Sketching and annotating vascular structures to support medical teaching treatment planning and patient education*. Eurographics Medical Prize.
- Saalfeld, S., Berg, P., Niemann, A., Luz, M., Preim, B., & Beuing, O. (2018b). Semiautomatic neck curve reconstruction for intracranial aneurysm rupture risk assessment based on morphological parameters. *International Journal of Computer Assisted Radiology and Surgery (IJCARS)*, 13(11), 1781–1793.
- Saalfeld, S., Berg, P., Hirsch, J., & Preim, B. (2017c). Visualization of variations due to ensemble simulations for a bifurcation ia. In *Proc. of Computer-Supported and Robot-Assisted Surgery (CURAC)* (pp. 95–100).
- Saalfeld, S., Voss, S., Preim, B., Beuing, O., & Berg, P. (2019). Flow-splitting-based computation of outlet boundary conditions for improved cerebrovascular simulation in multiple intracranial aneurysms. *International Journal of Computer Assisted Radiology and Surgery (IJCARS)*. doi:<https://doi.org/10.1007/s11548-019-02036-7>
- Schöberl, J. (1997). Netgen: An Advancing Front 2D/3D-Mesh Generator based on Abstract Rules. *Computing and Visualization in Science* 1, 41–52.
- Seibert, B., Tummala, R., Chow, R., Faridar, A., Mousavi, S. A., & Divani, A. A. (2011). Intracranial aneurysms: Review of current treatment options and outcomes. *Frontiers in Neurology*, 2, 45.
- Serbinnenko, F. (1974). Balloon catheterization and occlusion of major cerebral vessels. *Journal of Neurosurgery*, 41(2), 125–145.
- Shamir, A. (2008). A survey on mesh segmentation techniques. *Computer Graphics Forum*, 27(6), 1539–1556.
- Spetzler, R. F., McDougall, C. G., Zabramski, J. M., Albuquerque, F. C., Hills, N. K., Nakaji, P., Karis, J. P., & Wallace, R. C. (2019). Ten-year analysis of saccular aneurysms in the barrow ruptured aneurysm trial. *Journal of Neurosurgery*, 1(aop), 1–6.
- Steenblik, R. A. (1987). The chromostereoscopic process: A novel single image stereoscopic process. In *Proc. of SPIE 0761, True Three-Dimensional Imaging Techniques & Display Technologies* (pp. 27–35).
- Suarez, J. I., Selman, W. R., & Tarr, R. (2006). Aneurysmal subarachnoid hemorrhage. *New England Journal of Medicine*, 354, 387–396.
- Subcommittee on Arteriosclerosis: Andrus, E. C., Allen, E. V., Merritt, H. H., Duff, G. L., Moore, R. A., Kendall, F. E., Shumacker Jr, H. B., Levy, R. L.,

- & Wright, I. S. (2015). The pathogenesis of arteriosclerosis. *International Journal of Epidemiology*, *44*(6), 1791–1793.
- Takao, H., Murayama, Y., Otsuka, S., Qian, Y., Mohamed, A., Masuda, S., Yamamoto, M., & Abe, T. (2012). Hemodynamic differences between unruptured and ruptured intracranial aneurysms during observation. *Stroke*, *43*(5), 1436–1439.
- Tanaka, H., Fujita, N., Enoki, T., Matsumoto, K., Watanabe, Y., Murase, K., & Nakamura, H. (2006). Relationship between variations in the circle of willis and flow rates in internal carotid and basilar arteries determined by means of magnetic resonance imaging with semiautomated lumen segmentation: Reference data from 125 healthy volunteers. *American Journal of Neuroradiology*, *27*(8), 1770–1775.
- The Vascular Modeling Toolkit website. (2019). [www.vmtk.org](http://www.vmtk.org). [Online; accessed 05-July-2019].
- Titford, M. (2005). The long history of hematoxylin. *Biotechnic & Histochemistry*, *80*(2), 73–78.
- Tomycz, L., Bansal, N. K., Hawley, C. R., Goddard, T. L., Ayad, M. J., & Mericle, R. A. (2011). “real-world” comparison of non-invasive imaging to conventional catheter angiography in the diagnosis of cerebral aneurysms. *Surgical Neurology International*, *2*(134).
- Tsakanikas, V. D., Maichalis, L. K., Fotiadis, D. I., Naka, K. K., & Bourantas, C. V. (2012). *Intravascular Imaging: Current Applications and Research Developments*. IGI Global.
- Ustun, C. (2004). Dr. Thomas Willis’ famous eponym: the Circle of Willis. *Turkish Journal of Medical Sciences*, *34*, 271–274.
- Valen-Sendstad, K., Bergersen, A. W., Shimogonya, Y., Goubergrits, L., Bruening, J., Pallares, J., Vernet, A., Piskin, S., Pekkan, K., Geers, A. J., Larrabide, I., Rapaka, S., Mihalef, V., Fu, W., Qiao, A., Jain, K., Roller, S., Mardal, K. A., Kamakoti, R., Spirka, T., Ashton, N., Revell, A., Aristokleous, N., Houston, J. G., Ishida, F., Tsuji, M., Menon, P. G., Browne, L. D., Broderick, S., Shojima, M., Koizumi, S., Barbour, M., Aliseda, A., Morales, H. G., Lefevre, T., Hodis, S., Al-Smadi, Y., Tran, J. S., Marsden, A. L., Vaippummadhom, S., Srinivasan, A., Brown, A. G., Debus, K., Niizuma, K., Rashad, S. M., Owais Khan, M. O., Updegrove, A. R., Shadden, S. C., Cornelissen, B. M., Majoie, C. B., Berg, P., Saalfeld, S., Kono, K., & Steinman, D. A. (2018). Real-world variability in the prediction of intracranial aneurysm wall shear stress: The 2015 international aneurysm CFD challenge. *Cardiovascular Engineering and Technology*, *9*(4), 544–564.
- Valen-Sendstad, K., Piccinelli, M., Krishnankutty, R. R., & Steinman, D. A. (2015). Estimation of inlet flow rates for image-based aneurysm cfd models: Where and how to begin? *Annals of Biomedical Engineering*, *43*(6), 1422–1431.

- Valen-Sendstad, K., & Steinman, D. A. (2014). Mind the gap: Impact of computational fluid dynamics solution strategy on prediction of intracranial aneurysm hemodynamics and rupture status indicators. *American Journal of Neuroradiology*, *35*(3), 536–543.
- van der Marel, K., Gounis, M., King, R., Wakhloo, A., & Puri, A. (2014). P-001 high-resolution optical and angiographic CT imaging of flow-diverter stents for assessment of vessel wall apposition. *Journal of Neurointerventional Surgery*, *6*(Suppl 1), A21–A21.
- Van Pelt, R., Bescos, J. O., Breeuwer, M., Clough, R. E., Groller, M. E., ter Haar Romenij, B., & Vilanova, A. (2010). Exploration of 4D MRI blood flow using stylistic visualization. *IEEE Transactions on Visualization and Computer Graphics*, *16*(6), 1339–1347.
- Van Pelt, R., Gasteiger, R., Lawonn, K., Meuschke, M., & Preim, B. (2014). Comparative blood flow visualization for cerebral aneurysm treatment assessment. *Computer Graphics Forum*, *33*(3), 131–140.
- Vanrossomme, A. E., Eker, O. F., Thiran, J. P., Courbebaisse, G. P., & Zouaoui Boudjeltia, K. (2015). Intracranial aneurysms: Wall motion analysis for prediction of rupture. *American Journal of Neuroradiology*, *36*(10), 1796–1802.
- Varble, N., Rajabzadeh-Oghaz, H., Wang, J., Siddiqui, A., Meng, H., & Mowla, A. (2017). Differences in morphologic and hemodynamic characteristics for phases-based intracranial aneurysm locations. *American Journal of Neuroradiology*, *38*(11), 2105–2110.
- Voß, S., Glaßer, S., Hoffmann, T., Beuing, O., Weigand, S., Jachau, K., Preim, B., Thévenin, D., Janiga, G., & Berg, P. (2016). Fluid-Structure Simulations of a Ruptured Intracranial Aneurysm - Constant versus Patient-Specific Wall Thickness. *Computational and Mathematical Methods in Medicine*, 9854539.
- Voß, S., Berg, P., Janiga, G., Skalej, M., & Beuing, O. (2017). Variability of intra-aneurysmal hemodynamics caused by stent-induced vessel deformation. *Current Directions in Biomedical Engineering*, *3*(2), 305–308.
- Voß, S., Saalfeld, P., Saalfeld, S., Beuing, O., Janiga, G., & Preim, B. (2018a). Impact of gradual vascular deformations on the intra-aneurysmal hemodynamics. In *Proc. of Bildverarbeitung für die Medizin (BVM)* (pp. 359–364).
- Voß, S., Saalfeld, S., Hoffmann, T., Janiga, G., Beuing, O., & Berg, P. (2018b). Fluid-structure interaction in intracranial vessel walls: The role of patient-specific wall thickness. *Current Directions in Biomedical Engineering*, *4*(1), 587–590.
- Wanke, I., & Dörfler, A. (2008). *Intracranial vascular malformations and aneurysms*. Springer Berlin Heidelberg.
- Weigand, S., Saalfeld, S., Hoffmann, T., Eppler, E., Kalinski, T., Jachau, K., & Skalej, M. (2019). Suitability of intravascular imaging for assessment of

- cerebrovascular diseases. *European Journal of Neuroradiology*, 61(9), 1093–1101.
- Weir, B., Amidei, C., Kongable, G., Findlay, J. M., Kassell, N. F., Kelly, J., Dai, L., & Karrison, T. G. (2003). The aspect ratio (dome/neck) of ruptured and unruptured aneurysms. *Journal of Neurosurgery*, 99(3), 447–451.
- Wermer, M. J., van der Schaaf, I. C., Algra, A., & Rinke, G. J. (2007). Risk of rupture of unruptured intracranial aneurysms in relation to patient and aneurysm characteristics: an updated meta-analysis. *Stroke*, 38(4), 1404–1410.
- Wiebers, D. O. (2003). Unruptured intracranial aneurysms: Natural history, clinical outcome, and risks of surgical and endovascular treatment. *The Lancet*, 378, 103–110.
- Wong, S. C., Nawawi, O., Ramli, N., & Kadir, K. A. A. (2012). Benefits of 3D rotational DSA compared with 2D DSA in the evaluation of intracranial aneurysm. *Academic Radiology*, 19(6), 701–707.
- Xiang, J., Natarajan, S. K., Tremmel, M., Ma, D., Mocco, J., Hopkins, L. N., Siddiqui, A. H., Levy, E. I., & Meng, H. (2011). Hemodynamic-morphologic discriminants for intracranial aneurysm rupture. *Stroke*, 42(1), 144–152.
- Xiao, W., Qi, T., He, S., Li, Z., Ou, S., Zhang, G., Liu, X., Huang, Z., & Liang, F. (2018). Low wall shear stress is associated with local aneurysm wall enhancement on high-resolution MR vessel wall imaging. *American Journal of Neuroradiology*, 39(11), 2082–2087.
- Yoshimura, S., Kawasaki, M., Yamada, K., & et al. (2012). Visualization of internal carotid artery atherosclerotic plaques in symptomatic and asymptomatic patients: A comparison of optical coherence tomography and intravascular ultrasound. *American Journal of Neuroradiology*, 33(2), 308–313.



---

## SELBSTÄNDIGKEITSERKLÄRUNG

---

Hiermit erkläre ich, dass ich die Habilitationsschrift und die im Verzeichnis meiner wissenschaftlichen Veröffentlichungen angegebenen Werke selbständig verfasst und keine anderen als die angegebenen Quellen und Hilfsmittel verwendet habe.

*Magdeburg, den 03.06.2020*

  
Sylvia Saalfeld



#### COLOPHON

This document was typeset using the typographical look-and-feel `classicthesis` developed by André Miede. The style was inspired by Robert Bringhurst's seminal book on typography "*The Elements of Typographic Style*". `classicthesis` is available for both L<sup>A</sup>T<sub>E</sub>X and L<sup>Y</sup>X:

<https://bitbucket.org/amiede/classicthesis/>